Elaboration of new hole transporting materials for hybrid perovskite solar cells

Huong Le

UNIVERSITÉ DE CERGY-PONTOISE
UNIVERSITÉ PARIS-SEINE
ECOLE DOCTORALE SCIENCES ET INGENIERIE

LABORATOIRE DE PHYSICOCHIMIE DES POLYMÈRES ET DES INTERFACES

THÈSE DE DOCTORAT

Presentée par

Thi Huong LE

Pour obtenir de grade de DOCTEUR DE L'UNIVERSITÉ CERGY-PONTOISE
SPECIALITE: Chimie organique, minérale, industrielle

ELABORATION OF NEW HOLE TRANSPORTING MATERIALS FOR HYBRID PEROVSKITE SOLAR CELLS

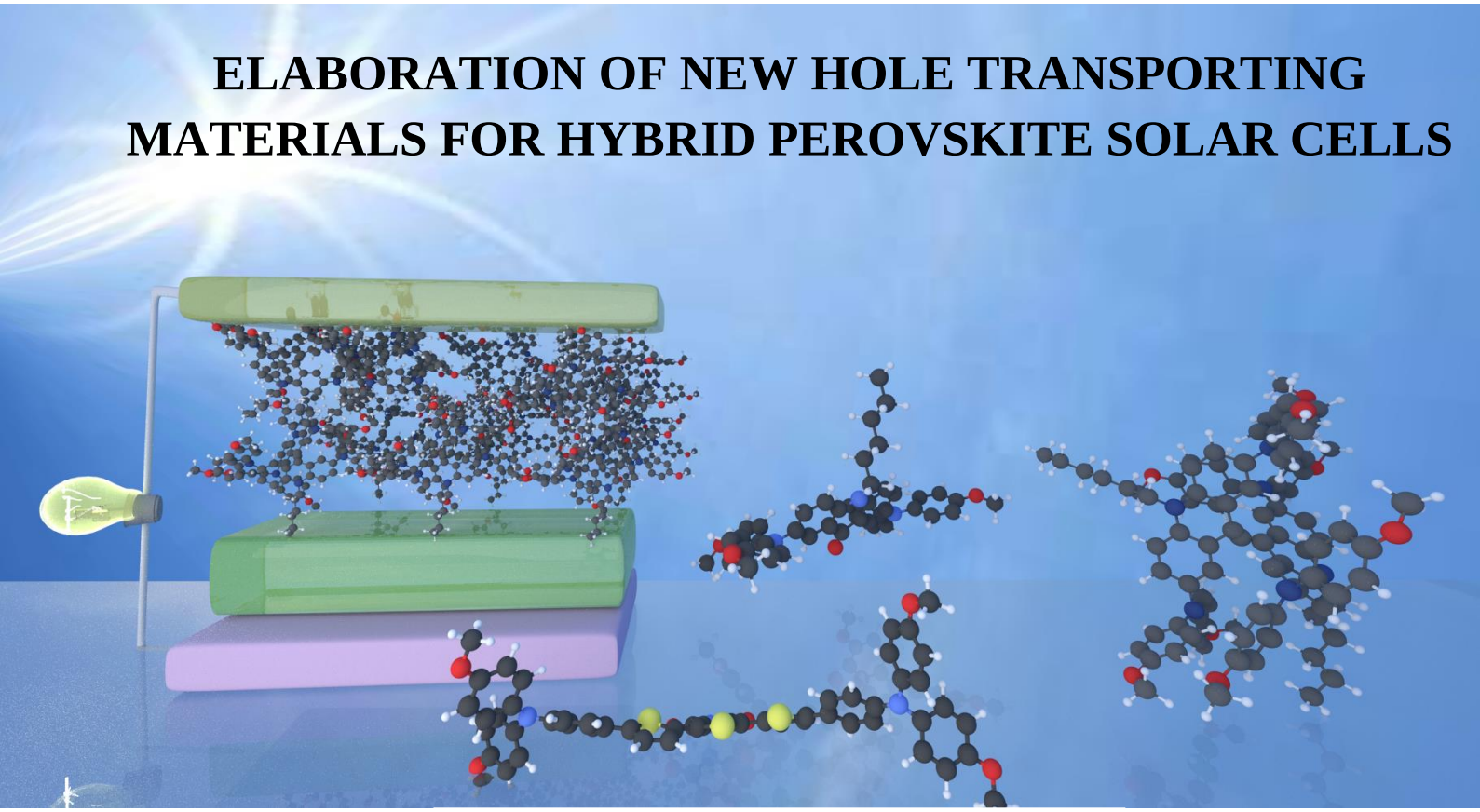

Date soutenance: 22 November 2018

Rapporteurs:	Pr. Jean-Christophe Lacroix, Université Paris Diderot Dr. Nicolas Leclerc, Université de Strasbourg
Examinateurs:	Dr. Céline Olivier, Université de Bordeaux Pr. Jacques Lalevée, Université de Haute-Alsace
Directeur de thèse:	Pr. Fabrice Goubard, Université de Cergy-Pontoise
Encadrant:	Dr. Thanh-Tuân Bui, Université de Cergy-Pontoise

THÈSE DE DOCTORAT

Pour obtenir le grade de DOCTEUR DE L'UNIVERSITE CERGY-PONTOISE

ECOLE DOCTORALE SCIENCES ET INGENIERIE
LABORATOIRE DE PHYSICOCHIMIE DES POLYMÈRES ET DES INTERFACES

ELABORATION OF NEW HOLE TRANSPORTING MATERIALS FOR HYBRID PEROVSKITE SOLAR CELLS

Presentée par

Thi Huong LE

Directeur de thèse: Pr. Fabrice Goubard, Université de Cergy-Pontoise

Encadrant: Dr. Thanh-Tuân Bui, Université de Cergy-Pontoise

Rapporteurs: Pr. Jean-Christophe Lacroix, Université Paris Diderot

Dr. Nicolas Leclerc, Université de Strasbourg

Examinateurs: Dr. Céline Olivier, Université de Bordeaux

Pr. Jacques Lalevée, Université de Haute-Alsace

Cergy, 22 November 2018

ACKNOWLEDGMENTS

The PhD thesis has been mainly done in Laboratoire de Physicochimie des Polymères et des Interfaces (LPPI), University of Cergy-Pontoise. In three years, probably the best moment in my life science, I have worked with a great number of people coming from LPPI and Nam-Gyu Park's group at Sungkyunkwan University, Korea. Without their understanding and continuous supports, this work could be not finished. It is a pleasure to express my gratitude to all with my deep acknowledgment.

First of all, I would like to acknowledge the Vietnam International Education Development (VIED)-Ministry of Education and Training of Vietnam for funding me a PhD fellowship through the Vietnam-France University (USTH) program. I would like to thank Ecole doctorale Sciences et Ingénierie, the university of Cergy-Pontoise and the LPPI laboratory for accepting me as a doctorant student.

I wish to express my deep gratitude to my advisors, Professor Fabrice GOUBARD and Dr. Thanh-Tuan BUI for their patience, continuous guidance and support. I am thankful for generously providing all the resources and always being available for discussion and recommendation. I deeply appreciate the opportunities given to me during three years and all of yours valuable contributions to this work.

I would like to send my great thanks to all members of the committee, Prof. Jean Christophe Lacroix (ITODYs, Université Paris Diderot), Dr. Nicolas Leclerc (CNRS researcher, ICPEES, Université de Strasbourg), Dr. Céline Olivier (CNRS researcher, ISM, Université de Bordeaux) and Prof. Jacques Lalevée (Université de Haute-Alsace) for their devoted time to consider my work.

I gratefully acknowledge all members in LPPI's laboratory, especially Dr. Xavier Sallenave for sufficient discussion and advices of organic chemistry reactions. I also express my gratitude to Dr. Sébastien Peralta for DFT calculation, contact angle measurement and Dr. Phuong Nghiem in I-Mat for AFM measurement and Prof. Pierre-Henri Aubert for his help in electrochemistry and valuable discussion. I wish to express my deep gratitude to all staff and secretary in LPPI for their helps.

Parts of this work are the result of collaboration between Photovoltaic's group in LPPI and Nam-Gyu Park's group. I would like to thank prof. Nam-Gyu Park at Sungkyunkwan University for providing good opportunity, experiment conditions for device fabrication, valuable discussion and inviting me to his group. I also would like to thank all members in Nam-Gyu Park's group, especially An-Na Cho (PhD student) for her help. I would like to thank to Dr. Quang-Duy Dao at Osaka University for his work in device fabrication and photovoltaic measurement and Dr. Quoc-Nghi Pham at Université Paris-Sud for his X-ray characterization. For Thailand collaboration, I wish to send my gratitude to Dr. Nawee Kungwan at Chiang Mai University for his DFT calculation.

Very special thanks are sent all students at LPPI and to my Vietnamese friends in France. You all gave me great energy and pleasant environment inside and outside laboratory to overcome the difficulties during my stay in Paris. Many thanks!

Finally, I would like to say deeply appreciate to my family, my parent, my parent-in-law, my sister for plentiful encouragement, continuous support and love. To my daughters, thanks you all for much consideration and tremendous motivation. To my husband, who inspires me to science, there is no limit of love, unconditional support and encouragement to me. Thank you for everything.

Thi Huong LE

Cergy, November 2018

CONTENTS

LIST OF ABBREVIATION

1D	One dimensional
2D	Two dimensional
3D	Three dimensional
Au	Gold
AFM	Atomic force microscope
$CDCl_3$	Deuterated chloroform
CV	Cyclic voltammetry
D-A	Donor-Acceptor
DCM	Dicholoromethane
DFT	Density functional theory
DMF	N,N-Dimethylformamide
DMSO-d_6	Deuterated Dimethyl sulfoxide
DPA	4,4'-dimethoxydiphenylamine
DSC	Differential scanning calorimetry
DSSCs	Dye-sensitized solar cells
DTP	dithieno[3,2-*b*:2′,3′-*d*]pyrrole
Eg	Optical band gap
E_{HOMO}	HOMO energy
E_{LUMO}	LUMO energy
E_{ox}	Oxidation potential
eq	Equivalent
E_{red}	Reduction potential
ETM	Electron transporting materials
eV	Electron-volt
Fc/Fc^+	Ferrocene/Ferrocenium
FF	Fill factor
FK209	Tris(2-(1H-pyrazol-1-yl)-4-tert-butylpyridine)cobalt(III) tri[bis(trifluoromethane)sulfonimide
FTO	Fluorine-doped tin oxide
HOMO	Highest occupied molecular orbital
HTM	Hole transporting materials
Hz	Hertz
HRMS	High resolution mass spectrometry
IR	Infrared
ICT	Intramolecular charge transfer
J_{SC}	Short-circuit current

J-V	Current density-current
Li-TFSI	Lithium bis(trifluomethanesulfonyl)imide
LUMO	Lowest unoccupied molecular orbital
λ	Lambda
MAI	Methylamonium
ε	Molar absorption coefficient
Na^tBuO	Sodium tert-butoxide
NBS	N-bromosuccinimide
NMR	Nuclear magnetic resonance
PCE	Power conversion efficient
ppm	Parts-per-million
PSCs	Perovskite solar cells
r.p.m	Revolutions per minute
r.t	Room temperature
SEM	Scanning electron microscopy
Spiro-OMeTAD	N^2,N^2,$N^{2'}$,$N^{2'}$,N^7,N^7,$N^{7'}$,$N^{7'}$-octakis(4-methoxyphenyl)-9,9′-spirobi[9H-fluorene]-2,2′,7,7′-tetramine.
Tg	Glass transition temperature
Td	Decomposition temperature
Tc	Crystallization temperature
Tm	Melting temperature
$TBA.PF_6$	Tetrabutylammonium hexafluorophosphate
t-bP	4-Tert-butylpyridine
TCO	Transparent conducting oxide
TT	Thieno[3,2-*b*]thiophene
TGA	Thermogravimetric analysis
THF	Tetrahydrofuran
TPA	4,4'-dimethoxytriphenylamine
TPD	Thieno[3,4-*c*]Pyrrole-4,6-Dione
UV-vis	Ultraviolet-visible
V	Volt
V_{OC}	Open-circuit voltage
XRD	X-ray diffraction
λ	Wavelength
δ	sigma
µL	microlitre

ABSTRACT

The aim of the thesis is to develop and study the potential of organic hole transporting materials (HTMs) for photovoltaic applications using perovskite-based solar cells (PSCs). Several families of HTM molecules have been prepared and deposited in solution for the fabrication of solar cells. Since the main objective is to study and provide information on the relationship between the molecular structure of new hole transport materials and the photovoltaic performances obtained, this study contributes to a better fundamental understanding of the required properties of hole transport materials for better photovoltaic performance.

The first study concerns the development of p-type molecules based on Thieno [3,2-b] thiophene as a central unit and π-linker with dimethoxytriphenylamine as end-capping electron donors. Different configurations are designed and revealed significantly different photovoltaic performances in the PSC devices. Remarkable, a planar structure with linear conjugation shows higher values of mobility and conductivity than others, thus it improved device performances.

In the second study, donor-acceptor molecules based on 9(10H)Acridone derivatives as an acceptor were developed. By incorporating different electron-donating fragments, we obtain structures with favorable characteristics for both good intramolecular charge transfer (ICT) character and adequate HOMO-LUMO energy levels. Their energy levels are suitable for collecting and injecting the holes from perovskite to the metal electrode through the HTM. Similar studies have been done with Thioxanthone.

Using a cheap precursor and facile preparation, the third study synthesized a 9.9'-biacridone derivative. These p-type molecules possess a three-dimensional structure which is similar to that of Spiro-OMeTAD, state-of-the-art molecule for PSCs.

Finally, the last study focus on the development of donor-acceptor molecules based on thieno [3,4-c] pyrrole-4,6-dione (TPD). The objective is elaboration of the planar structure molecule which could be improved the π-π stacking effect in the device fabrication without grain boundaries. These molecules also own a strong ICT character, an extended π-conjugation on the whole structure and a good solubility which makes it an ideal candidate for the dopant-free HTM in PSCs.

RÉSUMÉ

La thèse a pour but d'élaborer et d'étudier les potentialités des semi-conducteurs organiques, transporteurs de trous (HTMs) pour l'application photovoltaïque à l'aide de cellules solaires à base de pérovskite (PSCs). Plusieurs familles de molécules HTM ont été préparées et déposées en solution pour l'élaboration des cellules solaires. L'objectif principal étant d'étudier et d'apporter des informations sur la relation entre la structure moléculaire des nouveaux matériaux de transport de trous et les performances photovoltaïques obtenues, cette étude contribue à une meilleure compréhension fondamentale des propriétés requises des matériaux de transport de trous pour de meilleures performances photovoltaïques.

La première étude concerne l'élaboration d'une molécule de type *p* à base de thieno [3,2-b] thiophène comme élément central avec des dérivés de dimethoxytriphenylamine comme donneurs d'électrons aux extrémités. Différentes conformations sont proposées et révèlent des performances photovoltaïques significativement différentes dans les dispositifs PSC. Notons par exemple, qu'une conformation de structure planaire favorisent la conjugaison avec des valeurs élevées de mobilités et conductivités obtenues.

Dans la seconde étude, des molécules donneur-accepteurs à base de dérivés d'acridone 9 (10H) comme accepteur ont été élaborés. En y associant différents fragments donneurs d'électrons, on obtient des structures présentant des caractéristiques favorables à la fois pour de bons transferts de charge intramoléculaire (ICT) et des niveaux d'énergie HOMO-LUMO adaptés et favorisant l'injection des trous de la pérovskite vers l'électrode métallique via le HTM. Des études similaires ont été effectuées avec la thioxanthone.

A partir d'un précurseur bon marché et d'une préparation aisée, la troisième étude a permis de synthétiser un dérivé de 9,9'-biacridone, molécule push-pull de type p révélant une structure tridimensionnelle, similaire à celle du Spiro-OMeTAD, molécule référence pour les PSCs.

Enfin, la dernière étude concerne l'élaboration de molécules donneur-accepteur à base de thiéno [3,4-c] pyrrole-4,6-dione (TPD). La motivation de cette partie est le développement de la molécule à structure planaire améliorant l'empilement π-π dans la fabrication de dispositifs sans joints de grains. Ces molécules possèdent également un fort caractère ICT, une conjugaison π étendue sur toute la structure et une bonne solubilité ce qui en fait un candidat HTM idéal pour la réalisation d'un dispositif PSCs sans dopant.

GENERAL INTRODUCTION

In 1839, a French experimental physicist, Edmund Becquerel discovered photovoltaic effect while doing experiment with an electrolytic cell made by two metal electrodes[1]. In 1883, the first solar cell was made by the American inventor Charles Fritts[2] and he used selenium as active layer and an extremely thin layer of gold as electrode. Energy conversion efficiency was between 1% and 2%. At that time, photovoltaic effect could not be well understood; therefore it could not be compared to electromagnetic effect which was basic theory for electric generator run by coal-fired steam or water force. However, fossil fuels such as coal, natural oil or gas are not endless resources and human's demand is rising as fast as increasing of population. In fact, solar, wind, hydropower, biomass, geothermal as renewable energy resources are sufficient alternative solutions. Among them, solar energy is promising resource and photovoltaic solar cells can directly convert sunlight to electricity. According to global energy potential, solar energy with huge potential power can alone supply power to the earth. Nowadays, the photovoltaic solar cells have been developing from various technologies and materials to obtain high efficiency and long-term operation.

Simultaneously, in 1839, the German mineralogist Gustrav Rose found perovskite material – a calcium titanate based mineral which named for the Russian mineralogist Lev von Perovsky. Perovskites have been used in wide range utilizations from conductors to insulators. In particular, perovskite materials have been studied in various structure modifications and applied in numerous applications[3] such as condensers, electromechanical transducers, resistors, piezoelectric resonators, gas sensors, lasers, luminescent light-emitting devices, nonlinear optical crystal for optoelectronic and so on. In photovoltaic and opto-electronic applications, perovskite materials have attracted much attention due to their superior light-harvesting characteristics, strong and wide range light absorbing, direct band gap, high charge carrier mobility and small exciton binding energy[4]. In 2009, perovskites $CH_3NH_3PbX_3$ (X = Br or I) were first attempted as photosensitizer in liquid electrolyte-based dye-sensitized solar cells (DSSCs) by Miyasaka's group[5] with an efficiency around 3-4 %. Due to the instability of the deposited perovskite in liquid electrolyte, solid hole conductor Spiro-OMeTAD was employed and consequently efficiency increased up to 9.7% and stability improved as well [6]. In very short time from August 2012 to March 2013, power conversion efficiency

(PCE) with perovskite sensitizer improved as high as 14.1%. Nowadays, the highest efficiency is 22.7% (NREL best research-cell efficiencies) for perovskite single junction architecture. Therefore, perovskite solar cells are the fastest-advancing solar technology to date[7].

One of the main questions is "what is limitation of perovskite solar cells?" The statements are both high efficiency and stability which are still possible through structural modification and devices optimization. In a bright expectation, PSCs with outstanding properties could achieve a higher efficiency than GaAs solar cells[8]. To improve efficiency of PSCs, the physical properties of each component and their interfaces should be optimized. To enhance stability of PSCs, the mixed perovskite structure materials, additive-free charge transport materials and encapsulation technique must be taken into account. Moreover, solution processing and thin layer devices are effective solutions to reduce cost of PSCs. For environment sustainability, lead-free PSCs and non-toxic solvents in device fabrication should be applied. Among different layers of the PSC's structure, hole transporting materials (HTMs) is one of the key point materials and plays important role for device operation. They collect holes from valence band of perovskite absorber and transport them to the metal electrode.

My doctoral thesis concerns the design and the synthesis of new organic semiconducting materials for efficient HTMs. In the first chapter, basic theory and techniques of PSCs elaboration and device measurements will be described. Especially, hole transporting materials and their fundamental structure-property will be discussed in detail.

In the second chapter, a series of electron donor materials based Thieno[3,2-*b*] thiophene will be studied. The impact of different molecular configurations to photovoltaic performance will be briefly demonstrated. Therefore, they will provide the idea how to elaborate new efficient HTMs for PSCs.

In the third chapter, two classes of donor-acceptor molecules will be studied based on 9(10H)-Acridone and Thioxanthone precursors. Due to rich chemistry possibilities, low-cost, facile preparation and chemical modification, they will be designed and synthesized to act as new HTMs. These materials were expected to have intramolecular charge transfer (ICT) property due to their push-pull effect. The ICT property might improve hole mobility/conductivity of these molecules. By changing from amine group

(=N-H) in Acridone to sulfur atoms (=S) in Thioxanthone molecules, their thermal, optical and electrochemical properties will be investigated and comparatively studied. The sulfur atoms in Thioxanthone could improve the interfacial contact between the HTM and the perovskite due to the compatibility of lead cations and sulfur atoms. Finally, p-type molecules based on 9,9'-biacridone will be developed from 9(10H)-Acridone molecule. The obtained three-dimensional structure is similar to state-of-the-art Spiro-OMeTAD. Therefore, these materials will be also characterized with some expecting properties such as amorphous structure, large steric hindrance and homogenous film morphology.

In the fourth and the last chapter, another series of donor-acceptor molecules based on Thieno[3,4-*c*]pyrrole-4,6-dione will be designed and synthesized according to fundamental understanding of previous studied HTMs. Their planar structures are expected to improve intermolecular π-π stacking effect. By incorporating of different electron donor moieties (TPA(-OCH_3) and TPA(-SCH_3), and different π-bridge length (thiophene, thieno[3,2-b]thiophene and dithieno[3,2-*b*:2',3'-*d*]pyrrole, these materials would express some interesting properties such as wide absorption region, low energy band gap, high fluorescence property, strong π-π stacking effect and high hole mobility. They are expected to be efficient additive-free HTM for PSCs.

All of these molecules were investigated by thermal (TGA-DSC), optical (absorption-emission), electrochemical (cyclic voltammetry), morphological (AFM-XRD diffraction) characterizations and then some of them have been used as new HTMs in PSCs. Additionally, the theoretical study (DFT calculation) was employed and obtained data was compared to the experimental results. The relationship of structure-properties-device performance will be clearly discussed in each chapter when it is possible.

After all, a summary on my work will be given and some perspective will be suggested.

Chapter I

Hole transporting materials for hybrid perovskite solar cells

CHAPTER I: HOLE TRANSPORTING MATERIALS FOR HYBRID PEROVSKITE SOLAR CELLS

I.1. Perovskite solar cells

Renewable energy resources are effective solutions to alternative exhausting fossil fuel on the earth. Solar, wind, geothermal, hydrogen, tidal, wave, hydroelectric, biomass, nuclear energy have been employing and developing for huge human demand. Among them, solar energy is likely an unlimited source which we are only using a small amount. They can be used everywhere in the earth, even on satellite and spacecraft[9]. Up to now, photovoltaic solar cells, which directly convert sunlight to electricity, have been developed for over two centuries from many technologies. Crystalline Si-based cells, single-junction, multi-junction cells, thin-film technologies have been studied and optimized. The racing of different kinds of solar cells is going faster and more competitive based on cost-effective, high efficiency and long-term stability criteria (***Figure 1***).

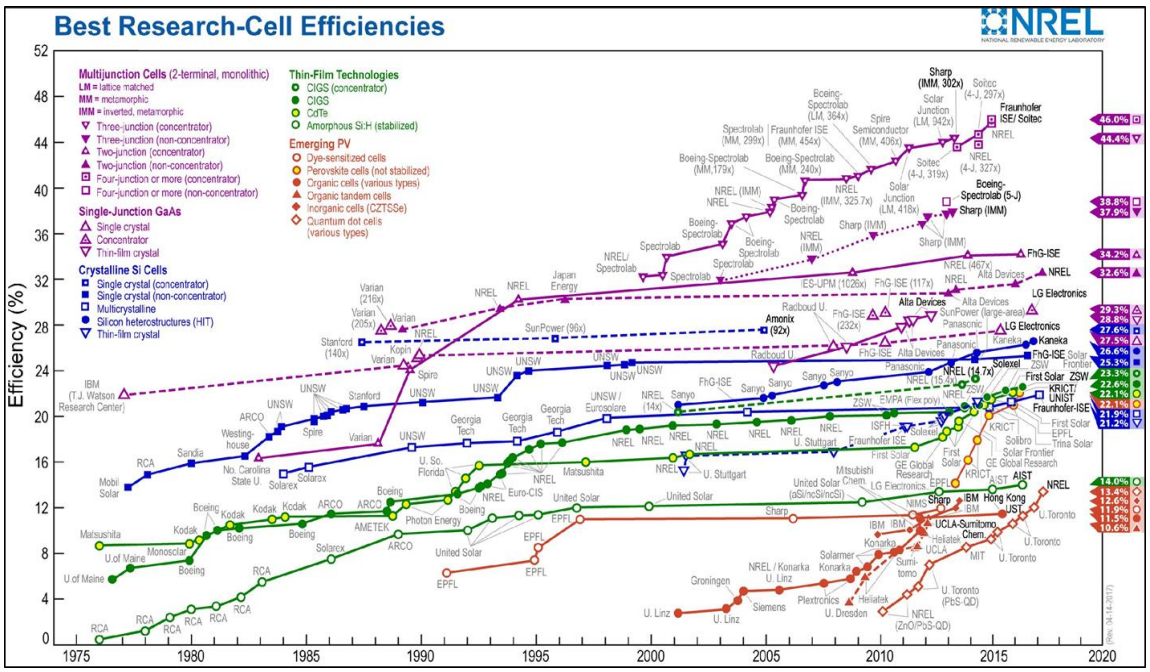

Figure 1: Efficiency chart of different solar cell technologies. Figure adapted from National Renewable Energy Laboratory (NREL), Golden, CO, USA.

Recently, the emerging third generation photovoltaic solar cells have been developing such as dye-sensitized solar cells (DSSCs)[10], perovskite solar cells (PSCs)[8], organic solar cells (OPVs)[11], and quantum dot solar cells[12]. As a newcomer, the efficiency

of perovskite materials-based solar cells have been dramatically increased from 3.8% in 2009[5] to 22.7% in late 2017[13] and becoming the fastest-advancing photovoltaic technology to date.

Inorganic-organic hybrid perovskites are remarkable materials for photovoltaic[14] as well as optoelectronic[15] and photonic[16] applications. Due to their interesting optical properties in low-dimensional structure and large wavelength absorption, it permits variety functionalization of light generation, emission, transmission and detection[17]. For instance, perovskite materials have been studying in enormous applications such as LED[18,19], photodetector[20], waveguide[21], nanolaser[22] and flexible, printable solar cells[23]. (***Figure 2***)

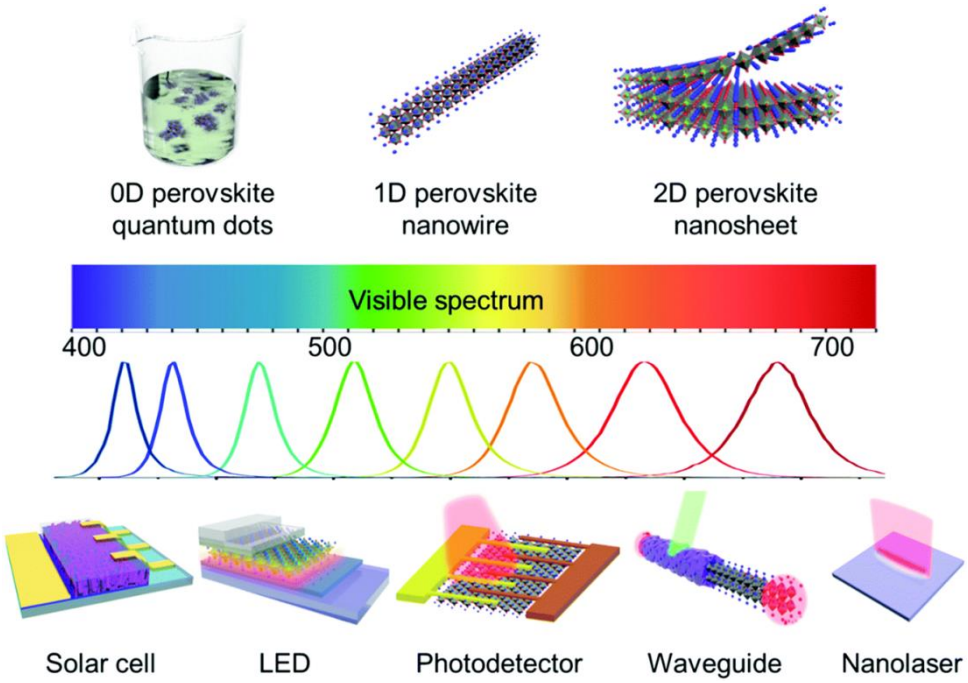

Figure 2: Spectrum range and abundant applications of all-dimension metal-halide perovskite. Figure adapted from ref[17]

In photovoltaic application, perovskite has been first employed as photo-sensitizer in dye-sensitized solar cells (DSSCs)[5] in 2009 and high efficiency PSCs over 15%[24,25] was obtained in solid-state inorganic-organic hybrid perovskite solar cells. In which, the dimensionality (or morphology)[26] of the perovskite absorber affects to the light absorption, excitation dissociation and carrier transport properties and thus concerns to the photovoltaic performance. For example, Im *et al*[27] reported a PCE of 6.5% with $MAPbI_3$ quantum dot (0D perovskite) solar cells, one of the highest value for certified quantum dot sensitizers. Notably, in quantum dot state with tunable grain size ~2-20nm, they exhibit optical and electronic behaviors completely different compared with other

dimensional structures. Quantum dot in perovskite solids[28] exhibit large extinction coefficient, high photoluminescence quantum yield and multiple-exciton generation characteristics, thus useful for optoelectronic devices. Thereafter, Im *et al*[29] also published 100 nm-diameter of perovskite nanowire (1D perovskite) in PSCs which exhibits high photocarrier extraction and lateral conductivity and obtained PCE of 14.71%.

In parallel, 2D perovskite have been also investigated as light-absorbing materials for solar cells. Zhang *et al*[30] employed hybrid $(C_4H_9NH_3)_2(CH_3NH_3)_3Pb_4I_{13}$ doped Cs^+ ion in PSCs and obtained high PCE of 13% and good moisture resistance. It improved environmental stability because the bulkier organic component is more hydrophobic than $CH_3NH_3^+$ ions; therefore it requires more energy to remove an organic part from 2D-structure than $CH_3NH_3^+$ in 3D nanocuboid-structure. It can be a promising applicant for environmental-stable PSCs. However, their limitations are low absorption coefficient, poor charge transport and large exciton binding energy.

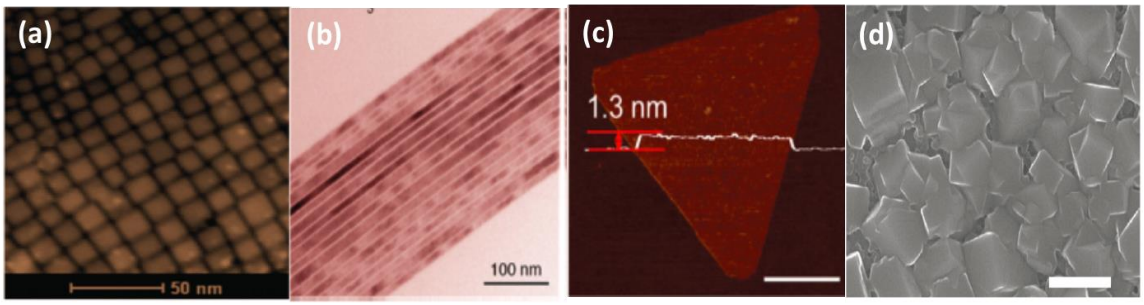

Figure 3: Low-dimensional structure of perovskite materials. (a) STEM image of $CsPbBr_3$ quantum dots (0D perovskite). Figure adapted from ref[31]. (b) TEM image of $CsPbBr_3$ nanowires (1D perovskite). Figure adapted from ref[32]. (c) AFM image of ultrathin $CH_3NH_3PbI_3$ nanosheet with a thickness of 1.3 nm (2D perovskite). Figure adapted from ref[33]. (d) SEM image of $CH_3NH_3PbI_3$ cuboid with a cuboid size of ~360 nm (3D perovskite). Figure adapted from ref[34].

Figure 3 shows examples of low-dimensional structure of perovskite-based materials. By each various dimensions, they exhibit different properties and thus leading to numerous electronic and optoelectronic applications.

Interestingly, 3D-structure perovskite also shows abundant prospects for solar cells. For example, it possesses high extinction coefficient[35], appropriate-direct band gap[36], small excitation binding energy[37], long exciton and charge diffusion length[38]. Furthermore, it exhibits wide light absorption throughout the visible and near infrared spectrum, long carrier lifetime, resulting in long diffusion length up to few microns and so that the carriers can be transported safely across thick perovskite absorber without

recombination[39]. Therefore, perovskite with ideal cubic structure has been mostly using in PSCs.

Based on 3D-structure configuration, the structure of PSCs devices have been optimized and the structural evolution of PSCs is shown in ***Figure 4***. Perovskite was first used as photo-absorber which is replaced to dye in DSSCs[5]. In ***Figure 4a***, nano-dot perovskite is absorbed by mesoporous oxide layer (TiO_2-electron transporting layer) and then HTM layer is infiltrated inside the mesoporous layer to promote heterojunction. The role of TiO_2 is needed for separating the photo-excited electrons in perovskite. However, PSCs was confirmed to work without electron transporting layers (ETLs) and electron transportation through the perovskite layer is much faster than through the n-type TiO_2[40]. Therefore, insulating Al_2O_3 film has been used as scaffold[41] and perovskite layer was coated on the top. Consequently, electron transfer process occurred into the perovskite layer (***Figure 4b***). The PCE is slightly improved, so the optimization approach could focus on perovskite layer. Back of mesoporous TiO_2 layer, a pillared structure was proposed in which perovskite is fulfilled in mesoporous film instead of coating on surface (***Figure 4c***). The PCE is significantly increased from 9.7%[42] (***4a***) to 12%[43] (***4c***) and 15%[25] in case of two-step spin-coating. In additional, a *p-i-n* junction PSCs has been also studied which consists of perovskite film as intrinsic layer, *n*-type thin TiO_2 film and *p*-type HTM film (***Figure 4d***). This planar PSCs structure is fabricated by co-evaporation of CH_3NH_3I and $PbCl_2$ and PCE was recorded over 15%[24].

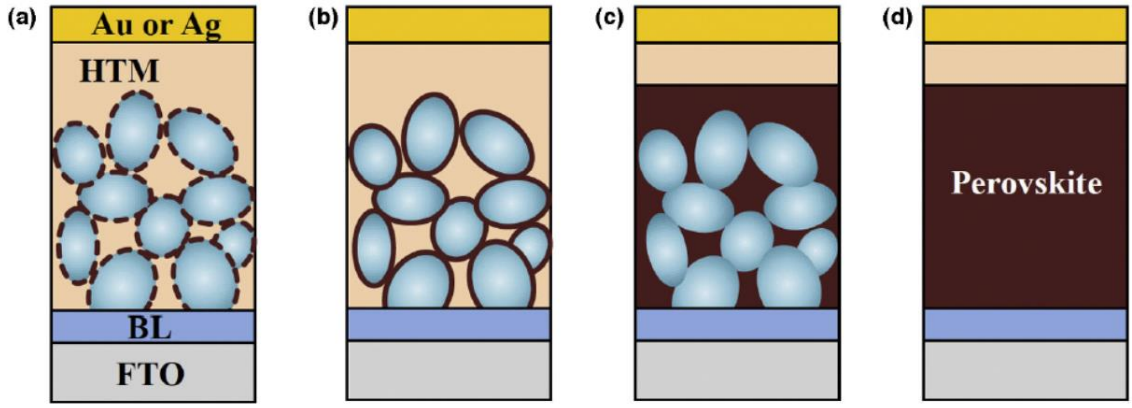

Figure 4: Structural evolution of perovskite solar cells. (a) Sensitization concept with surface absorption of nanodot perovskite, (b) PSCs with non-injecting Al_2O_3 scaffold layer, (c) pillared structure PSCs and (d) planar p-i-n heterojunction concept. Figure adapted from ref[44].

Recently, *p-n* junction PSCs approach has been also obtained attention. $CH_3NH_3PbI_3$ can be used as p-type semiconductor and thick nano-sheet of TiO_2 film is used as n-type layer. The PCE improved from 5.5%[45] (with nano-sheet TiO_2 film) to 8%[46]

(with thin nanoparticles TiO_2 film) and then up to 11%[47] because of optimization of depletion region width at the TiO_2-perovskite junction. A certified PCE of 12.8%[48] was obtained and displayed high stability for over 1000 hours in ambient air under full sunlight. In this case, HTM-free PSCs can be taken consider for cost-effective solar cells.

I.1.1 Structure and operation

Perovskite materials-based PSCs can be presented by a general formula ABX_3, in which A can be an organic cations such as methylamonium[49] ($CH_3NH_3^+$), formamidium[50] ($NH=CHNH_3^+$) (FA) or phenylamonium[51] ($C_6H_5NH_3^+$) or inorganic cations[52] such as Cs^+ or Rb^+. B is heavy metal cations such as Pb^{2+}, Sn^{2+}, Sb^{3+}, Bi^{3+} [53] and X is halide anions such as I^-, Cl^- or Br^-[54] (***Figure 5a***). By modifying each components of perovskite, their absorption and optical-electrical properties would be tuned[55–58]. For example, the optical band gap of perovskite could be changed from 1.48 eV to 1.57 eV and to 1.73 eV for $FAPbI_3$, $MAPbI_3$ and $CsPbI_3$, respectively[59]. When changing halide ion from I to Br, they changed colors and the optical band gap increased from 1.57 eV ($MAPbI_3$) to 2.2 eV ($MAPbBr_3$)[60].

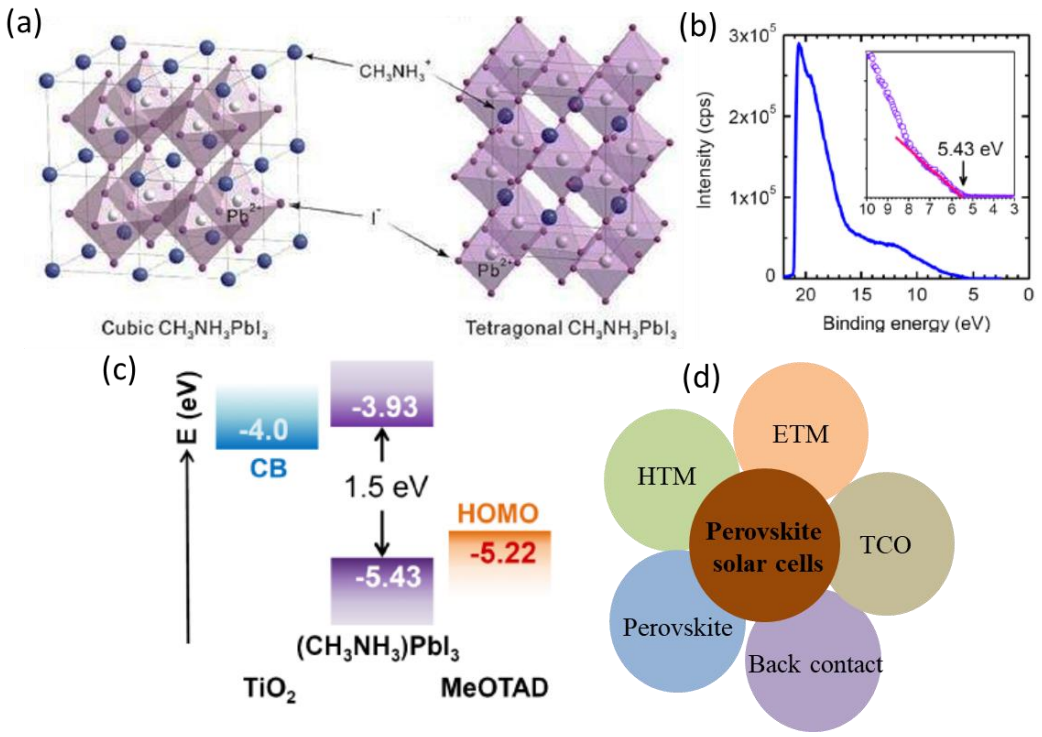

Figure 5: (a) Atomic models of $MAPbI_3$ with cubic phase and tetragonal phase. Figure adapted from ref[61]. (b) XRD spectra of the $MAPbI_3$ tetragonal phase and cubic phase. Figure adapted from ref[62]. (c) UPS spectrum of the $MAPbI_3$-sensitized TiO_2 film and (d) schematic energy level diagram of TiO_2, perovskite $MAPbI_3$, Spiro-OMeTAD. Figure adapted from ref[42]. (e) Illustration of the PSC as a multi layers device.

However, the high PCE has been recorded over 20% with band gap of around 1.55 eV by using $MAPbI_3$[63]. It possesses a cubic structure at high temperature and transfer to a tetragonal structure close to room temperature[64]. In fact, there are no critical differences between the two phases, except slight rotation of PbI_6 octahedral along the c-axis. Ideally, they exit in cubic crystal structure, in which the corner sharing BX_6 octahedral and the A-cation are located at interstitial space created by the eight adjacent octahedral in the 3D structure. Thus, $MAPbI_3$ is still favorable perovskite materials in PSCs.

The energy level and band gap of $MAPbI_3$ perovskite were determined and shown in ***Figure 5b-c***. Valence band energy (E_{VB}) is estimated to -5.43eV below vacuum level and conduction band energy (E_{CB}) is corresponded to -3.93 eV, slightly higher than E_{CB} of TiO_2, which is well aligned for charge separation. ***Figure 5d*** illustrates combination of different layers in PSCs. A transparent conducting oxide (TCO) such as fluorine-doped tin oxide (FTO) or indium-doped tin oxide (ITO) is coated on glass substrate, faces to incoming sunlight and acts as the anode. A nanoporous metal oxide, generally TiO_2, is deposited as blocking layer on TCO to avoid contact of the TCO-HTM and reduce recombination. A mesoporous layer of metal oxide is then deposited on compact TiO_2 as a scaffold and/or ETM for the perovskite layer. Herein, we are discussing about TiO_2-conducting layer, so the electrons transfer mechanism takes place by injection through the mesoporous layer. In contrary, a mesoporous Al_2O_3-insulating layer is also used scaffold. However, electron injection from perovskite to Al_2O_3 is not allowed, this process is occurred by different mechanism[40]. Otherwise, ETM could be replaced by different metal oxide such as ZnO, SnO_2, SiO_2, ZrO_2 or organic materials such as phenyl-C_{61}-butyric acid methyl ester ($PC_{61}BM$) and indene C_{60} bisadduct (ICBA)[65]. To date, the most commonly ETM used in PSCs is mesoporous TiO_2. The thickness, pore size and porosity of mesoporous TiO_2 are crucial parameters and they need to be carefully controlled. After that, perovskite filled to mesoporous TiO_2 layer and perovskite crystals are formed by annealing. The suitable HTM is then deposited on the top of perovskite layer and finally, the back metal electrode is thermal evaporated.

Basically, two mainly kinds of PSCs structures are normal configuration (*p-i-n* structure) and inverted configuration (*n-i-p* structure) and mechanism of charge carrier transport in each structure are shown in ***Figure 6***. For example, normal configuration PSCs consists of FTO/compact-TiO_2/mesoporous-TiO_2/perovskite/HTM/Au while inverted PSCs structure contains ITO/PEDOT:PSS/HTM/perovskite/PCBM/Al. When sunlight illuminates the perovskite absorber layer, it generates both electrons and holes,

simultaneously. Electrons will be injected to ETM and hole will be transported by HTM, then they are collected by working and counter electrodes, respectively. These charge carrier species will be transported to external circuit and produce photocurrent. The new ETMs and HTMs are being investigated to improving device performances. The PSCs performance could be determined according to many factors such as power conversion efficiency (PCE), reproducibility of devices, long-term operation and environmental stability.

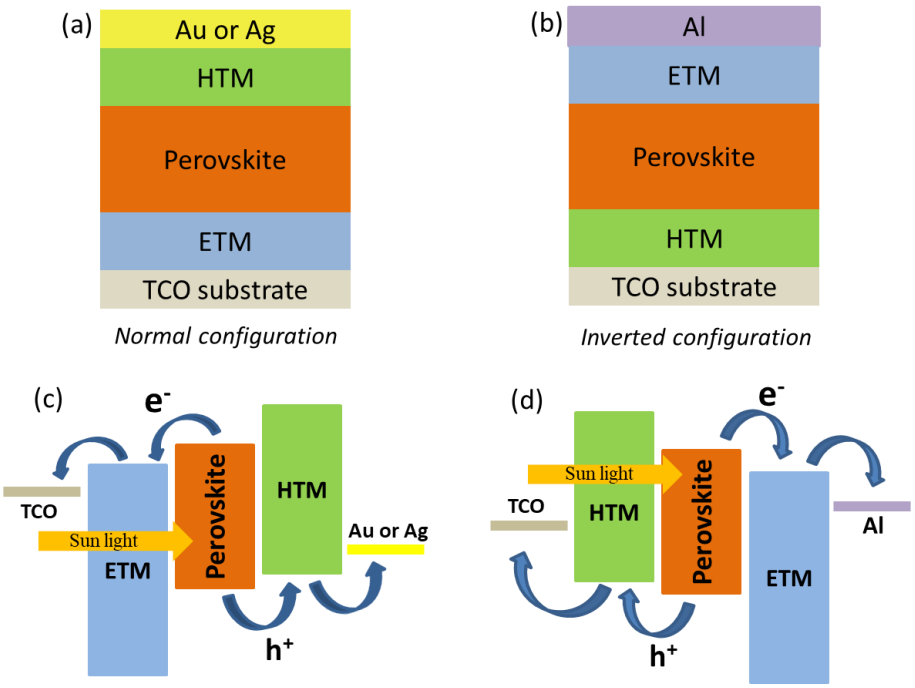

Figure 6: (a) Normal structure of PSCs with n-type ETM facing incoming light. (b) Inverted structure of PSCs with p-type HTM facing incoming light. (c) Mechanism of carrier transport in normal configuration and (d) Mechanism of carrier transport in inverted configuration.

Noticeably, perovskite layer is one of the most importance layers which significantly affect PSCs performances. In laboratory scale, the $CH_3NH_3PbI_3$ perovskite layer can be formed through either one-step or sequential two-steps spin-coating method[54] (***Figure 7a***). The solution casting method and thermal evaporation[24] are also possible techniques (***Figure 7b***). Park *et al*[66] studied the impact of perovskite's morphology on device performances. It depends on the fabrication methods of $CH_3NH_3PbI_3$. In one-step spin-coating, dimethylacatamide (DMA) is first used to dissolve equimolar of PbI_2 and CH_3NH_3I and then this mixture is spin-coated on the top of the mesoporous TiO_2 layer. When only DMA or dimethylformamide (DMF) is employed and evaporated during annealing, it generated small and non-uniform perovskite crystals. So far, DMA is then replaced by mixture of solvents as DMF and dimethyl sulfoxide (DMSO). In this case,

DMSO is used as Lewis base adduct which can control crystal growth and generate homogenous pinholes-free perovskite film[67].

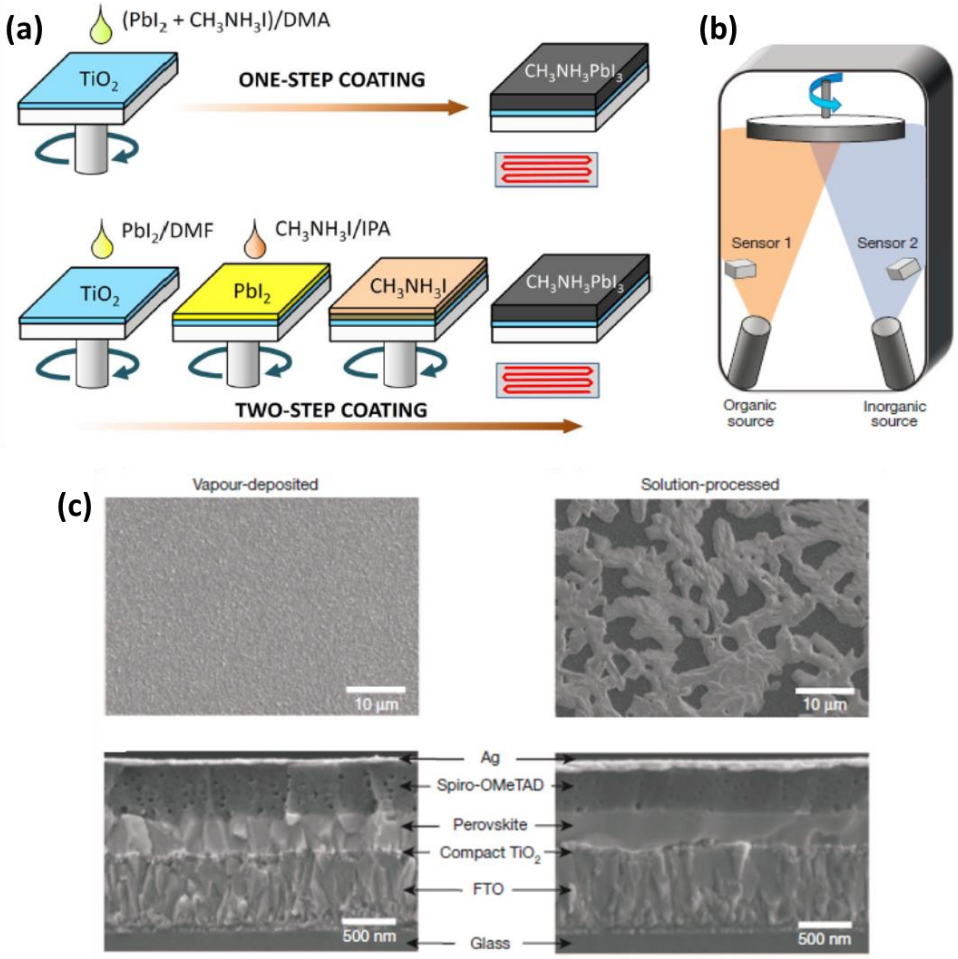

Figure 7: (a) One-step and two-step spin-coating procedures for $CH_3CH_3PbI_3$ formation. Figure adapted from ref[66]. (b) Dual-source thermal evaporation system for depositing the perovskite absorber. Figure adapted from ref[24]. (c) SEM top viewed (top) and cross-sectional viewed (bottom) of complete solar cells constructed by vapor-deposited and solution-processed methods. Figure adapted from ref[24].

In sequential two-step spin-coating method, PbI2 is dissolved in DMF and spin-coated on mesoporous TiO2, then the solution of methylammonium (MAI) in 2-propanol is loaded on the PbI2-coated substrate, followed by annealing. In this method, the size of perovskite crystals is controlled by the pore size of TiO¬2, thus small perovskite crystals are formed. In two-step deposition, TiO2 layer was fully covered by perovskite layer while one-step method leads to incomplete coverage and uncontrolled variation in morphology, results to a poor reproducibility of device performance. This significant improvement is depend on anti-solvents such as toluene, chlorobenzene, ethers, trifluorotoluene and etc. The role of anti-solvents is increase heterogeneous nucleation via the creation of an instantaneous local supersaturation on the spinning substrate and without dissolve final perovskite film68. This solvent engineering approach was

considered to be effective and resulted good quality perovskite. According to this enhancement, the PCE of over 20% in mesoscopic PSCs with very small hysteresis effect13 was reached.

Additionally, vapor-deposited film method has been also taken into account to form extremely uniform and generate hundreds of nanometers length scale of perovskite crystals[24] while large scale (ten of micrometer) of perovskite crystals are formed via solution-processed. The top-view and cross-sectional of SEM images (***Figure 7c***) highlighted the differences of film morphologies which are fabricated by vapor-deposited and solution-processed method. The thickness of perovskite film is a key parameter that is necessary to be optimized. If the film is too thin, it will not absorb sufficient sunlight. Inversely, if the film is too thick, it can impact to diffusion length and charges will not be collected at the p-type and n-type heterojunctions. Full coverage by perovskite layer will avoid direct contact between HTMs and the TiO_2 compact layer, improving fill factor and open-circuit voltage. Another distinct advantage of solution deposition over evaporation processing is the compatibility with thin-film solar cells production technologies. This infrastructure could already be employed for large scale PSCs production.

Furthermore, PSCs have been also fabricated by various methods[69] in lab-sized and large scale such as drop-casting, ultrasonic spray-coating, blow-drying, blade-coating, slot die coating, brush printing, electrochemical deposition, reactive ink-jet printing, chemical or physical vapor deposition and so on. In larger scale production, roll-to-roll (R2R) printing technique has been widely employed to produce large area flexible PSCs[70].

To evaluate the device performance, a typical current-voltage characteristic of a solar cell is measured in dark and under illumination (***Figure 8***).

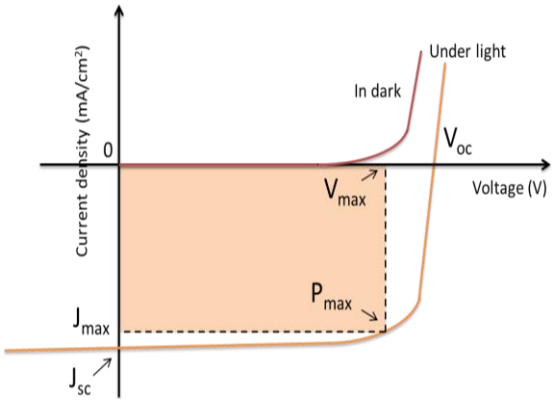

Figure 8: Current-voltage characteristics of photovoltaic solar cells in dark and under illumination.

The power conversion efficiency of a cell can be determined by the area enclosed by the fourth quadrant of the curve under illumination. In which, V_{OC}, J_{SC} and fill factor (FF) are the important parameters which evaluate directly to PCE of solar cells. Depending on materials, deposition methods and device fabrications, these values could be adjusted and enhanced PCE.

The metrics highlighted in the ***Figure 8*** are:

- J_{max} : Current density at maximum power
- V_{max} : Voltage at maximum power
- P_{max} : The maximum output power
- J_{SC} : Short-circuit current density
- V_{OC} : Open-circuit voltage

Particularly, power conversion efficiency of solar cells can be calculated by following equation:

$$PCE = \frac{P_{out}}{P_{in}} = \frac{J_{SC}.V_{OC}.FF}{P_{in}} \qquad FF = \frac{J_{max}V_{max}}{J_{SC}V_{OC}}$$

In solar cells, the short-circuit current density J_{SC} value was affected by the absorption characteristics of the photoactive layer and the charge generation/transport/extraction properties of the charge transporting layer while open-circuit voltage V_{OC} was affected by energy levels of the photoactive materials, work function of electrode materials and charge carrier recombination rate. Therefore, high efficiency is still possible achieved through structural modification of entire PSC components. In the perovskite layer, the optical band gap and perovskite crystalline structure could be tuned by modifying component of perovskite materials. For electron transport layer, it could be doped to enhance electrical conductivity[71]. In case of hole transporting layer, hole mobility and conductivity are crucial properties which should be determined and improved by either molecular engineering or doping process. In particularly, hole carrier drift mobility can be determined by various methods such as time-of-flight (TOF)[72], analysis of steady-state, trap-free, space-charge limited current (steady-state TF-SCLC)[73,74], analysis of dark injection space-charge-limited current (DI-SCLC)[73,75], analysis of the performance of OFETs (FET technique)[76] and so on. Among these methods, the SCLC method and FET technique have been most used to measure the carrier drift mobility of organic semiconductors. However, due to the low charge carriers mobility in organic semiconductors, the injected carrier forms a space charge. This space

charge creates a field that opposes the applied bias and thus decreases the voltage drop across junction; as a result, space charge limited currents (SCLCs) have been proposed as the dominant conduction mechanism in organic semiconductors by many scientists[75]. ***Figure 9a*** showed structure of a hole-only device used in steady-state TF-SCLC which consists of a thin organic semiconductor (~200 nm to 2 μm in thickness) sandwiched between two electrodes. In this technique, it requires one hole injection contact (PEDOT:PSS layer) and one injection-blocking contact (Au electrode). Theoretical calculation and experimental evidence indicate the injection barrier should not higher than 0.3 eV for SCLC experiments[77]. Thus, to enhance the hole injection, ca. 50 nm of PEDOT:PSS layer is coated on ITO before apply of HTM film.

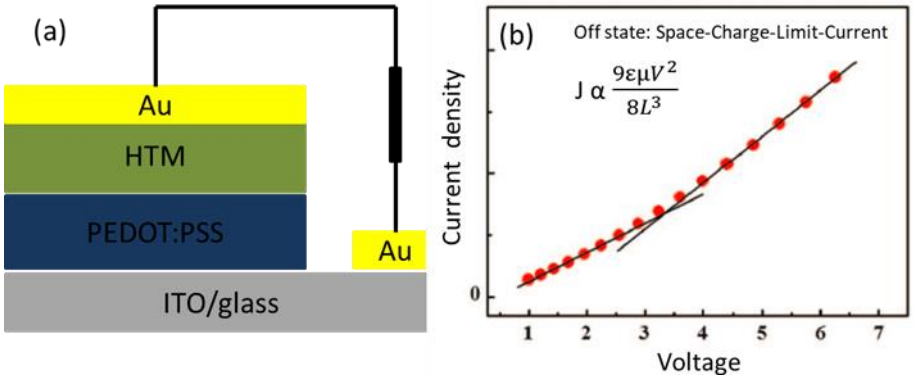

Figure 9: (a) Schematic structure of hole-only device used in steady-state TF-SCLC method. (b) The hole mobility characteristic of semiconducting materials from SCLC method in the dark condition.

The measurement of carrier drift mobility by the steady-state TF-SCLC method is based on the analysis of current density-applied voltage characteristic in the dark (***Figure 9b***). In general, the *J-V* curve is linear at low voltage, showing ohmic behavior and at high applied voltage the *J-V* characteristics become space-charge-limited because of the injection of charge carrier from one electrode. When the contact between the electrode and the organic layer is ohmic and the current is transport-limited instead of injection-limited, the space charge limited current J is calculated by following equation, which so-called Mott-Gurney equation[78]:

$$J = \frac{9}{8}\varepsilon_{r.}\varepsilon_{0.}\mu_{h0.}e^{0.89.\gamma\sqrt{E}}.\frac{V^2}{L^3}$$

where ε_o is the permittivity of free charge, ε_r is the dielectric constant of the active layer and μ_{h0} is the zero-field hole mobility. V is the voltage drop across the device and L is the HTM material thickness. However, the mobility values are different depending on the thickness of samples, especially for low-mobility dispersive materials[79].

Conductivity is also fundamental physical property which is measured by using four-point probe methodology[80] through resistivity measurement. In this characterization, some parameters such as sample thickness, dimensionally, anisotropy, the relative size and geometry of the sample with respect to the contact assembly are need to be considered[81]. In general, the conductivity of organic materials are low (in the range of 10^{-15} to 10^{1} S/cm^{2})[82], thus doping process is necessary to increase electrical conductivity of these organic semiconductors.

I.1.2 Role of HTMs in PSCs

As mentioned above, it is reasonable to make *p-n* junction HTM-free PSCs because perovskite exhibits ambipolar behavior; it can work as light absorber, act as *n*-type and *p*-type materials and charge can be efficiently performed in few hundred nanometer-thick of perovskite layer. The HTM-free solar cells possess simple structure, thus reducing the cost. In 2012, Etgar *et al*[45] has first reported a heterojunction solar cells by mean of HTM-free mesoscopic $MAPbI_3$ perovskite as p-type material, *ca*. 500 nm of anatase TiO_2 film as n-type material and gold film as back contact. The remarkable results were obtained with J_{SC} = 16.1 mA/cm^2 and a fill factor FF = 0.57, corresponding to PCE of 5.5% under AM 1.5. Thereafter, various researches have been developed HTM-free PSCs to realize low-cost, high efficiency of solar cells. Li *et al*[83] have successful studied HTMs-free PSCs with inverted configuration and obtained high PCE of 16% (***Figure 10a***) with very low hysteresis and maintained PCE about 1000 hours in glovebox. The device consist of ITO/$MAPbI_3$/C_{60}/BCP/Ag in which C_{60} was deposited on the perovskite film as an electron transport layer (ETL) and the 2,9-dimethyl-4,7-diphenyl-1,10-phenanthroline (BCP) layer was coated over C_{60} as a hole blocking layer.

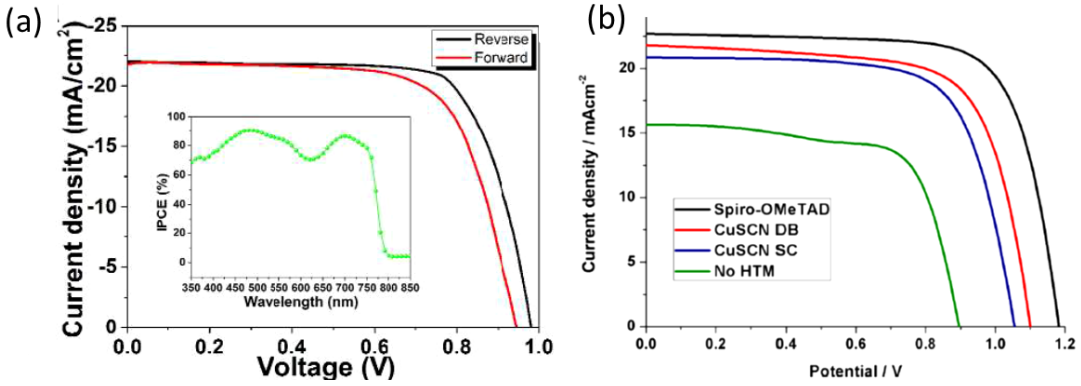

Figure 10: (a) Forward-reverse bias current density–voltage characteristics of the HTM-free PSCs and IPCE spectrum (inset). Figure adapter from ref[83]. (b) J–V curves of mixed perovskite solar cells based on CuSCN, spiro-OMeTAD, and no hole-transporting materials. Figure adapted from ref[84].

Although HTMs-free PSCs is promising approach for cost-effective solar cells, the highest certified PCE of 22.7% is attributed by mesoscopic PSCs employed organic HTMs[13]. A comparison between organic HTM (i.e., Spiro-OMeTAD), inorganic HTM (i.e., CuSCN) and HTM-free has been studied and those devices showed different *J-V* curves (***Figure 10b***). In this study, the device performance of PSCs which employed Spiro-OMeTAD as organic HTM, the value of J_{SC}, V_{OC} and FF are higher than inorganic HTM, significant improved than HTM-free device in the similar conditions. Herein, all the components of PSCs are kept constant and HTM layer would be optimized. We will focus on studying of HTMs in such PSCs. The HTMs plays key role in PSCs such as collecting and transporting holes from valence band of perovskite layer to back contact metal, protecting perovskite layer out of moisture, and minimizing charge recombination. Therefore, HTMs is an important part of PSCs for improving PCE and stability of devices. In coming section, a detail summary of HTMs will be introduced.

I.1.3 Challenges and optimizations

Currently, Both PSC photovoltaic performance and stability have been improved thanks to an increasing of carrier diffusion length to hundreds of microns, low exciton binding energy and high optical absorption coefficient of perovskite-based materials[44]. In fact, perovskite has important role not only as photo-absorber but also as central recombination and good interface of ETMs and HTMs. Therefore, one of the strategies to improve device performance is deal with perovskite's issues. First issue comes from the band gap of perovskite, which is direct band gap[36] or indirect band gap[85] depend on perovskite-based materials[86]. For example, in direct band gap, it exhibits higher absorption coefficient but faster recombination rate compare to indirect band gap. Secondly, the energy alignment between the light absorber and the charge transporting materials (ETMs and HTMs) need to be considered. The energy level of these layers should be appropriate for beneficial charge collection and transport process. The interfaces of these layers should be controlled to optimize morphology and minimized pinholes formations in devices. Large defect density could be formed within or near the surface of materials and hysteresis phenomena in PSCs could be identified by current-voltage (***Figure 11a***). Alongside, this phenomena could be explained by ferroelectric properties of perovskites or excess ions which leads to unstable film during device operation[87]. Thirdly, the *J-V* hysteresis of PSCs could be caused by many factors such as:

scan direction, scan rate, voltage range, precondition, architecture of PSCs[88]. Especially, the main drawback of perovskite is its sensitivity to environment like moisture, light or temperature which results to degradation. In ***Figure 11b-c***, the degradation of perovskite was determined by XRD spectra, in which the presence of PbI_2 peaks was clearly observed. Creation of mixed halide perovskite is one of the alternative solutions, for example, $CH_3NH_3PbI_3$ and $CH_3NH_3PbBr_3$ to form $CH_3NH_3PbI_{3-x}Br_x$ (x=0-3)[60]. Triiodide and tribromide perovskite have different band gap, the mixture of anions will lead to changing of the band gap and thus adjusting the absorption wavelength. Cubic $CH_3NH_3PbI_{3-x}Br_x$ perovskite was confirmed to be stable with humidity soaking test and the presence of bromide ion in $CH_3NH_3PbI_3$ lattice might enhance the stability of $CH_3NH_3^+$ cation.

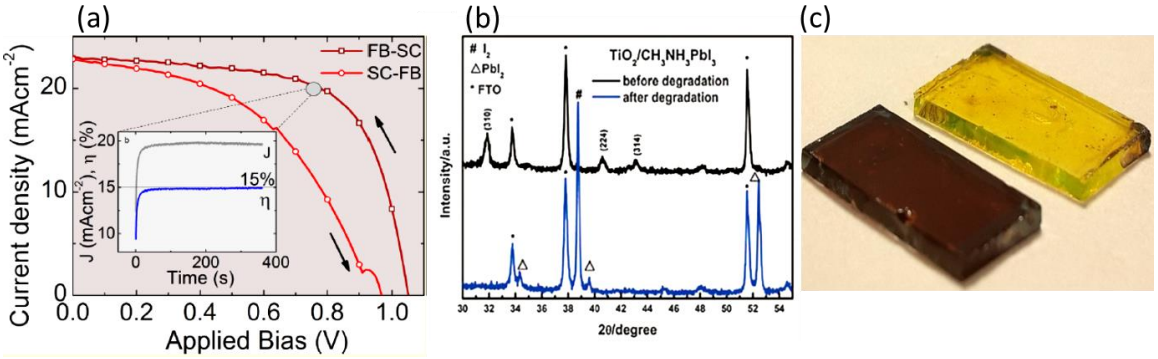

Figure 11: (a) Hysteresis of PSCs. Figure adapted from ref[87]. (b) XRD of perovskite-sensitized TiO2 before and after degradation. Figure adapted from ref[89]. (c) Appearance of perovskite film before and after degradation.

Finally, the toxicity of lead in perovskite structure needs to be taken into consideration. Lead-based perovskite tends to release toxic PbI_2 in degradation. Therefore, it should be preferable to find an alternative cation. The most obvious choice for Pb replacement is to use another group 14 metal, such as Sn or Ge. From recent researches, Sn-based halide perovskite exhibits very promising properties for optoelectronic applications due to their optical band gaps in the red/infrared region and good charge-carrier mobilities.[90] However, by computational studies, scientists realized that no other metal cation is able to match the unique optoelectronic properties such of Pb- and Sn-based perovskites[91,92]. Even though, by partially or totally Pb replacement, this is a promising new research direction in perovskite solar cells and halide-based optoelectronics application.

I.1.4 Conclusions and outlooks

One of the most important potential advantages of PSCs is its low cost. According to cheap and ease chemical modification, perovskite exhibits many interesting properties which have been used in numerous optoelectronic applications. Therefore, it is able to produce cost-effective PSCs and many perovskite-based electronic devices.

However, aforementioned challenges of PSCs will have to be addressed and solved before producing large-scale tandem PSCs. High efficiency; long operating lifetime and eco-friendly degradation are some optimizations we are developing toward. Higher efficiency can be obtained through molecular engineering of HTMs and structural modification of entire PSCs components. Solar cells require operating in intensive sunlight without degradation for many years. To achieve, 2D-structure perovskite or mixed halide perovskite are possible solutions because both of the two methods could enhance stability of perovskite layer. Lead-free PSCs is also a considered tendency to avoid toxic chemical degradation and Sn, Ge are prominent replacement. Moreover, encapsulation technique, humidity resistance and photo-stability materials should be developed.

Now, it is time for commercialization because perovskite materials is suitable for outstanding flexibility solid state PSCs. Thin layer devices, printable and flexible PSCs will be certainly commercialized in near future.

I.2 Hole transporting materials in PSCs

The main function of the hole transporting materials is to collect and carry holes from the valence band of the perovskite layer to the back contact metal (cathode). To be efficient HTMs, they should have some prerequisite properties such as:

- The HOMO energy level of HTMs should be located slightly higher than the valence band of the perovskite and its LUMO energy level should effectively block the recombination between the electrons in perovskite and hole in HTMs.
- High hole mobility and conductivity.
- High thermal and photochemical stability, solution-processing.

To date, many research groups have developed and optimized hundreds of HTM to obtain high PCE and long-term stability. In general, they have been categorized into some main types such as inorganic and organic HTMs. In organic HTMs, they were

subdivided to conjugated polymers, coordination compounds and small molecules HTMs (***Figure 12***).

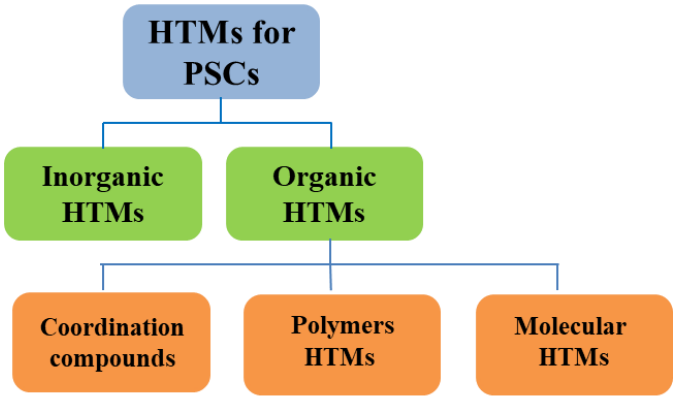

Figure 12: Classification of hole transporting materials for PSCs

Herein, the characteristics, advantages, disadvantages of each class of HTMs in PSCs will be summarized. Then, we can discuss how they can be further modified-optimized and how we can design and develop new efficient HTMs.

I.2.1 Inorganic p-type semiconductors as HTMs

Recently, inorganic *p*-type semiconductors has been widely developed as hole transporting layer due to their wide-direct band gap, high intrinsic stability, extremely high hole mobility, good optical transmittance and low cost fabrication, solution processibility[93,94]. Additionally, inorganic materials are predicted to be more stable than organic materials in case of high temperature and moisture stability. Therefore, various inorganic HTMs have been studied and employed in PSCs such as copper-based (*i.e.* CuI[95], CuO_x[96], CuSCN[97], CuS[98], Cu_2ZnSnS_4[99]), Ni oxide (NiO_x)[100], carbon-based[101] (*i.e.* graphene, carbon nano tube and nanographene), transistion metal oxide (*i.e.* CoO_x[102], VO_x[103], WO_3 and MoO_x[104]), hybrid HTMs[105–108] (organic-inorganic composite HTMs) or quantum dots[109–111]. The energy level diagram of representative inorganic HTMs is given in ***Figure 13.***

(a)

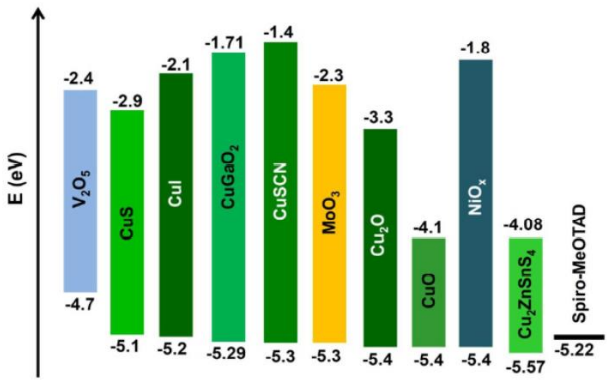

(b)

HTM	Hole mobility (cm^2/Vs)
spiro-MeOTAD	4×10^{-5}
Cu_2ZnSnS_4	6-30
Cu_2O	100
CuO	0.129
CuSCN	0.01-0.1
$CuAlO_2$	3.6
$CuCrO_2$	7.7
$CuGaO_2$	0.01–10

Figure 13: (a) The energy level diagram of representative inorganic HTMs along with HOMO level of Spiro-OMeTAD. (b) Hole mobility of some inorganic HTMs compared to Spiro-OMeTAD. The figure and table adapted from ref [94]**.**

The first inorganic HTMs, CuI, has been employed in PSCs with a PCE equal to 6%[112] while Spiro-OMeTAD yielded 7.9% without additives/dopants. Although high hole mobility (~ 9.3 $cm^2V^{-1}s^{-1}$), the ammonia solution could dissolve CuI as well as perovskite layer. Moreover, iodine free atoms in CuI could act as valence band trap and work as a recombination channel, thus leading to reduce V_{OC}. To overcome, Chen *et al*[113] optimized the device by using CuI in inverted planar PSCs and showed an interesting PCE ~ 13.6%. Another example is Cu_2O, which possesses extremely high hole mobility (~100 $cm^2V^{-1}s^{-1}$), long carrier diffusion length and direct band gap (~2.17 eV). In inverted configuration ITO/Cu_2O/$CH_3NH_3PbI_3$/PCBM/Ca/Al[96], this device performance showed V_{OC} ~1.07 V, J_{SC} ~ 16.52 $mA.cm^{-2}$, FF ~0.75 and high PCE ~13.35%. It is comparable with V_{OC} ~0.95 V, J_{SC} ~ 14.82 $mA.cm^{-2}$, FF ~0.78 and PCE ~11.04% for PEDOT:PSS-based device. Furthermore, by using CuO_x from facile solution-processed in inverted planar PSCs, the highest PCE ~17% was reported by Sun *et al*[114]. Remarkably, by using CuSCN as HTM, an impressive PCE of up to 20.4% was obtained in regular PSCs and 17.5% in inverted PSCs[115], which is competitive with 20.9% of Spiro-OMeTAD[116].

Recently, hybrid HTMs which is mixed of organic-inorganic, inorganic-inorganic, composite or bilayer HTMs have been applying and obtained positive signals. Some

examples of efficient hybrid HTMs are CuSCN/Spiro-OMeTAD (18.02%)[117], $CuAlO_2$/PEDOT:PSS (14.52%)[118], r-GO/PTAA (17.2%)[107], PTAA/MoS_2 (16.89%)[119], NiO_x/GO (graphene oxide) (11.2%)[120] and so on[94]. Clearly, by that combination, organic HTMs layer can be protected by inorganic HTMs and/or proportional alignment between two kinds of HTMs is beneficial for improving hole extraction and minimizing recombination. They can amplify good features and reduce imperfection.

To summarize, inorganic HTMs could be optimized in some points to improve PCE and stability. First, energy level of inorganic HTMs should be controlled to be compatible with the VB of the perovskite layer. Second, the HTMs-perovskite interface interaction should be optimized for high-quality thin film HTMs. Here, the "interface" meaning is focus on interface defect passivation, interface compatibility, charge transfer kinetics and interface templated oriented grain growth. And finally, deposition techniques should be developed to obtain homogenous, less defect HTMs layer and avoid dissolve of perovskite layer.

I.2.2 Organic HTMs

A huge number of organic HTMs have been developed due to their facile preparation and purification, and their properties are able to be modified through chemical modification. New organic HTMs should have some features such as optical transparent in visible spectrum with no absorption screen effect toward the active materials/absorber; an amorphous phase is also required with a glass transition temperature above 100^oC to avoid crystallization in device processing. Homogenous film forming and full coverage of perovskite layer are both favorable properties. Moreover, it should own adequate hole mobility (possibly >10^{-3} cm^2/V.s) in order to carry the hole and avoid charge recombination.

In literature, state-of-the art Spiro-OMeTAD has been used as sufficient HTMs in DSSCs and PSCs. To date, the best PSCs performance is 22.7%[13] of PCE by $CH_3NH_3PbI_3$-based perovskite and Spiro-OMeTAD as p-type HTMs.

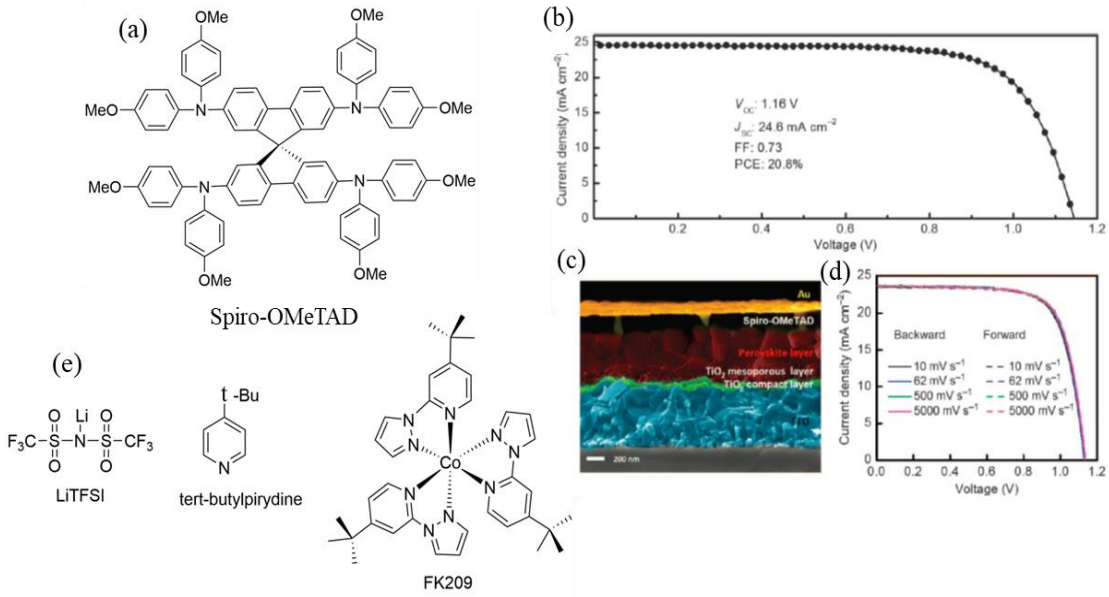

Figure 14: (a) Chemical structure of p,p-Spiro-OMeTAD (b) J-V characteristic of champion PSCs used Spiro-OMeTAD under AM 1.5 G illumination. (c) Cross-sectional SEM image of champion device. (d) Hysteresis measurements of one device at different scanning speeds under AM 1.5 G illumination. Figure (b-d) adapted from ref[121],(e) additives/dopants most used in PSCs are Li-TFSI, t-BP, FK209.

Spiro-OMeTAD is still one of the most important HTMs. It maintains amorphous nature leading to smooth film morphology, high glass transition temperature (125°C)[122], electrochemical stability and optical transparent. In ***Figure 15a***, Spiro-OMeTAD employed as a HTM predominantly quench the perovskite emission, demonstrating efficient charge extraction and reducing charge-carrier recombination in steady-state photoluminescence spectra.

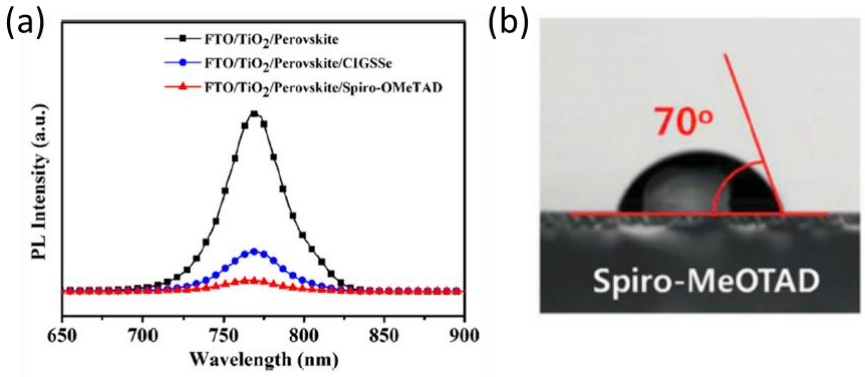

Figure 15: (a) Steady-state photoluminescence (PL) spectra for $MAPbI_3$, $MAPbI_3$ /copper indium gallium disulfoselenide (CIGSSe), and $MAPbI_3$/ Spiro-OMeTAD layers deposited on FTO/bl-TiO_2/mp-TiO_2 substrates. Figure adapted from ref[123] (b) Water contact angles of the spiro-MeOTAD coated on FTO substrate. Figure adapted from ref[124].

In contrast, Spiro-OMeTAD exhibits some drawbacks such as:

(a) Low hole mobility/conductivity: in pristine form, Spiro-OMeTAD shows low hole mobility and conductivity ($1.67.10^{-5}$ $cm^2/V.s$ and $3.54.10^{-7}$ S/cm, respectively)[125]. Therefore, it needs to be oxidized by additives/dopants to enhance hole mobility/conductivity ten-fold and improve PSCs performance. On the other side, hygroscopic additives/dopants are main reasons for device degradation.

(b) Negative impact on stability: by using hygroscopic additives in Spiro-OMeTAD, it effected to long-term stability of the devices. For example, the contact angle of coated Spiro-OMeTAD film is 70^o which showed low hydrophobicity, it could impact to water penetration into the perovskite layer (***Figure 15b***). Qi *et al*[126] demonstrated that small molecules in the air could be passed freely through small pinholes in the amorphous materials. Moreover, the foreign molecules such as water and other gas molecules from the air can be diffused through pathway of pinhole to thin film layer. Then, they become impurities and leading to decay of device and diminish of PCE.

(c) Multi-steps preparation: Spiro-OMeTAD is expensive chemical due to multi-steps and complicated preparation. Its synthesis requires low temperature (-78^oC), sensitive precursors (*n*-BuLi or Grignard regent), combative Br_2 reagent involved or costly sublimation step for purification. However, recent price of Spiro-OMeTAD (in high purity > 99%) is comparable and lower than others well-known HTMs. As survey, price of Spiro-OMeTAD, P3HT and PTAA are 311€, 441€ and 1905€ (for 1g packing) respectively but most of these molecules fail to show performance similar to that of Spiro-OMeTAD[127].

Therefore, it is necessary to find new efficient HTMs that cost-effective, construct the PSCs with high efficiency and long-term stability.

I.2.2.1 Coordination compounds as HTMs

Recently, coordination compounds have been also investigated as HTMs in PSCs. Up to date, the promising candidate molecules are phthalocyanines (Pc) and porphyrin since they are less expensive and more stable[128–130]. They possess low band gap, electronic delocalization with strong π-π interaction, rich redox property and relative high

hole mobility. The optical and electronic properties of Pc can be easily modified by changing the central metal and the peripheral substituents[131]. Moreover, they possess a very good solubility in a wide range of organic solvents, thus they are suitable for solution processing PSCs.

However, Pc is approaching to both form aggregates on the metal oxide semiconductor surface and to have a lack of directionality in the excited state, which limit the efficiency performance[132]. To overcome these drawbacks, long alkyl chain or phenoxy group at the peripheral sites can avoid aggregation and should improve PSCs performance.

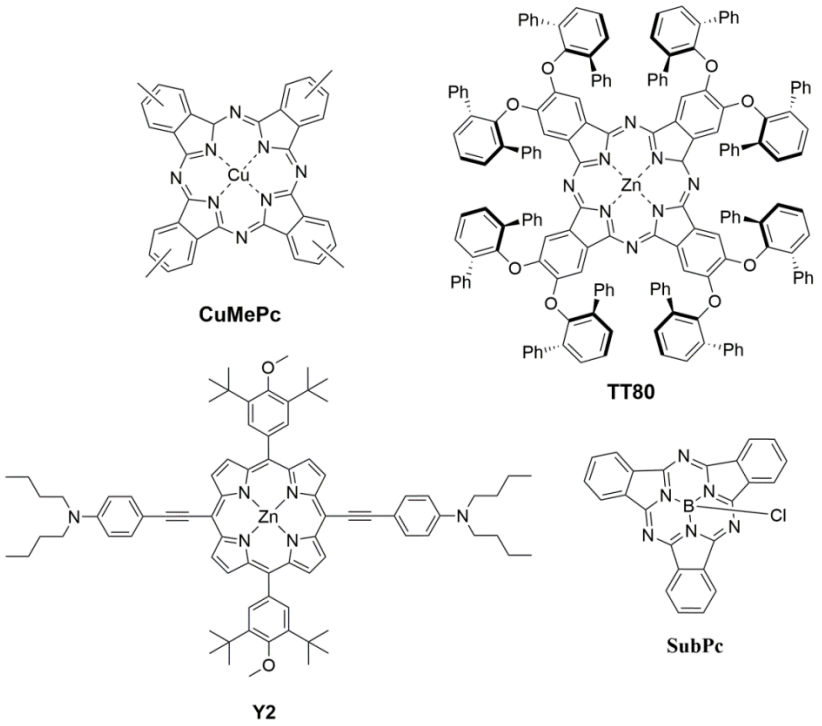

Figure 16: Representative molecules of coordination compounds used as HTMs in PSCs.

Figure 16 shows some examples of coordination compounds as HTMs which have been used in PSCs. For example, PSCs employed tetramethyl-substituted CuMePc[133] as HTMs, achieving PCE of 5.2%, V_{OC} ~0.7 V, J_{SC} ~16.9 mA/cm^2 and FF~0.4. This work confirmed that methyl substitution allows strong π-π interaction and higher charge carrier mobility[134]. Interestingly, substitutions by phenoxy units improve significant solubility of **TT80** and efficiency PCE reach a value of 6.7%[135] by solution-processed and increased up to 15.42%[136] by fully vacuum-processed. Remarkably, this un-encapsulated device was confirmed more stable than with Spiro-OMeTAD and only 2.78% of initial PCE lost under continuously 1000h of illumination. Subphthalocyanines are also potential candidate for sufficient HTMs because their crystal packing can be

adjusted by adequately substituting the porphyrinoid and improved π-π stacking effect. Lianos *et al*[137] have used symmetrical 14-π aromatic boron subphthalocyanines (SubPc) as HTMs and achieved a PCE of 6.6% without dopants/additives.

Porphyrin derivatives have been used as efficient photosensitizer in DSSCs[138] in spite of its superior light-harvesting property which could competitive absorb to photosensitizer material. For instance, zinc porphyrin (**Y2**)[139] has been also employed in PSCs and surprisingly, it worked well and showed PCE of 16.6% competitively to 18% of Spiro-OMeTAD. Therefore, this kind of materials could be used as HTM in PSCs.

I.2.2.2 Conjugated polymers as HTMs

Conjugated polymers are also good candidates HTMs which exhibit higher hole mobility than small molecules[140] and widely used in solid state-DSSCs and PSCs. In addition, they exhibit low energy band gap, appropriate solubility and high conductivity. ***Figure 17*** shows chemical structure of most common conjugated polymers which have been used in PSCs. They are poly(3-hexylthiophene (P3HT), polytriarylamine (PTAA) and poly(3,4-ethylenedioxythiophene): poly(styrenesulfonate) (PEDOT:PSS) which achieved the best PCE in PSCs, 15.3%[141], 22.1%[50] and 18.1%[142] until now, respectively.

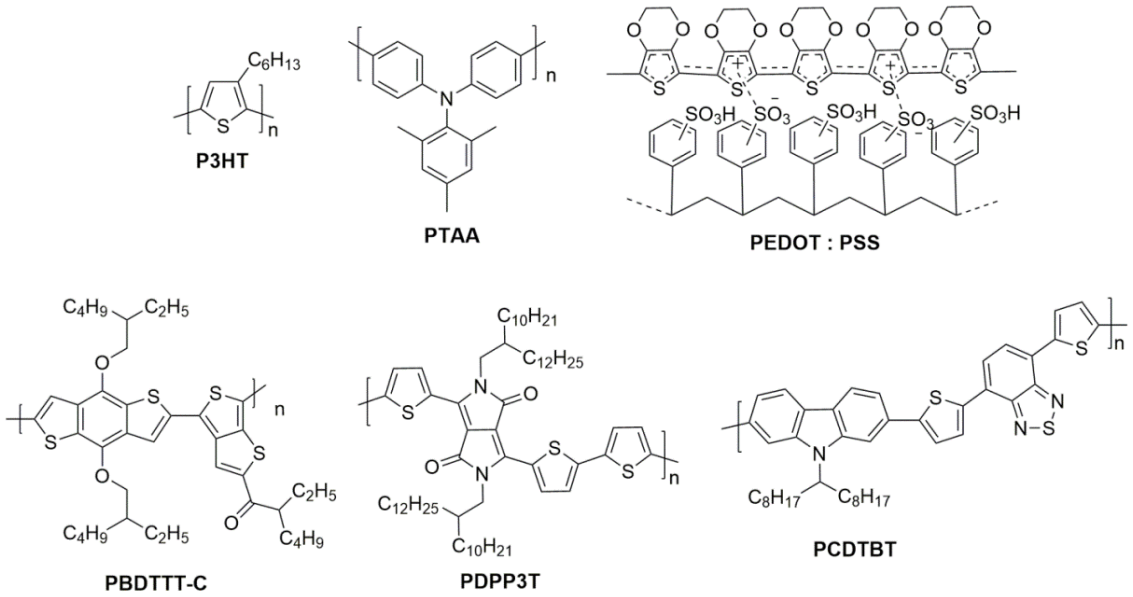

Figure 17: Representative of conjugated polymers used as HTMs in PSCs.

At the early state, P3HT based PSCs was first reported and obtained PCE of ~ 7%. Due to flat structure, molecular packing oriented to strong π-π interaction and enhance intermolecular charge transfer (ICT)[143]. After that, planar PSCs with optimized P3HT

thickness and sequential vacuum evaporation method for perovskite deposition showed a remarkable PCE of 13.7% and high V_{OC} ~0.96V[144]. Snaith *et al*[141] obtained significantly improvement when P3HT and single-wall carbon nanotubes composite embedded in insulating polymer and obtained breakthrough PCE of 15.3% (V_{OC} ~1.02V and FF~0.66). Thus, by this composite structure, they demonstrated that thermal degradation was retarded and water resistance property was improved. Moreover, P3HT is also used as HTM in fiber-shaped PSCs, which is opening tendency for PSCs in wearable electronics and textiles application[145].

Another example of conjugated polymer in PSCs is polytriarylamine (PTAA) which owns higher hole mobility (10^{-2} to 10^{-3} $cm^2V^{-1}s^{-1}$)[146] than P3HT (~3.10^{-4} $cm^2V^{-1}s^{-1}$)[147]. Due to its high molecular weight, interface with perovskite layer is low, leading to high series resistance R_S and low FF. However, once large crystalline grains of perovskite are created, used PTAA in PSCs could form uniform morphology, reduce charge trap density and effort the PCE to ~18.1%[148]. Recently, PSCs employed large-grain sized $FAPbI_3$ and PTAA as HTM that is reported highest PCE ~ 22.1%[50].

Most common conducting polymer poly(3,4-ethylenedioxythiophene) polystyrene sulfonate (PEDOT:PSS) has been used as HTM in PSCs because of its high conductivity ~10 S/cm[149] but it could be increased up to 4000 S/cm[150] by post-treatments and/or additives. It owns also both good film forming property and transparence. Moreover, its work function (~5.2 eV)[151] is compatible to valence band of $CH_3NH_3PbI_3$ for a good charge injection. Therefore, it is not only used in inverted planar structure PSCs but also suitable for flexible or low temperature PSCs. Recently, those devices obtained high performance PCE ~17% (V_{OC} ~1.05V and extremely high FF ~0.82)[152] and PCE ~18.1%[142] by limiting hysteresis and improving interfacial charge transfer. Nevertheless, devices contained PEDOT:PSS are less stable because of its hygroscopic nature as well as inefficient electron blocking behavior and acidic property affects to corrosion at substrate[153].

In fact, polymeric HTM are being targeted in PSCs. They are functionalized with sufficient properties such as high conductivity-mobility, broad absorption region and adequate film morphology. By the way, donor-acceptor (D-A) based copolymer have been designed, synthesized to make balance between charge carrier and light absorber properties. For example, Seok *et al*[43] reported PCDTBT which consist of benzothiadiazole as electron acceptor unit and carbazole as electron donor unit, but the performance of the device was low (4.2%). It could be explained by weakly D-A

interaction, low hole mobility leading to low J_{SC} value. By incorporating of benzo[1,2-b;4,5-b']dithiophene and thieno[3,4-b]thiophene in PBDTTT-C as HTM, an ETM-free planar structure PSCs obtained PCE of 9%[154] without any additives. Homogeneous film was obtained by varying number of long alkyl chain and improved compatibility with perovskite layer. Another dopant-free polymer PDPP3T was investigated by Qiao *et al*[155], they combined long alkyl chain and S...O interaction to perform planar molecular structure. Thank to enhanced intermolecular charge transfer character, PCE of 12.3% was obtained without using Li-TFSI and *t*-BP as additives. This material provides new trend for additive-free HTMs to improve device stability.

I.2.2.3 Molecular HTMs

Molecular HTM show some advantages such as high purity materials and well defined molecular structures compared to polymer-HTMs. Their good film forming ability, adequate interface contact and desirable solution processing are beneficial properties for device fabrication. In this section, two main classes of molecular HTMs are p-type small molecules and donor-acceptor molecules (push-pull molecules). We will discuss about properties of well-known HTM materials and how to construct structure of new HTM with these basic properties to compatible to PSCs and hybrid PSCs.

I.2.2.3.1 P-type molecules based small-organic HTMs

As aforementioned, Spiro-OMeTAD is one of the most well-known organic HTMs due to amorphous nature, good stability and transparence in UV-vis region. But the main drawback is its low hole mobility and conductivity, so doping is required to increase these values and improve PCE. However, based on its structure and properties, there are many studies to simplify and optimize of alternative HTMs.

Some efficient *p*-type HTMs are shown in ***Figure 18***. According to original Spiro-OMeTAD structure, Seok and co-worker[156] synthesized the three Spiro-OMeTAD derivatives by changing position of methoxy group (-OCH_3) in the aromatic ring. It revealed that methoxy groups were incorporated in Spiro-OMeTAD in order to control the oxidation potential of the materials and increase solubility. Moreover, Hammett reported that methoxy group exhibits two opposite resonance effects. They are electron-donating units at the para position and electron-accepting units at the meta position[157]. In this study, the derivative *po*-OCH_3 substituent showed effective characters in either

blocking of electrons or transporting of holes from perovskite layer to Au electrode. The methoxy groups in ortho- and para- positions exhibit electron donating ability and interaction between O...H in neighbor phenyl rings could support for hole transfer process. It obtained PCE of 16.7% higher than traditional *pp*-OCH_3 derivative (14.9%) and even higher than commercial *pp*- Spiro-OMeTAD (15.2%). Following to twisted spirofluorene, FDT was built from fluorene-dithiophene core as donor and methoxy triphenylamine side groups as acceptor. It showed good thermal and optoelectrical properties similar to Spiro-OMeTAD and attained PCE of 20.2% in PSCs[158]. The best performance was achieved because strong interaction of methoxy groups in small molecule FDT- perovskite layer and sulfur-iodine affinity promotes for high-quality film forming.

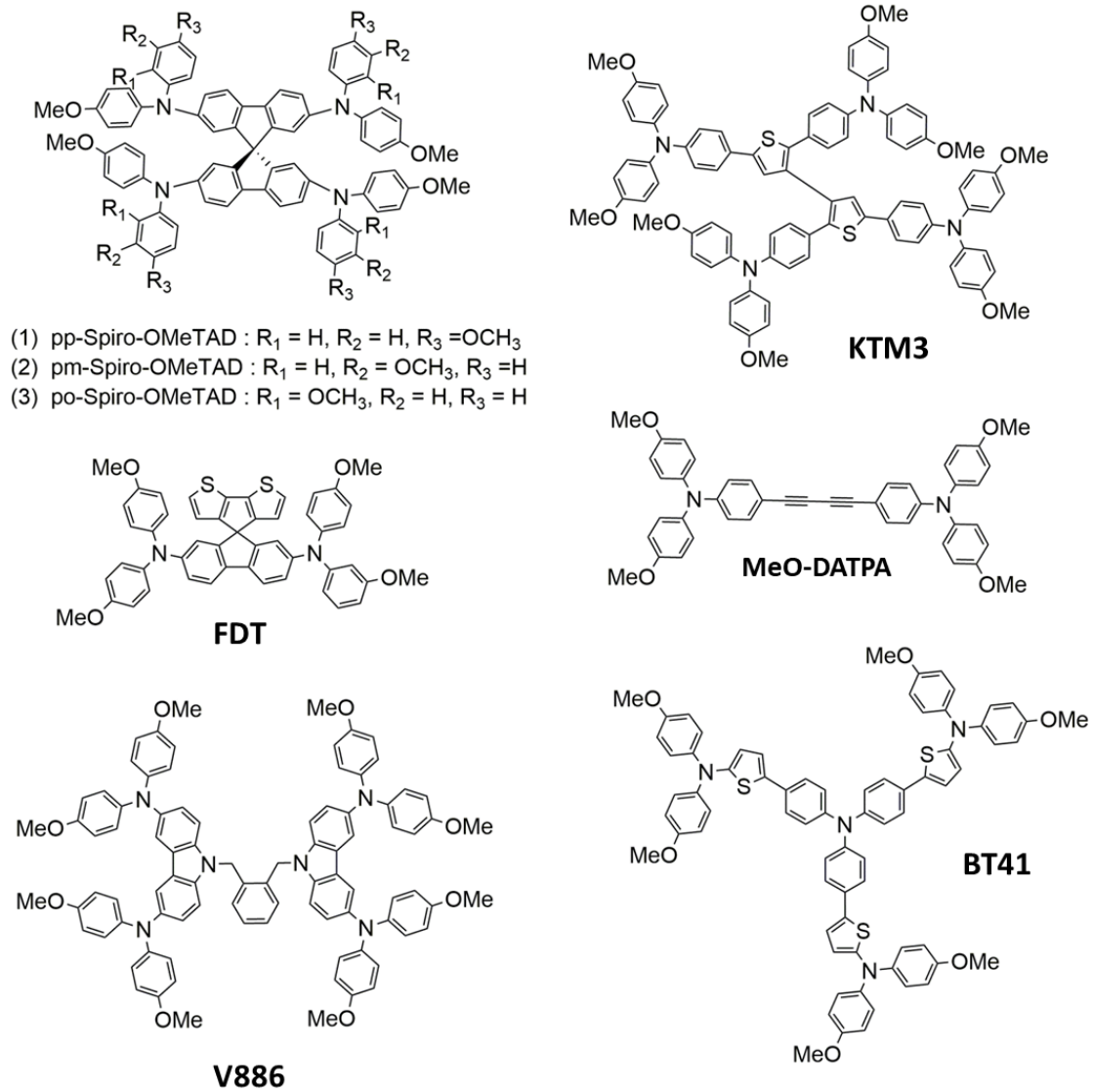

Figure 18: Representative of sufficient p-type molecules based organic HTMs.

Symmetric structures of HTM are also examined. A methoxydiphenylamine-substituted carbazole twin derivative, V886, was reported PCE of 16.91% comparable to Spiro-OMeTAD (18.4%)[159]. This cheap, two-steps synthesized HTM showed productively results as moderate hole-drift mobility (2.10^{-5} $cm^2.V^{-1}.s^{-1}$), V_{OC} ~1.085 V, J_{SC} ~21.38 mA/cm^2 and FF~0.734. It could be useful for large-scale production of low-cost PSCs. Another symmetric investigated HTM is swivel-cruciform 3,3'-bithiophene-based KTM3. It exhibited suitable HOMO level, good solubility, low recombination rate and optimized PCE of ~11% was received with Co (III) complex (FK269) as dopant. In general, most of typical HTM are combined with strong electron-donor groups such as triphenylamine, diphenylamine or carbazole. These groups collect holes from perovskite layer and effectively transport holes to metal electrode. Hence, in simple structure, two methoxy-triphenylamine groups are connected directly by diacetyl-bridge in MeO-DATPA[160]. Due to central diacetylide moieties, its molecular geometry is relatively planar and in the solid state the molecules arranged in a herringbone fashion that run in alternative direction. The electron density distribution of the HOMO is localized over the whole molecule, resulting to strong hole-donor capability and the best performance obtained PCE of 8.8%.

Besides that, star-shaped small HTMs have also attracted much attention due to tridimensional structures which tend to form amorphous molecules, increase the glass transition temperature and create uniform thin film without grain boundaries on the perovskite layer[161]. Bui *et al*[162] synthesized BT41 as star-shaped molecule with amorphous nature and high glass temperature (Tg ~ 99^0C). The authors studied the influence and the role of additives/dopants to PSCs performance. In its pristine, low PCE was obtained but significantly increased up to 9% in presence of LiTFSI and *t*-BP as additives. In fact, small molecular HTMs need to be oxidized by additives/dopants to improve hole mobility/conductivity. But at the same statement, these doping species reduce stability of devices and increase the cost. To avoid additives/dopants, HTMs should have high enough hole mobility and conductivity. One of the strategies is to incorporate donor-acceptor moieties in the whole molecule. Thus, due to push-pull effect, intramolecular charge transfer character could be increased and by molecular engineering, intermolecular charge transfer could be enhanced as well. Both of these features are favorable for improving hole mobility/conductivity.

I.2.2.3.2 Donor-acceptor molecules based organic HTMs

Donor-acceptor molecules or push-pull molecules are compounds in which electron-donor group and electron-acceptor group are combined in one structure. Recently, they have been attracted a lot of attention because they bring a good intramolecular charge transfer (ICT) property. Even if intermolecular charge transfer is the key limiting step for conductivity, ICT effect would improve charge transporting property inside the molecule due to the strong difference electron ability between the two moieties involving push-pull effect. Moreover, it can promote significant charge separation to form zwitterionic resonance in the ground state, potential induce electron delocalization[163,164]. In this system, a new energy molecular orbital are formed, providing possibility to manipulate HOMO-LUMO energy level of new materials by organizing variety of donor or acceptor moieties. This strategy can be used to modulate energy level of HTMs in PSCs.

Figure 19 shows some illustrative push-pull molecules which have been investigated in PSCs.

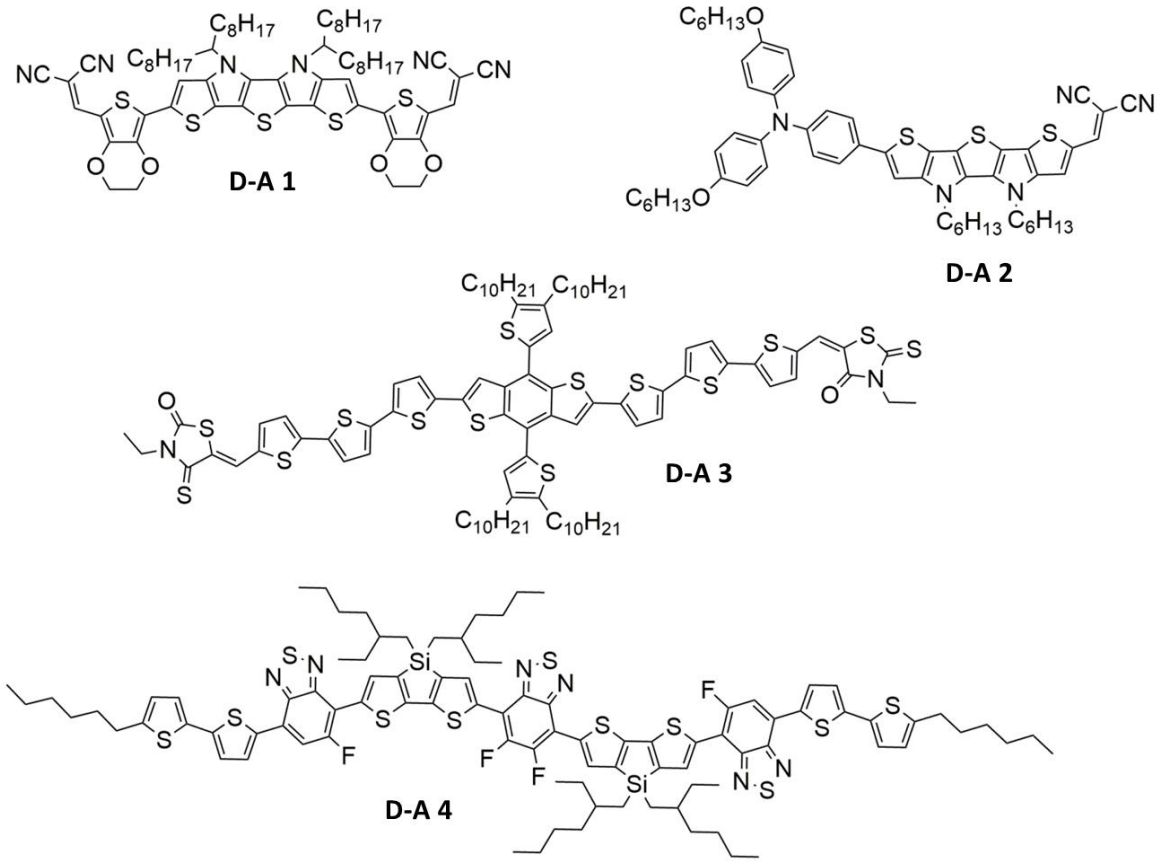

Figure 19: Representative of sufficient donor-acceptor molecules based organic HTMs.

For example, **D-A 1** has been recorded PCE of 11.4% without using any dopants[165]. This molecule was constructed by thiophene-pyrrole derivative and EDOT, linked by planar S,N-heteropentacene central unit and end-capped by dicyanovinyl acceptor group. Due to strong D-A interaction, it exhibited strong ICT feature, broad absorption in the visible and near-infrared region, thus narrows energy band gap. It also contributes to the charge transport, moderate photocurrent J_{SC} and hole mobility ($4.2.10^{-5}$ $cm^2.V^{-1}.s^{-1}$).

Similar backbone to **D-A 1**, unsymmetrical molecule **D-A 2** is composed of TPA as donor and dicyanovinyl as acceptor. Highly conjugated pathway molecule leads to large absorption band, moderate band gap (1.86 eV) and significant quenching perovskite emission promotes more efficient charge extraction.[166] As a result, PSCs employed **D-A 2** showed remarkable PCE of 17.7%, J_{SC} = 22.5 mA/cm^2 and high V_{OC} ~1.043 V, FF ~0.724 with negligible hysteresis.

Another example is D-A 3 which includes benzothiophene as core central block and ethylrhodamine as acceptor moieties[167]. This planar structure possesses high hole mobility (10^{-4} $cm^2.V^{-1}.s^{-1}$) and interestingly, it showed high hydrophobic property (contact angle ~107.4^o), thus improve stability of PSCs. Moreover, PCE of 8.8% was obtained by support small amount of polydimethylsiloxane (PDMS) compare to 8.9% of Spiro-OMeTAD with LiTFSI and t-BP. Herein, PDMS was used as an additive which is inert, non-toxic and non-flammable material. It helps to perform non-wetting surface material and to render uniform HTM film. The stability of PSCs was tested under relative high humidity 50% and PCE decreased from 8.8% to 8.0%. Therefore, this study opened a new tendency to alternative novel additives which can replace to conventional additives, LiTFSI and t-BP.

Recently, the hot topic for HTMs used in PSCs is dopant-free HTMs. They could increase PCE but mainly they could improve stability of device. JH. Heo and co-worker[168] studied D'-A-D-A-D-A-D' structure in which D, D' are donor groups and A is acceptor group was constructed to **D-A 4** as efficient hole extraction/collection material. In this first example of dopant-free HTM, 5-fluorobenzo[c][1,2,5]thiadiazole block as good electron-deficient moiety; 4,4-bis(2-ethylhexyl)-4H-silolo[3,2- b:4,5-b']dithiophene stabilizes sufficiently the quinoidal π-feature of molecular and enhance its planar conformation[169]. Due to increasing molecular size, formation of a compact HTM film with good molecular packing, this material improved charge transport properties, especially intermolecular charge transfer. Consequently, the PCE of 17.3% was recorded

for dopant-free PSCs; stability test reported remain 80% of PCE during 500h continuous light-soaking without encapsulation under ~60% humidity. This breakthrough achievement was obtained due to incorporation of different donor moieties and acceptor moieties in one structure which could provide better properties than simple D-A structure.

Therefore, donor-acceptor structure HTMs seems to be up-and-coming strategy for efficient dopant-free HTMs. By incorporation of variety donor and acceptor moieties, they are able both to tune HOMO-LUMO energy level and to reduce optical bandgap. Good hole extraction/collection/transport, high hole mobility/conductivity, hydrophobic nature, compact molecular packing are some desirable properties.

From literature overviews, nonplanar HTMs structure (star-shape or 3D structure) exhibits some profits such as readily form stable amorphous glasses with well-defined glass transition temperature (T_g) and permit to form of smooth, uniform film, minimize grain boundaries by either thermal deposition or solution deposition[170]. In contrary, planar conformation of molecular structure also provides some crucial characters which are desirable for charge transport property and molecular packing in device. In particular, it provides 2D π-system with planar structure which is prominent for intermolecular charge transfer[171,172]. The lifetime of the charge-separated state is increased by the electron delocalization of generated excitons over a planar structure, resulting an increase of hole mobility[173,174]. Therefore, these molecules have been studied, employed to PSCs and obtained optimistic device performances. Some of small organic HTMs with planar structure are given in ***Figure 20***. According to these molecules, the fundamental-advanced approaches to design new HTMs are established.

According to planar pyrene core, a strong electron delocalized in polycyclic hydrocarbon was combined with strong electron-donor groups as dimethoxydiphenylamine DPA. These DPA group helps to avoid aggregation. The compound Py-C showed good PSC performances as an efficient HTM, with a PCE equal to 12.4%[175] , close to 12.7% obtained with Spiro-OMeTAD. This result point out the symmetrical structure, isotropic charge transport property in pyrene core, electron-blocking ability and low series resistance. Besides, it also exhibited higher FF value (0.69) than that of Spiro-OMeTAD (0.59) due to thin film (less than 100 nm compare to 180 nm of Spiro-OMeTAD) and pinhole-free formation.

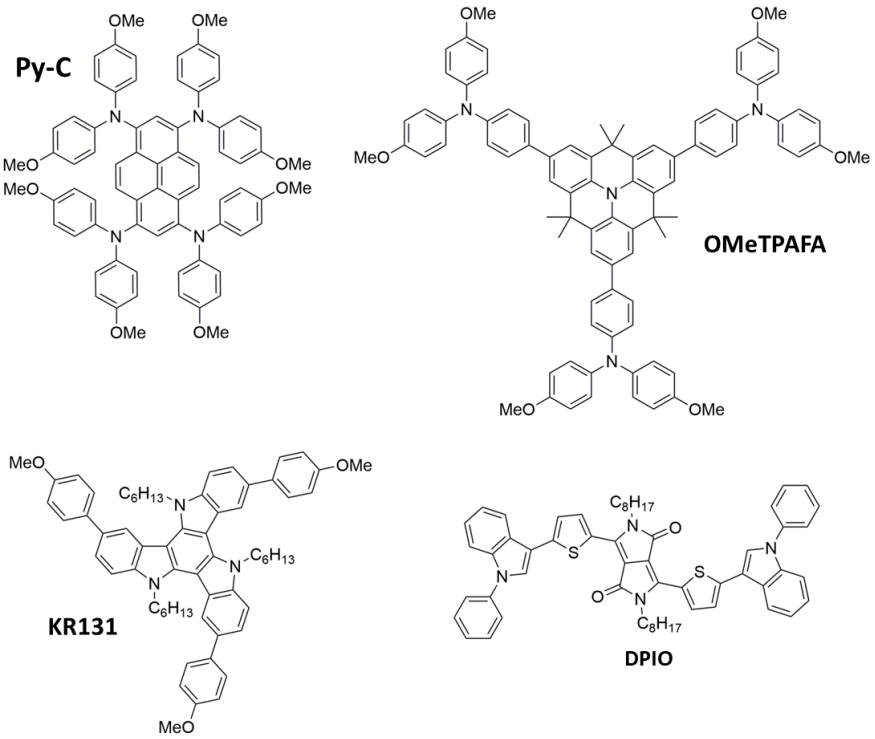

Figure 20: Representative of sufficient planar structure molecules based organic HTMs.

Triphenylamine unit (TPA), as mentioned above, is one of the most used building blocks for optoelectronic materials. Ko *et al*[176] combined fused-TPA and capped by TPA to construct planar structure of OMeTPAFA. Long lifetime of charge-separated state is deduced by delocalization of cations over the planar amine in the fused TPA core-based HTMs, leading to the good device performance equal to 13.63 % compared to 14.68% of Spiro-OMeTAD as reference. Another example is triazatruxenes which is also impressive building blocks used in optoelectronic devices. Because a flat framework is made by three indole units linked to central phenyl ring which provide a large aromatic surface to overlap to each other and extend delocalization in the π-system, hence efficient intermolecular charge transfer. They could be easily chemical modified to adjust the optoelectrical properties. Therefore, by using the star-shaped triazatruxenes-based KR131[177] as a HTMs, these devices obtained remarkable PCE of 18.3%, which is higher than that of Spiro-OMeTAD. Specially, this material showed maximum absorption in near UV domain, thus avoiding screen effect to absorption of perovskite.

As a planar D-A small molecule, diketopyrrolopyrrole (DPP) core is nearly planar which shows intermolecular interaction in solid state (N-H bonding and O) and strong π-π interaction between the bordering bicyclic lactam ring[178]. Due to its nature as strong electron-accepting moiety, DPP-based small molecules could be combined to electron-

donating moiety and formed push-pull small molecule. High hole mobility/conductivity up to 1 $cm^2.V^{-1}s^{-1}$ could be reasonable obtained. **DPIO (Figure 20)** has been employed as HTM in PSCs and reported PCE of 10%[179] compared to that Spiro-OMeTAD (7.87%) without additives/dopant. This small molecule showed strong absorption in longer wavelength region and aggregation-assisted enhance electrical property.

I.2.3 Conclusions

Spiro-OMeTAD, two decades after its introduction, still remains as a state-of-the art HTM in solid-state DSSCs and PSCs. However, the alternative HTMs are necessary due to the multi-step preparations for high purity, UV-sensitivity, low hole mobility of Spiro-OMeTAD. Conducting polymers, coordination compounds and inorganic *p*-type semiconductors based HTMs have been investigated and continuously developed. Especially, a majority of the used HTMs were based on small molecules, and showed the best performances.

By analyzing different classes of HTMs, the development of HTMs should follow some suggestions for further high-quality PSCs.

- Dopants are required but it is one of the reasons of device degradation. Finding a HTM with high hole mobility/conductivity in pristine form is favorable. Alongside, hydrophobic doping agent is approaching to replace of hydroscopic lithium salt. Furthermore, incorporating of inorganic materials (such as CuSCN, CuI, single-walled carbon nanotube, graphene, *etc*.) could increase the hole mobility/conductivity.
- To date, most of HTMs consists of triphenylamine or thiophene in chemical structure. A breakthrough of novel HTMs with complementary long absorption region (UV-vis-near IR) could significant improves the current density of PSCs. Furthermore, combination of novel HTMs with hydrophobic groups such as amide or ester can enhance the hydrophobicity of materials involving an increase of the stability of PSCs.
- In theoretical, the energy level of valence band of HTMs should located above the conductance band of perovskite for effective hole collection and extraction. However, direct bandgap property of perovskite also lead to high rate charge carrier recombination. Therefore, the interface between the HTM and the perovskite should be well-controlled. This will avoid direct contact of perovskite

layer to metal electrode, minimize recombination losses and encourage enforced driving force for hole injection.

- The prospect for small organic-HTM in PSCs is extremely bright because small molecules are monodisperse, distinctive molecular weight with well-defined structure. They offer unlimited various of chemical modifications and by that, their optoelectrical properties such as band gap, HOMO-LUMO energy level, hole mobility-hole conductivity can be tailored.

To summarize, hole transporting materials plays a key part of perovskite solar cells in hole extraction and transportation. Up to now, the best PSCs performance achieved photo-voltage up to 1.2V, short circuit current up to 24.6 mA/cm^2 and 0.77 of FF value. By this processing, fill factor could be exceed to 80% and then PCE can be reached beyond 24%. Therefore, band alignment of interface, optimization of doping process, reduction of recombination losses and development of new HTMs as well for device optimization are upcoming research approaches.

In the near future, it is possible to obtain high-efficiency and cost-effective PSCs devices and promote them to commercialization. To obtain high-performance devices, the optimization of three main parts of PSCs (hole transporting materials, electron transporting materials and sandwiched perovskite layer) is essential. However, the utilization of Pb-based materials should be limited due to their intrinsic toxicity. Presently research approach is going to replace Pb-free materials by mono-replacements (Ge and Sn are the best alternative choices to Pb) or binary replacements (by mixing Ca/Si and Zn/Si) and so on. So far, 1000h operation time has been guaranteed but this result is not enough to commercialize PSCs. The deep understand of the degradation mechanism, the development of new materials as well as encapsulation technology should be promoted for more than 20-years operation lifetime.

I. 3 General conclusions

In this chapter, several concepts of perovskite solar cells have been introduced such as different configuration of PSCs and their operation mechanism, variety structure of metal-halide perovskite corresponding to optoelectronic properties, and briefly summary on different configuration of hole transporting materials. Such important background will help to design and develop new HTMs, which correspond to my main PhD work. During my doctoral thesis, I will study hole transporting materials including

design, synthesis of new HTMs based on fundamental properties of many successful representative HTMs and then to determine their physical-chemical properties by studying of both theoretical calculation and experimental characterization methods. The main objective is to develop new HTMs from cheap precursors by facile preparation. They should have high hole mobility and conductivity, thermal and photochemical stability. Various series compounds will be investigated such as *p*-type organic HTMs, donor-acceptor small molecular HTMs and planar structure molecular HTMs. Thereafter, these materials will be employed as new HTMs in PSCs to evaluate device performance. Several issues will be appeared in each chapter and we expect to solve to some of them.

References

(1) Blandford, R.; Watkins, M. Bell Labs Demonstrates the First Practical Silicon Solar Cell. *APS News* **2009**, *18*, 2.

(2) Fritts, C. E. On the Fritts Selenium Cells and Batteries. *J. Franklin Inst.* **1885**, *119*, 221–232.

(3) Gagliardi, F. E. M. *Perovskite Solar Cells: Materials, Fabrication and Global Markets*; 2018.

(4) Kazim, S.; Nazeeruddin, M. K.; Grätzel, M.; Ahmad, S. Perovskite as Light Harvester: A Game Changer in Photovoltaics. *Angew. Chemie - Int. Ed.* **2014**, *53*, 2812–2824.

(5) Akihiro Kojima; Teshima, K.; Shirai, Y.; Miyasaka, T. Organometal Halide Perovskites as Visible-Light Sensitizers for Photovoltaic Cells. *J Am Chem Soc* **2009**, *131*, 6050–6051.

(6) Kim, H.-S.; Lee, C.-R.; Im, J.-H.; Lee, K.-B.; Moehl, T.; Marchioro, A.; Moon, S.-J.; Humphry-Baker, R.; Yum, J.-H.; Moser, J. E.; *et al.* Lead Iodide Perovskite Sensitized All-Solid-State Submicron Thin Film Mesoscopic Solar Cell with Efficiency Exceeding 9%. *Sci. Rep.* **2012**, *2*, 591.

(7) Manser, J. S.; Christians, J. A.; Kamat, P. V. Intriguing Optoelectronic Properties of Metal Halide Perovskites. *Chem. Rev.* **2016**, *116*, 12956–13008.

(8) Park, N. G. Perovskite Solar Cells: An Emerging Photovoltaic Technology. *Mater. Today* **2015**, *18*, 65–72.

(9) Jones, P. A.; Spence, B. R. Spacecraft Solar Array Technology Trends. *Aerosp. Conf. IEEE* **1998**, 141–152.

(10) Hagfeldt, A.; Boschloo, G.; Sun, L.; Kloo, L.; Pettersson, H. Dye-Sensitized Solar Cells. *Chem. Rev.* **2010**, *110*, 6595–6663.

(11) Chamberlain, G. A. Organic Solar Cells : A Review. *Sol. cells* **1983**, *8*, 47–83.

(12) Bera, D.; Qian, L.; Tseng, T. K.; Holloway, P. H. Quantum Dots and Their Multimodal Applications: A Review. *Materials (Basel).* **2010**, *3*, 2260–2345.

(13) Best-Research-Cell-Efficiencies. Best_Research-Cell_Efficiencies.

(14) Yan, Y.; Yin, W.-J.; Shi, T.; Meng, W.; Feng, C. *Organic-Inorganic Halide Perovskite Photovoltaics*; 2016.

(15) Chen, Q.; De Marco, N.; Yang, Y.; Song, T. Bin; Chen, C. C.; Zhao, H.; Hong, Z.; Zhou, H.; Yang, Y. Under the Spotlight: The Organic-Inorganic Hybrid Halide Perovskite for Optoelectronic Applications. *Nano Today* **2015**, *10*, 355–396.

(16) Zhang, X.; Chen, S.; Wang, X.; Pan, A. Controlled Synthesis and Photonics Applications of Metal Halide Perovskite Nanowires. *Small Methods* **2018**, *1800294*, 1800294.

(17) Zhang, Y.; Liu, J.; Wang, Z.; Xue, Y.; Ou, Q.; Polavarapu, L.; Zheng, J.; Qi, X.; Bao, Q. Synthesis, Properties, and Optical Applications of Low-Dimensional Perovskites. *Chem. Commun.* **2016**, *52*, 13637–13655.

(18) Kumawat, N. K.; Gupta, D.; Kabra, D. Recent Advances in Metal Halide-Based Perovskite Light-Emitting Diodes. *Energy Technol.* **2017**, *5*, 1734–1749.

(19) Zhang, L.; Yang, X.; Jiang, Q.; Wang, P.; Yin, Z.; Zhang, X.; Tan, H.; Yang, Y. M.; Wei, M.; Sutherland, B. R.; *et al.* Ultra-Bright and Highly Efficient Inorganic Based Perovskite Light-Emitting Diodes. *Nat. Commun.* **2017**, *8*, 1–8.

(20) Wang, H.; Kim, D. H. Perovskite-Based Photodetectors: Materials and Devices. *Chem. Soc. Rev.*

2017, *46*, 5204–5236.

(21) Zhang, X.; Yang, S.; Zhou, H.; Liang, J.; Liu, H.; Xia, H.; Zhu, X.; Jiang, Y.; Zhang, Q.; Hu, W.; *et al.* Perovskite–Erbium Silicate Nanosheet Hybrid Waveguide Photodetectors at the Near-Infrared Telecommunication Band. *Adv. Mater.* **2017**, *29*.

(22) huang, can; Sun, W.; Fan, Y.; Wang, Y.; Gao, Y.; Zhang, N.; Wang, K.; Liu, S.; wang, shuai; Xiao, S.; *et al.* Formation of Lead Halide Perovskite Based Plasmonic Nanolaser and Nanolaser Array by Tailoring the Substrate. *ACS Nano* **2018**, acsnano.8b01206.

(23) Li, X.; Tang, X.; Ye, T.; Wu, D.; Wang, H.; Wang, X. Fully Printable Organic and Perovskite Solar Cells with Transfer-Printed Flexible Electrodes. *ACS Appl. Mater. Interfaces* **2017**, *9*, 18730–18738.

(24) Liu, M.; Johnston, M. B.; Snaith, H. J. Efficient Planar Heterojunction Perovskite Solar Cells by Vapour Deposition. *Nature* **2013**, *501*, 395–398.

(25) Burschka, J.; Pellet, N.; Moon, S.-J.; Humphry-Baker, R.; Gao, P.; Nazeeruddin, M. K.; Grätzel, M. Sequential Deposition as a Route to High-Performance Perovskite-Sensitized Solar Cells. *Nature* **2013**, *499*.

(26) Gao, P.; Bin Mohd Yusoff, A. R.; Nazeeruddin, M. K. Dimensionality Engineering of Hybrid Halide Perovskite Light Absorbers. *Nat. Commun.* **2018**, *9*, 5028.

(27) Im, J.-H.; Lee, C.-R.; Lee, J.-W.; Park, S.-W.; Park, N.-G. 6.5% Efficient Perovskite Quantum-Dot-Sensitized Solar Cell. *Nanoscale* **2011**, *3*, 4088.

(28) Ning, Z.; Gong, X.; Comin, R.; Walters, G.; Fan, F.; Voznyy, O.; Yassitepe, E.; Buin, A.; Hoogland, S.; Sargent, E. H. Quantum-Dot-in-Perovskite Solids. *Nature* **2015**, *523*, 324.

(29) Im, J.; Luo, J.; Franckevic, M.; Pellet, N.; Gao, P.; Moehl, T.; Zakeeruddin, S. M.; Nazeeruddin, M. K.; Gratzel, M.; Park, N. Nanowire Perovskite Solar Cell. *Nano Lett.* **2015**, *15*, 2120–2126.

(30) Xu Zhang, Xiaodong Ren, Bin Liu, Rahim Munir, Xuejie Zhu, Dong Yang, Jianbo Li, Yucheng Liu, Detlef-M. Smilgies, Ruipeng Li, d Zhou Yang, Tianqi Niu, Xiuli Wang, Aram Amassian, K. Z. and S. (Frank) L. Stable High Efficiency Two-Dimensional Perovskite Solar Cells via Cesium Doping. *Energy Environ. Sci.* **2013**, 1–3.

(31) Song, J.; Li, J.; Li, X.; Xu, L.; Dong, Y.; Zeng, H. Quantum Dot Light-Emitting Diodes Based on Inorganic Perovskite Cesium Lead Halides (CsPbX3). *Adv. Mater.* **2015**, *27*, 7162–7167.

(32) Zhang, D.; Eaton, S. W.; Yu, Y.; Dou, L.; Yang, P. Solution-Phase Synthesis of Cesium Lead Halide Perovskite Nanowires. *J. Am. Chem. Soc.* **2015**, *137*, 9230–9233.

(33) Jingying Liu, Yunzhou Xue, Ziyu Wang, Zai-Quan Xu, Changxi Zheng, Bent Weber, Jingchao Song, Yusheng Wang, Yuerui Lu, Yupeng Zhang, and Q. B. Two-Dimensional CH3NH3PbI3Perovskite: Synthesis and Optoelectronic Application. *ACS Nano* **2016**, *10*, 3536–3542.

(34) Im, J.-H.; Jang, I.-H.; Pellet, N.; Grätzel, M.; Park, N.-G. Growth of CH3NH3PbI3 Cuboids with Controlled Size for High-Efficiency Perovskite Solar Cells. *Nat. Nanotechnol.* **2014**, *9*.

(35) Mitzi, D. B.; Chondroudis, K.; Kagan, C. R. Design, Structure, and Optical Properties of Organic−Inorganic Perovskites Containing an Oligothiophene Chromophore. *Inorg. Chem.* **1999**, *38*, 6246–6256.

(36) Baikie, T.; Fang, Y.; Kadro, J. M.; Schreyer, M.; Wei, F.; Mhaisalkar, S. G.; Graetzel, M.; White, T. J. Synthesis and Crystal Chemistry of the Hybrid Perovskite (CH3NH3)PbI3 for Solid-State Sensitised Solar Cell Applications. *J. Mater. Chem. A* **2013**, *1*, 5628.

(37) Miyata, A.; Mitioglu, A.; Plochocka, P.; Portugall, O.; Tse-wei, J.; Stranks, S. D.; Snaith, H. J.; Nicholas, R. J. Direct Measurement of the Exciton Binding Energy and Effective Masses for Charge Carriers in an Organic-Inorganic Tri-Halide Perovskite. *Nat. Phys.* **2015**, *11*, 582–587.

(38) Guichuan Xing, Nripan Mathews, Shuangyong Sun, Swee Sien Lim, Yeng Ming Lam, Michael Grätzel, Subodh Mhaisalkar, T. C. S. Long-Range Balanced Electron-and Hole-Transport Lengths in Organic-Inorganic CH3NH3PbI3. *Science (80-.).* **2013**, *342*, 344–347.

(39) Calió, L.; Kazim, S.; Grätzel, M.; Ahmad, S. Hole-Transport Materials for Perovskite Solar Cells. *Angew. Chemie Int. Ed.* **2016**, *55*, 14522–14545.

(40) Lee, M. M.; Teuscher, J.; Miyasaka, T.; Murakami, T. N.; Snaith, H. J. Efficient Hybrid Solar Cells Based on Meso-Superstructured Organometal Halide Perovskites. *Science (80-.).* **2012**, *338*, 643 LP-647.

(41) Li, W.; Liu, J.; Zhao, D. Mesoporous Materials for Energy. *Nat. Rev. Mater.* **2016**, *1*, 17.

(42) Kim, H. S.; Lee, C. R.; Im, J. H.; Lee, K. B.; Moehl, T.; Marchioro, A.; Moon, S. J.; Humphry-Baker, R.; Yum, J. H.; Moser, J. E.; *et al.* Lead Iodide Perovskite Sensitized All-Solid-State Submicron Thin Film Mesoscopic Solar Cell with Efficiency Exceeding 9%. *Sci. Rep.* **2012**, *2*, 1–7.

(43) Hyuck, H. J.; Sang, H. I.; Hong, N. J.; N, M. T.; Lim Choong-Sun; Jeong Ah Chang, Yong Hui Lee, K. H.; , Arpita Sarkar, M. K. N.; Michael, G.; Il, S. S. Efficient Inorganic-Organic Hybrid Heterojunction Solar Cells Containing Perovskite Compound and Polymeric Hole Conductors. *Nat. Photonics* **2013**, *7*, 486–491.

(44) Park, N. G. Perovskite Solar Cells: An Emerging Photovoltaic Technology. *Materials Today*, 2015, *18*, 65–72.

(45) Etgar, L.; Gao, P.; Xue, Z.; Peng, Q.; Chandiran, A. K.; Liu, B.; Nazeeruddin, M. K.; Gratzel, M. Mesoscopic CH3NH3PbI3/TiO2 Heterojunction Solar Cells. *J. Am. Chem. Soc.* **2012**, *134*, 17396–17399.

(46) Laban, W. A.; Etgar, L. Depleted Hole Conductor-Free Lead Halide Iodide Heterojunction Solar Cells. *Energy Environ. Sci.* **2013**, *6*, 3249–3253.

(47) Aharon, S.; Gamliel, S.; Cohen, B. El; Etgar, L. Depletion Region Effect of Highly Efficient Hole Conductor Free $CH_3NH_3PbI_3$ Perovskite Solar Cells. *Phys. Chem. Chem. Phys.* **2014**, *16*, 10512–10518.

(48) Anyi Mei, Xiong Li, Linfeng Liu, Zhiliang Ku, Tongfa Liu, Yaoguang Rong, Mi Xu, Min Hu, Jiangzhao Chen, Ying Yang, Michael Grätzel, H. H. A Hole-Conductor-Free, Fully Printable Mesoscopic Perovskite Solar Cell with High Stability. *Science (80-.).* **2014**, *345*, 295–298.

(49) Boix, P. P.; Agarwala, S.; Koh, T. M.; Mathews, N.; Mhaisalkar, S. G. Perovskite Solar Cells: Beyond Methylammonium Lead Iodide. *J. Phys. Chem. Lett.* **2015**, *6*, 898–907.

(50) Woon Seok Yang, Byung-Wook Park, Eui Hyuk Jung, Nam Joong Jeon, Young Chan Kim, Dong Uk Lee, Seong Sik Shin, Jangwon Seo, Eun Kyu Kim, Jun Hong Noh, S. I. S. Iodide Management in Formamidinium-Lead-Halide–based Perovskite Layers for Efficient Solar Cells. *Science (80-.).*

2017, *356*, 1376–1379.

(51) Cohen, B. El; Wierzbowska, M.; Etgar, L. High Efficiency Quasi 2D Lead Bromide Perovskite Solar Cells Using Various Barrier Molecules. *Sustain. Energy Fuels* **2017**, *1*, 1935–1943.

(52) Hu, Y.; Hutter, E. M.; Rieder, P.; Grill, I.; Hanisch, J.; Aygüler, M. F.; Hufnagel, A. G.; Handloser, M.; Bein, T.; Hartschuh, A.; *et al.* Understanding the Role of Cesium and Rubidium Additives in Perovskite Solar Cells: Trap States, Charge Transport, and Recombination. *Adv. Energy Mater.* **2018**, *8*, 1–11.

(53) Nazeeruddin, M. K. Organohalide Lead Perovskites for Photovoltaic Applications. **2016**.

(54) Kim, H.; Im, S. H.; Park, N. Organolead Halide Perovskite : New Horizons in Solar Cell Research. *J. Phys. Chem. C* **2014**, *118*, 5615–5625.

(55) McMeekin, D. P.; Sadoughi, G.; Rehman, W.; Eperon, G. E.; Saliba, M.; Horantner, M. T.; Haghighirad, A.; Sakai, N.; Korte, L.; Rech, B.; *et al.* A Mixed-Cation Lead Mixed-Halide Perovskite Absorber for Tandem Solar Cells. *Science (80-.).* **2016**, *351*, 151–155.

(56) Kulkarni, S. A.; Baikie, T.; Boix, P. P.; Yantara, N.; Mathews, N.; Mhaisalkar, S. Band-Gap Tuning of Lead Halide Perovskites Using a Sequential Deposition Process. *J. Mater. Chem. A* **2014**, *2*, 9221–9225.

(57) Hoke, E. T.; Slotcavage, D. J.; Dohner, E. R.; Bowring, A. R.; Karunadasa, H. I.; McGehee, M. D. Reversible Photo-Induced Trap Formation in Mixed-Halide Hybrid Perovskites for Photovoltaics. *Chem. Sci.* **2015**, *6*, 613–617.

(58) Online, V. A.; Gao, P.; Nazeeruddin, M. K. Environmental Science Organohalide Lead Perovskites for Photovoltaic Applications. *Energy Environ. Sci.* **2014**, *1*, 2448–2463.

(59) Eperon, G. E.; Stranks, S. D.; Menelaou, C.; Johnston, M. B.; Herz, L. M.; Snaith, H. J. Formamidinium Lead Trihalide: A Broadly Tunable Perovskite for Efficient Planar Heterojunction Solar Cells. *Energy Environ. Sci.* **2014**, *7*, 982–988.

(60) Noh, J. H.; Im, S. H.; Heo, J. H.; Mandal, T. N.; Seok, S. Il. Chemical Management for Colorful, Efficient, and Stable Inorganic-Organic Hybrid Nanostructured Solar Cells. *Nano Lett.* **2013**, *13*, 1764–1769.

(61) Luo, S.; Daoud, W. Crystal Structure Formation of CH3NH3PbI3-XClx Perovskite. *Materials (Basel).* **2016**, *9*, 123.

(62) Rajendra Kumar, G.; Dennyson Savariraj, A.; Karthick, S. N.; Selvam, S.; Balamuralitharan, B.; Kim, H. J.; Viswanathan, K. K.; Vijaykumar, M.; Prabakar, K. Phase Transition Kinetics and Surface Binding States of Methylammonium Lead Iodide Perovskite. *Phys. Chem. Chem. Phys.* **2016**, *18*, 7284–7292.

(63) Yang, W. S.; Noh, J. H.; Jeon, N. J.; Kim, Y. C.; Ryu, S.; Seo, J.; Seok, S. I. High-Performance Photovoltaic Perovskite Layers Fabricated through Intramolecular Exchange. *Sci. (80-.).* **2015**, *348*, 1234–1237.

(64) Grånäs, O.; Vinichenko, D.; Kaxiras, E. Establishing the Limits of Efficiency of Perovskite Solar Cells from First Principles Modeling. *Sci. Rep.* **2016**, *6*, 1–6.

(65) Mahmood, K.; Sarwar, S.; Mehran, M. T. Current Status of Electron Transport Layers in Perovskite Solar Cells: Materials and Properties. *RSC Adv.* **2017**, *7*, 17044–17062.

(66) Im, J. H.; Kim, H. S.; Park, N. G. Morphology-Photovoltaic Property Correlation in Perovskite Solar Cells: One-Step versus Two-Step Deposition of CH3NH3PbI 3. *APL Mater.* **2014**, *2*.

(67) Ahn, N.; Son, D. Y.; Jang, I. H.; Kang, S. M.; Choi, M.; Park, N. G. Highly Reproducible Perovskite Solar Cells with Average Efficiency of 18.3% and Best Efficiency of 19.7% Fabricated via Lewis Base Adduct of Lead(II) Iodide. *J. Am. Chem. Soc.* **2015**, *137*, 8696–8699.

(68) Paek, S.; Schouwink, P.; Athanasopoulou, E. N.; Cho, K. T.; Grancini, G.; Lee, Y.; Zhang, Y.; Stellacci, F.; Nazeeruddin, M. K.; Gao, P. From Nano- to Micrometer Scale: The Role of Antisolvent Treatment on High Performance Perovskite Solar Cells. *Chem. Mater.* **2017**, *29*, 3490–3498.

(69) Kajal, P.; Powar, S. Manufacturing Techniques of Perovskite Solar Cells. In *Applications of Solar Energy*; 2018.

(70) Razza, S.; Castro-Hermosa, S.; Di Carlo, A.; Brown, T. M. Research Update: Large-Area Deposition, Coating, Printing, and Processing Techniques for the Upscaling of Perovskite Solar Cell Technology. *APL Mater.* **2016**, *4*.

(71) Wu, M. C.; Chan, S. H.; Jao, M. H.; Su, W. F. Enhanced Short-Circuit Current Density of Perovskite Solar Cells Using Zn-Doped TiO2as Electron Transport Layer. *Sol. Energy Mater. Sol. Cells* **2016**, *157*, 447–453.

(72) Haber, K. S.; Albrecht, A. C. Time-of-Flight Technique for Mobility Measurements in the Condensed Phase. *J. Phys. Chem.* **1984**, *88*, 6025–6030.

(73) Lampert, M. A.; Schilling, R. B. Current Injection in Solids: The Regional Approximation Method. In *Semiconductors and Semimetals*; Academic Press, Newyork, 1970; Vol. 6, pp. 1–96.

(74) An, Z.; Yu, J.; Jones, S. C.; Barlow, S.; Yoo, S.; Domercq, B.; Prins, P.; Siebbeles, L. D. A.; Kippelen, B.; Marder, S. R. High Electron Mobility in Room-Temperature Discotic Liquid-Crystalline Perylene Diimides. *Adv. Mater.* **2005**, *17*, 2580–2583.

(75) Kokil, A.; Yang, K.; Kumar, J. Techniques for Characterization of Charge Carrier Mobility in Organic Semiconductors. *J. Polym. Sci. Part B Polym. Phys.* **2012**, *50*, 1130–1144.

(76) Sze S.M. *Physics of Semiconductor Devices*; 2nd ed.; Wiley-VCH: New York, 1981.

(77) Malliaras, G. G.; Scott, J. C. Numerical Simulations of the Electrical Characteristics and the Efficiencies of Single-Layer Organic Light Emitting Diodes. *J. Appl. Phys.* **1999**, *85*, 7426–7432.

(78) N.F, M.; R.W, G. *Electronic Processes in Ionic Crystals*; Oxford university Press: london, 1940.

(79) Poplavskyy, D.; Nelson, J. Nondispersive Hole Transport in Amorphous Films of Methoxy-Spirofluorene-Arylamine Organic Compound. *J. Appl. Phys.* **2003**, *93*, 341–346.

(80) Smits, F. M. Measurement of Sheet Resistivities with the Four-Point Probe. *Bell Syst. Tech. J.* **1958**, *37*, 711–718.

(81) Miccoli, I.; Edler, F.; Pfnür, H.; Tegenkamp, C. The 100th Anniversary of the Four-Point Probe Technique: The Role of Probe Geometries in Isotropic and Anisotropic Systems. *J. Phys. Condens. Matter* **2015**, *27*.

(82) Dubpernell, G. Electroplating , Electrochemistry and Electronics By. In *61st AES Annual Convention*; Chicago, illinois, 2016; Vol. 80, pp. 1–44.

(83) Li, Y.; Ye, S.; Sun, W.; Yan, W.; Li, Y.; Bian, Z.; Liu, Z.; Wang, S.; Huang, C. Hole-Conductor-

Free Planar Perovskite Solar Cells with 16.0% Efficiency. *J. Mater. Chem. A* **2015**, *3*, 18389–18394.

(84) Madhavan, V. E.; Zimmermann, I.; Roldán-Carmona, C.; Grancini, G.; Buffiere, M.; Belaidi, A.; Nazeeruddin, M. K. Copper Thiocyanate Inorganic Hole-Transporting Material for High-Efficiency Perovskite Solar Cells. *ACS Energy Lett.* **2016**, *1*, 1112–1117.

(85) Zhang, Y.; Yin, J.; Parida, M. R.; Ahmed, G. H.; Pan, J.; Bakr, O. M.; Brédas, J. L.; Mohammed, O. F. Direct-Indirect Nature of the Bandgap in Lead-Free Perovskite Nanocrystals. *J. Phys. Chem. Lett.* **2017**, *8*, 3173–3177.

(86) Hutter, E. M.; Gélvez-Rueda, M. C.; Osherov, A.; Bulović, V.; Grozema, F. C.; Stranks, S. D.; Savenije, T. J. Direct-Indirect Character of the Bandgap in Methylammonium Lead Iodide Perovskite. *Nat. Mater.* **2017**, *16*, 115–120.

(87) Snaith, H. J.; Abate, A.; Ball, J. M.; Eperon, G. E.; Leijtens, T.; Noel, N. K.; Stranks, S. D.; Wang, J. T. W.; Wojciechowski, K.; Zhang, W. Anomalous Hysteresis in Perovskite Solar Cells. *J. Phys. Chem. Lett.* **2014**, *5*, 1511–1515.

(88) Chen, B.; Yang, M.; Priya, S.; Zhu, K. Origin of J-V Hysteresis in Perovskite Solar Cells. *J. Phys. Chem. Lett.* **2016**, *7*, 905–917.

(89) Taame Abraha Berhe, Wei-Nien Su, Ching-Hsiang Chen, Chun-Jern Pan, Ju-Hsiang Cheng, Hung-Ming Chen, Meng-Che Tsai, Liang-Yih Chen, A. A. D. and B.-J. H. Organometal Halide Perovskite Solar Cells: Degradation and Stability. *Energy Environ. Sci.* **2016**, *9*, 323–356.

(90) Stoumpos, C. C.; Malliakas, C. D.; Kanatzidis, M. G. Organic Tin and Lead Iodide Perovskites with Organic Cations : Unique Semiconductors , with Phase Transitions and Near- - - Infrared Photoluminescent Properties. *Inorg. Chem.* **2013**, *52*, 9019–9038.

(91) Filip, M. R.; Giustino, F. Computational Screening of Homovalent Lead Substitution in Organic-Inorganic Halide Perovskites. *J. Phys. Chem. C* **2016**, *120*, 166–173.

(92) Körbel, S.; Marques, M. A. L.; Botti, S. Stability and Electronic Properties of New Inorganic Perovskites from High-Throughput: Ab Initio Calculations. *J. Mater. Chem. C* **2016**, *4*, 3157–3167.

(93) L.Sun. Inorganic Hole-Transporting Materials for Perovskite Solar Cell. *Small Methods* **2018**, *1700280*.

(94) Chen, J.; Park, N.-G. Inorganic Hole Transporting Materials for Stable and High Efficiency Perovskite Solar Cells. *J. Phys. Chem. C* **2018**, acs.jpcc.8b01177.

(95) Christians, J. A.; Fung, R. C. M.; Kamat, P. V. An Inorganic Hole Conductor for Organo-Lead Halide Perovskite Solar Cells. Improved Hole Conductivity with Copper Iodide. *J. Am. Chem. Soc.* **2014**, *136*.

(96) Zuo, C.; Ding, L. Solution-Processed Cu2O and CuO as Hole Transport Materials for Efficient Perovskite Solar Cells. *Small* **2015**, *11*, 5528–5532.

(97) Qin, P.; Tanaka, S.; Ito, S.; Tetreault, N.; Manabe, K.; Nishino, H.; Nazeeruddin, M. K.; Grätzel, M. Inorganic Hole Conductor-Based Lead Halide Perovskite Solar Cells with 12.4% Conversion Efficiency. *Nat. Commun.* **2014**, *5*, 1–6.

(98) Rao, H.; Sun, W.; Ye, S.; Yan, W.; Li, Y.; Peng, H.; Liu, Z.; Bian, Z.; Huang, C. Solution-Processed CuS NPs as an Inorganic Hole-Selective Contact Material for Inverted Planar Perovskite

Solar Cells. *ACS Appl. Mater. Interfaces* **2016**, *8*, 7800–7805.

(99) Wu, Q.; Xue, C.; Li, Y.; Zhou, P.; Liu, W.; Zhu, J.; Dai, S.; Zhu, C.; Yang, S. Kesterite Cu2ZnSnS4as a Low-Cost Inorganic Hole-Transporting Material for High-Efficiency Perovskite Solar Cells. *ACS Appl. Mater. Interfaces* **2015**, *7*, 28466–28473.

(100) Jeng, J. Y.; Chen, K. C.; Chiang, T. Y.; Lin, P. Y.; Tsai, T. Da; Chang, Y. C.; Guo, T. F.; Chen, P.; Wen, T. C.; Hsu, Y. J. Nickel Oxide Electrode Interlayer in CH3NH3PbI3perovskite/PCBM Planar-Heterojunction Hybrid Solar Cells. *Adv. Mater.* **2014**, *26*, 4107–4113.

(101) Wang, F.; Endo, M.; Mouri, S.; Miyauchi, Y.; Ohno, Y.; Wakamiya, A.; Murata, Y.; Matsuda, K. Highly Stable Perovskite Solar Cells with an All-Carbon Hole Transport Layer. *Nanoscale* **2016**, *8*, 11882–11888.

(102) Amna Bashir, Sudhanshu Shukla, Lew Jia Haur, Shashwat Shukla, Annalisa Bruno, Disha Gupta, Tom Baikie, Rahul Patidar, Zareen Akhter, Anish Priyadarshi, Nripan Mathews, and S. G. M. Spinel Co3O4 Nanomaterials for Efficient and Stable Large Area Carbon-Based Printed Perovskite Solar Cells. *Nanoscale* **2013**, 1–3.

(103) Cheng, M.; Li, Y.; Safdari, M.; Chen, C.; Liu, P.; Kloo, L.; Sun, L. Efficient Perovskite Solar Cells Based on a Solution Processable Nickel(II) Phthalocyanine and Vanadium Oxide Integrated Hole Transport Layer. *Adv. Energy Mater.* **2017**, *7*, 1–7.

(104) Tseng, Z. L.; Chen, L. C.; Chiang, C. H.; Chang, S. H.; Chen, C. C.; Wu, C. G. Efficient Inverted-Type Perovskite Solar Cells Using UV-Ozone Treated MoOxand WOxas Hole Transporting Layers. *Sol. Energy* **2016**, *139*, 484–488.

(105) Aitola, K.; Sveinbjörnsson, K.; Correa-Baena, J.-P.; Kaskela, A.; Abate, A.; Tian, Y.; Johansson, E. M. J.; Grätzel, M.; Kauppinen, E. I.; Hagfeldt, A.; *et al.* Carbon Nanotube-Based Hybrid Hole-Transporting Material and Selective Contact for High Efficiency Perovskite Solar Cells. *Energy Environ. Sci.* **2016**, *9*, 461–466.

(106) Yoon, S.; Ha, T.-J.; Kang, D.-W. Improving the Performance and Reliability of Inverted Planar Perovskite Solar Cells with a Carbon Nanotubes/PEDOT:PSS Hybrid Hole Collector. *Nanoscale* **2017**, *9*, 9754–9761.

(107) Zhou, Z.; Li, X.; Cai, M.; Xie, F.; Wu, Y.; Lan, Z.; Yang, X.; Qiang, Y.; Islam, A.; Han, L. Stable Inverted Planar Perovskite Solar Cells with Low-Temperature-Processed Hole-Transport Bilayer. *Adv. Energy Mater.* **2017**, *7*.

(108) Cao, J.; Yu, H.; Zhou, S.; Qin, M.; Lau, T.-K.; Lu, X.; Zhao, N.; Wong, C.-P. Low-Temperature Solution-Processed NiO_x Films for Air-Stable Perovskite Solar Cells. *J. Mater. Chem. A* **2017**, *5*, 11071–11077.

(109) Zhao, T.; Goodwin, E. D.; Guo, J.; Wang, H.; Diroll, B. T.; Murray, C. B.; Kagan, C. R. Advanced Architecture for Colloidal PbS Quantum Dot Solar Cells Exploiting a CdSe Quantum Dot Buffer Layer. *ACS Nano* **2016**, *10*, 9267–9273.

(110) Etgar, L.; Gao, P.; Qin, P.; Graetzel, M.; Nazeeruddin, M. K. A Hybrid Lead Iodide Perovskite and Lead Sulfide QD Heterojunction Solar Cell to Obtain a Panchromatic Response. *J. Mater. Chem. A* **2014**, *2*, 11586–11590.

(111) Lv, M.; Zhu, J.; Huang, Y.; Li, Y.; Shao, Z.; Xu, Y.; Dai, S. Colloidal $CuInS_2$ Quantum Dots as

Inorganic Hole-Transporting Material in Perovskite Solar Cells. *ACS Appl. Mater. Interfaces* **2015**, *7*, 17482–17488.

(112) Christians, J. A.; Fung, R. C. M.; Kamat, P. V. An Inorganic Hole Conductor for Organo-Lead Halide Perovskite Solar Cells. Improved Hole Conductivity with Copper Iodide. *J. Am. Chem. Soc.* **2014**, *136*, 758–764.

(113) Chen, W.-Y.; Deng, L.-L.; Dai, S.-M.; Wang, X.; Tian, C.-B.; Zhan, X.-X.; Xie, S.-Y.; Huang, R.-B.; Zheng, L.-S. Low-Cost Solution-Processed Copper Iodide as an Alternative to PEDOT:PSS Hole Transport Layer for Efficient and Stable Inverted Planar Heterojunction Perovskite Solar Cells. *J. Mater. Chem. A* **2015**, *3*, 19353–19359.

(114) Weihai Sun, Yunlong Li, Senyun Ye, Haixia Rao, Weibo Yan, Haitao Peng, Yu Li, Zhiwei Liu, ShufengWang, Zhijian Chen, Lixin Xiao, Z. B. and C. H. High-Performance Inverted Planar Heterojunction Perovskite Solar Cells Based on a Solution-Processed CuOx Hole Transport Layer. *Nanoscale* **2016**, *8*, 10806–10813.

(115) Nilushi Wijeyasinghe, Anna Regoutz, Flurin Eisner, Tian Du, Leonidas Tsetseris, Yen-Hung Lin, Hendrik Faber, Pichaya Pattanasattayavong, Jinhua Li, Feng Yan, Martyn A. McLachlan, David J. Payne, Martin Heeney, and T. D. A. Copper(I) Thiocyanate (CuSCN) Hole-Transport Layers Processed from Aqueous Precursor Solutions and Their Application in Thin-Film Transistors and Highly Efficient Organic and Organometal Halide Perovskite Solar Cells. *Adv. Funct. Mater.* **2017**, *27*, 1–13.

(116) Arora, N.; Dar, M. I.; Hinderhofer, A.; Pellet, N.; Schreiber, F.; Zakeeruddin, S. M.; Grätzel, M. Perovskite Solar Cells with CuSCN Hole Extraction Layers Yield Stabilized Efficiencies Greater than 20%. *Science (80-.).* **2017**, *358*, 768–771.

(117) Li, M.; Wang, Z. K.; Yang, Y. G.; Hu, Y.; Feng, S. L.; Wang, J. M.; Gao, X. Y.; Liao, L. S. Copper Salts Doped Spiro-OMeTAD for High-Performance Perovskite Solar Cells. *Adv. Energy Mater.* **2016**, *6*.

(118) Igbari, F.; Li, M.; Hu, Y.; Wang, Z.-K.; Liao, L.-S. A Room-Temperature $CuAlO_2$ Hole Interfacial Layer for Efficient and Stable Planar Perovskite Solar Cells. *J. Mater. Chem. A* **2016**, *4*, 1326–1335.

(119) George Kakavelakis, Ioannis Paradisanos, Barbara Paci, Amanda Generosi, Michael Papachatzakis, Temur Maksudov, Leyla Najafi, Antonio Esaú Del Rio Castillo, George Kioseoglou, Emmanuel Stratakis, Francesco Bonaccorso, and E. K. Extending the Continuous Operating Lifetime of Perovskite Solar Cells with a Molybdenum Disulfide Hole Extraction Interlayer. *Adv. Energy Mater.* **2018**, *8*, 1–15.

(120) Nouri, E.; Mohammadi, M. R.; Lianos, P. Improving the Stability of Inverted Perovskite Solar Cells under Ambient Conditions with Graphene-Based Inorganic Charge Transporting Layers. *Carbon N. Y.* **2018**, *126*, 208–214.

(121) Abate, A.; Giordano, F.; Baena, J. C.; Decoppet, J. Efficient Luminescent Solar Cells Based on Tailored Mixed-Cation Perovskites Efficient Luminescent Solar Cells Based on Tailored Mixed-Cation Perovskites. *Sci. Adv.* **2016**, *2*.

(122) Snaith, H. J.; Humphry-Baker, R.; Chen, P.; Cesar, I.; Zakeeruddin, S. M.; Grätzel, M. Charge

Collection and Pore Filling in Solid-State Dye-Sensitized Solar Cells. *Nanotechnology* **2008**, *19*.

(123) Xu, L.; Deng, L. L.; Cao, J.; Wang, X.; Chen, W. Y.; Jiang, Z. Solution-Processed Cu(In, Ga)(S, Se)2Nanocrystal as Inorganic Hole-Transporting Material for Efficient and Stable Perovskite Solar Cells. *Nanoscale Res. Lett.* **2017**, *12*.

(124) Kwon, Y. S.; Lim, J.; Yun, H.-J.; Kim, Y.-H.; Park, T. A Diketopyrrolopyrrole-Containing Hole Transporting Conjugated Polymer for Use in Efficient Stable Organic–inorganic Hybrid Solar Cells Based on a Perovskite. *Energy Environ. Sci.* **2014**, *7*, 1454.

(125) XU, B. *Advanced Organic Hole Transport Materials for Solution-Processed Photovoltaic Devices Bo Xu*; 2015.

(126) Hawash, Z.; Ono, L. K.; Raga, S. R.; Lee, M. V; Qi, Y. Air-Exposure Induced Dopant Redistribution and Energy Level Shifts in Spin-Coated Spiro-MeOTAD Films. *Chem. Mater.* **2015**, *27*, 562–569.

(127) Dhingra, P.; Singh, P.; Rana, P. J. S.; Garg, A.; Kar, P. Hole-Transporting Materials for Perovskite-Sensitized Solar Cells. *Energy Technol.* **2016**, *4*, 891–938.

(128) De La Torre, G.; Claessens, C. G.; Torres, T. Phthalocyanines: Old Dyes, New Materials. Putting Color in Nanotechnology. *Chem. Commun.* **2007**, 2000–2015.

(129) Claessens, C. G.; Hahn, U.; Torres, T. Phthalocyanines: From Outstanding Electronic Properties to Emerging Applications. *Chem. Rec.* **2008**, *8*, 75–97.

(130) Mack, J.; Kobayashi, N. Low Symmetry Phthalocyanines and Their Analogues. *Chem. Rev.* **2011**, *111*, 281–321.

(131) Zhang, Y.; Paek, S.; Urbani, M.; Medel, M.; Zimmermann, I.; Cho, K. T.; Ince, M.; Nazeeruddin, M. K.; Torres, T. Unsymmetrical and Symmetrical Zn(II) Phthalocyanines as Hole-Transporting Materials for Perovskite Solar Cells. *ACS Appl. Energy Mater.* **2018**, *1*, 2399–2404.

(132) Walter, M. G.; Rudine, A. B.; Wamser, C. C. Porphyrins and Phthalocyanines in Solar Photovoltaic Cells. *J. Porphyr. Phthalocyanines* **2010**, *14*, 759–792.

(133) Sfyri, G.; Kumar, C. V.; Wang, Y. L.; Xu, Z. X.; Krontiras, C. A.; Lianos, P. Tetra Methyl Substituted Cu(II) Phthalocyanine as Alternative Hole Transporting Material for Organometal Halide Perovskite Solar Cells. *Appl. Surf. Sci.* **2016**, *360*, 767–771.

(134) Vijay Kumar, C.; Sfyri, G.; Dimitrios Raptis, ab; Elias Stathatos, ac; Lianos, P. Perovskite Solar Cell with Low Cost Cu-Phthalocyanine as Hole Transporting Material. *RSC Adv.* **2014**, *5*.

(135) Ramos, F. J.; Ince, M.; Urbani, M.; Abate, A.; Grätzel, M.; Ahmad, S.; Torres, T.; Nazeeruddin, M. K. Non-Aggregated Zn(II)Octa(2,6-Diphenylphenoxy) Phthalocyanine as a Hole Transporting Material for Efficient Perovskite Solar Cells. *Dalt. Trans.* **2015**, *44*.

(136) Ke, W.; Zhao, D.; Grice, C. R.; Cimaroli, A. J.; Fang, G.; Yan, Y. Efficient Fully-Vacuum-Processed Perovskite Solar Cells Using Copper Phthalocyanine as Hole Selective Layers. *J. Mater. Chem. A* **2015**, *3*, 23888–23894.

(137) Sfyri, G.; Kumar, C. V.; Sabapathi, G.; Giribabu, L.; Andrikopoulos, K. S.; Stathatos, E.; Lianos, P. Subphthalocyanine as Hole Transporting Material for Perovskite Solar Cells. *RSC Adv.* **2015**.

(138) Urbani, M.; Grätzel, M.; Nazeeruddin, M. K.; Torres, T. Meso-Substituted Porphyrins for Dye-Sensitized Solar Cells. *Chem. Rev.* **2014**, *114*, 12330–12396.

(139) Chou, H. H.; Chiang, Y. H.; Li, M. H.; Shen, P. S.; Wei, H. J.; Mai, C. L.; Chen, P.; Yeh, C. Y. Zinc Porphyrin-Ethynylaniline Conjugates as Novel Hole-Transporting Materials for Perovskite Solar Cells with Power Conversion Efficiency of 16.6%. *ACS Energy Lett.* **2016**, *1*, 956–962.

(140) Bakr, Z. H.; Wali, Q.; Fakharuddin, A.; Schmidt-Mende, L.; Brown, T. M.; Jose, R. Advances in Hole Transport Materials Engineering for Stable and Efficient Perovskite Solar Cells. *Nano Energy* **2017**, *34*, 271–305.

(141) Habisreutinger, S. N.; Leijtens, T.; Eperon, G. E.; Stranks, S. D.; Nicholas, R. J.; Snaith, H. J. Carbon Nanotube/Polymer Composites as a Highly Stable Hole Collection Layer in Perovskite Solar Cells. *Nano Lett.* **2014**, *14*, 5561–5568.

(142) Lijun Hu, Kuan Sun, Ming Wang, Wei Chen, Bo Yang, Jiehao Fu, Zhuang Xiong, Xinyi Li, Xiaosheng Tang, Zhigang Zang, Shupeng Zhang, Lidong Sun, and M. L. Inverted Planar Perovskite Solar Cells with a High Fill Factor and Negligible Hysteresis by the Dual Effect of NaCl-Doped PEDOT:PSS. *ACS Appl. Mater. Interfaces* **2017**, *9*, 43902–43909.

(143) Bi, D.; Yang, L.; Boschloo, G.; Hagfeldt, A.; Johansson, E. M. J. Effect of Different Hole Transport Materials on Recombination in CH 3NH3PbI3 Perovskite-Sensitized Mesoscopic Solar Cells. *J. Phys. Chem. Lett.* **2013**, *4*, 1532–1536.

(144) Abbas, H. A.; Kottokkaran, R.; Ganapathy, B.; Samiee, M.; Zhang, L.; Kitahara, A.; Noack, M.; Dalal, V. L. High Efficiency Sequentially Vapor Grown N-i-p CH3NH3PbI3 Perovskite Solar Cells with Undoped P3HT as p-Type Heterojunction Layer. *APL Mater.* **2015**, *3*.

(145) Li, R.; Xiang, X.; Tong, X.; Zou, J.; Li, Q. Wearable Double-Twisted Fibrous Perovskite Solar Cell. *Adv. Mater.* **2015**, *27*, 3831–3835.

(146) McCulloch, I.; Heeney, M. Polytriarylamine Semiconductors. *Mater. Matters (Milwaukee, WI, United States)* **2009**, *4*, 70–71.

(147) Namkoong, G.; Boland, P.; Lee, K.; Dean, J. Design of Organic Tandem Solar Cells Using PCPDTBT: PC61BM and P3HT: PC71BM. *J. Appl. Phys.* **2010**, *107*.

(148) Bi, C.; Wang, Q.; Shao, Y.; Yuan, Y.; Xiao, Z.; Huang, J. Non-Wetting Surface-Driven High-Aspect-Ratio Crystalline Grain Growth for Efficient Hybrid Perovskite Solar Cells. *Nat. Commun.* **2015**, *6*, 1–7.

(149) Kim, Y. H.; Sachse, C.; MacHala, M. L.; May, C.; Müller-Meskamp, L.; Leo, K. Highly Conductive PEDOT:PSS Electrode with Optimized Solvent and Thermal Post-Treatment for ITO-Free Organic Solar Cells. *Adv. Funct. Mater.* **2011**, *21*, 1076–1081.

(150) Shi, H.; Liu, C.; Jiang, Q.; Xu, J. Effective Approaches to Improve the Electrical Conductivity of PEDOT:PSS: A Review. *Adv. Electron. Mater.* **2015**, *1*, 1–16.

(151) Tae-Woo Lee, Ohyun Kwon, Mu-Gyeom Kim, Sang Hun Park, Jaegwan Chung, Sang Yeol Kim, Youngsu Chung, Joon-Yong Park, Eunsil Han, Dal Ho Huh, Jong-Jin Park, and L. P. Hole-Injecting Conducting-Polymer Compositions for Highly Efficient and Stable Organic Light-Emitting Diodes. *Appl. Phys. Lett.* **2005**, *87*, 1–3.

(152) Jingbi You, Yang (Michael) Yang, Ziruo Hong, Tze-Bin Song, Lei Meng, Yongsheng Liu, Chengyang Jiang, Huanping Zhou, Wei-Hsuan Chang, Gang Li, and Y. Y. Moisture Assisted Perovskite Film Growth for High Performance Solar Cells. *Appl. Phys. Lett.* **2014**, *105*, 183902.

(153) Norrman, K.; Madsen, M. V.; Gevorgyan, S. a.; Krebs, F. C. Degradation Patterns in Water and Oxygen of an Inverted Polymer Solar Cell. *J. Am. Chem. Soc.* **2010**, *132*, 16883–16892.

(154) Chen, W.; Bao, X.; Zhu, Q.; Zhu, D.; Qiu, M.; Sun, M.; Yang, R. Simple Planar Perovskite Solar Cells with a Dopant-Free Benzodithiophene Conjugated Polymer as Hole Transporting Material. *J. Mater. Chem. C* **2015**, *3*, 10070–10073.

(155) Dubey, A.; Adhikari, N.; Venkatesan, S.; Gu, S.; Khatiwada, D.; Wang, Q.; Mohammad, L.; Kumar, M.; Qiao, Q. Solution Processed Pristine PDPP3T Polymer as Hole Transport Layer for Efficient Perovskite Solar Cells with Slower Degradation. *Sol. Energy Mater. Sol. Cells* **2016**, *145*, 193–199.

(156) Jeon, N. J.; Lee, H. G.; Kim, Y. C.; Seo, J.; Noh, J. H.; Lee, J.; Seok, S. Il. O-Methoxy Substituents in Spiro-OMeTAD for Efficient Inorganic-Organic Hybrid Perovskite Solar Cells. *J. Am. Chem. Soc.* **2014**, *136*, 7837–7840.

(157) Hammett, L. P. The Effect of Structure upon the Reactions of Organic Compounds. Benzene Derivatives. *J. Am. Chem. Soc.* **1937**, *59*, 96–103.

(158) Michael Saliba, Simonetta Orlandi, Taisuke Matsui, Sadig Aghazada, Marco Cavazzini, Juan-Pablo Correa-Baena, Peng Gao, Rosario Scopelliti, Edoardo Mosconi, Klaus-Hermann Dahmen, Filippo De Angelis, Antonio Abate, Anders Hagfeldt, Gianluca Poz, M. G. and M. K. N. A Molecularly Engineered Hole-Transporting Material for Efficient Perovskite Solar Cells. *Nat. Energy* **2016**, *1*, 15017.

(159) Gratia, P.; Magomedov, A.; Malinauskas, T.; Daskeviciene, M.; Abate, A.; Ahmad, S.; Grätzel, M.; Getautis, V.; Nazeeruddin, M. K. Methoxydiphenylamine-Substituted Carbazole Twin Derivative: An Efficient Hole-Transporting Material for Perovskite Solar Cells. *Angew. Chemie Int. Ed.* **2015**, n/a-n/a.

(160) Abate, A.; Planells, M.; Hollman, D. J.; Barthi, V.; Chand, S.; Snaith, H. J.; Robertson, N. Hole-Transport Materials with Greatly-Differing Redox Potentials Give Efficient TiO 2 – [CH 3 NH 3][PbX 3] Perovskite Solar Cells. *Phys. Chem. Chem. Phys. Phys. Chem. Chem. Phys* **2015**, *17*, 2335–2338.

(161) Shirota, Y. Photo- and Electroactive Amorphous Molecular Materials—molecular Design, Syntheses, Reactions, Properties, and Applications. *J. Mater. Chem.* **2005**, *15*, 75–93.

(162) Cho, A.-N.; Kim, H.-S.; Bui, T.-T.; Sallenave, X.; Goubard, F.; Park, N.-G. Role of LiTFSI in High T_g Triphenylamine-Based Hole Transporting Material in Perovskite Solar Cell. *RSC Adv.* **2016**, *6*, 68553–68559.

(163) Yulia A. Getmanenko, Joel M. Hales, Mihaela Balu, Jie Fu, Egbert Zojer, Ohyun Kwon, Jeffrey Mendez, S. Thayumanavan, Gregory Walker, Qing Zhang, Scott D. Bunge, Jean-Luc Bredas, D. J. H.; Eric W. Van Stryland, S. B. and S. R. M. Characterisation of a Dipolar Chromophore with Third-Harmonic Generation Applications in the near-IR. *J. Mater. Chem.* **2012**, *22*, 4371–4382.

(164) Zeng, Z.; Lee, S.; Son, M.; Fukuda, K.; Burrezo, P. M.; Zhu, X.; Qi, Q.; Li, R. W.; Navarrete, J. T. L.; Ding, J.; *et al.* Push-Pull Type Oligo(N -Annulated Perylene)Quinodimethanes: Chain Length and Solvent-Dependent Ground States and Physical Properties. *J. Am. Chem. Soc.* **2015**, *137*, 8572–8583.

(165) Mishra, A.; Steck, C.; Franckevičius, M.; Zakeeruddin, S. M.; Baeuerle, P.; Grätzel, M. A-D-A-Type S,N-Heteropentacene-Based Hole Transport Materials for Dopant-Free Perovskite Solar Cells. *J. Mater. Chem. A* **2015**.

(166) Arora, N.; Wetzel, C.; Dar, M. I.; Mishra, A.; Yadav, P.; Steck, C.; Zakeeruddin, S. M.; Bäuerle, P.; Grätzel, M. Donor-Acceptor-Type S,N-Heteroacene Based Hole Transporting Materials for Efficient Perovskite Solar Cells. *ACS Appl. Mater. Interfaces* **2017**, acsami.7b10039.

(167) Zheng, L.; Chung, Y.-H.; Ma, Y.; Zhang, L.; Xiao, L.; Chen, Z.; Wang, S.; Qu, B.; Gong, Q. A Hydrophobic Hole Transporting Oligothiophene for Planar Perovskite Solar Cells with Improved Stability. *Chem. Commun.* **2014**, *50*, 11196–11199.

(168) Heo, J. H.; Park, S.; Im, S. H.; Son, H. J. Development of Dopant-Free Donor-Acceptor-Type Hole Transporting Material for Highly Efficient and Stable Perovskite Solar Cells. *ACS Appl. Mater. Interfaces* **2017**, *9*, 39511–39518.

(169) Van Der Poll, T. S.; Love, J. A.; Nguyen, T. Q.; Bazan, G. C. Non-Basic High-Performance Molecules for Solution-Processed Organic Solar Cells. *Adv. Mater.* **2012**, *24*, 3646–3649.

(170) Hiroshi Kageyama, Hitoshi Ohishi, Masatake Tanaka, Y. O. and Y. S. High-Performance Organic Photovoltaic Devices Using a New Amorphous Molecular Material with High Hole Drift Mobility, Tris[4-(5-Phenylthiophen-2-Yl)Phenyl]Amine. *IEEE* **2010**, *16*, 1528–1536.

(171) Zang, L.; Che, Y.; S.Moore, J. One-Dimensional Self-Assembly of Planar π-Conjugated Molecules: Adaptable Building Blocks for Organic Nanodevices. *Acc. Chem. Res.* **2008**, *41*, 1596–1608.

(172) Kafer, D.; El Helou, M.; Gemel, C.; Witte, G. Packing of Planar Organic Molcules: Interplay of van Der Waals and Electronic Interaction. *Cryst. Growth Des.* **2008**, *8*, 3053–3057.

(173) Yoshihara, T.; Druzhinin, S. I.; Zachariasse, K. A. Fast Intramolecular Charge Transfer with a Planar Rigidized Electron Donor/Acceptor Molecule. *J. Am. Chem. Soc.* **2004**, *126*, 8535–8539.

(174) Roy, B.; Reddy, M. C.; Hazra, P. Developing the Structure-Property Relationship to Design Solid State Multi-Stimuli Responsive Materials and Their Potential Applications in Different Fields. *Chem. Sci.* **2018**, *9*, 3592–3606.

(175) Jeon, N. J.; Lee, J.; Noh, J. H.; Nazeeruddin, M. K.; Grätzel, M.; Seok, S. Il. Efficient Inorganic-Organic Hybrid Perovskite Solar Cells Based on Pyrene Arylamine Derivatives as Hole-Transporting Materials. *J. Am. Chem. Soc.* **2013**, *135*, 19087–19090.

(176) Choi, H.; Paek, S.; Lim, N.; Lee, Y. H.; Nazeeruddin, M. K.; Ko, J. Efficient Perovskite Solar Cells with 13.63 % Efficiency Based on Planar Triphenylamine Hole Conductors. *Chem. Eur. J* **2014**, *20*, 10894–10899.

(177) Kasparas Rakstys, Antonio Abate, M. Ibrahim Dar, Peng Gao, Vygintas Jankauskas, Gwénolé Jacopin, Egidijus Kamarauskas, Samrana Kazim, Shahzada Ahmad, Michael Grätzel, and M. K. N. Triazatruxene-Based Hole Transporting Materials for Highly Efficient Perovskite Solar Cells. *J. Am. Chem. Soc.* **2015**, *137*, 16172–16178.

(178) Tang, A.; Zhan, C.; Yao, J.; Zhou, E. Design of Diketopyrrolopyrrole (DPP)-Based Small Molecules for Organic-Solar-Cell Applications. *Adv. Mater.* **2017**, *29*.

(179) Jeon, S.; Thakur, U. K.; Lee, D.; Wenping, Y.; Kim, D.; Lee, S.; Ahn, T. K.; Park, H. J.; Kim, B. G. N-Phenylindole-Diketopyrrolopyrrole-Containing Narrow Band-Gap Materials for Dopant-Free

Hole Transporting Layer of Perovskite Solar Cell. *Org. Electron.* **2016**, *37*, 134–140.

Chapter II

Thienothiophene derivatives based hole transporting materials

CHAPTER 2 : THIENOTHIOPHENE DERIVATIVES-BASED HTMS

Abstract

*In this chapter, three hole transporting materials containing thieno[3,2-b]thiophene as core and π-linker substituted by 4,4'-dimethoxytriphenylamine donor groups in 2,5- ; 3,6- and 2,3,5,6-position are presented. The influence of variety substituted position in these new materials on the photophysical, electrochemical, thermal properties, crystallographic structure, morphological and photovoltaic performance in perovskite solar cells are investigated. Synthesis and characterizations were carried out in LPPI and morphological properties was measured by Dr. Nghiem and coworkers at the Federation iMAT- Cergy Pontoise University. Crystallographic structure was analyzed by Dr Pham and coworkers at ICMMO- Paris Sud University. The DFT calculations was completed by Dr. Peralta and thanks to synthesis of compound 3,6-dibromothieno[3,2-b]thiophene by Dr. Sallenave in LPPI; PSCs devices fabrication was carried out and optimized by Dr.Dao and coworkers at EEI-Osaka University. Although thermal, morphological and hydrophobic properties of TT-2,5TPA and TT-3,6TPA are similar, their optoelectrochemical and photovoltaic performance are completely distinctive. Due to different of linear conjugation and cross conjugation, the compound TT-2,5TPA showed better power conversion efficiency (13.6%) in hybrid perovskite solar cells than that of TT-3,6TPA (0.7%).The detail studied was presented in an article published in the Chemistry-A Asian journal (**Triphenylamine-thienothiophene organic charge transport molecular materials: impact of arylamine substitution position on thermal, photoelectrochemical and photovoltaic properties-DOI: 10.1002/asia.201701790**).The TT-4TPA was also employed as HTMs in PSCs and obtained remarkable results on photovoltaics performance (13.66%) while Spiro-OMeTAD as control devive (16.87%).This compound is going underoptimization to improve efficiency as well as device stability.*

II.1 Introduction

As mentioned in ***Chapter I***, hole transporting materials (HTMs) play a key role in perovskite solar cells (PSCs) as well as organic photovoltaics (OPVs). Among plentiful organic HTMs, our interest has been focused on arylamine derivatives, one of the most applied building blocks in OLEDs[1], DSSCs[2], OPVs[3] and OFETs[4]. Indeed, a number of simple donor-π-donor molecule HTMs have been synthesized by varying the central π-linker and the endcapping arylamine derivatives.[5–7] Triphenylamine (TPA) presents some features such as convenience in chemical modification, propeller-like structure, strong electron-donating ability, interesting electrochemical property, good charge transport property, high thermal and morphological stability.[8,9] OPVs, dye-sensitized solar cells (DSSCs) and PSCs have used TPA-based materials and have exceeded 14.2%, 14% and 20% respectively, which are among the best obtained results of these three kinds of

devices[8]. Moreover, the methoxy groups (-OCH_3) render the molecules more soluble in organic solvents and they play electron-donating function in *para*-positions of phenyl rings of the diphenylamine moiety, thus favor the charge transport properties, reduce charge recombination and provide high device performance.[10–12]

Thiophene and its derivatives represent a critical class which are intensively used as building blocks for organic semiconductor materials owing to their optoelectrical properties. In particular, they own high hole mobility which is an important feature for HTM design[7,13–16]. The presence of sulfur atoms in heterocyclic building blocks might promote good HTM/perovskite interface due to Pb-S interaction[16,17]. These HTMs are designed through changing the conjugation length and/or the terminal amine moiety positions.[16,18]. However, the comparative study of the influence of molecular geometry, by simply changing the arylamine substituent position on the thiophene-type π-linker, on the PSCs performances is rarely reported[19].

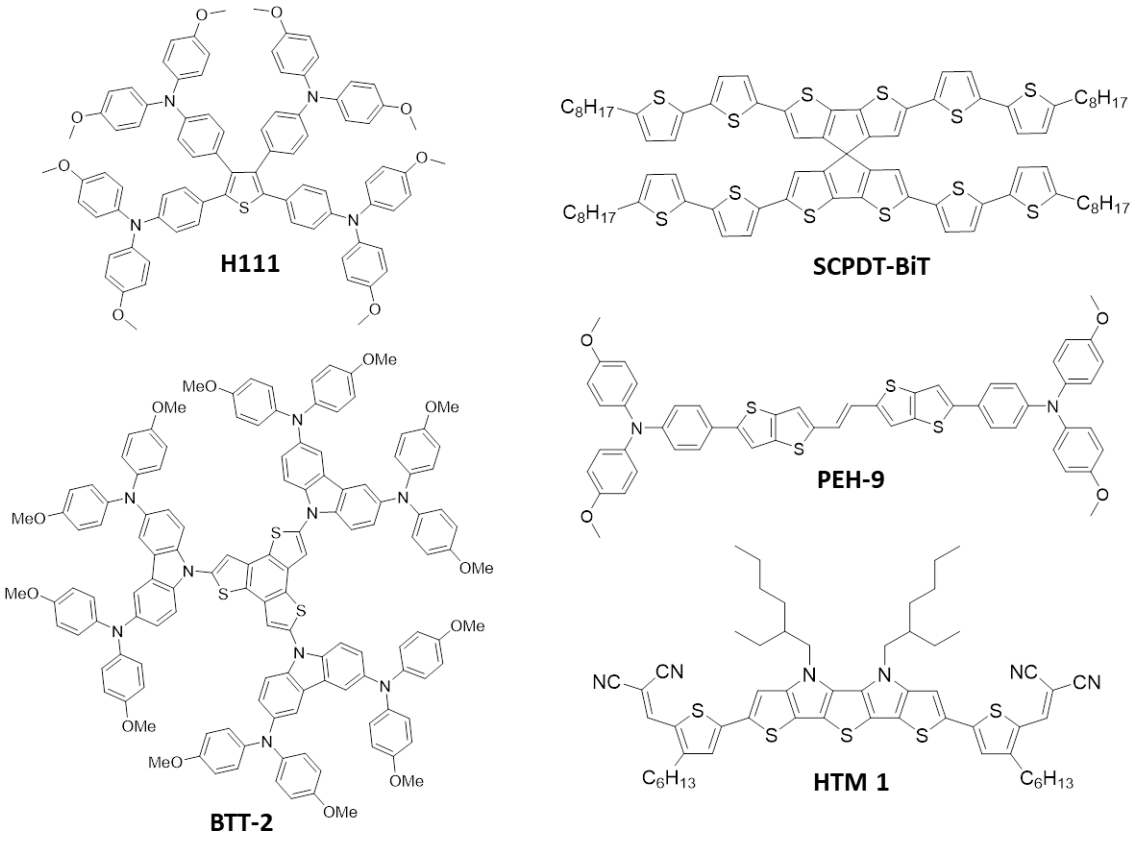

Figure 1: Examples of some representative successful HTMs small molecules based on thiophene and thiophene derivatives in solution processes PSCs.

As compared to thiophenes, fused thiophenes have a more rigid structure which possess an extended π-conjugation. They could be employed for adjusting the band gap of

organic materials and increasing intermolecular interactions in the solid state.[20,21] Particularly, thienothiophene is widely used due to their good symmetric planar structure, electron-rich unit, high hole mobility and conductivity. Thus, it is often used to construct organic semiconductor materials.

Some representative successful HTMs based on thiophene and thiophene derivatives were reported in ***Figure 1***. Similar to Spiro-OMeTAD structure, compound **H111** incoporated thiophene with strong electron donor group 4,4'-dimethoxytriphenylamine. With high glass transistion (100^{o}C) and HOMO/LUMO equal to -5.31/-2.53 eV, this compoud leads to a PCE equal to 15.4% while a value of 14.4% is obtained with Spiro-OMeTAD in PSCs[22]. It also showed excellent solubility in common organic solvents thanks to copious methoxy groups and bulky structure, which minimize the molecular aggregation. A star-shaped structure (compound **BTT-2**) is constructed by fused benzotrithiophene as a core, carbazole as electron donor groups and end-capped by 4,4'-dimethoxydiphenylamine. The planar structure of benzotrithiophene core is forseen to promote a strong π-π intermolecular interaction. This star-shape molecules shows high glass transistion (216^{o}C) and exhibited remarkable PCE of 17.5%, which is similar to that of Spiro-OMeTAD[23]. In order to expand the Spiro family, Wang, Tu *et al*[24] have synthesized thiophene-spiro typed (compound **SCPDT-BiT**) by short-steps and employed as efficient hole conductor for PSCs. Comparison with 9,9'-spirobifluorene core, the thiophene-based spiro core is easier for redox reaction because thiophene possesses higher electron density and lower aromaticity properties[25]. As a result, the optical, electrochemical and electrical properties of this derivative are different from Spiro-OMeTAD[26]. Based on strong electron-donating property of bithiophene groups, linear conjugation system and star-shaped structure, it induced hole mobility equal to $4.5.10^{-6}$ $cm^2\ V^{-1}\ s^{-1}$ vs $1.45.10^{-5}$ $cm^2\ V^{-1}\ s^{-1}$ of Spiro-OMeTAD before annealing and $5.96.10^{-5}$ $cm^2\ V^{-1}\ s^{-1}$ vs 5.37. 10^{-5} $cm^2\ V^{-1}\ s^{-1}$ of Spiro-OMeTAD after pre-annealing treatment. In fact, annealing treatment could support for molecular rearrangement, improve packing effect and then increase hole mobility. The higher hole mobility of SCPDT-BiT could be belonged to the high charge carrier mobility of the thiophene unit. PCE of 10.39% was obtained comparable to 13.27% of Spiro-OMeTAD[24]. By incorporating thieno[3,2-*b*]thiophene group with 4,4'-dimethoxy-triphenylamine through ethylene unit as the π-brigde (compound **PEH-9**), its conjugation are prolonged and short intermolecular (π…π) distances (3.36 Å) are noticed. As a result, a good film-forming on top of

perovskite layer are observed and remarkable PCE close to 17% was achieved. Good thermal stability was confirmed by only 7% of PCE lost after 400h soaking[27].

The incorporation of donor (D) and acceptor (A) groups based on push-pull molecules display intermolecular-intramolecular charge transfer properties. Indeed, P. Gao *et al*[28] reported the incorporation of a rigid S,N-heteropentacene central unit and dicyanovinylene acceptor groups in compound HTM 1**.** This latter shows very low bandgap (1.49 eV), broad absorption in the visible and near-IR region, which consequently plays role as a light absorber as well as hole conductor. As a result, high devices performance comprising of perovskite/compound HTM 1 can be prepared and 10.5% of PCE were achieved without the use of any additives/dopants. Therefiore, it could avoid degradation and improve the stability of PSCs.

II. 2 Objectives and strategies

This chapter is aimed to design and synthesize new family of HTMs materials based on bisarylamine substituted thieno[3,2-b]thiophene. Thieno[3,2-b]thiophene was chosen due to good symmetric planar structure, high mobility and conductivity[29]. In this sudy, it could be used as a π-bridge connecting two TPA moieties. Moreover, the sulfur atoms play important role because it affects to the distribution of electrons density of HOMO state, then affect to hole carrier property[30]. The structure of these compounds was designed based on organic semiconductor materials (***Figure 2***).

Thieno[3,2-b]thiophene are end-capped by the strong electron-donating group 4,4'-dimethoxytriphenylamine groups (TPA) in 2,5-positions (compound TT-2,5 TPA); 3,6-positions (compound TT-3,6 TPA) and 2,3,5,6-positions (compound TT-4 TPA). A comparison between TT-2,5 TPA (linear conjugated molecule) and TT-3,6 TPA (non-linear conjugated molecule) will be comparative discussed by investigation of their physical-chemical properties and evaluation of their device performance[31].

According to 3D structure of TT-4-TPA, the arrangement of the four moieties leads to a rigid structure with large steric hindrance. The developement of spiro-like structure results to high glass temperature (T_g) and improves their morphological stability in the solid state. It is expected to be an amorphous structure with homogenous film morphology and could be a promising candidate for optoelectronics applications.

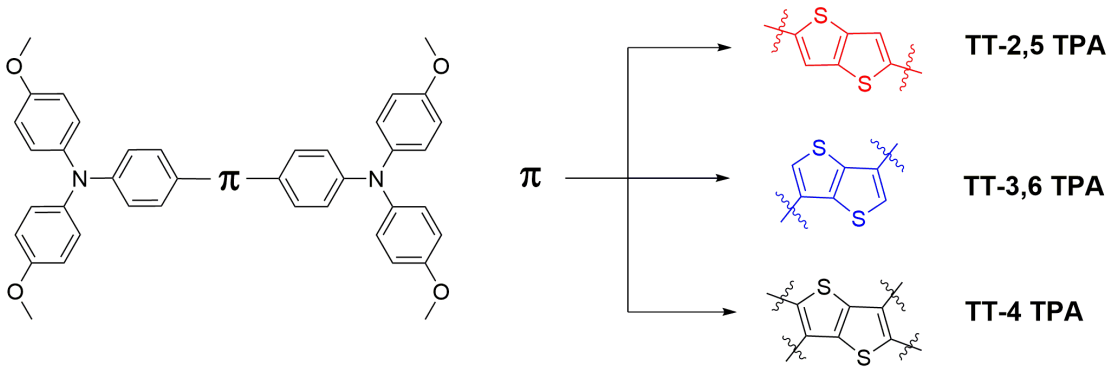

Figure 2: Chemical structure of Thienothiophene derivatives in this study.

The objective in this study is to compare linear-conjugated molecule with non linear-conjugated molecule and investigate quasi-3D structure molecule based on Thienothiophene core. A better understanding on the influence of molecular structure arrangement on their thermal, morphological, optical, electrochemical properties were developed. Finally, these HTMs were applied on PSCs, and corresponding photovoltaic performances were discussed.

II. 3 Results and discussions

Synthesis of the materials

The synthetic route toward targeted molecules is summarized in ***Scheme 1***. All compounds were synthetized by mean of Suzuki coupling reaction between the 4-(4,4,5,5-tetramethyl-1,3,2-dioxaborolan-2-yl)-N,N-bis(4-methoxyphenyl)aniline (compound 1) and brominated thienothiophenes (compound 2-4).

Compound 1 is a known compound and its synthesis was adapted from the literature[32]. In the first attempts, 4-iodoanisole was reacted with aniline under different Buchwald-Hartwig amination conditions in presence of $Pd(OAc)_2$, $^tBu_3P$ and NaOtBu as catalysts. However, the synthetic yield of the desired product (TPA) was very low due to formation of mono-coupling 4,4'-dimethoxydiphenylamine (DPA) (main product). Finally, TPA was synthetized in good yield (90% yield) under Ullman amination coupling condition (Cu, K_2CO_3 and 18-crown-6) using large excess of 4-iodoanisole as solvent. TPA was the main product and excess 4-iodoanisole was easily recovered by means of chromatography purification and could be reused to resynthesize TPA.

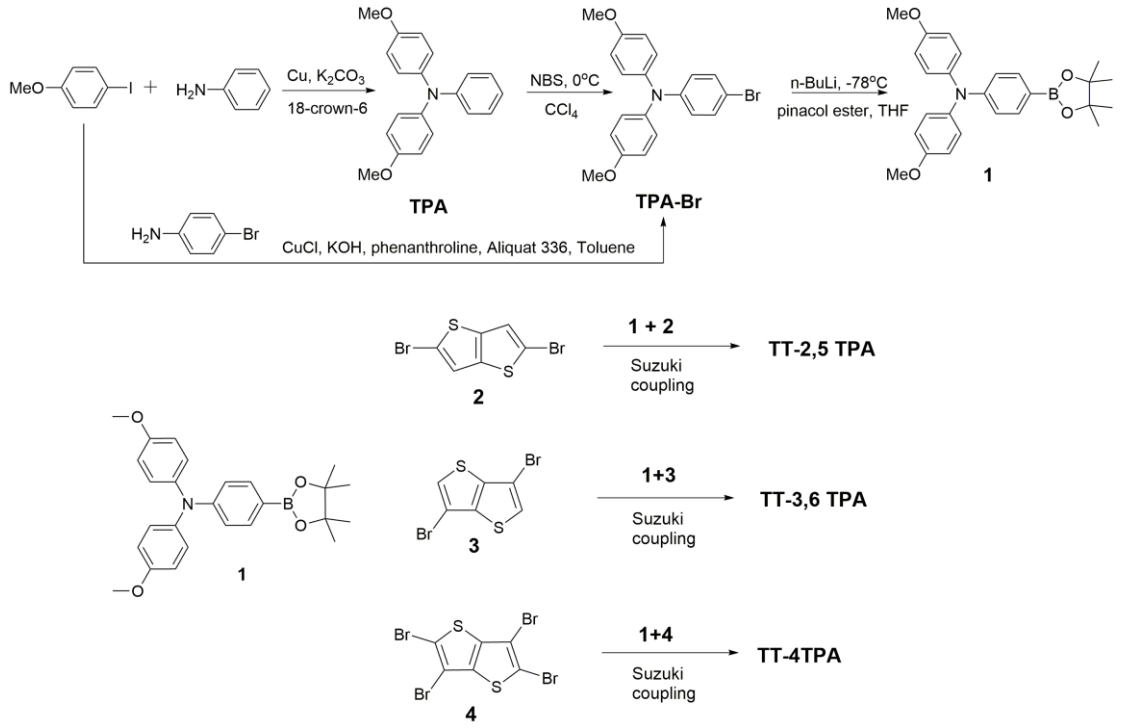

Scheme 1: Synthetic route of Thienothiophene-based HTMs and precursors. Suzuki coupling reaction conditions : $Pd(PPh_3)_4$, K_2CO_3, Aliquat 336, Toluene, 110°C, 24h.

In the next step, TPA was subjected to the bromination reaction by N-bromosuccinimide (NBS). The desired product (TPA-Br) was obtained in low yield (<10%) with chloroform or DMF as solvents. It was found that CCl_4 is a better solvent, leading to obtain TPA-Br in high yield (~80%). However, the existence of large amount of side-products as well as the toxicity of CCl_4 is drawbacks. Therefore, the alternative reaction's condition with high efficiency, mild-conditions was necessary required. Finally, the conversion of suitable substituted 4-iodoanisole with 4-bromoaniline to the directly corresponding bromide-substituted TPA was realized in good yields via Ullman coupling reaction by using copper (I) chloride, 1,10-phenanthroline, KOH and Aliquat 336 as catalyst systems. In this case, the diamine ligand was critical to the success of the reaction and mild conditions such as short time reaction and low temperature (boiling point of toluene 105°C) were some advantages. Then, the synthesis of boronic acid pinacolates was achieved via metal halogen exchange using n-butyllithium in THF at -78°C and followed by isopropyl pinacol borate in good yield conversion.

The synthetic route for construction of the thieno[3,2-b]thiophene precursors was briefly overviewed[33] in the ***Scheme 2***. The starting material 3-bromothiophene is available commercially.

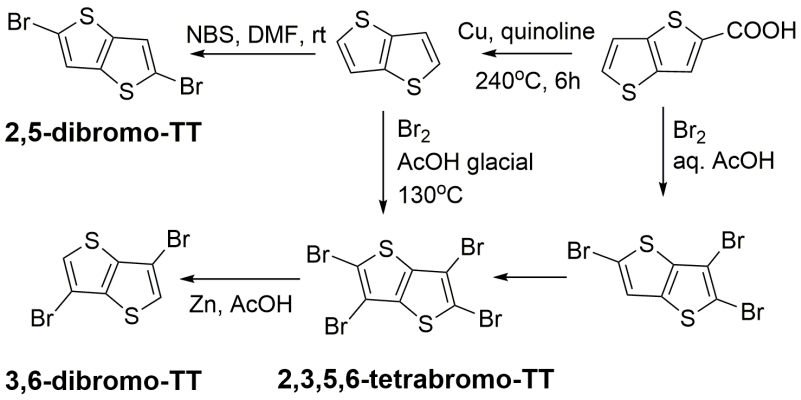

Scheme 2: Synthetic route of thieno[3,2-b]thiophene ring systems.Figure adapted from reference[33]

The bromo-substitued derivatives of thieno[3,2-*b*]thiophene were synthesized though several steps. In this study, some precursors were synthesized in our laboratory. For example, thieno[3,2-*b*]thiophene was synthesized from 2-thieno[3,2-*b*]thiophene carboxylic with quinoline as high boiling point solvent and Cu as catalyst at 240^{o}C for 6 hours (or until no more bubble). Compound 2,3,5,6-tetrabromo-TT can be synthesized via 2,3,5-tribromothieno[3,2-*b*]thiophene or thieno[3,2-*b*]thiophene. Indeed, thieno[3,2-*b*]thiophene was reacted with Br_2 solution in glacial acid acetic at 130^{o}C. The first formation is mono-bromthienothiophene, then the reaction was monitored by TLC (thin layer chromatography) until all starting material was consumed and an off-white precipitate was formed. The latter was filtered off and recrystallized in toluene twice to obtain needle-shaped white crystals 2,3,5,6-tetrabromo-TT (~50% yield). Otherwise, compound 2,5-dibromo-TT was formed via bromination of thieno[3,2-*b*]thiophene by NBS in DMF at room temperature. The desired product was obtained high yield due to 2 hydrogen atoms in 2,5-position are very active. Compound 3,6-dibromo-TT was converted from compound 2,3,5,6-tetrabromo-TT by zinc and acetic acid and obtain 70% yield. Both of intermediate 2,5-dibromo-TT and 3,6-dibromo-TT compounds were supported by colleagues in our laboratory. Therefore, these precursors was synthesized throughout carefully steps, leads to its expensive commercially product.

Finally, the target compounds have been prepared from **1** and **2-4** in ***Scheme 1***. TT-2,5 TPA and TT-36-TPA were obtained in good yield (70%). However, TT-4TPA was obtained in low yield (34%) due to formation of various side products such as mono-, di- or tri-substituted TPA groups on thienothiophene unit and residue starting materials. Additionally, compound TT-4TPA owns bulky structure and high steric hindrance which could explain the lower yield and difficultly to be purified by column chromatography.

All compounds were identified structure by NMR and HRMS spectra. Final molecules were further analyzed by single crystal X-ray diffraction. No suitable single crystals of TT-4TPA were obtained.

These target compounds have good solubility in common organic solvents, such as dichloromethane, chloroform, tetrahydrofuran, (di)chlorobenzene, and toluene rendering these molecules suitable for application in solution-processed organic electronic devices.

II.3.1 Thermal and morphological properties.

Thermal behaviors of new materials were first investigated by thermogravimetric analysis (TGA) and differential scanning calorimetry (DSC) under argon atmosphere. Their TGA and DSC curves are given in ***Figure 3*** and their values of thermal decomposition ($T_{d\ 5\%}$) and glass transition (T_g) are summarized in ***Table 1***.

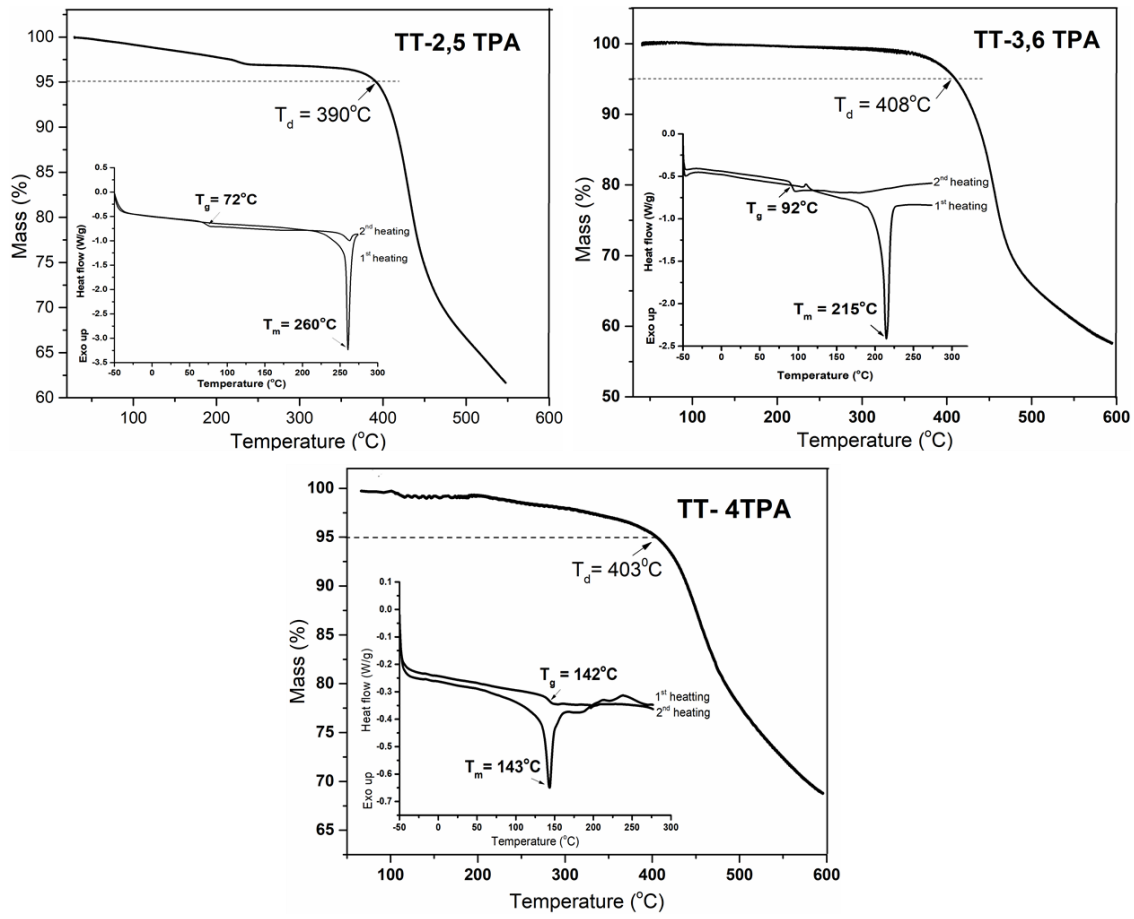

Figure 3: DSC-TGA of TT-2,5 TPA, TT-3,6 TPA and TT-4TPA.

These compounds showed significant thermal stability (390oC, 408oC and 403oC for TT-2,5-TPA, TT-3,6-TPA and TT-4-TPA, respectively), which prevent decomposition in device fabrication. DSC studies revealed the molecular glass forming

properties of all compounds. Although TT-2,5 TPA and TT-3,6 TPA possess the same molecular weight, but because of different molecular geometry and rigidity, it invloves a different glass transition temperature (72oC and 92oC, respectively). TT-3,6 TPA exhibits higher Tg which could provide better homogenous films, expecting to lead to a better interface contact with perovskite layer. The compound TT-4TPA shows much higher Tg than others (142oC) due to high molecular weight and bulky structure. These relatively high Tg are expected to form homogenous film and avoid crystallization in device fabrication.

The film forming property of these HTMs were then examined by atomic force microscopy (AFM). A solution of these HTMs (~30mg/1ml of chlorobenzene) was deposited on cleaned-glass substrates by spin-coating and these film morphology images were recorded and shown in ***Figure 4***.

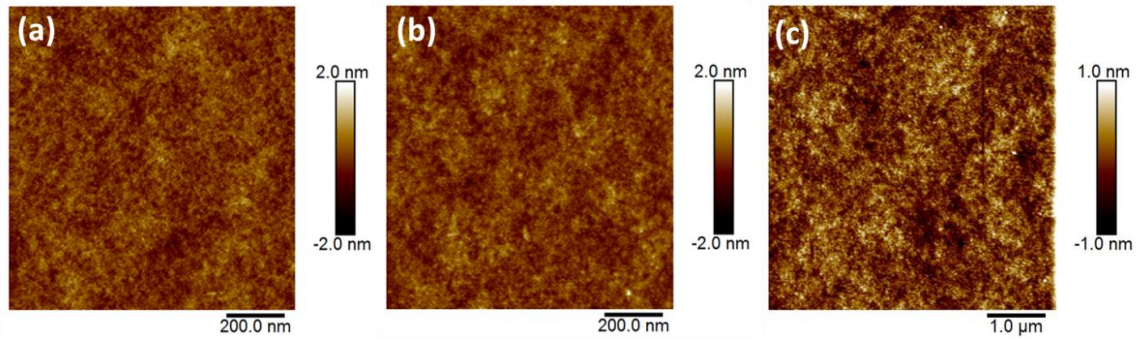

Figure 4: AFM images of (a) TT-2,5-TPA,(b) TT-3,6-TPA and (c) TT-4-TPA.

As expected for amorphous organic materials, all compounds show smooth surfaces. The surface roughness was estimated and the values ranges of 0.28 nm were found for both of TT-2,5 TPA and TT-3,6 TPA. Compound TT-4 TPA was also deposited on glass substrate and its solid state was characterized by AFM. The surface roughness average of TT-4 TPA shows 0.57 nm because it possesses more steric structure and involve an inefficient arrangement in solid state via spin-coating. However, these smooth surfaces are expected to provide good HTM/perovskite contact, therefore increasing facilitate holes transfer from perovskite to HTM.

In addition to its charge separation and transport roles, the HTM layer must protect the perovskite layer from moisture and thus improve the device stability in the presence of moisture in the operation environment. Hydrophilic HTM layers will be more readily water wet and thus more susceptible to moisture ingress than the more hydrophobic ones. Even if the permeability to liquid water/moisture can also depend on other factors such as thin film porosity, it remains that hydrophobicity should play a key role in moisture resistance for films of similar smoothness and compactness. Therefore,

we performed water contact angle measurements on those HTM layers in this study and the obtained results are given in the ***Figure 5***.

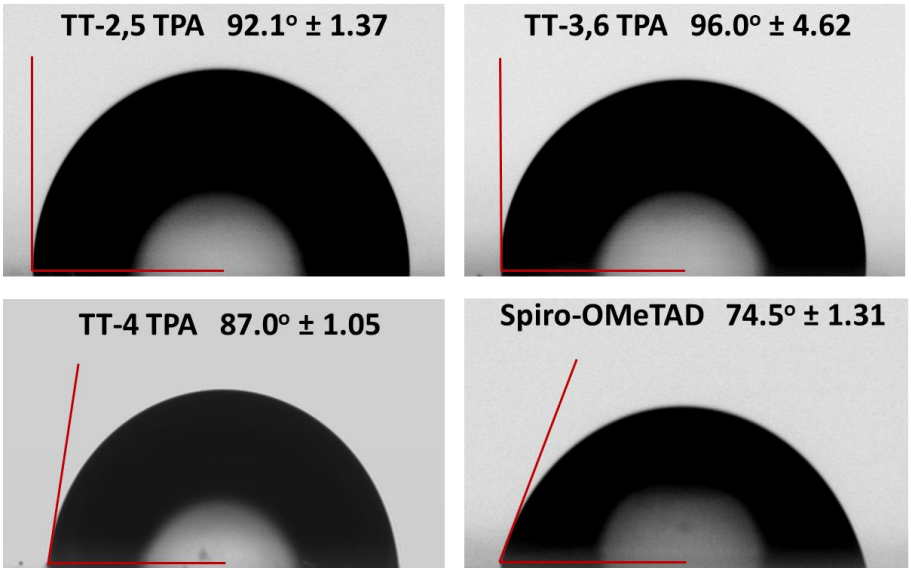

Figure 5: Contact angle measurements taken of water droplet on film on glass of pristine materials.

These compounds were determined hydrophobicity by contact angles, which are 92.1 ± 1.37° for TT-2,5-TPA and 96.0 ± 4.62° for TT-3,6-TPA. They show high hydrophobic properties, which could sufficient protect perovskite layer out of moisture. TT-4 TPA shows less hydrophobic (87.0 ° ± 1.05) than the others due to abundant –OCH_3 moieties. For comparison purpose: these values are higher than that measured for Spiro-OMeTAD under the same condition (74.5 ± 1.31°). It has been demonstrated that such hydrophobic properties are extremely beneficial to PSC stability.[34]

II.3.2 Optical properties

Optical properties of synthesized compounds were then examined by UV/Vis absorption and fluorescent spectra in dilute dicholoromethane solution (***Figure 6***) and on thin films (***Figure 7***), related data are summarized in ***Table 1.***

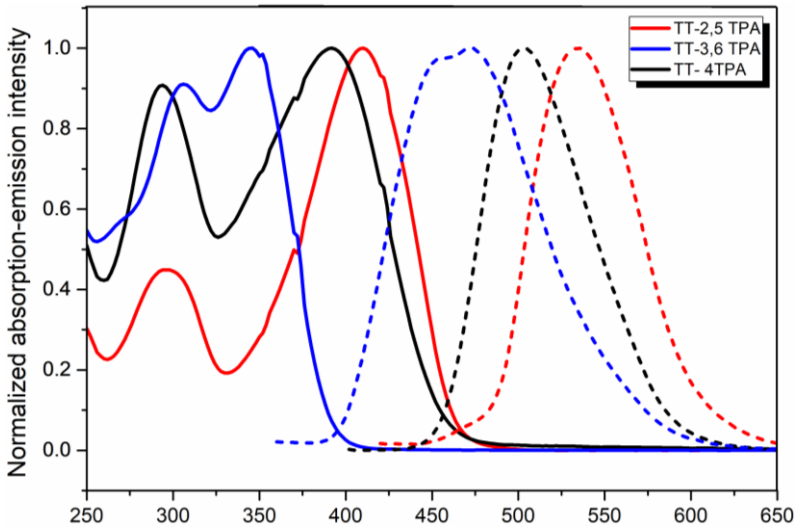

Figure 6: Normalized absorption (solid line) and emission (dash line) of TT-2,5 TPA (red), TT-3,6 TPA (blue) and TT-4 TPA (black) in dichloromethane.

TT-2,5 TPA shows an absorption maximum centered at 410 nm, which due to the π-π^* transition of the conjugated system while that of TT-3,6 TPA are blue shifted to 344 nm because of shorter conjugation. The conjugation pathway of 2,5-isomer is extended on the whole molecule but the electronic coupling of 3,6-isomer is interrupted at the middle of backbone, as a result the shorter the conjugation length, the wider bandgap. However, TT-3,6 TPA absorbed in UV domain, which could avoid screen effect to perovskite. In emission spectra, TT-2,5 TPA is red-shifted ($\lambda_{emiss\ max}$ ~534 nm) compare to that of TT-3,6 TPA ($\lambda_{emiss\ max}$ ~ 472 nm). For TT-4 TPA, its absorbed (391 nm) and emitted (503 nm) in average spectra region between TT-2,5 TPA and TT-3,6 TPA spectra.

In the thin solid film state, the absorption bands of three compounds are slightly broadened due to the 3D structure nature of molecules, which limit the aggregation of materials in solid state (***Figure 7***).

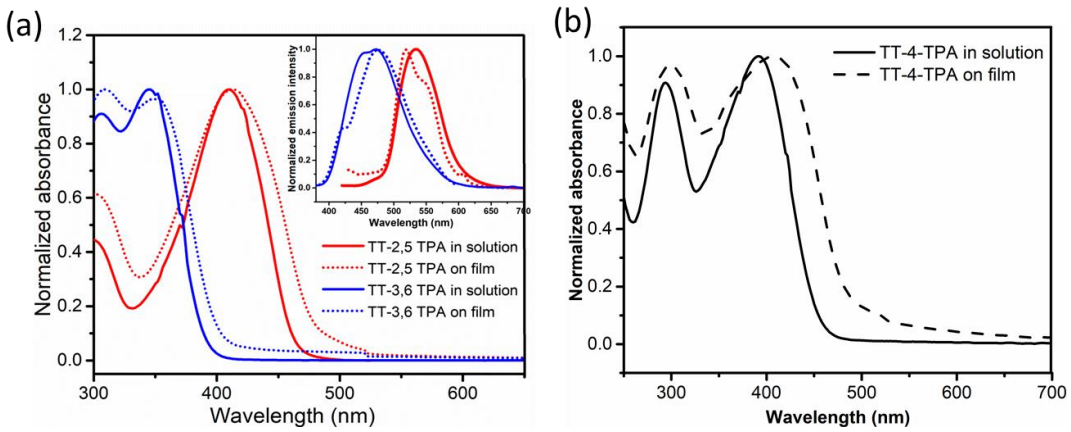

Figure 7: (a)Normalized absorption and emission (onset) spectra of TT-2,5-TPA, TT-3,6-TPA and (b) TT-4TPA in solution (solid lines) and as thin films (dotted lines)

These observations are in good accordance with the absence of intermolecular π-stacking in the crystalline state of TT-3,6 TPA (see Figure 11). The emission spectra shows TT-2,5 TPA emits at lower energy (534 nm) in comparison with TT-3,6 TPA (472 nm) and three compounds have large Stokes shifts of about 124, 128 and 112 nm respectively, which predict large changes in the geometrical configuration of the molecules upon excitation. However, in the case of TT-4 TPA, it exhibits absorption maximum (390 nm) and emission spectra (502 nm) in the midle region of those in TT-2,5 TPA and TT-3,6 TPA . It can be explained by the important steric hindrance between four TPA moieties, thus the effective conjugation of the molecule is less than that of TT-2,5-TPA. The optical bandgaps of these materials could be estimated from either the value onset of absorption bands or intersection between absorption and emission spectra. These values are summarized in Table 2.

II.3.3 Electrochemical properties

Electrochemical cyclic voltammetry (CV) has been employed to investigate the redox behavior of synthesized molecules and to determine their frontier HOMO-LUMO energy values. In this study, the CV of thienothiophene derivatives showing only their oxidations, are given on ***Figure 8*** and summarized in ***Table 1***.

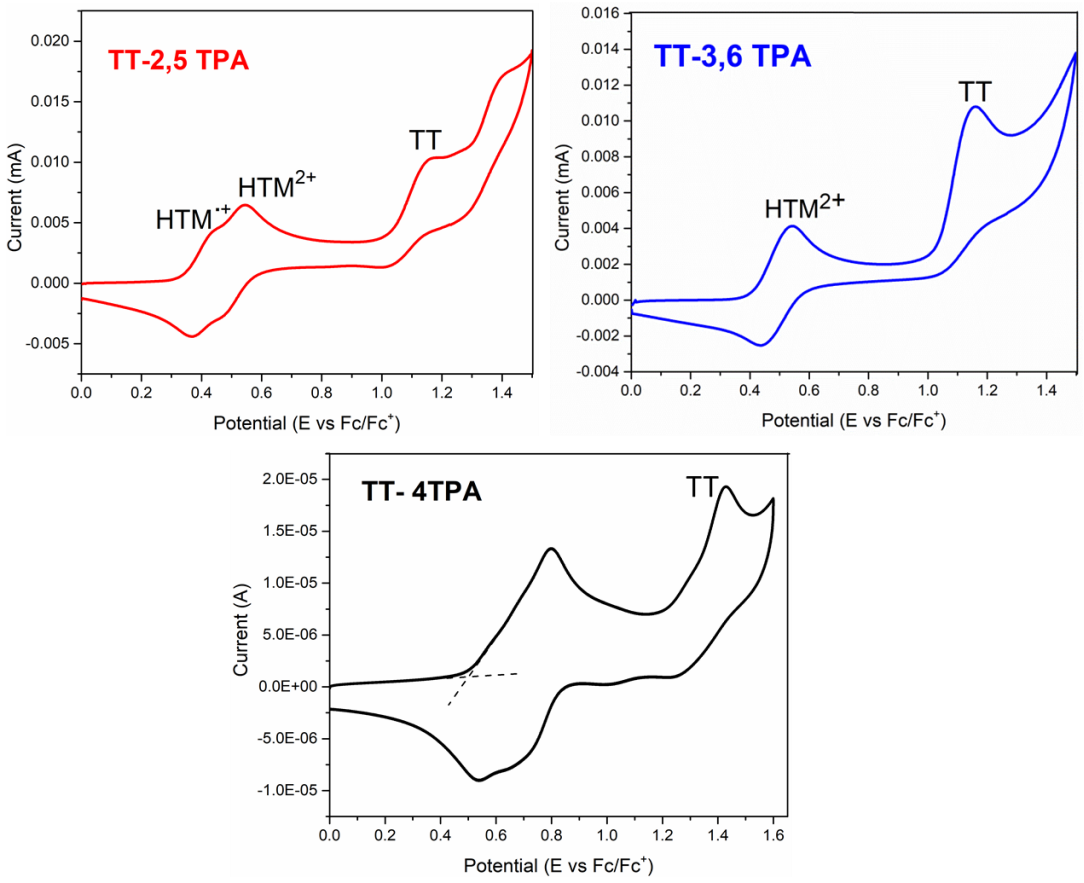

Figure 8: Cyclic voltammogram of thieno[3,2-b]thiophene derivatives.

The HOMO energy values were estimated by using the ferrocene (Fc) ionization potential value (4.8 eV vs. vacuum) as the external reference, which based on calculations of Pommerehne et al35. All compounds show multiple redox processes. In the low potential region, the TPA moieties were oxidized in the range of 0.3V to 0.6V. The irreversible peak in the range 1.1 V-1.3 V belonged to oxidation of thienothiophene core.

In CV of the 2,5-isomer, it shows two sequential electron transfer reversible process[36]. The two arylamine moieties were sequential oxidized, giving two close oxidation signals and by each one-electron transfer process (ΔE_p value is 70mV). The first single electron transfer occurrs at 0.33 V vs $E^{1/2}$ of Fc/Fc^+ and the second electron transfer become less thermodynamically favorable, it was oxidized at 0.47V. It could be explained by conjugated structure and high electronic interactions between 2,5-substitution and thienothiophene core. In contrast, only one oxidation signal for 3,6-substitution was recorded at 0.41 V vs Fc/Fc^+. The mechanism could be proposed with a coupled chemical reaction. The reversible electron transfer followed irreversible homogenous chemical reaction[37] (***Scheme 3***).

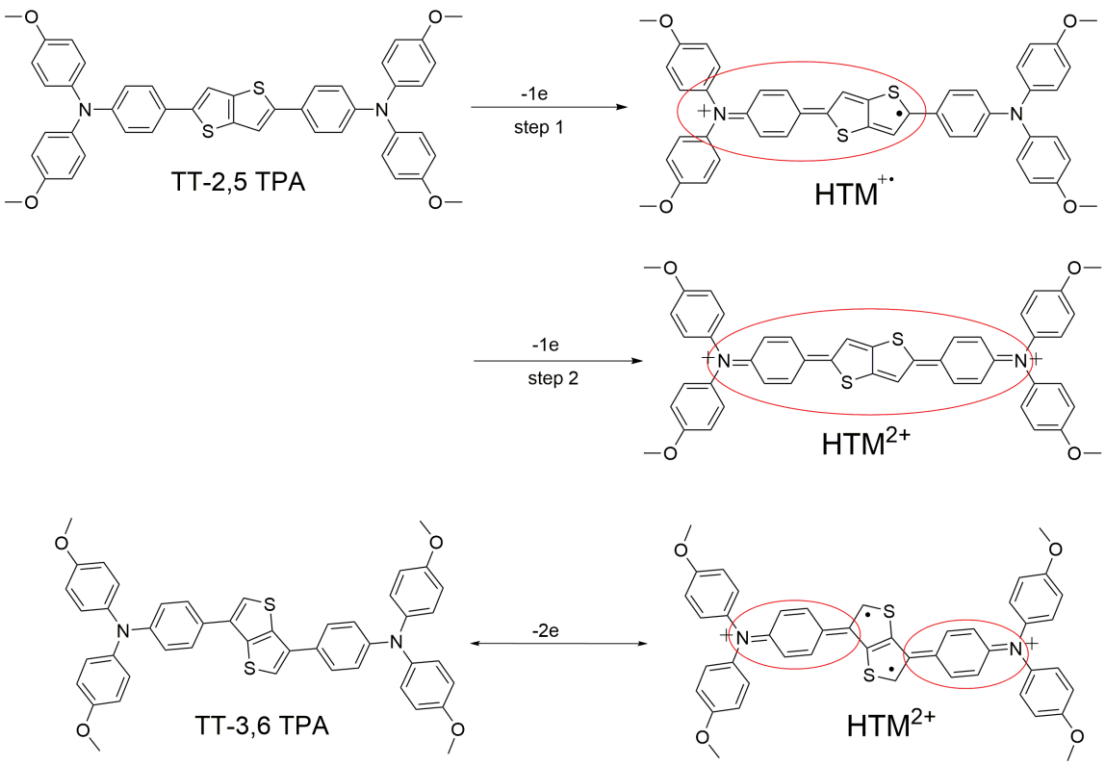

Scheme 3: Oxidation of TT-2,5 TPA and TT-3,6 TPA in electrochemistry.

Once the first TPA moiety was oxidized, due to slow electron transfer process in thienothiophene core and another TPA moiety, the mechanism in this case is more

complicated. The determined ΔE_p is around 103 mV, which does not respect to Nersnt equation. This is attributed to the interruption of the

electronic communications of the two arylamine side. The peaks observed at higher potentials could belong to the oxidation of the thienothiophene core (1.02 V in case of TT-2,5 TPA and TT-3,6 TPA and 1.23 V in case of TT-4 TPA). The electrochemical oxidation of these compounds can be explained by reversible transformation from aromatic state to quinoid state (***Scheme 3***) in electrochemistry[20]. In the case of TT-4 TPA, the CV was recorded as multi-electron transfer processes. The substitution of four arms TPA in compound TT- 4TPA leads them to oxidize in higher potential and these oxidation peaks could be overlapped by a variety different of oxidations.

The highest occupied molecular orbital (HOMO) energy values of these compounds were calculated from the onset of the first oxidation potential E_{ox}^{onset} and $E^{1/2}$ of Fc^+/Fc in vacumn. These values are -5.13 and -5.2 eV for TT-2,5 TPA and TT-3,6 TPA, respectively. The HOMO energy value of TT-4 TPA is lower than others, obtained -5.29 eV . The lower HOMO energy value could be expected for higher open-circuit voltage (V_{OC}) in PSCs performance[38]. These HOMO energy values are located above than valence band of perovskite (approximately -5.4 eV)[5] suggesting that they could be efficient for hole transfer processes in PSCs. The lowest unoccupied molecular orbital (LUMO) energy values were calculated from the HOMO values and optical bandgap E_g and were listed in ***Table 1***. The experimental LUMO values of three compounds are -2.48, -2.08 and -2.60 eV for TT-2,5 TPA, TT-3,6 TPA and TT-4 TPA, respectively. These values are high enough which are sufficient to avoid electron transfer back to perovskite layer.

	T_d (°C)	T_g (°C)	λabs max/onset (nm)	λemiss max (nm)	Eg^{opt} (eV)	Eox^{onset} (V)	E_{HOMO} (eV)	E_{LUMO} (eV)
TT-2,5 TPA	390	72	410 / 467	534	2.65	0.33	-5.13 (-5.65)	-2.48 (-1.34)
TT-3,6 TPA	408	92	344 / 396	472	3.13	0.41	-5.20 (-5.41)	-2.08 (-1.19)
TT-4 TPA	403	142	391 / 456	503	2.69	0.49	-5.29	-2.60

Table 1: Summary of photophysical, thermal and electrochemical data of these compounds. $E_g^{opt} = 1240/\lambda_{onset\ abs}$ (eV). $E_{HOMO} = -(E_{ox}^{onset}$ vs $E_{ox}^{1/2}$ of $Fc/Fc^+ + 4.8)$ eV. $E_{LUMO} = E_{HOMO} - E_g^{opt}$. Glass transition temperature T_g is obtained from the onset values of DSC and decomposition temperature T_d is recorded

by 5% weight loss in TGA. The HOMO-LUMO energy level obtained from DFT calculation are given in parenthesis.

To better understand the distinctive electrochemical properties of these molecules, time-dependent (TD) DFT calculations were performed by at the B3LYP/6-311G** level of theory using Gaussian 09 programs. Dichloromethane as the solvent and the polarizable continuum model (PCM) as the solvent model were used for the TDDFT calculations.

The calculated UV/Vis spectra of TT-2,5 TPA; TT-3,6 TPA and TT-4 TPA exhibit maximum absorption bands at λ = 455, 371 and 431 nm, respectively (***Figure 9***). These values are in good agreement to those of experimental results.

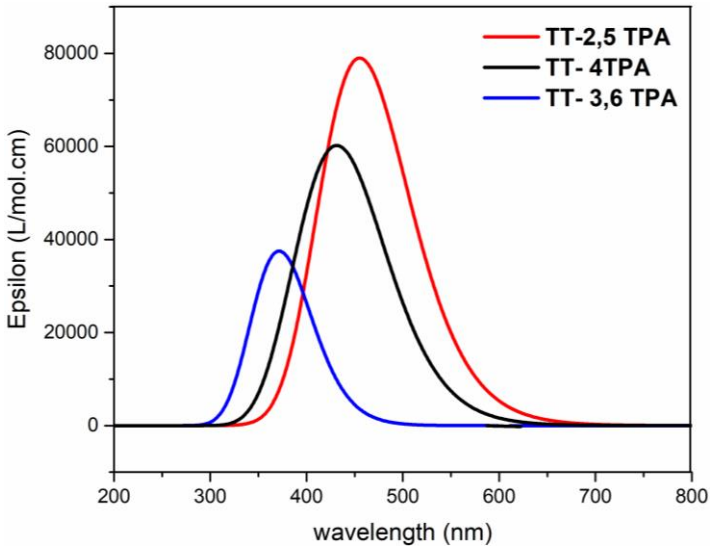

Figure 9: Simulated absorption spectra of TT-2,5 TPA; TT-3,6 TPA and TT-4 TPA in dichloromethane.

As shown in ***Table 1***, the corresponding calculated HOMO/LUMO energy values of TT-2,5 TPA and TT-3,6 TPA are -5.65/-1.34 eV and -5.41/-1.19 eV, respectively.

The optimized molecular geometries and electron density distribution diagram are given in ***Table 2***. From the frontier HOMO/LUMO electron density distribution diagram, it is observed that the HOMO of TT-2,5 TPA is delocalized over the whole molecule whereas the LUMO is mainly localized on the central thienothiophene and benzene units. This could be benefical for intramolecular charge transfer. In contrast, the electronic density distribution of HOMO of TT-3,6 TPA is interrupted at the middle of the thienothiophene linker and this could reduce intramolecular charge transfer. Thus, these results clearly illustrate that TT-2,5 TPA shows better conjugation than that of TT-3,6 TPA. The hole mobility of TT-2,5 TPA can be improved relative to that of 3,6-isomer due to larger electronic distribution over the whole molecule.

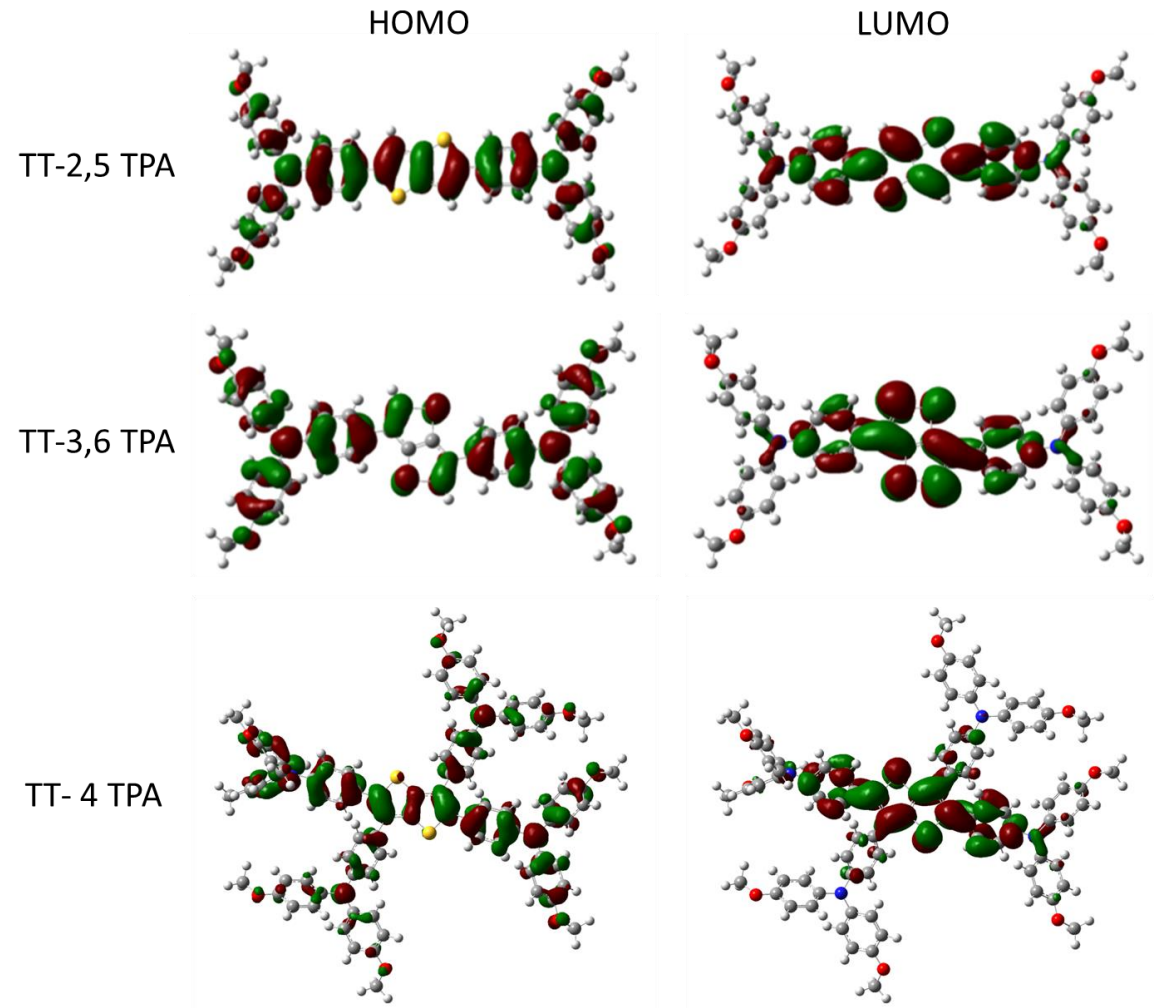

Table 2: The optimized molecular geometries and electronic density distributions of the frontier HOMOs and LUMOs energy level for TT-2,5 TPA, TT-3,6 TPA and TT-4 TPA.

In prediction, electron density distribution in HOMO state of TT-4 TPA is localized in all electron donor moieties, meaning that a charge distribution in the whole molecule. In contrary, they are mainly spread along 2,5-isomer side. It could affect to hole mobility property of material in full devices. These calculated data are in excellent agreement with the experimental results, suggesting a better π-conjugation ability in the 2,5-isomer.

II.3.4 Solid state crystallographic molecular structure

TT-3,6 TPA single crystals have been obtained by slow evaporation methods and these crystal structures have been analyzed by X-ray diffraction (CCDC 1811031). The solid state single crystal X ray structure of TT-2,5 TPA has been reported elsewhere.[27] A detailed description of the solid state structure of TT-3,6 TPA is given below and the data of TT-2,5 TPA from literature[27] are also cited for comparison purpose (***Table 3***).

Compound	**TT-2,5-TPA**	**TT-3,6-TPA**
Empirical Formula	C_{46} H_{38} N_2 O_4 S_2	C_{46} H_{38} N_2 O_4 S_2
M_r	745	746.90
Crystal size, mm^3		0.11 x 0.05 x 0.04
Crystal system	monoclinic	monoclinic
Space group	$P2_1/n$	$P2_1/n$
a, Å	11.0264	14.0999(9)
b, Å	10.3433	20.7067(12)
c, Å	17.0214	6.9783(4)
α, °	90	90
β, °	93.313	111.177(2)
γ, °	90	90
Cell volume, $Å^3$	1938.037	1899.8(2)
Z ; Z’	2 ; 1/2	2 ; 1/2
T, K	120(1)	100(1)
Radiation type ; wavelength Å	MoKα ; 0.71073	MoKα ; 0.71073
F_{000}		784
μ, mm^{-1}		0.187
θ range, °		2.504 - 30.585
Reflection collected	5 567	76 701
Reflections unique	4 221	5 817
R_{int}	0.038	0.0442
GOF	1.164	1.020
Refl. obs. (I>2σ(I))	4 221	4 945
Parameters / restraints		246 / 0
wR_2 (all data)	0.1335	0.0928
R value (I>2σ(I))	0.0525	0.0358
Largest diff. peak and hole (e-.$Å^{-3}$)	0.385 ; -0.352	0.420 ; -0.305
CCDC	1446684	
Short contact distance (Å)		
π- π	3.34	
CH-π	2.96	2.71
CH-O	2.50	2.61
CH-π	2.70	

Table 3: Crystallographic data and structure refinement details of TT-3,6 TPA. The data of TT-2,5 TPA were given for comparison purpose.

The Oak Ridge Thermal-Ellipsoid Plot Program (ORTEP) view depicted in ***Figure 10*** displays the structure of TT-3,6 TPA.

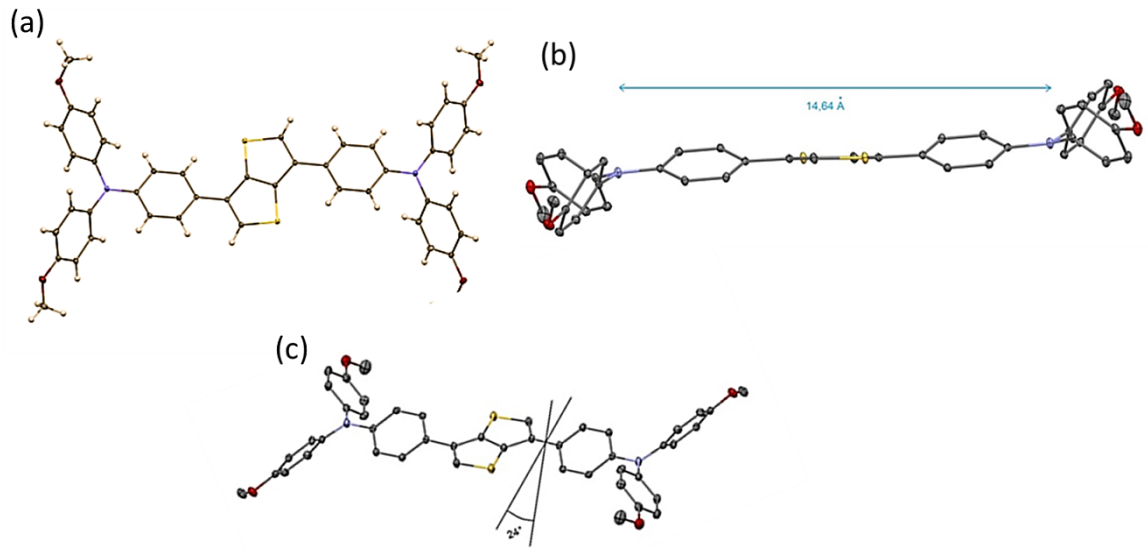

Figure 10: X-ray structure of TT-3,6 TPA. (a) an ORTEP top view with thermal ellipsoids are shown at the 30% level. (b) Side view of TT-3,6-TPA at 100 K with thermal ellipsoids are set at 50% probability. The red-, yellow-, purple-, and gray-colored atoms represent O, S, N, and C, respectively. All of the hydrogen atoms have been omitted for clarity. (c) Dihedral angles between the triphenyl amine and center π system.

Despite the same formulae and the same space group (P 2_1/n), we observed consequent differences between the 3,6- and 2,5- molecules in term of crystal structure. The dihedral angles between the triphenylamine and center π system is about 24° for the TT-3,6 TPA compared to 22° for the 2,5 isomeric counterpart. As expected, the bridge length is shorter in case of 3,6-isomer (14.64 Å), as compared to 16.06 Å in TT-2,5 TPA[27]. Consequently, the cell volume of TT-2,5 TPA is smaller. Moreover, in case of TT-3,6 TPA, each layer shows a waved conformation within which the interlaced molecules interact with each other via eight CH-π hydrogen bonds (along a axis). However, the distance between each layer is quite large (about 7Å) and no π-π interaction was possible. It would negatively impact to intermolecular charge transfer property. On the contrary, the π-π interactions are observed in between each 2,5 molecule and two adjacent molecules with the same longitudinal orientation. Other bonds such as CH…S and CH…π interaction are also identified in the last case. Those lead to different packing modes of 3,6- and 2,5-molecules (***Figure 11*** and ***Figure 12***).

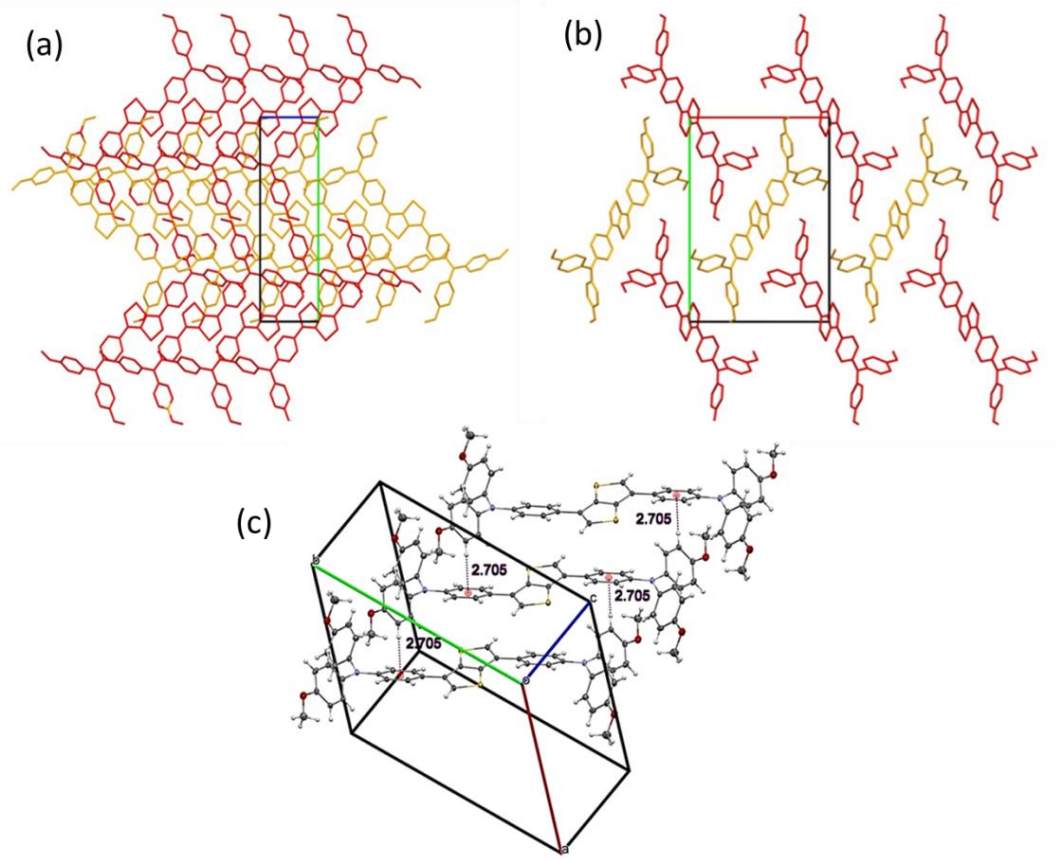

Figure 11: Crystal packing observed in TT-3,6 TPA as viewed along the a (a) and b (b) cell direction and CH-π distance in its crystal (c).

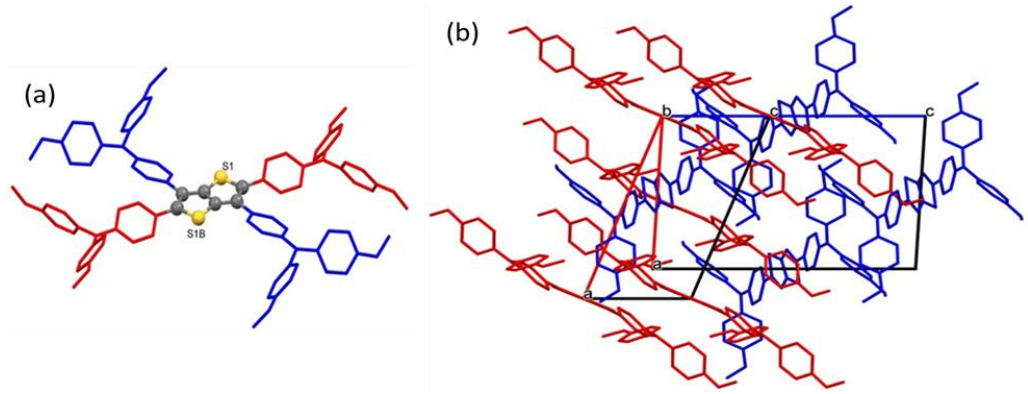

Figure 12: Representation of the superposition of the relative molecular structures of compounds TT-3,6 TPA (blue) and TT-2,5 TPA (red).

Thus, by strong π-π stacking effect, it will enhance intermolecular charge transfer and improve hole mobility. We could explain this fact by a stereo factor. Being shorter in bridge length, the two extreme "heads" induce a larger distance between 3,6-molecules. The results of crystal structure and DFT calculation of TT-2,5 TPA suggested better intra/intermolecular charge transfer properties than that of TT-3,6 TPA. The crystal

structure of TT-4TPA have not been formed, so its molecular packing could not discuss in this study.

II.3.5 Hybrid perovskite solar cells application.

To complete this study, compounds TT-2,5 TPA and TT-3,6 TPA have been used in PSCs, particularly using $CH_3NH_3PbI_3$ as the absorber material. The devices fabrication and hole mobility measurements were described in General Appendix. Typical mesoscopic PSC device structures as well as the energy of device components are shown in ***Figure 13***. An optimized device was comprised of a thin compact TiO_2 layer as hole blocking layer, a mesoporous TiO_2 layer as electron-transporting layer was filled and capped by the $CH_3NH_3PbI_3$ perovskite layer, then a thin HTM layer and finally Au layer as metal back contact was thermally evaporated.[39,40].

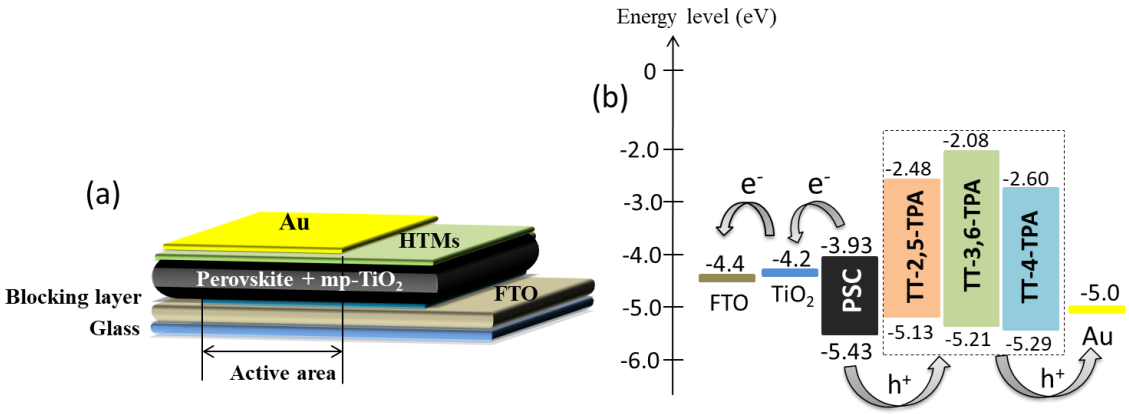

Figure 13: Typical mesoscopic PSC device structures (a) and the energy of device components (b).

According to our theoretical and experimental energy band diagrams, these compounds could be suitable as promising HTMs for PSCs. The steady-state photoluminescence (PL) spectra (***Figure 14a***) and the best current-density-voltage (*J*–*V*) curves for the various HTMs (***Figure 14b***) are recorded. Strong PL quenching was observed when these HTM materials were coated on the perovskite films. For two HTM materials applied perovskite films, the PL intensity was immediately reduced compared to perovskite film, indicating that both of TT-2,5 TPA and TT-3,6 TPA would extract efficiently charge carriers from perovskite layer.

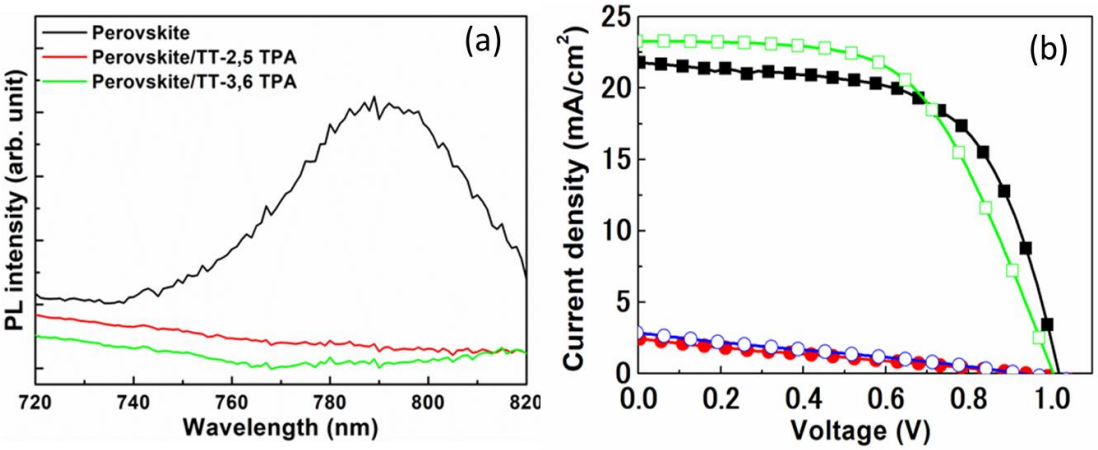

Figure 14: (a) Photoluminescene spectra for different materials as films on glass and (b) J-V characteristics in the forward (filled symbols) or reverse bias (empty symbols) directions of PSCs utilizing TT-2,5 TPA (rectangles) or TT-3.6 TPA (circles) HTMs.

In ***Figure 14b*** shows the current-voltage *J-V* characteristics of PSCs using TT-2,5 TPA or TT-3,6 TPA as a HTM layer, under AM 1.5 G illumination at an intensity of 100 mW cm^{-2}. The statistical data of the PSCs is summarized in ***Table 4***. The PSCs utilizing TT-3,6 TPA HTM layers exhibited the deficient photovoltaic performance with the efficiency of 0.7%. The low efficiency of the PSCs utilizing TT-3,6 TPA HTM layers was resulted from low Jsc (2.4 mA/cm^2) and FF (0.25). In contrast, by applying the TT-2,5 TPA as HTM layers, the Jsc and FF were dramatically improved to 22.7 mA/cm^2 and 0.57, respectively. As a result, the relatively high efficiency of 13.6% was achieved. The differences in photovoltaic performances could be explained due to bad off electronic coupling and relatively low hole mobility in TT-3,6 TPA (6.10^{-6} cm^2 V^{-1} s^{-1}) compared to TT-2,5 TPA (1.10^{-5} cm^2 V^{-1} s^{-1})

HTMs		V_{OC} (V)	J_{SC} (mA cm^{-2})	FF	Efficiency (%)	Best efficiency (%)
TT-2,5 TPA	Forward	1±0.02	21.3±0.9	0.59±0.02	12.7±0.9	**13.6**
	Reverse	0.98±0.02	22.7±0.9	0.57±0.03	12.8±0.6	**13.4**
TT-3,6 TPA	Forward	0.96±0.01	2±0.5	0.22±0.02	0.5±0.2	**0.6**
	Reverse	0.94±0.01	2.4±0.5	0.25±0.02	0.6±0.2	**0.7**

Table 4: Cell characteristics of the PSCs utilizing TT-2,5 TPA or TT-3.6 TPA HTM. Error values represent the standard deviation of the mean of 6 devices.

Compound TT- 4TPA has been also investigated photovoltaic properties in $CH_3NH_3PbI_3$ PSCs. The device fabrication was partially modified and summarized in

General Appendix. The ***Figure 15*** shows the best of current-voltage (*I-V*) characteristics of PSCs employed TT-4TPA as a HTM based on mesoscopic structure FTO/cp-TiO_2/mp-TiO_2/$CH_3NH_3PbI_3$/HTMs/Au. Spiro-OMeTAD was used as control devices.

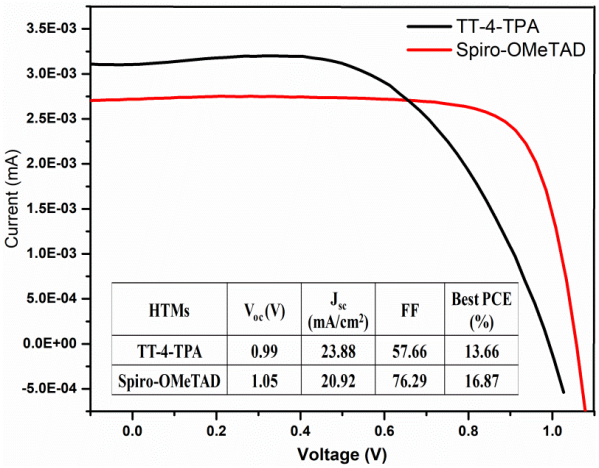

HTMs	V_{oc} (V)	J_{sc} (mA/cm^2)	FF	Best PCE (%)
TT-4-TPA	0.99	23.88	57.66	13.66
Spiro-OMeTAD	1.05	20.92	76.29	16.87

Figure 15: The best I-V characteristics of the PSCs based on TT-4-TPA and Spiro-OMeTAD as a control devices in forward direction scans.

The optimization device procedure have been done in different conditions such as concentration of HTMs, amount of dopant/additives (with and without additives) as well as back metal electrodes (Ag and Au). Due to unstable and non-reproductive of perovskite layer, this optimization were difficult. Both Spiro-OMeTAD and TT-4 TPA are containing Li-TFSI and t-BP as additives. The PSCs applying TT-4 TPA as HTM layer exhibited the photovoltaic performance efficiency of 13.66 % while the control device showed PCE of 16.87%. The devices showed quite high V_{OC} (0.99 V) certainly due to low HOMO value. Remarkably, the J_{SC} value of TT-4 TPA (23.88 mA/cm^2) is higher than that of Spiro-OMeTAD, which could be interpretated to probably a higher hole mobility for TT-4 TPA. Unfortunatly, a low value of FF (57.66) and high hysteresis in forward-reverse scan were observed. It could be explained by the presence of pinholes and defects in the perovskite layer and on the surface of HTM layer. The results reminded that the steric interaction of TT-4TPA might affect on morphological coverage. In fact, these devices have a poor stability and are currently non-reproducible. Therefore, the quality of perovskite layer should be controled to obtain stable photoabsorber layer. Moreover, these devices need to be optimized by studying of concentration of HTM and thin film processing which help to control thickness of HTM layer and provide better perovskite/HTM interfaces. Measurement of hole mobility/conductivity of these new HTMs are necessary and amount of additives/dopant should be optimized.

II.4 Conclusions and perspectives

In this chapter, three new hole transporting materials based on thieno[3,2-*b*]thiophene were obtained by modifying the position of TPA moiety position on the central π-bridge. Theoretical and experimental investigation showed high thermal stability, adequate morphology and improved hydrophobic properties of these target compounds. They also possess suitable frontier energy levels to those of PSCs components. The photovoltaic performance of compound TT-2,5TPA is 13.6% while compound TT-3,6TPA is only 0.7%. These results demonstrated that linear-conjugation at 2,5-position which is longer length conjugation, showed better charge transport property leading to high-quality device performance than non-linear conjugation molecule. It highlighted the importance of molecular arrangement of the construction of charge transporting materials for hybrid perovskite solar cells.

Interestingly, the promising 3D compound TT-4 TPA showed initial remarkable photovoltaic performances. It could be optimized to be efficient HTM material on PSCs as well as promising candidate for organic optoelectronic applications.

II.5 Experimental section

Synthesis of 4-(4,4,5,5-tetramethyl-1,3,2-dioxaborolan-2-yl)-N,N-bis(4-methoxyphenyl) aniline (compound 1)

In dry Schlenk flask, 4-Bromo-N,N-bis(4-methoxyphenyl)aniline (0.5g, 1eq) and 30 ml of distilled THF are stirred vigorously under argon atmosphere. The temperature is cooled down to -78^{0}C by N_2 liquid and, n-BuLi (1.7ml, 1.1 eq) is added dropwise to solution during 30 minutes. After 1 hour, the temperature is slowly to room temperature and isopropoxyboronic acid pinacol ester (1ml, 1.1 eq) is added slowly by syringe. The reaction is kept overnight. Color changed from light yellow to red yellow. Solvent is removed under reduced pressure, then extract crude product by DCM and water three times, collected organic phase and dried over $MgSO_4$. The crude product is concentrated and precipitated in methanol, obtained white solid (0.8g, 70% yield). ^{1}H NMR (250 MHz, DMSO-d_6) δ 7.42 (d, *J* = 8.5 Hz, 2H, Ar), 7.06 (d, *J* =2.5 Hz, 4H, Ar), 7.02 (d, *J*=2.5 Hz, 4H, Ar), 6.65 (d, *J* =8.5 Hz, 2H, Ar), 3.73 (s, 3H, -OCH_3), 1.23 (s, 12H, -CH_3). ^{13}C NMR (62.5 MHz, DMSO-d_6) 156.7, 151.6, 139.8, 136.1, 127.9, 117.3, 115.5, 85.58, 55.7, 25.1.

Synthesis of 2,3,5,6-tetrabromothieno[3,2-b]thiophene (compound 2,3,5,6-tetrabromo-TT)

Thieno[3,2-*b*]thiophene (0.5g, 1eq) is added in 20ml of glacial acid acetic in round-bottom connected to condenser. Then, 10ml of Br_2 solution (20eq) are added to the mixture and the reaction is refluxed at 130^0C overnight. The reaction is quenched by solution of $Na_2S_2O_3$ 10% and filtered to obtained off-white precipitate. This crude product is then recrystallized in toluene twice times to obtained needle-shape crystals of pure compound 4. This compound is insoluble in organic solvents, so the NMR spectra could not be recorded. The chemical structure of compound 4 is confirmed by using single-crystal X-ray diffraction analysis and displayed below.

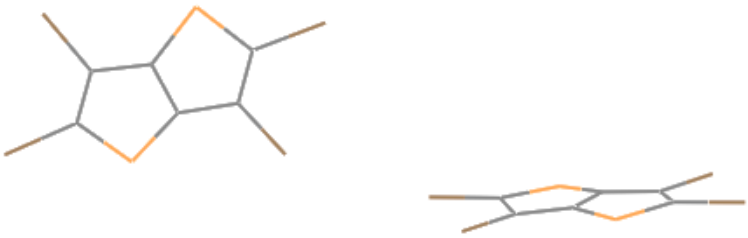

Figure 16: ORTEP of 2,3,5,6-tetrabromothieno[3,2-b]thiophene. S yellow, Br brown, C gray.

General procedure for the synthesis of TT-2,5 TPA, TT-3,6 TPA and TT-4TPA:

In a dry Schlenk flask, 2,7-dibromothieno[3,2-*b*]thiophene or 3,6-dibromothieno[3,2-b]thiophene or 2,3,6,7-tetrabromothieno[3,2-*b*]thiophene (1eq), 4-methoxy-N-(4-methoxyphenyl)N-N(4-(4,4,5,5-tetramethyl-1,3,2-dioxaborol)-N-2-yl)phenyl)aniline) (360mg, 2.5 eq for two substitutions and 6eq for four substitutions), K_2CO_3 (20eq) , $Pd(PPh_3)_4$ (0.1 eq), few drops of Aliquat 336 as phase transfer catalyst and 15 ml of toluene were added, respectively. Vacuum and argon were supplied several times to remove totally air. The temperature was kept at 110^oC under argon atmosphere. The reaction was kept overnight and monitored by thin layer chromatography (TLC). The reaction was then quenched and quickly filtered through silice layer, using dichloromethane as eluent. The filtrate was then washed with water, dried over $MgSO_4$ and concentrated under reduced pressure. The crude product was then subjected to column chromatography with cyclohexane and ethylacetate (9:1 v/v) as eluent giving the pure tilted compound.

4,4'-(thieno[3,2-b]thiophene-2,5-diyl)bis(N,N-bis(4-methoxyphenyl)aniline) (TT-2,5 TPA)

The compound TT-2,5 TPA was obtained as yellow solid (170mg, 70% yield). ^{1}H NMR (250 MHz, DMSO-d_6) δ 7.63 (s, 1H, TT-backbone), 7.47 (d, *J*=10 Hz, 2H, Ar), 7.05 (d, *J*=7.5 Hz, 4H, Ar), 6.91 (d, *J*=7.5 Hz, 4H, Ar), 6.77 (d, *J*=10 Hz, 2H, Ar), 3.73 (s, 6H, -OCH_3). ^{13}C NMR (62.5 MHz, DMSO-d_6) δ 156.4, 148.5, 145.1, 140.1, 138.2, 127.3, 126.5, 126.0, 119.6, 115.4, 115.0, 55.7. HRMS (ESI-MS): calculated for $C_{46}H_{38}N_2O_4S_2$ $[M+H]^+$, 746.2273 ; found: 746.2263.

4,4'-(thieno[3,2-b]thiophene-3,6-diyl)bis(N,N-bis(4-methoxyphenyl)aniline) (TT-3,6 TPA)

The compound TT-3,6 TPA was obtained as white solid (176mg, 70% yield). ^{1}H NMR (250MHz, DMSO-d_6) δ 7.84 (s, 1H, TT-backbone), 7.6 (d, *J*=7.5 Hz, 2H, Ar), 7.07 (d, *J*=10 Hz, 4H, Ar), 6.92 (d, *J*=10 Hz, 4H, Ar), 6.85 (d, *J*=7.5 Hz, 2H, Ar), 3.74 (s, 6H, -OCH_3). ^{13}C NMR (62.5 MHz, CD_2Cl_2) δ 156.4, 148.5, 144.2, 140.4, 137.6, 126.0, 120.2, 119.5, 116.1, 115.6, 106, 55.7. HRMS (ESI-MS): calculated for $C_{46}H_{38}N_2O_4S_2$ $[M+H]^+$, 746.2273 ; found: 746.2257.

(4,4',4'',4'''-(thieno[3,2-b]thiophene-2,3,5,6-tetrayl)tetrakis(N,N-bis(4-methoxyphenyl) aniline) (TT-4 TPA)

The compound TT-4 TPA was obtained as yellow solid (100mg, 34 % yield). ^{1}H NMR (250 MHz, $CDCl_3$) δ 7.21-7.15 (m, 4H), 7.08-7.01 (m, 8H), 6.91-6.87 (m, 8H), 6.7-6.58 (m, 4H), 3.71 (s, 12H, -OCH_3). ^{13}C NMR (62.5 MHz, CD_2Cl_2) δ 156.4, 156.43, 151.4, 149.3, 147.5, 144.2, 140.93, 139.99, 139.3, 137.81, 135.57, 132.77, 129.36, 127.33, 126.42, 123.66, 120.86, 118.7, 118.06, 114.77, 114.65, 114.57, 98.59, 83.31, 55.38, 53.81, 53.38, 52.95. HRMS (ESI-MS): calculated for $C_{86}H_{72}N_4O_8S_2$ $[M+H]^+$, 1352.4792; found: 1352.4791.

References

(1) Li, Z. R. *Organic Light-Emitting Materials and Devices*; 2015.

(2) Hagfeldt, A.; Boschloo, G.; Sun, L.; Kloo, L.; Pettersson, H. Dye-Sensitized Solar Cells. *Chem. Rev.* **2010**, *110*, 6595–6663.

(3) Kippelen, B.; Brédas, J. L. *Organic Photovoltaics*; 2009; Vol. 2.

(4) Ning, Z.; Tian, H.; Allard, S.; Forster, M.; Souharce, B.; Thiem, H.; Scherf, U. Organic Semiconductors for Solution-Processable Field-Effect Transistors (OFETs). *Angew. Chemie* **2008**, *47*, 4070–4098.

(5) Ameen, S.; Nazeeruddin, M. K. Perovskite Solar Cells: Influence of Hole Transporting Materials on Power Conversion Efficiency. *ChemSusChem* **2016**, *9*, 10–27.

(6) Calió, L.; Kazim, S.; Grätzel, M.; Ahmad, S. Hole-Transport Materials for Perovskite Solar Cells. *Angew. Chemie Int. Ed.* **2016**, *55*, 14522–14545.

(7) Yu, Z.; Sun, L. Recent Progress on Hole-Transporting Materials for Emerging Organometal Halide Perovskite Solar Cells. *Adv. Energy Mater.* **2015**, 1500213.

(8) Wang, J.; Liu, K.; Ma, L.; Zhan, X. Triarylamine: Versatile Platform for Organic, Dye-Sensitized, and Perovskite Solar Cells. *Chem. Rev.* **2016**, *116*, 14675–14725.

(9) Ning, Z.; Tian, H. Triarylamine: A Promising Core Unit for Efficient Photovoltaic Materials. *Chem. Commun.* **2009**, 5483–5495.

(10) Park, S. J.; Jeon, S.; Lee, I. K.; Zhang, J.; Jeong, H.; Park, J.-Y.; Bang, J.; Ahn, T. K.; Shin, H.-W.; Kim, B.-G.; *et al.* Inverted Planar Perovskite Solar Cells with Dopant Free Hole Transporting Material: Lewis Base-Assisted Passivation and Reduced Charge Recombination. *J. Mater. Chem. A* **2017**, *5*, 13220–13227.

(11) Mimaite, V.; Ostrauskaite, J.; Gudeika, D.; Grazulevicius, J. V.; Jankauskas, V. Structure–properties Relationship of Hydrazones Containing Methoxy-Substituted Triphenylamino Groups. *Synth. Met.* **2011**, *161*, 1575–1581.

(12) Sakalyte, A.; Simokaitiene, J.; Tomkeviciene, A.; Keruckas, J.; Buika, G.; Grazulevicius, J. V.; Jankauskas, V.; Hsu, C.-P.; Yang, C.-H. Effect of Methoxy Substituents on the Properties of the Derivatives of Carbazole and Diphenylamine. *J. Phys. Chem. C* **2011**, *115*, 4856–4862.

(13) Molina-Ontoria, A.; Zimmermann, I.; Garcia-Benito, I.; Gratia, P.; Roldán-Carmona, C.; Aghazada, S.; Graetzel, M.; Nazeeruddin, M. K.; Martín, N. Benzotrithiophene-Based Hole-Transporting Materials for 18.2 % Perovskite Solar Cells. *Angew. Chemie Int. Ed.* **2016**, *55*, 6270–6274.

(14) Chen, J.; Chen, B.-X.; Zhang, F.-S.; Yu, H.-J.; Ma, S.; Kuang, D.-B.; Shao, G.; Su, C.-Y. 3,4-Phenylenedioxythiophene (PheDOT) Based Hole-Transporting Materials for Perovskite Solar Cells. *Chem. - An Asian J.* **2016**, *11*, 1043–1049.

(15) Krishna, A.; Sabba, D.; Yin, J.; Bruno, A.; Boix, P. P.; Gao, Y.; Dewi, H. A.; Gurzadyan, G. G.; Soci, C.; Mhaisalkar, S. G.; *et al.* Facile Synthesis of a Furan–Arylamine Hole-Transporting Material for High-Efficiency, Mesoscopic Perovskite Solar Cells. *Chem. Eur. J* **2015**, *21*, 1–6.

(16) Xuepeng Liu , Fantai Kong , Fuling Guo , Tai Cheng , Wangchao Chen, T. Y.; Jian Chen , Zhan'ao Tan, S. D. Influence of π-Linker on Triphenylamine-Based Hole Transporting Materials in

Perovskite Solar Cells. *Dye. Pigment.* **2016**, *139*, 129–135.

(17) Michael Saliba, Simonetta Orlandi, Taisuke Matsui, Sadig Aghazada, Marco Cavazzini, Juan-Pablo Correa-Baena, Peng Gao, Rosario Scopelliti, Edoardo Mosconi, Klaus-Hermann Dahmen, Filippo De Angelis, Antonio Abate, Anders Hagfeldt, Gianluca Poz, M. G. and M. K. N. A Molecularly Engineered Hole-Transporting Material for Efficient Perovskite Solar Cells. *Nat. Energy* **2016**, *1*, 15017.

(18) Chi, W.-J.; Zheng, D.-Y.; Chen, X.-F.; Li, Z.-S. Optimizing Thienothiophene Chain Lengths of D–π–D Hole Transport Materials in Perovskite Solar Cells for Improving Energy Levels and Hole Mobility. *J. Mater. Chem. C* **2017**, *5*, 10055–10060.

(19) Liu, X.; Kong, F.; Ghadari, R.; Jin, S.; Chen, W.; Yu, T.; Hayat, T.; Alsaedi, A.; Guo, F.; Tan, Z.; *et al.* Thiophene-Arylamine Hole-Transporting Materials in Perovskite Solar Cells: Substitution Position Effect. *Energy Technol.* **2017**, *5*, 1788–1794.

(20) Roncali, J. Conjugated Poly(Thiophenes): Synthesis, Functionalization, and Applications. *Chem. Rev.* **1992**, *92*, 711–738.

(21) Roncali, J. Synthetic Principles for Bandgap Control in Linear π-Conjugated Systems. *Chem. Rev.* **1997**, *97*, 173–206.

(22) Li, H.; Fu, K.; Boix, P. P.; Wong, L. H.; Hagfeldt, A.; Grätzel, M.; Mhaisalkar, S. G.; Grimsdale, A. C. Hole-Transporting Small Molecules Based on Thiophene Cores for High Efficiency Perovskite Solar Cells. *ChemSusChem* **2014**, *7*, 3420–3425.

(23) Molina-Ontoria, A.; Zimmermann, I.; Garcia-Benito, I.; Gratia, P.; RoldÃ¡n-Carmona, C.; Aghazada, S.; Graetzel, M.; Nazeeruddin, M. K.; MartÃ-n, N. Benzotrithiophene-Based Hole-Transporting Materials for 18.2 % Perovskite Solar Cells. *Angew. Chemie - Int. Ed.* **2016**, *55*, 6270–6274.

(24) Ma, S.; Zhang, H.; Zhao, N.; Cheng, Y.; Wang, M.; Shen, Y.; Tu, G. Spiro-Thiophene Derivatives as Hole-Transport Materials for Perovskite Solar Cells. *J. Mater. Chem. A Mater. energy Sustain.* **2015**, *3*, 12139–12144.

(25) Yang, S. Y.; Kan, Y. H.; Yang, G. C.; Su, Z. M.; Zhao, L. TD-DFT Investigation on the Low-Lying Excited States of Spiro-Bithiophene. *Chem. Phys. Lett.* **2006**, *429*, 180–184.

(26) Pozzi, G.; Orlandi, S.; Cavazzini, M.; Minudri, D.; Macor, L.; Otero, L.; Fungo, F. Synthesis and Photovoltaic Applications of a 4,4′- Spirobi[Cyclopenta[2,1-b;3,4-B′]Dithiophene]-Bridged Donor/Acceptor Dye. *Org. Lett.* **2013**, *15*, 4642–4645.

(27) S. Paek, I. Zimmermann, P. Gao, P. Gratia, a K. Rakstys, G. Grancini, Mohammad Khaja Nazeeruddin, Malik Abdul Rub, b Samia A. Kosa, K. A. A. and A. M. A. Donor–π–donor Type Hole Transporting Materials: Marked π-Bridge Effects on Optoelectronic Properties, Solid-State Structure, and Perovskite Solar Cell Efficiency. *Chem. Sci.* **2016**, *7*, 6068–6075.

(28) Qin, P.; Kast, H.; Nazeeruddin, M. K.; Zakeeruddin, S. M.; Mishra, A.; Auerle, P.; Atzel, M. G. Low Band Gap S,N-Heteroacene-Based Oligothiophenes as Hole-Transporting and Light Absorbing Materials for Efficient Perovskite-Based Solar Cells. *Energy Environ. Sci.* **2014**, *7*, 2981–2985.

(29) Cinar, M. E.; Ozturk, T. Thienothiophenes, Dithienothiophenes, and Thienoacenes: Syntheses, Oligomers, Polymers, and Properties. *Chem. Rev.* **2015**, *115*, 3036–3140.

(30) Takimiya, K.; Shinamura, S.; Osaka, I.; Miyazaki, E. Thienoacene-Based Organic Semiconductors. *Adv. Mater.* **2011**, *23*, 4347–4370.

(31) Thi Huong Le Dr. Quang-Duy Dao Dr. Mai-Phuong Nghiêm Prof. Sébastien Péralta Dr. Regis Guillot Prof. Quoc Nghi Pham Prof. Akihiko Fujii Prof. Masanori Ozaki Prof. Fabrice Goubard Prof. Thanh-Tuân Bui. Triphenylamine–Thienothiophene Organic Charge-Transport Molecular Materials: Effect of Substitution Pattern on Their Thermal, Photoelectrochemical, and Photovoltaic Properties. *Chem. Asian J.* **2018**, *13*, 1302–1311.

(32) Daniel Lumpi, Brigitte Holzer, Johannes Bintinger, Ernst Horkel, Simon Waid, Heinz D. Wanzenbock, Martina Marchetti-Deschmann, D.; Christian Hametner, Emmerich Bertagnolli, I. K. and J. F. Substituted Triphenylamines as Building Blocks for Star Shaped Organic Electronic Materials. *New J. Chem.* **2015**, *39*, 1840–1851.

(33) Fuller, L. S.; Iddon, B.; Smith, K. a. Bromine → Lithium Exchange Reactions of Thieno [3 , 2-B] Thiophene and Its Polybromo Derivatives. *J. Chem. Soc., Perkin Trans.* **1997**, *1*, 3465–3470.

(34) Leijtens, T.; Giovenzana, T.; Habisreutinger, S. N.; Tinkham, J. S.; Noel, N. K.; Kamino, B. A.; Sadoughi, G.; Sellinger, A.; Snaith, H. J. Hydrophobic Organic Hole Transporters for Improved Moisture Resistance in Metal Halide Perovskite Solar Cells. *ACS Appl. Mater. Interfaces* **2016**, *8*, 5981–5989.

(35) Pomrnerehne, J.; Vestweber, H.; Guss, W.; Muhrt, R. E.; Bassler, H.; Porsch, M.; Daub, J. Efficient Two Layer Leds on a Polymer Blend Basis. *Adv. Mater.* **1995**, *7*, 551–554.

(36) J.Bard, A.; Larry R.Faulkner. *Electrochemical Methods: Fundamentals and Applications*; second.; JOHN WILEY and SONs, 2000.

(37) Elgrishi, N.; Rountree, K. J.; McCarthy, B. D.; Rountree, E. S.; Eisenhart, T. T.; Dempsey, J. L. A Practical Beginner's Guide to Cyclic Voltammetry. *J. Chem. Educ.* **2018**, *95*, 197–206.

(38) Kazim, S.; Ramos, F. J.; Gao, P.; Nazeeruddin, M. K.; Grä Tzel, M.; Ahmad, S. A Dopant Free Linear Acene Derivative as a Hole Transport Material for Perovskite Pigmented Solar Cells. *Energy Environ. Sci. Energy Environ. Sci* **2015**, *8*, 1816–1823.

(39) Dao, Q.-D.; Tsuji, R.; Fujii, A.; Ozaki, M. Study on Degradation Mechanism of Perovskite Solar Cell and Their Recovering Effects by Introducing CH3NH3I Layers. *Org. Electron.* **2017**, *43*, 229–234.

(40) Dao, Q.-D.; Fujii, A.; Tsuji, R.; Takeoka, Y.; Ozaki, M. Efficiency Enhancement in Perovskite Solar Cell Utilizing Solution-Processable Phthalocyanine Hole Transport Layer with Thermal Annealing. *Org. Electron.* **2017**, *43*, 156–161.

Chapter III

Donor-Acceptor

Hole transporting materials

PART 1: DONOR-ACCEPTOR HTMs WITH 9(10H)-ACRIDONE SPECIES

III.1.1 Introduction

Recently, push-pull molecules/polymers with both electron donor (D) and electron acceptor (A) groups have drawn much interest for their extensive application in advance functional materials as well as electronic and optoelectronic devices[1–4]. D-A molecules with low band gap and tunable highest occupied and lowest unoccupied molecular orbital (HOMO and LUMO, respectively) have many potential use in electronic and light-harvesting materials, especially in solar cells[5]. In photovoltaic application, the adequate HOMO energy level of active layer to conductance band of photo-absorber materials and optical band gap are crucial factors for hole collection and extraction properties.[6,7] ***Figure 1*** shows how qualitative interactions between the frontier orbitals of donor and acceptor units change the optical transition energy of a donor-acceptor system. For instance, the donor-acceptor (D-A) interaction leads to new molecular orbital formed and reduced energy band gap. The intramolecular charge transfer (ICT) in D-A system involves also interesting photophysical properties, which helps to increase hole mobility and can be investigated from absorption/emission spectra.[8]

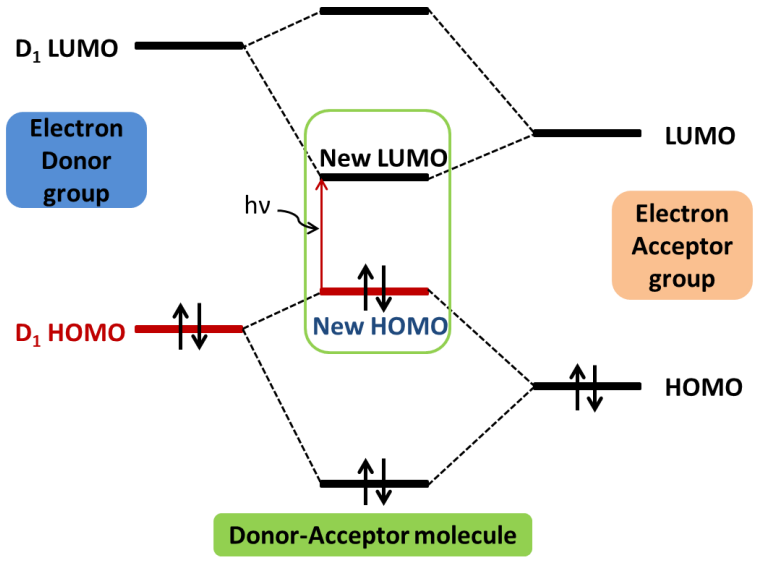

Figure 1: Frontier energy level and optical transition energy trend in modular donor - acceptor interaction model.

Therefore, many researches are devoted to promote new strategy in designing and developing new donor-acceptor organic molecules for organic electronic applications.

Some precursor structures consist on polycyclic organic molecules with electron donor moiety (NH-group) and electron acceptor moiety (C=O group) in structure and they have been employed as backbone in photovoltaic field such as naphthalene diimide[9,10], diketopyrrolopyrrole[11–13], thienopyrrolodione[14,15], quinacridone[16], indigo[17], (***Figure 2)***. For example, naphthalene diimide (NDI) have large electron affinity which often used to construct *n*-type polymers and showing excellent electron mobility[9]. Diketopyrrolopyrrole (DPP) molecule owns high charge mobility, it shows great performance in organic solar cells and organic transistors[12]. Another example is quinacridone, one of organic pigments, which show exceptional color and weather fastness; it shows high photoluminescence efficiency and good electrochemical stability[16]. Because its fluorescence lifetime (~20ns) is longer than that of typical organic donor materials, long exciton diffusion lengths in thin films, it would enhanced exciton collection yield in bulk heterojunction devices.

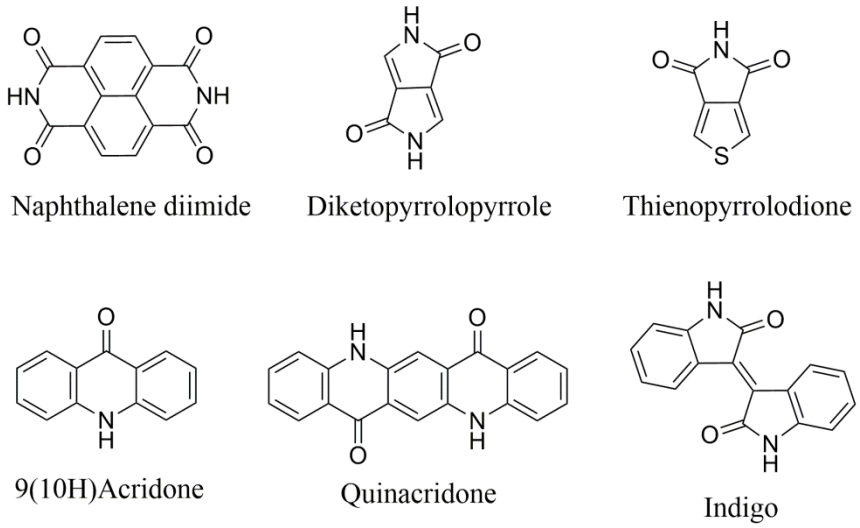

Figure 2 : Some Donor -Acceptor precursor's structure.

Herein, we studied 9(10H)-Acridone and its N-alkyl substituted derivatives as core for new functionalized HTMs. 9(10H)-acridone is one of heterocyclic aromatic molecular which offer a rich chemistry and an interesting building block for constructing push-pull materials. The compound contains an electron-donating moiety (N-H group at 10-position) and an electron-withdrawing one (C=O group at 9-position). Acridone own high fluorescent with quantum yield of 0.55[18]. Covalently linked π-conjugated D-A chromophores often participate in intramolecular charge transfer (ICT) excitations, therefore media sensitive absorption and/or emission properties.

Acridone derivatives have been applied in different applications such as anti-cancer drugs,[19] inhibitor of multi-drug resistance,[20] fluorescent markers,[21] and colorimetric sensor.[22] Acridone derivatives such as quinacridone, epindolidione have also been successfully applied in electronic devices (field-effect transitors,[23,24] organic light-emitting diodes (OLEDs),[25–27] photovoltaics[16,24]) ***(Figure 3).***

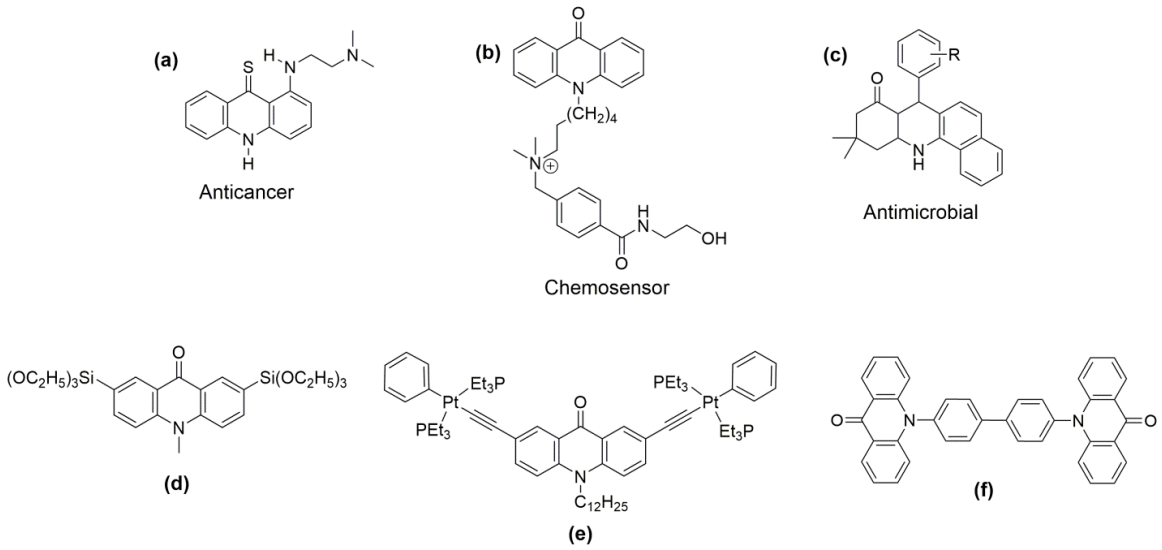

Figure 3 : Literature reported of acridone derivatives in biological applications (a, b, c) and optoelectronic devices (d, e, f). Figures adapted from references[28–32].

In this chapter, 9(10H)-Acridone is subjected for study because of its rich chemistry feasibility (***Figure 4***).

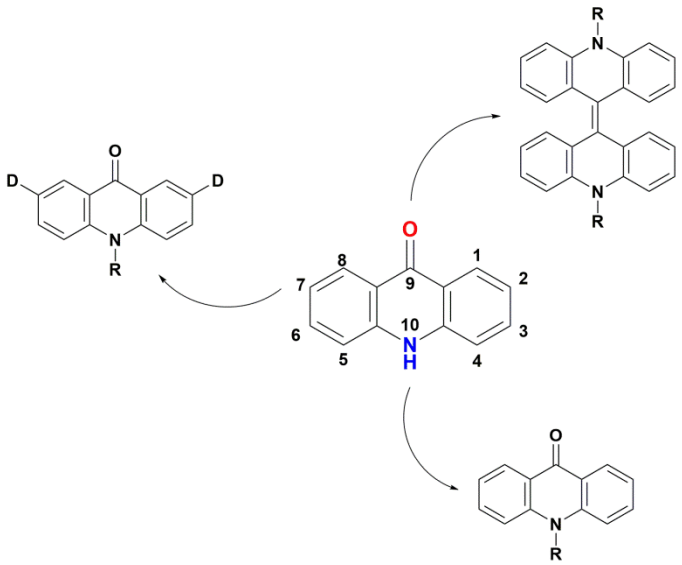

Figure 4 : Chemistry possibilities of 9(10H)Acridone precursor.

In particularly at 2,7-position, various functional groups (such as electron donor D/acceptor A moieties) could be substituted via halogen exchange reactions and coupling

reactions. At 10-position, hydrogen atom can be replaced by alkyl chain to improve solubility or by other functional groups. Moreover, at C=O position, we can replace by another acceptor moiety or prolong conjugation. We will discuss this issue on the section.

In the present work, we report herein the synthesis and characterization of two donor-acceptor (D-A) systems and donor-acceptor-donor (D-A-D) push-pull molecules based on acridone central platform. The chemical structures of these compounds are given in ***Figure 5***.

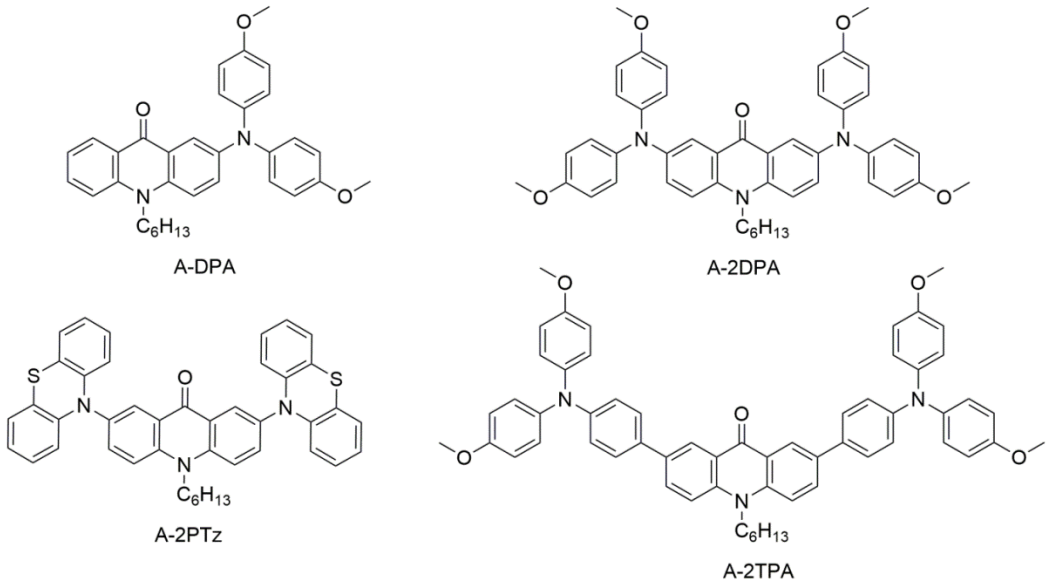

Figure 5 : Chemical structures of investigated arylamine-acridone derivatives

III.1.2 Objectives and strategies

In this chapter, we designed and synthesized two donor-acceptor (D-A) and donor-acceptor-donor (D-A-D) systems based on Acridone central platform. The molecular properties of D-A systems can be tailored by its replacement (stronger/weaker), addition (one or more donors) or position (conjugating/non conjugating arrangement) of the electron donor. Therefore, the designs of these push-pull molecules are based on some following considerations.

- First, various strong electron-donating groups such as 4,4'-dimethoxy-diphenylamine (DPA), 4,4'-dimethoxy-triphenylamine (TPA) and phenothiazine (PTz), which have been widely used to design efficient hole transporting materials, were incorporated to the 2,7-positions of the acridone central core.
- Second, the investigation of tuning HOMO-LUMO energy levels of final compounds could be compatible to perovskite solar cell components?

- Third, their properties were characterized by experimental and computational methods, therefore understanding of donor-acceptor system are studied and providing strategy for design and construct of ideal molecules structure for organic electronic devices.

These new materials were fully characterized by experimental techniques and computational method. Their characteristics suggest that these compounds could be promising charge transporting materials for hybrid solar cells and could be also photo-initiators for photoredox catalyzed polymerization process.

III.1.3 Results and discussion

Scheme 1 outlined the synthetic routes toward different targeted molecules. All compounds were synthesized from commercially available 9(10H)-acridone by short step syntheses. Compound 4,4'-dimethoxydipheylamine (DPA) and phenothiazine are available commercial products. Intermediate compound 4,4'-dimethoxytriphenylamine (TPA) has already been reported in ***Chapter II***.

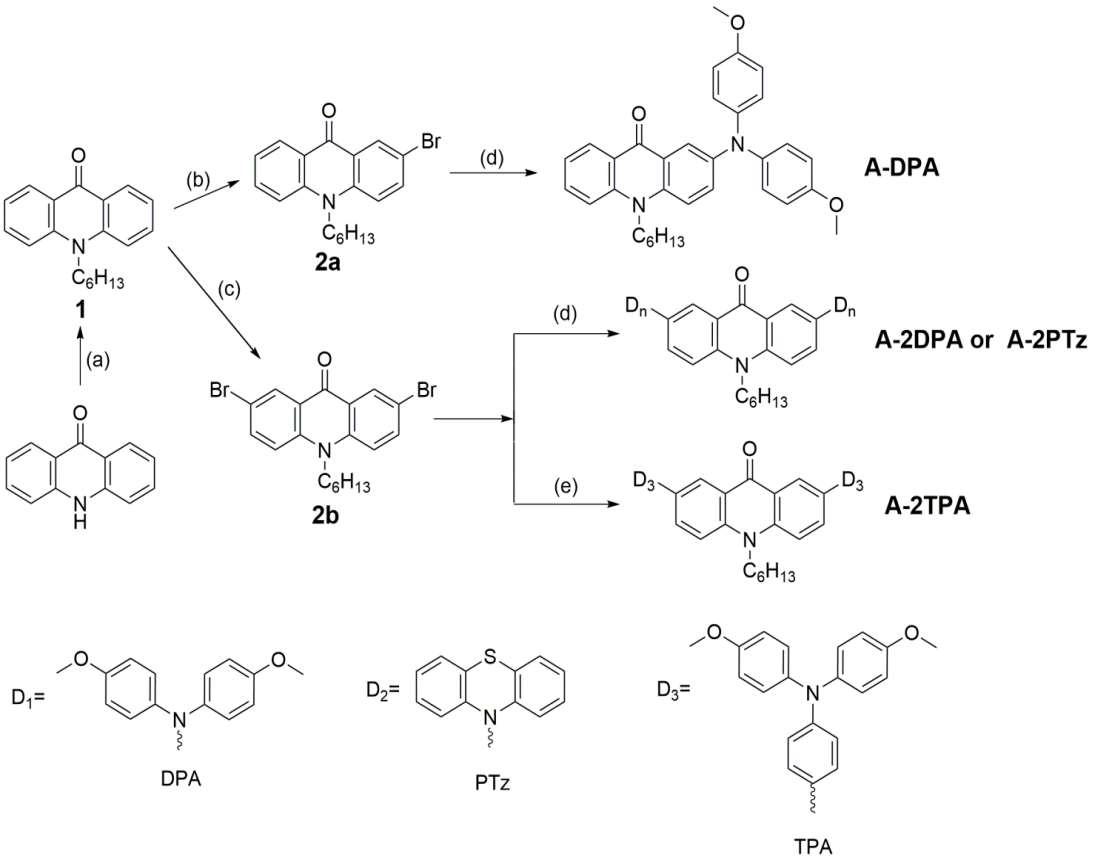

Scheme 1: Synthesis of acridone derivatives. Reagents and conditions: (a) NaOH, $C_6H_{13}Br$, DMSO, 140^0C, 24h. (b) NBS, $CHCl_3$, rt, 16h. (c) NBS, DMF, 70^0C, 24h. (d) D_n-H, NaO^tBu, $Pd(OAc)_2$, , tBu_3P, Toluene, 110^0C, 48h. (e) D_3-H, $Pd(PPh_3)_4$, K_2CO_3, Toluene, 110^oC, 48h.

Firstly, the *N*-hexyl acridone (compound **1**) has been isolated in high yields between 9(10H)-Acridone and 1-bromohexane in DMSO and strong basic medium as NaOH. Optimization of the reaction's conditions show that large excess of base (10 equivalences) and few drops of Aliquat 336 as phase transfer organic-inorganic catalysts are needed. The yield increased from 48% when 2 eq of NaOH used to 88% using 10eq of NaOH and with Aliquat 336.

Secondly, the treatment of compound **1** by N-bromosuccinimide (NBS) gave mono and di-brominated intermediates (**2a-b**). After optimization, treating **1** by 1eq of NBS in chloroform solution at room temperature gave 2a as main product (65% yields). However, 2b was successful synthesized by 4eq of NBS in DMF and kept 1 day at 70^{o}C. After evaporation of DMF, desired product was obtained (~100% yield) and used in next step without further purification.

The final step involved classical Pd-catalyzed Buchwald–Hartwig aminations between the freshly synthesized 2a-b and the commercial products: 4,4'-dimethoxyphenylamine (for A-DPA and A-2DPA) and phenothiazine (for A-2PTz). In case of A-2TPA, the later was constructed from 2b and 4-(4,4,5,5-tetramethyl-1,3,2-dioxaborolan-2-yl)-N,N-bis(4-methoxyphenyl)aniline[33] under Suzuki cross-coupling conditions. These final compounds were purified by column chromatography by appropriate solvent/mixture solvent afforded the desired project in good yield. Interestingly, A-2PTz contains of phenothiazine with sulfur atoms which are easily oxidized by oxidants, especially halogenated solvents. For example, chloroform dissolves this compound and changes color from yellow to green-off. The appearance of A-DPA and A-2DPA are similar, look like red-membrane glass forming while both of A-2TPA and A-2PTz are yellow powder.

NMR, IR and HRMS characterizations confirmed the molecular structures of these intermediate and final compounds. All targeted compounds were obtained in reasonable overall yields after purification and have good solubility in common organic solvents, such as dichloromethane, chloroform, tetrahydrofuran, (di)chlorobenzene and toluene. The good solubility renders these molecules suitable for application in solution-processed organic electronic devices.

III.1.3.1 Thermal properties

Thermal behaviors of newly synthetized acridone molecules were investigated by thermogravimetric analysis (TGA) and differential scanning calorimetry (DSC) under argon atmosphere. Their TGA and DSC curves are given in ***Figure 6*** and their values of thermal decomposition (T_d) and the glass transition (T_g) temperatures are summarized in ***Table 3***.

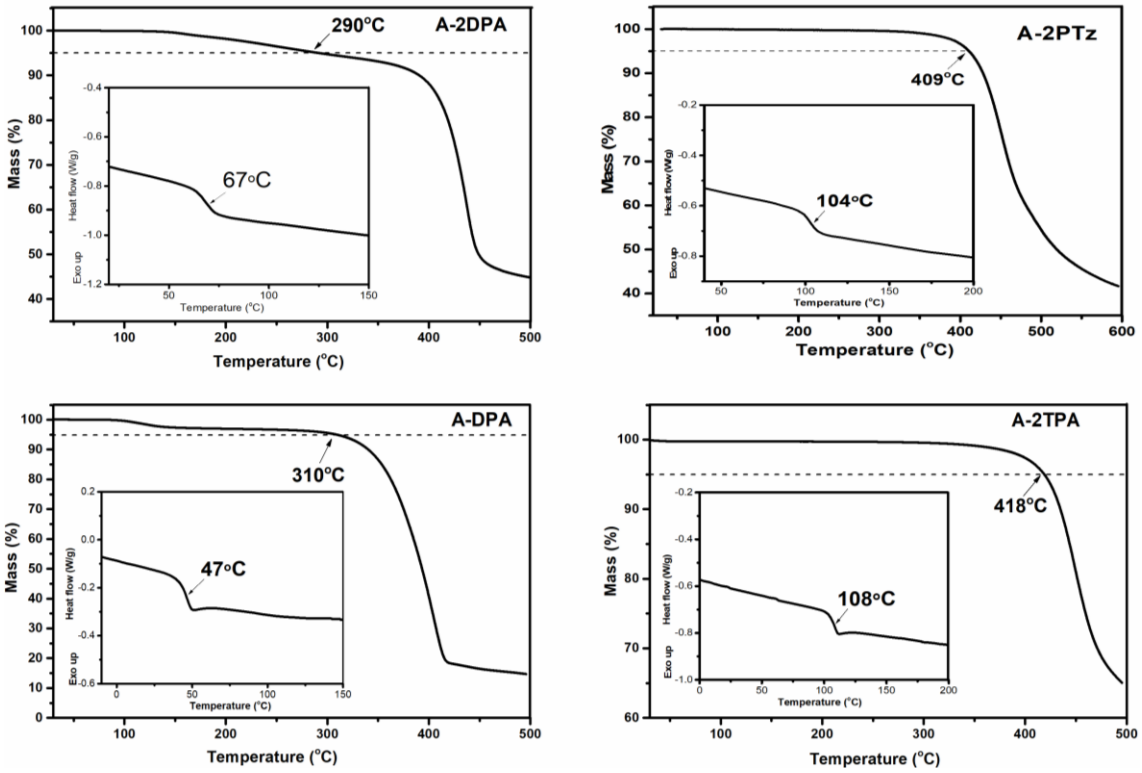

Figure 6 : TGA and DSC (inset) curves of studied acridone molecules

The T_d was determined at the 5% weight loss in TGA analyses. All compounds are thermally stable and decompose above 290^0C. Their thermal stability is thus high enough for the applications in organic electronic devices. DSC revealed molecular glass forming properties of all compounds with glass transition temperature of four compounds in the range of 47-108°C. A-DPA has the lowest T_g (47°C), because of the smallest molecular structure. Increasing the molecular weights leads to higher Tg (67°C for A-2DPA and 108°C for A-2TPA). A-2TPA exhibits high T_g which could be expected for more amorphous structure and good film morphology. Replacing the flexible diphenylamine by the rigid phenothiazine significantly increase the molecular rigidity, thus higher T_g (67°C of A-2DPA *versus* 104°C of A-2PTz).

To understand the thermal properties of all acridone-amine derivatives at the molecular level, the ground state geometries were calculated and optimized. Dihedral

angles and bond distances between the acridone-core and the substituted group were found to be dependent on the nature of the side groups (listed in ***Figure 7***)

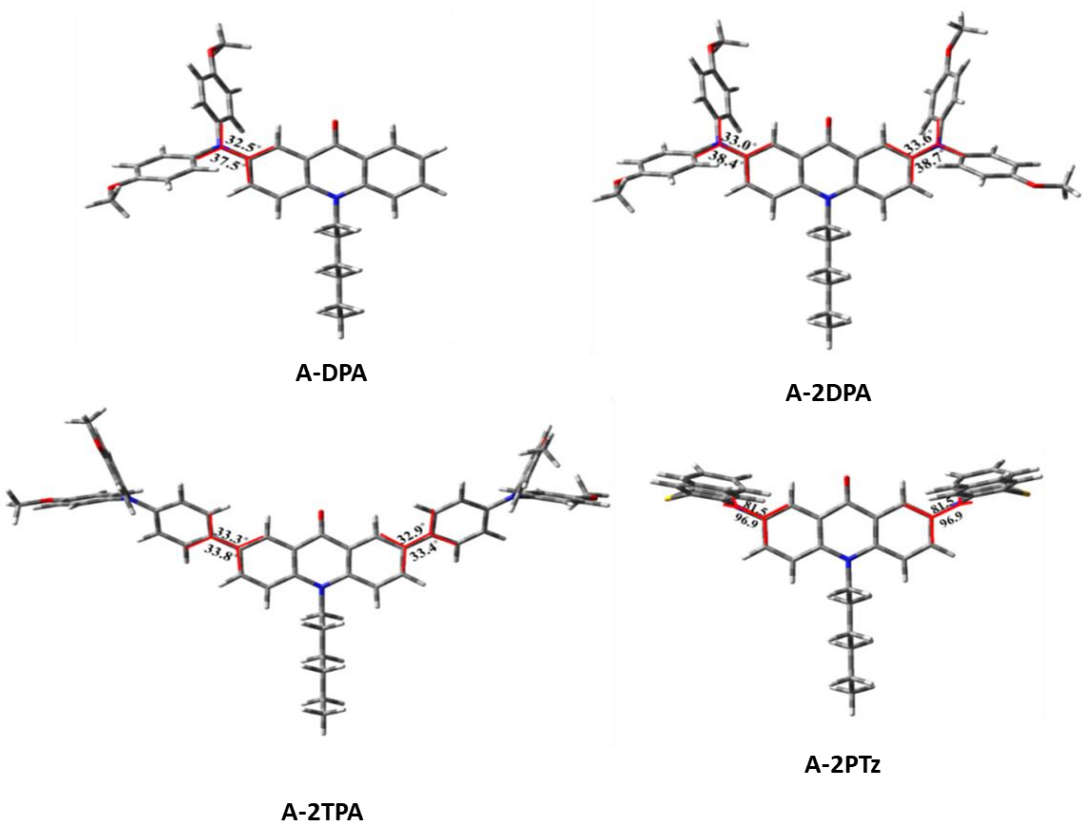

Figure 7 : Optimized structures along with the dihedral angles (°) of all compounds simulated by B3LYP/6-31G(d) in dichloromethane

Double diphenylamine-substituted A-2DPA had nearly identical dihedral angles compared to those of A-DPA. However, rigid phenothiazine group significantly increased the dihedral angles (from about 32° in A-2DPA to 97º in A-2PTz). This is in concordance with the significantly higher T_g of A-2PTz in comparison with that of A-2DPA as discussed above. The triphenylamine and diphenylamine caused small dihedral angles with the acridone core (approximately 32-38^o). All compounds possess 3D structure, which could prevent the π-π aggregation in the solid thin film.

III.1.3.2 Optical properties

Optical properties of synthesized compounds were studied by both experimental methods and DFT calculation. UV/Vis absorption and emission spectra were given in ***Figure 8*** and related data were summarized in ***Table 3***.

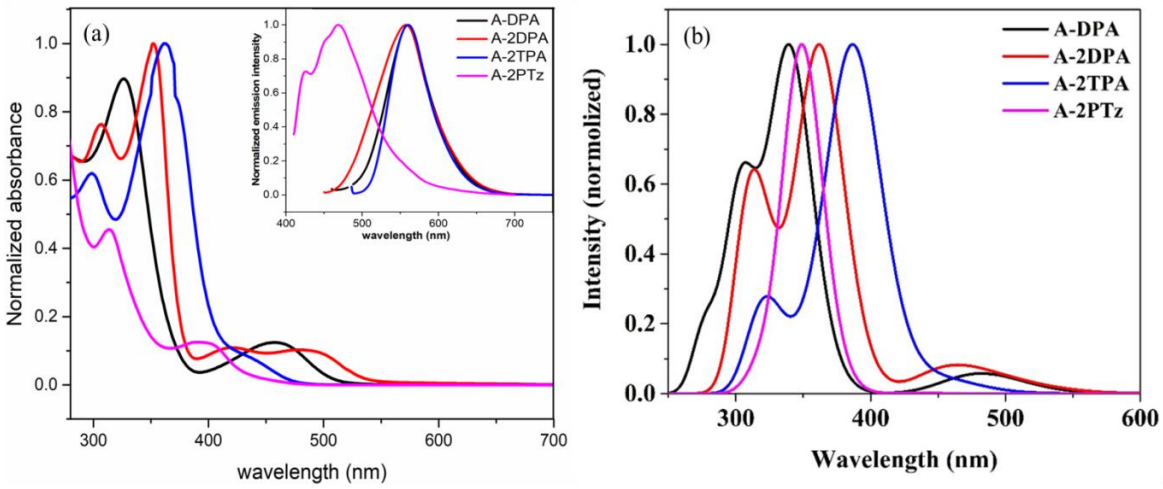

Figure 8 : (a) Experimental absorption spectra and emission spectra (inset) and (b) theoretical absorption spectra of studied compound in dilute dichloromethane

All compounds shows strong absorption bands located in the UV domain due to δ-π^* transitions. The weaker absorption bands can be observed at the longer wavelength in the visible region due to π-π^* transitions. A-DPA showed λ_{max} at 450 nm while A-2DPA showed two maximum absorptions at 406 nm and 475 nm, respectively. These signals in the range of 360 nm-550 nm exhibit intramolecular charge transfer (ICT). These ICT are generated by interaction between electron-donor units (diphenylamine groups) and electron-acceptor unit (carbonyl group in acridone core). Once increasing the number of electron rich moieties, it leads to red-shifted in absorption region. The electron donating ability of phenothiazine is generally weaker than that of diphenylamine[34]. Due to rigid structure, phenothiazine units increase the dihedral angles to acridone core. Thus, A-2PTz shows 81.5/96.9^o between phenothiazine and acridone core while A-2DPA shows 32.9/33.4^o between diphenylamine and acridone core. The D-A interactions in A-2PTz are reduced and therefore, the absorption band is more blue-shifted. A-2TPA showed a small shoulder peak in the range of 400-430 nm, which is blue-shifted compare to A-2DPA. It could be explained due to less conjugated molecular structure of A-2TPA and reducing D-A interaction. The theoretical absorption spectra of these compounds have been studied in dichloromethane. In ***Figure 8b***, strong ICT was observed in A-DPA and A-2DPA spectra while this character was not recorded in A-2PTz and A-2TPA. The calculated study is similar and confirms the experimental characterizations.

Otherwise, D-A system featured ICT transitions can reduce emission energy[5,35]. In ***Figure 9***, A-C_6H_{13} (compound 1-***scheme 1***) exhibits λ_{abs} and λ_{emiss} maxima at 401 and 436 nm, respectively. And this compound does not contain either electron donor group or

ICT, so it only absorbs in a range of UV region. In contrast, A-2DPA showed longer λ_{abs} and λ_{emiss} maxima of 475 and 550 nm, respectively. This compound absorbed in visible domain indicated that strong ICT occurred between DPA groups and acridone core. It is clearer when we compare images of these solutions under daylight and under UV 365 nm. The transparent solution of A-C_6H_{13} emitted intensive violet fluorescence while the yellow solution of A-2DPA emitted moderate yellow fluorescence.

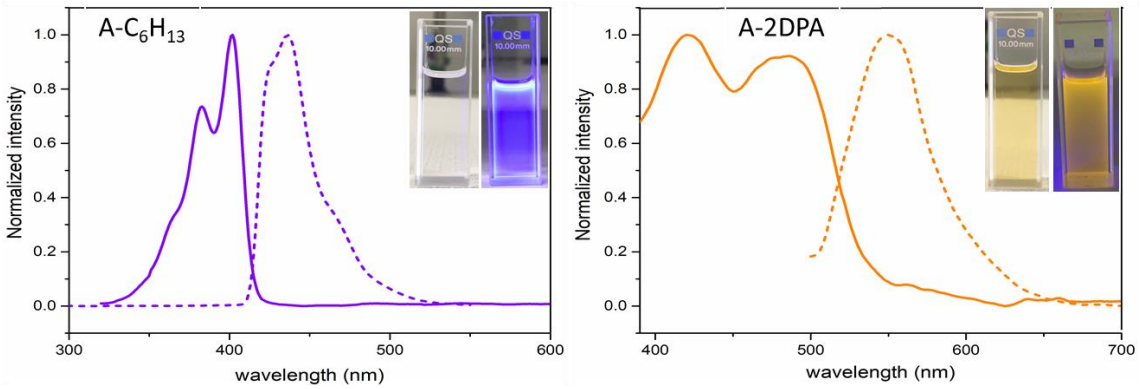

Figure 9 : Absorption (solid line) and emission (dashed line) spectra of A-C_6H_{13} and A-2DPA measured in diluted DCM. Inset: photographs of these solutions under daylight and UV 365 nm.

From the onset value of the lower energy absorption peaks, the optical bandgap of these molecules were determined and summarized in ***Table 3***. Fluorescence spectra were examined in dilute dichloromethane solution. These compounds emitted in green region with emission maxima in range of 475-595 nm. For example, A-DPA, A-2DPA and A-2TPA exhibit the same fluorescent properties and their λ_{max} emissions are very close. These three compounds have considerable Stokes shifts of about 120 nm, which can be explained by their high flexibility in the molecular structure. However, the emission property of A-2PTz is about 100nm blue-shifted. That could be explained with the weak D-A interaction between acridone core and phenothiazine moiety, leading to a reduced ICT in A-2PTz.

A set of solvents of different polarity was used to study the effect of polarity of solvent on optical properties of acridone derivatives. Absorption and fluorescent spectra of representative compound A-2DPA in variety of solvents were recorded at room temperature.

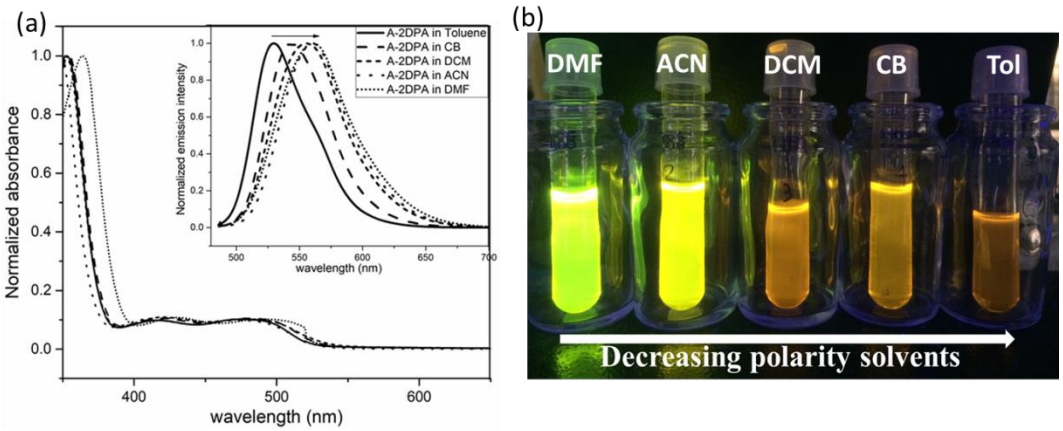

Figure 10 : Absorption and emission (inset) spectra (a) and appearance under UV 365nm (b) of A-2DPA in various solvents (from high polar DMF to nonpolar Toluene).

Absorption spectra of the compound A-2DPA in various solvents (from high polar to nonpolar solvent): DMF (polarity index P=6.4), acetonitrile (P=5.8), DCM (P=3.1), chlorobenzene (P=2.7) and toluene (P=2.4) have been carried out. Whatever the solvent, peaks are not really deviating from initial wavelength (352, 406 and 475 nm), indicating that solvent changes do not cause modification in ground state. However, the slight bathochromic shift is noticed while increasing polarity of solvents in emission spectra. A redshift in the emission spectra of these compounds is due to the increase in solvent polarity indicating the ICT character of the excited state. The Stokes shift was further increased in the more polar solvents, which suggests a charge transfer complex formation and interaction with the polar solvents. The optical properties of these compounds are in good agreement with data reported by Sharma *et al*[36] for a similar molecule. In this study, we used longer alkyl -C_6H_{13} chains to improve solubility of new materials, instead of methyl group in their study. Moreover, the long alkyl chain will improve hydrophobicity of these target molecules.

In order to better understand the optical properties and to evaluate the frontier molecular orbitals and energy levels of these acridone derivatives, the calculations of all compounds were carried out on the Gaussian09 program package[37] by using density functional theory (DFT) and time-dependent DFT (TDDFT). As displayed in ***Figure 11,*** all molecules adopt twisted structure in their optimized structure, except the case of A-2PTz which adopts a nearly orthogonal D–A conformation. The plot of HOMO and LUMO orbital distribution and the optical bandgap of all compounds were calculated. Because of the moderate electron-withdrawing characteristics of the carbonyl group, the LUMOs of all compounds are localized on the acridone backbone while the nitrogen

atom would provide its lone pair to form an extended conjugation from intra-acridone moiety to extra-donor moiety, the HOMOs of all compounds is mainly localized on the donor moiety.

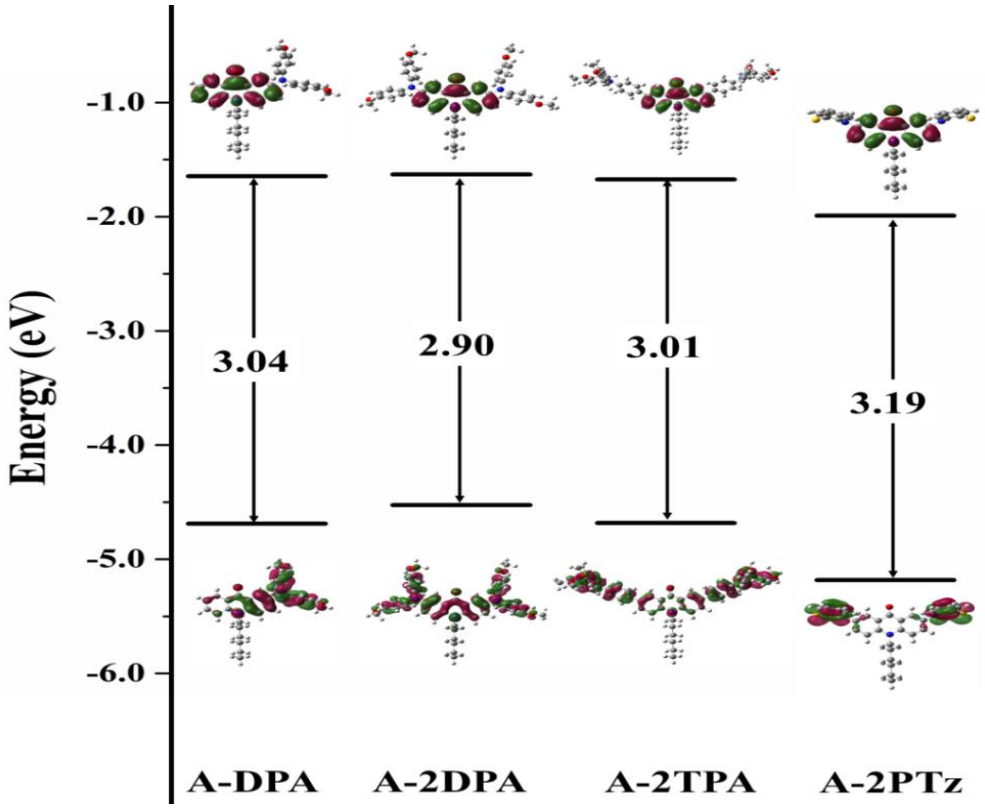

Figure 11 : Frontier molecular energy diagram of all molecular structures Calculated by B3LYP/6-31G(d).

The value HOMOs of A-DPA, A-2DPA and A-2TPA are distributed mainly on the side donor moieties and located over the whole molecule, which is beneficial for charge transport capability. Exceptionally, the HOMO of A-2PTz is fully located on the PTz moieties, due to its nearly perpendicular conformation between acridone and PTz, with torsional angle 81.5-96.9^{o}. The structure of 9(10H)-acridone is also considered cross-conjugated bridge. Therefore, it offers the good explanation for the disruption of the conjugation in the A-2PTz. The calculated HOMO energy levels of A-DPA, A-2DPA and A-2TPA (nearly -4.5 eV) are higher than that of A-2PTz (approximately -5.1 eV). Their electron densities are more occupied on the acridone and diphenylamine moieties but these densities are less populated on the acridone moiety for A-2TPA and A-2PTz. The calculated LUMO energy levels are about -1.6 eV except that of A-2PTz, which is about -1.9 eV and their electron, densities are mainly populated on the acridone core.

Such changes in electron density distribution in all compounds are attributed as the ICT effect upon the electronic excitation.

The simulated absorption spectra of all compounds are illustrated in ***Figure 12.***

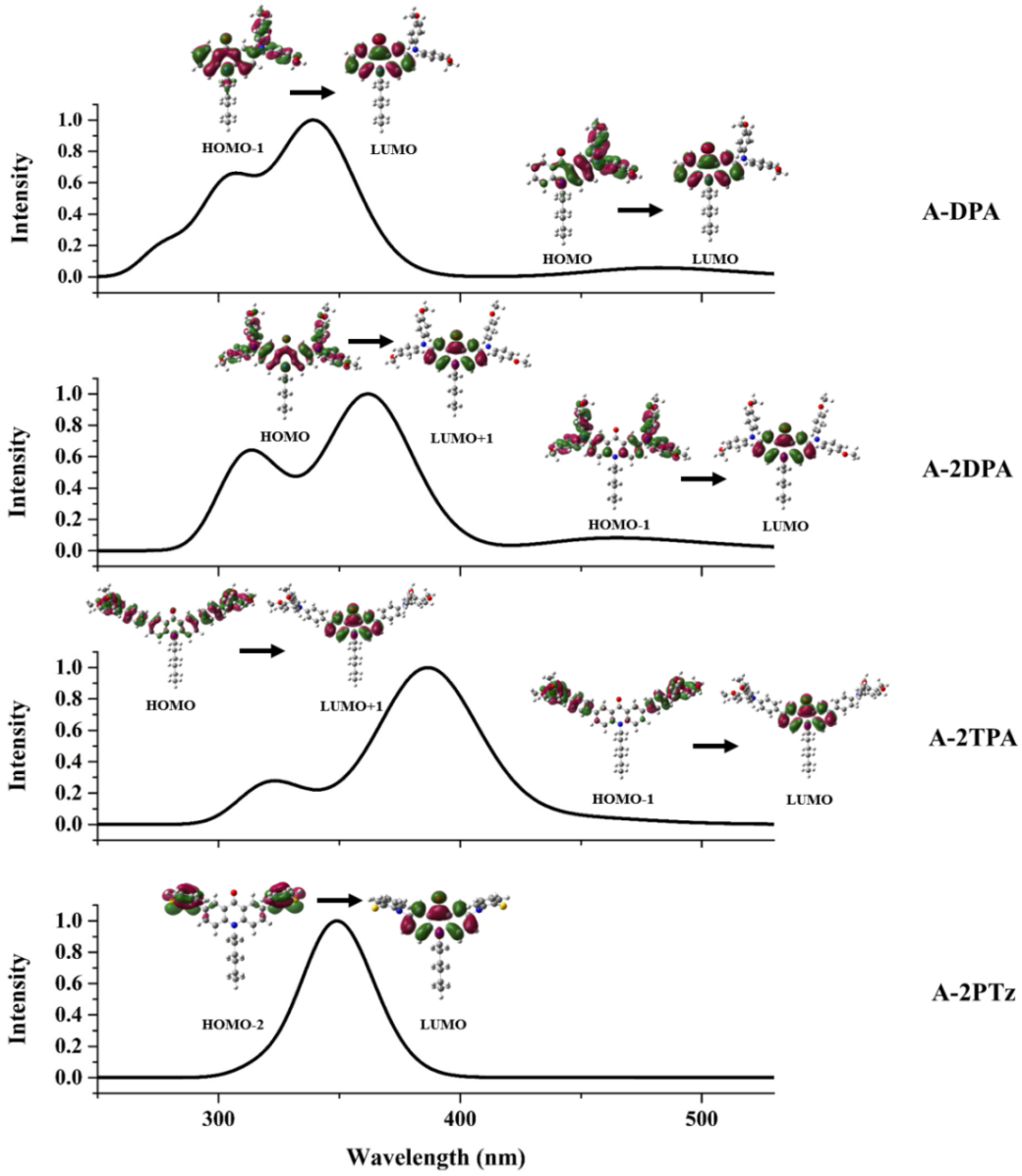

Figure 12 : Simulated absorption spectra of these new materials calculated by TD-B3LYP/6-31G(d) in dichloromethane.

Their excitation energies and the corresponding oscillator strength are given in ***Table 1*** and ***Table 2.*** All compounds except A-2PTz show main absorption peaks at the wavelength around 300-400 nm and minor peaks around 500 nm, which are in line with the experimental data.

Structure	Calculation (nm)	*f*	Composition (%)	Character	Experiment (nm)
A-DPA	482	0.0419	HOMO→LUMO (99%)	ICT	450
	349	0.2309	HOMO-1→LUMO (30%)	ICT	
			HOMO→LUMO+1 (66%)	π→π*	
	338	0.2733	HOMO-3→LUMO (14%)	π→π*	
			HOMO-1→LUMO (56%)	ICT	
			HOMO→LUMO+1 (24%)	π→π*	
	337	0.0544	HOMO-3→LUMO (83%)	π→π*	
	334	0.2089	HOMO→LUMO+2 (94%)	π→π*	
A-2DPA	503	0.0274	HOMO→LUMO (99%)	ICT	
	459	0.0724	HOMO-1→LUMO (98%)	ICT	475
	363	0.9247	HOMO→LUMO+1 (93%)	π→π*	
	345	0.1204	HOMO→LUMO+2 (89%)	π→π*	
	338	0.0010	HOMO-5→LUMO (91%)	π→π*	
A-2TPA	466	0.0036	HOMO→LUMO (99%)	ICT	
	452	0.0637	HOMO-1→LUMO (99%)	ICT	440
	388	1.5343	HOMO→LUMO+1 (92%)	ICT	
	366	0.1631	HOMO-1→LUMO+1 (87%)	ICT	
	361	0.1452	HOMO-2→LUMO (90%)	π→π*	
A-2TPz	463	0.0000	HOMO→LUMO (98%)	ICT	
	460	0.0001	HOMO-1→LUMO (98%)	ICT	
	359	0.0963	HOMO-2→LUMO (97%)	π→π*	396
	344	0.0016	HOMO-1→LUMO+3 (12%)	π→π*	
			HOMO→LUMO+1 (82%)	ICT	
	343	0.0003	HOMO-1→LUMO+1 (79%)	ICT	
			HOMO→LUMO+3 (13%)	π→π*	

ICT: intramolecular charge transfer

Table 1: The excitation energies, oscillator strengths (f), and transition compositions for the five lowest states by TD-B3LYP/6–31G(d,p) in dichloromethane solution using C-PCM.

For A-DPA as the parent compound, the overlapped peak appearing at 300-350 nm is assigned to the π to π* transition and the ICT transition which are contributing to the HOMO to LUMO and HOMO-1 to LUMO transition, respectively. For A-2DPA, this overlapped peak is still observed but the ICT transition is shifted to longer wavelength (from 350 to 370 nm), which is attributed to the HOMO to LUMO+1. For A-2TPA, the

ICT transition is more important causing a longer wavelength shifted around 390 nm. However, for A-2PTz, the combination between the π-π* transition and the ICT transition is not observed but only strong ICT around 350 nm is found which is solely assigned to HOMO-2 to LUMO. Moreover, the small but noticeable peak around 500 nm assigned to either π-π* transition or ICT transition are observed for all compounds except A-2PTz. Consideration of these orbitals in ***Figure 11***, introduction two groups of phenylamine into acridone slightly moves absorption peak. Moreover, by adding a phenyl ring as π-spacer between the phenylamine and acridone moieties, more red-shifted absorption can be achieved.

Structures	λ_1 (nm)	λ_2 (nm)	*f*	Main contribution	HOMO (eV)	LUMO (eV)	E_{gap} (eV)	$\lambda_{abs}^{exp.}$ (nm)	$E_{gap}^{exp.}$ (eV)
A-DPA	349	482	0.0419	HOMO → LUMO	-4.49	-1.65	3.04	450	2.48
A-2DPA	363	459	0.0724	HOMO-1 → LUMO	-4.53	-1.63	2.90	475	2.33
A-2TPA	388	452	0.0637	HOMO-1 → LUMO	-4.68	-1.67	3.01	440	2.89
A-2PTz	359	-	0.0963	HOMO-2 → LUMO	-5.17	-1.98	3.19	396	2.83

Table 2: Wavelength of absorption (λ_{abs}), oscillator strength (f), HOMO and LUMO energy (eV) and energy gap between HOMO and LUMO (E_{gap}) of compounds calculated by B3LYP/6-31G(d) level in dichloromethane.

III.1.3.3 Oxidized states of doped *p*-type molecules

It could be interesting now to study the impact of oxidizing agent on the molecular glasses. ***Figure 13*** shows a series of electronic spectra of A-DPA (representative of D-A molecular) and A-2DPA (representative of D-A-D molecular) with strong oxidant nitrosonium tetrafluoroborate ($NOBF_4$) in dichloromethane at various chemical doping levels.

While adding strong oxidant species as $NOBF_4$ in these solution, new absorption peaks grew up in the longer wavelength (600-1300 nm) with a concomitant decrease of intensity in the range 300-450 nm of π-π^* transition. The positions of these bands are independent of chemical species of the anions of dopants. These experimental results indicated that the ICT band of neutral compounds (around 350 nm) was decreasing while broad peaks in longer wavelength absorption band were growing during oxidation suggesting a highly delocalized cationic charge.

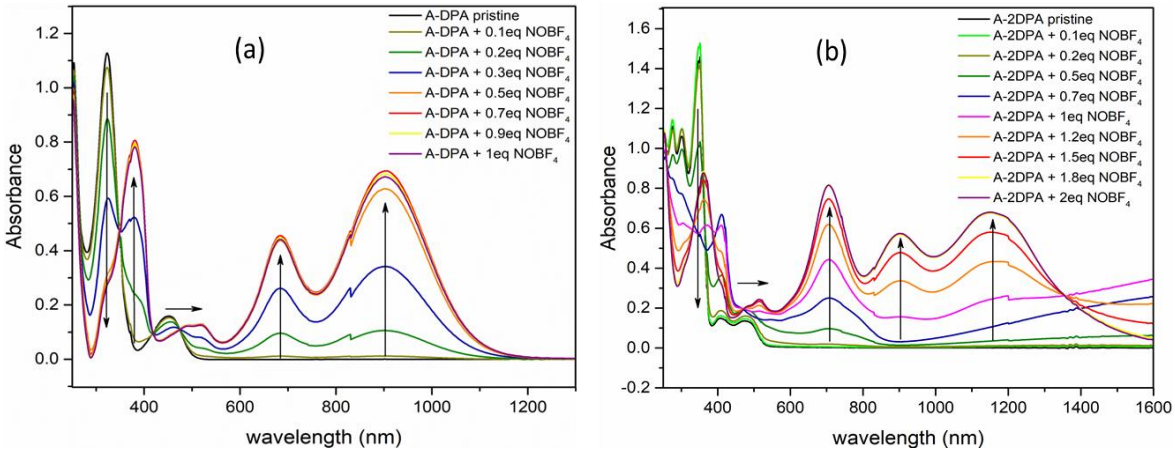

Figure 13 : Various doping levels of $NOBF_4$ in A-DPA (a) and A-2DPA (b)

During doping reaction, A-DPA shows two broad peaks (682 nm and 904 nm) which raise up as doping level of $NOBF_4$ increase up to 1eq molar. When the amount of $NOBF_4$ is more than 1 eq, their absorbance intensities did not change. The doping level has been calculated according to molar of the pristine compound and it is proportion to number of DPA units. Thus, A-2DPA shows three broad peaks (705, 898 and 1150 nm) while doping level of $NOBF_4$ is up to 2 molar eq. This broad low energy absorption is characteristic of π-delocalized cations. The color of oxidized compounds changes continuously from bright yellow to dark green with doping level and stable long time in ambient. The observation indicates certainly the formation of radical cations (polaron and bipolaron). Based on the literature [38–40] suggested mechanisms are given in ***Scheme 2***.

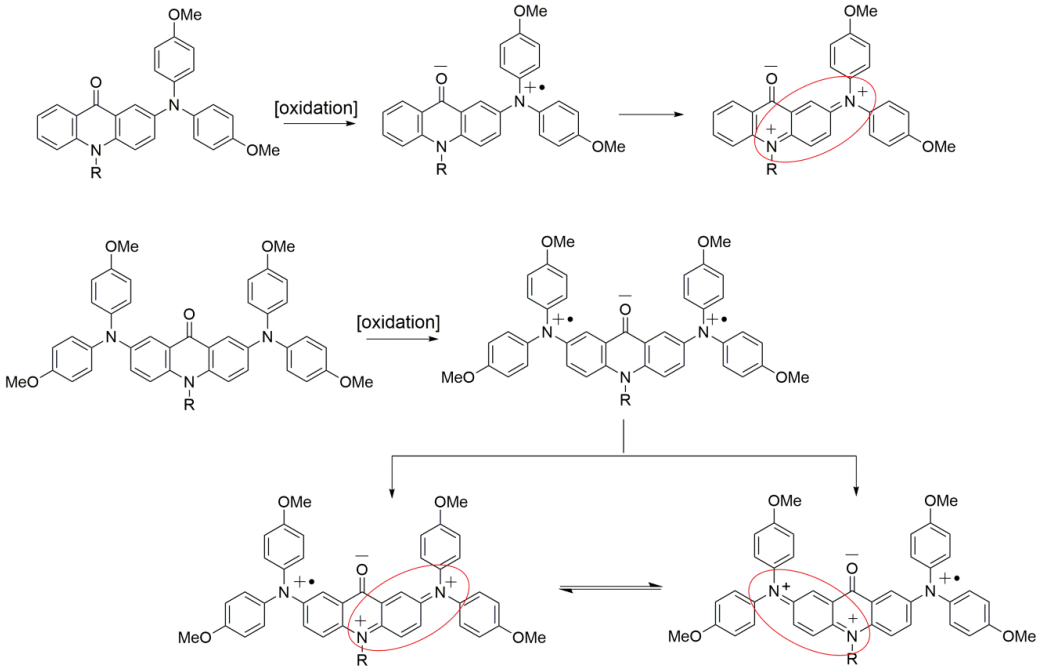

Scheme 2: Suggested mechanism of radical cation's formation of A-DPA (top) and A-2DPA (bottom) in presence of strong oxidant $NOBF_4$.

This study indicated that these compounds are well-effective by doping and cationic charges are increasing electron density delocalized from amine backbone (of acridone core) to amine part (of donor groups). Due to strong absorption in the near IR region, these oxidized species reduced optical band gap of doped molecules and would be increased charge mobility. However, since these molecules have been using as HTMs, the nature of dopants as well as their quantities should be optimized in device performance.

III.1.3.4 Electrochemical properties

Cyclic voltammetry has been employed to investigate the electrochemical behavior of synthesized molecules and to estimate their HOMO and LUMO energy levels (***Figure 14***). All compounds show multiple oxidation processes. The first oxidation potentials could be attributed to the formation of radical cation of the diphenylamine or phenothiazine moieties. Acridone core was then oxidized in higher potential.

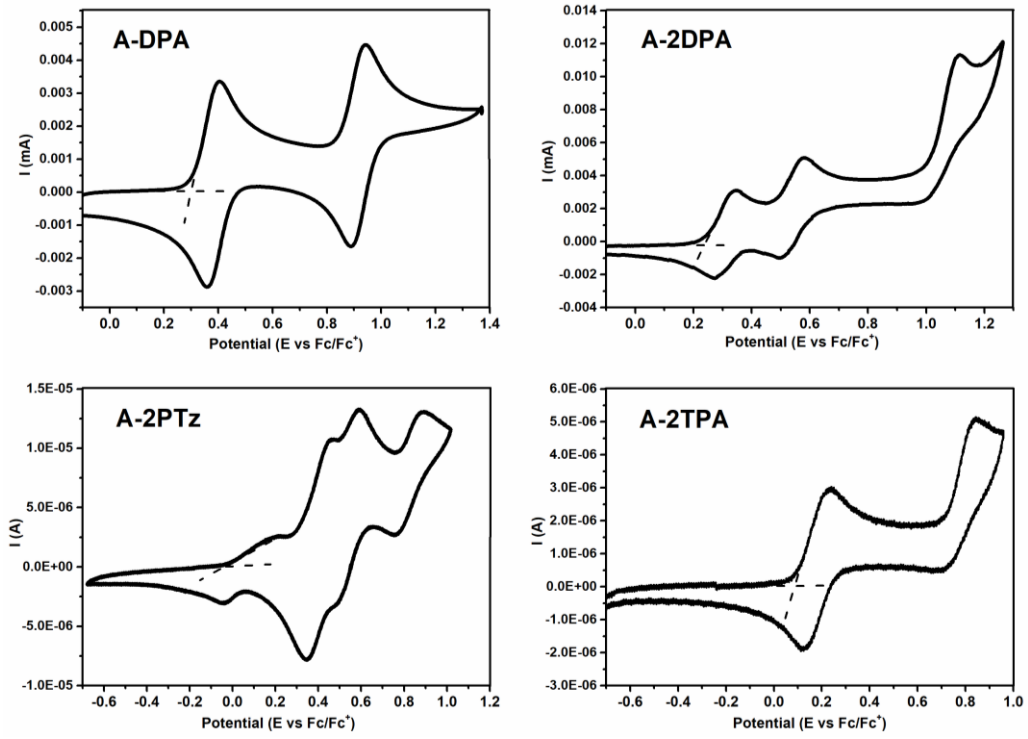

Figure 14 : Cyclic voltammogram of acridone derivatives compound.

A-DPA and A-2DPA have very close oxidation potentials with onset values of approximately 0.30 and 0.24 V versus $E^{1/2}$ of Fc/Fc^{+}. In CV of A-2DPA, two close oxidation peaks were attributed to the sequential oxidation of the two DPA moieties by single electron transfer processes. This compound possesses well-developed structure and strong interaction between electron donor units and acridone core. However, only one

oxidation peak was determined in case of A-2TPA. Considering a less conjugated molecules A-2TPA, the two TPA units could be oxidized at the same time. However in this case, the peak current should be double than that of Acridone core which apparently it's not the case. Additional experiences have to be done to study this behavior.

Electrochemical behavior of A-2PTz is similar to that of A-2DPA with two sequential oxidations at lower potential attributed to two phenothiazine moieties. The higher oxidation is originated from the acridone core. The observed shoulder at low potential could be from an impurity present in the product which was not effectively eliminated during the chromatographic purification.

The reduction process of these compounds could not be recorded in this condition due to the limited electrochemical window of the solvent ($TBA.BF_6$ as electrolyte in dried DCM).

Compound	T_g (^oC)	T_d (^oC)	λ_{abs}, nm in DCM	$\log_\varepsilon$ max	λ_{emiss}, nm in DCM	E_g, eV	E_{HOMO}, eV	E_{LUMO}, eV
A-DPA	47	310	450	4.37	565	2.48	-5.10	-2.22
A-2DPA	67	290	475	3.99	550	2.33	-5.04	-2.71
A-2TPA	108	418	440	3.66	552	2.89	-4.89	-1.99
A-2PTz	104	409	396	4.14	475	2.83	-4.8	-1.97

Table 3: Summary of photophysical, thermal and electrochemical data of these compounds. Glass transition temperature T_g is obtained from the onset values of DSC and decomposition temperature, T_d is recorded by 5% weight loss in TGA.

From the oxidation onset potential values, HOMO energy values of A-DPA and A-2DPA are -5.10 and -5.04 eV, respectively. A-2TPA possesses onset oxidation potentials at 0.09V vs leading the IP of -4.89 eV. A-2PTz has the lowest onset first oxidation (0V vs $E^{1/2}$ of Fc/Fc^+) corresponding to HOMO value of -4.80 eV. The LUMO energy values are determined by the optical bandgap and the HOMO energy values. Due to moderate electron acceptor ability, the LUMOs values are negligible changed.

As observed in ***Figure 15***, the energy level and band gap of these new materials were tuned by incorporation of various electron donor groups. Their HOMO energy levels are located above the ground-state level of the $CH_3NH_3PbI_3$ hybrid perovskite absorber (-5.4 eV). This could sufficient for hole charge extraction and transfer at the interface of perovskite/HTM. Additionally, their LUMO energy values are also much higher than that of perovskite (-3.9 eV), thus avoid back electron transfer process. Their

HOMO-LUMO energy levels are suitable for materials as hole transport materials in perovskite solar cells.

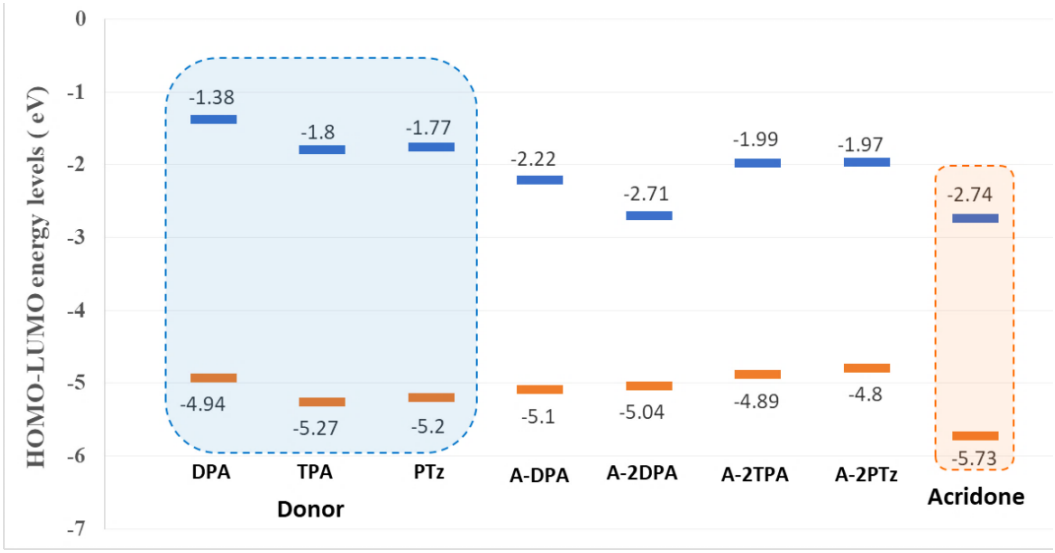

Figure 15 : Tuning of frontier HOMO-LUMO energy levels of these acridone derivatives compare to that of donor moieties and acridone core

III.1.3.5 Solid state crystallographic-morphology molecular structure

Evidence that the structure of A-2TPA was correctly assigned has also been obtained via a single crystal X-ray diffraction analysis. Single crystals of A-2TPA suitable for X-ray diffraction analysis were grown by slow evaporation of A-2TPA in DMF. A mercury view (3.9, CCDC, 2016) depicted in ***Figure 16*** displays the structure of A-2TPA and the detailed crystallographic data are given in ***Table 4***.

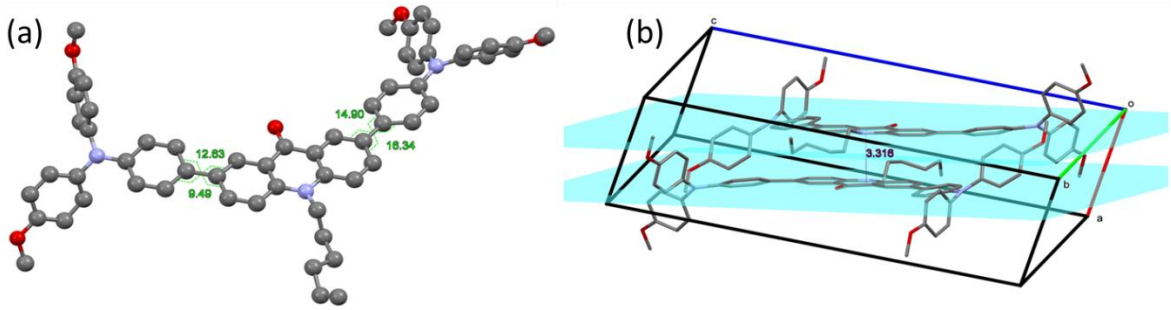

Figure 16 : (a) Single crystal of A-2TPA with dihedral angles and (b) π-π stacking interactions between two molecules of A-2TPA.

Packing interaction between two molecules of A-2TPA showed small π-π distance (3.316 Å), which are expected to facilitate charge transport property. The calculation of torsional angle value between acridone backbone and TPA moiety for A-2TPA is about

32°, however the x-ray crystallographic data show a value close to 9-12°. That difference was explained by the fact that the XRD experimental were carried out in the solid state while the calculation was simulated in solution.

Compound	A-2TPA
Empirical Formula	C_{59} H_{55} N_3 O_5
M_r	886.06
Crystal size, mm^3	0.08 x 0.03 x 0.01
Crystal system	triclinic
Space group	*P -1*
a, Å	7.083(5)
b, Å	14.108(10)
c, Å	24.222(18)
α, °	85.578(17)
β, °	81.92(2)
γ, °	82.778(19)
Cell volume, $Å^3$	2373(3)
Z ; Z'	2 ; 1
T, K	100(1)
Radiation type ; wavelength Å	Cu K_α ; 1.54178
F_{000}	940
μ, mm^{-1}	0.622
θ range, °	3.163 - 58.880
Reflection collected	18202
Reflections unique	5888
R_{int}	0.2062
GOF	0.951
Refl. obs. ($I>2\sigma(I)$)	1883
Parameters	630
wR_2 (all data)	0.2840
R value ($I>2\sigma(I)$)	0.0992
Largest different peak and hole (e-.$Å^{-3}$)	0.533 ; -0.386
CCDC	1827633

Table 4 : Crystallographic data and structure refinement details of A-2TPA

The film morphology of the Acridone molecules has been investigated by AFM measurements. ***Figure 17*** showed smooth thin films of A-DPA and A-2DPA. The average surface roughness of A-DPA and A-2DPA are 0.54 and 0.28 nm, respectively while A-2TPA film exhibited higher roughness (7.28 nm). Despite a high T_g (108°C) for A-2TPA which normally induce a homogeneous film, the rugosity can be explain by a low solubility of A-2TPA in inappropriate solvents. As a result, the quality of these films will affect on interface between HTM and perovskite. In prediction, A-DPA and A-2DPA could cover perovskite surface better than A-2TPA film.

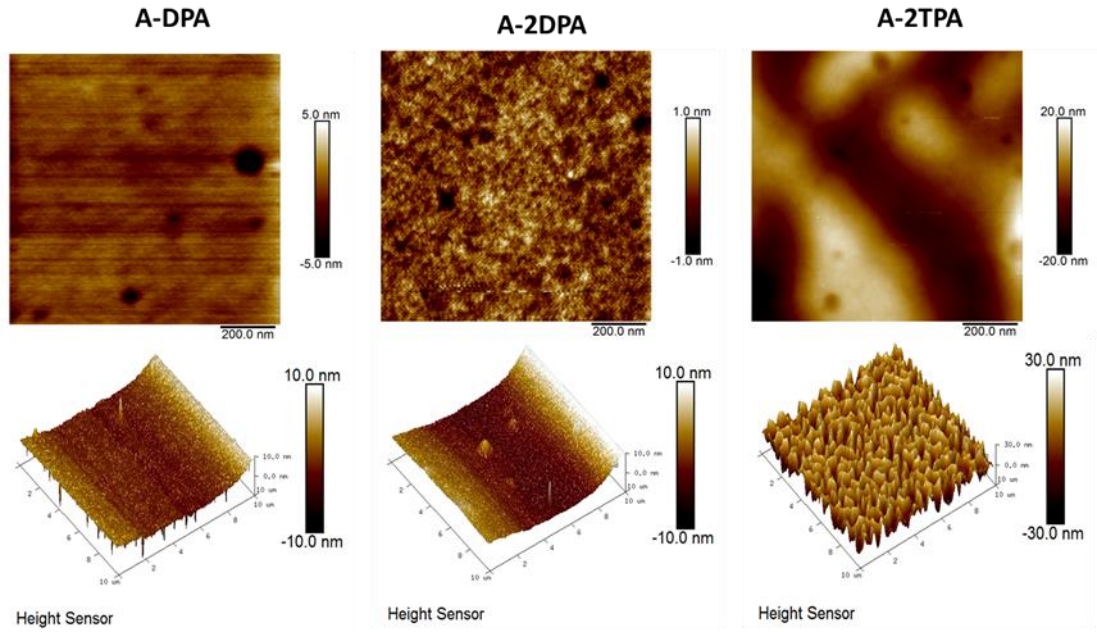

Figure 17 : AFM images of A-DPA, A-2DPA and A-2TPA materials coated on glass substrates (top) and 3D images of corresponding materials (bottom).

The contact angle measurements were carried out by water-drop method on coated film on glass substrate (***Figure 18***). All of these materials show hydrophobic properties due to high values of water contact angle. They indicated that these materials could well-coverage perovskite layer and protect absorber against moisture.

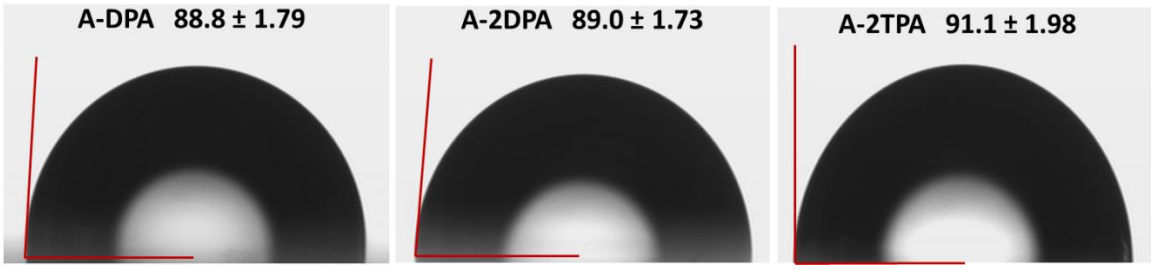

Figure 18 : Contact angle measurement (°) of A-DPA, A-2DPA and A-2TPA films coated on glass substrate.

III.1.3.6 Hybrid perovskite solar cells application

Finally, these new push-pull HTMs were employed as hole transporting materials in typical perovskite solar cells. All of acridone derivative molecules have been used as new HTMs for devices fabrication.

Figure 19 showed fabrication of typical mesoscopic PSCs[41]. Firstly, the blocking layer was coated on the etched FTO layer via spin coating. This blocking layer plays a crucial role, protecting against direct contact between FTO and perovskite, HTM or gold. Moreover, its presence allows a good adherence of mesoporous TiO_2 during post annealing and calcination. The post thermal treatment of blocking layer and mesoporous layer are carried out at 125°C in 5min to remove solvents.

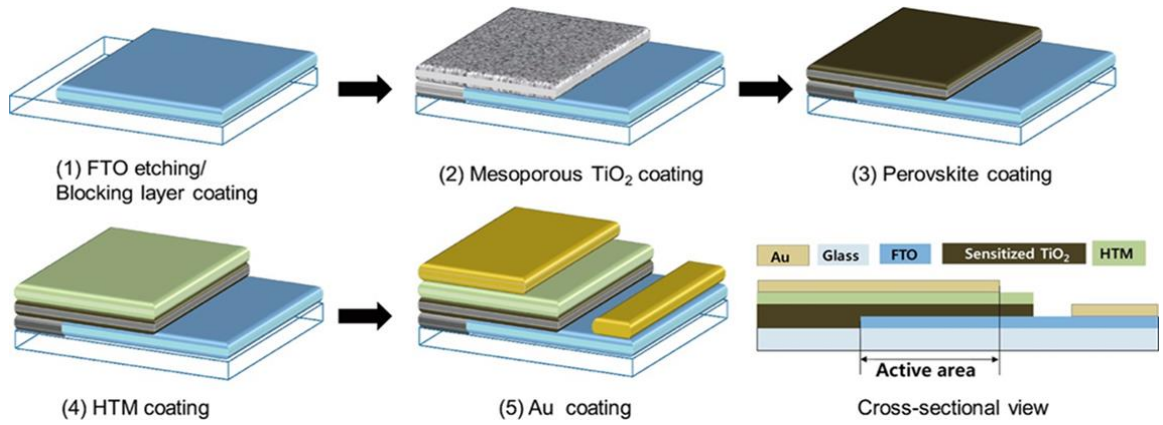

Figure 19 : Procedure to fabrication of typical mesoscopic perovskite solar cells. Figure adapted from ref[41]

Mesoporous TiO_2 film is deposited on the blocking layer, where film thickness, surface area, pore size, and porosity should be carefully controlled. It is important to control the thickness of TiO_2 as well as electron transport layers (ETLs), in general, to optimize device performance. Too thin ETLs could promote recombination of carriers as the perovskite layer could be in contact with the ITO substrate thereby decreasing device performance. While too thick ETLs would avoid electron injection across the perovskite layer[42]. Afterward, the calcination of mesoporous TiO_2 layer was carried out at 500°C in 1h. The perovskite layer forms in the TiO_2 matrix via a one-step coating method, followed by annealing at 100 °C. The post-annealing temperature and time which affect directly to structure of perovskite crystals should be carefully controlled. When the pores in the oxide film are filled with perovskite, a thin layer of HTM is added by spin-coating.

Gold or silver metals are deposited by evaporation on the HTM top-layer to complete the device.

In this thesis, the procedures of PSCs fabrication were precisely described in General Appendix. ***Figure 20a*** showed scanning electron microscope (SEM) image of mesoporous TiO_2 layer coated on blocking layer/FTO. It showed homogenous film with high porosity which is efficient scaffold for perovskite deposition. ***Figure 20b*** exhibited perovskite film coated on mesoporous TiO_2 layer with large crystal size is average ca.500 nm and mixed of small crystal. However, ***Figure 20c*** (in 200nm scale) exhibited existence of grain boundaries[43] which affect to fill factor and hysteresis of completed devices[44]. ***Figure 20d*** showed the appearance of real devices in which different compounds have been used as HTMs and back contact electrodes were also investigated. Gold electrode showed better device performance while silver could be formed aggregation to iodide atoms in perovskite layer and leading to degradation of PSCs.

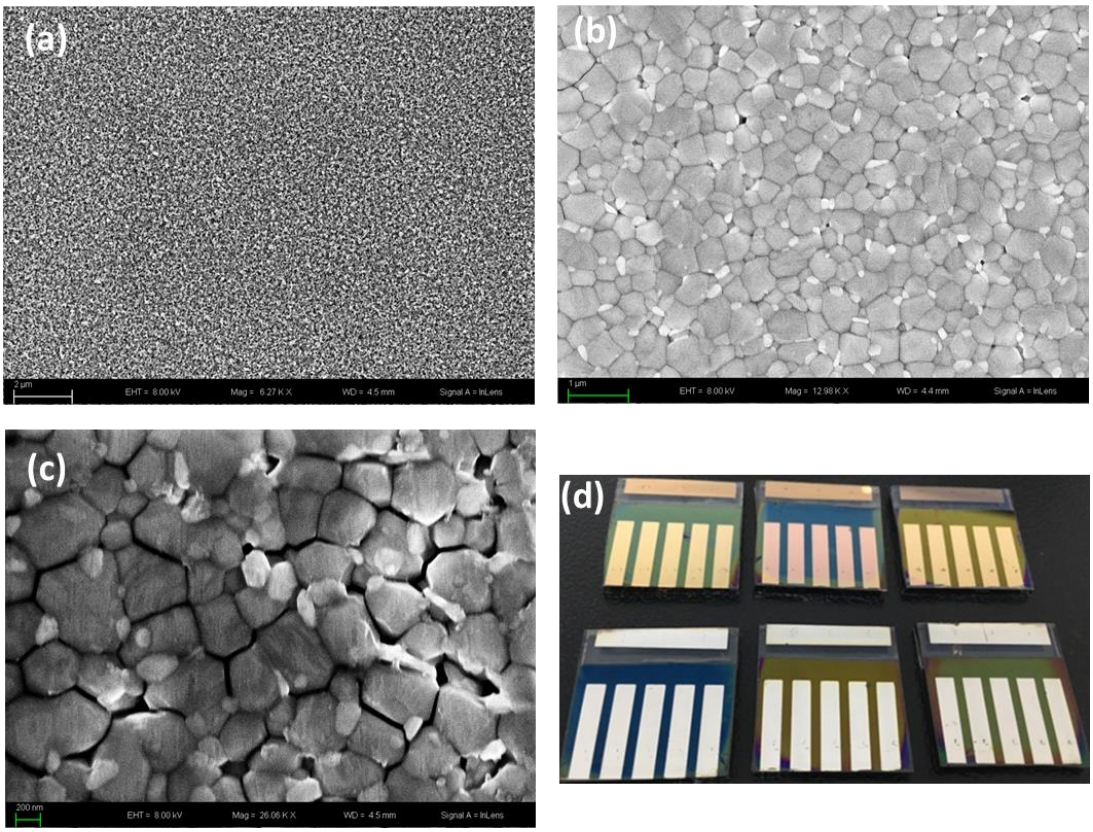

Figure 20 : SEM images of (a) Mesoporous TiO_2 layer (scale: 2µm). (b) Perovskite film coated on mesoporous TiO_2 layer (scale: 1µm) (c) Zoom in of perovskite layer with grain boundaries (scale: 200 nm). (d) Real devices with different HTMs and gold/silver as metal electrodes.

The well-known HTM Spiro-OMeTAD was used as control device. In case of Spiro-OMeTAD, the concentration of HTM was kept at 72.3mg/ml of chlorobenzene and

the mixture of additives (Li-TFSi and tert-butylpyridine) was employed to increasing of hole mobility and conductivity. In case of new materials, they were applied with similar procedure to Spiro-OMeTAD and testing with and without additives/dopant. Then, the optimization was carried out by changing conditions of concentration of HTMs, quantities of additives or various back contact electrodes (Ag or Au). Thickness of HTM is one of the most important factor to control, if the thickness of HTM layer is too thick, it will increase its strength of absorption sunlight and avoid Au/Ag penetrate through layers to get short-circuit phenomena[45–47]. Inversely, thin HTM layer could prevent charge recombination but leads to low open circuit voltage and maybe to unprotected perovskite against moisture[48]. Unfortunately, the optimization did not succeed due to unstable and non-reproducible perovskite film. Therefore, the generated photocurrent is very low and a quick degradation of devices under illumination was observed.

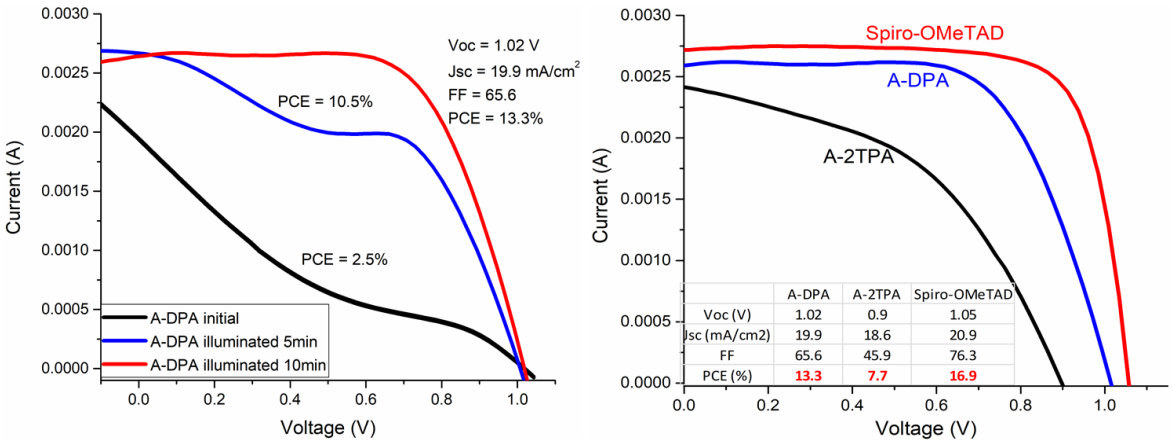

Figure 21 : I-V characterization of PSCs employed A-DPA and A-2TPA as new HTMs. Spiro-OMeTAD was used as control device.

The best device performance was obtained by A-DPA and A-2TPA used as new HTMs. The A-DPA and A-2TPA solutions were prepared with two additives. Lithium bis(trifluoro-methanesulfonyl)imide (3.3eq, Li-TFSI/acetonitrile (520mg/1mL) and 4-tertbutylpyridine (0.54 eq). In case of A-DPA, the best PCE 13.3% is obtained; the value of PCE increases while light exposure time is up to 10 min. The reason is that the thin film morphology of this small molecule which low Tg is sensitive to temperature. Under light illumination, the molecules are rearranged which modify the film morphology and minimized pinhole in devices[49], thus increase PCEs. But the PCE start decreasing after 10 min illumination due to the degradation of perovskite layer. Therefore, optimization of PSCs to A-DPA could be carried out, specifically in near future by modifying thickness of HTM film or the ratio of additives. Similar conditions to A-DPA, compound A-2TPA

was employed in PSCs and best PCE 7.7% is obtained. The device performance show low current density J_{SC} and fill factor FF due to pinholes and defects on surface of HTM and perovskite. The optimization of PSCs used these new materials is in progress and could obtain better photovoltaic performance.

III.1.4 Conclusion and perspectives

In summary, a series of new bipolar molecules capable of hole transporting have been constructed by incorporating by 9(10H)-acridone core and various electron donor moieties. The photophysical properties of these compounds have been investigated by experimental and computational methods. The HOMO-LUMO energy levels of these compounds were found suitable for perovskite solar cells. These compounds possess intramolecular charge transfer character which is interesting property of donor-acceptor system. But, intermolecular charge transfer is the main character affecting hole mobility and charge transport properties. First, these materials were designed as hole transport materials for photovoltaic application, especially for perovskite solar cells. In addition, thank to their absorption and emission properties, they could be applied as visible light absorbing photo-initiator for the polymerization[50]. Some of these molecules can have thermally activated delayed fluorescence (TADF) property which needs further investigation.

In future works, the optimization of these promising materials in PSCs will be continued to obtain higher PSCs performance with better devices stability.

III.1.5 Experimental section

Synthesis of materials

Compound 4-(4,4,5,5-tetramethyl-1,3,2-dioxaborolan-2-yl)-N,N-bis(4-methoxyphenyl) aniline was synthesized according to the literature.[33]

In dry Schlenk flask, 4-Bromo-N,N-bis(4-methoxyphenyl)aniline (0.5g, 1eq) and 30 ml of distilled THF are stirred vigorously under argon atmosphere. The temperature is cooled down to -78^0C by N_2 liquid and, n-BuLi (1.7ml, 1.1 eq) is added dropwise to solution during 30 minutes. After 1 hour, isopropoxyboronic acid pinacol ester (1ml, 1.1 eq) is added slowly by syringe. The reaction is kept overnight. Color changed from light yellow to red yellow. Solvent is removed under reduced pressure, then extract crude

product by DCM and water three times, collected organic phase and dried over $MgSO_4$. The crude product is concentrated and precipitated in methanol, obtained white solid (0.8g, 70% yield). ^{1}H NMR (250 MHz, DMSO-d_6) δ 7.42 (d, *J* = 8.5 Hz, 2H, Ar), 7.06 (d, *J* =2.5 Hz, 4H, Ar), 7.02 (d, *J*=2.5 Hz, 4H, Ar), 6.65 (d, *J* =8.5 Hz, 2H, Ar), 3.73 (s, 3H, -OCH_3), 1.23 (s, 12H, -CH_3). ^{13}C NMR (62.5 MHz, DMSO-d_6) 156.7, 151.6, 139.8, 136.1, 127.9, 117.3, 115.5, 85.58, 55.7, 25.1.

Formation of 10-hexyl-9-acridone (1):

In 100 ml 3-necks bottom, 9(10H)-acridone (400mg, 1eq) was dissolved in 15 ml of DMSO and then NaOH solution (1.02g of NaOH in 2 ml of water, 10eq) and few drops of Aliquat 336 were added. The temperature was increased to 110^{o}C and refluxed under argon atmosphere. After 3 hours stirring, 1-bromohexane (0.5ml, 1.5eq) was added dropwise to the mixture and then the reaction was kept overnight. The reaction was monitored by thin layer chromatography (TLC). After completion of the reaction, the mixture was reconstituted in dichloromethane (DCM), washed with water and the organic layer was dried over $MgSO_4$. The crude product was concentrated and then purified by silica gel column chromatography using DCM: ethyl acetate (EtOAc) (9:1 v/v) as eluent and then recrystallized in methanol. The final product is compound **1** as pale yellow crystals (478mg, 75%). ^{1}H NMR (250 MHz, $CDCl_3$): δ 8.6 (d, *J* = 5 Hz, 2H, Ar), 7.78 (t, *J* =5 Hz, 2H, Ar), 7.52 (d, *J* = 5 Hz, 2H, Ar), 7.33 (d, *J* = 5 Hz, 2H, Ar), 4.37 (t, *J* =5 Hz, 2H, -CH_2) 1.95-1.92 (m, 2H, alkyl chain), 1.67-1.41 (m, 6H, alkyl chain), 0.95 (*t, J* = 7.5, 3H, alkyl chain). ^{13}C NMR (62.5 MHz, $CDCl_3$): δ 177.96, 141.76, 133.91, 128.01, 122.42, 121.2, 114.54, 46.27, 31.51, 27.14, 26.6, 22.67, 14.02.

Formation of 2-bromo-10-hexyl-9-acridone (2a):

To a solution of 10-hexyl-9-acridone (520 mg, 1eq) in 20 ml of $CHCl_3$ under argon atmosphere, N-bromosuccinimide (NBS, 340 mg, 1eq) was added. The reaction was carried out overnight at room temperature. Then $CHCl_3$ was evaporated in a rotary evaporator. The crude product was then diluted with chloroform, washed with KOH 4% solution and water several times until neutral. The organic phase was collected, dried over anhydrous $MgSO_4$. The organic layer was concentrated, and column chromatography was done using petroleum ethers: EtOAc (9:1 v/v) as eluent. Main product is mono-bromo substituted, compound **2a** as a yellow solid (544mg, 80%). ^{1}H NMR (250 MHz, DMSO-d_6): δ 8.36-8.29 (m, 2H, Ar), 7.91-7.73 (m, 4H, Ar), 7.33 (t, *J* =7.5 Hz, 1H, Ar), 4.42-4.36

(t, *J* = 7.5 Hz, 2H, alkyl chain), 1.72-1.69 (d, *J* = 7.5 Hz, 2H, alkyl chain), 1.47-1.15 (m, 6H, alkyl chain), 0.88-0.83 (t, *J* =5 Hz, 3H, alkyl chain). ^{13}C NMR (62.5 MHz, DMSO-d_6): δ 175.75, 141.77, 140.82, 136.97, 135.09, 128.99, 127.23, 123.32, 122.17, 121.97, 119.31, 116.55, 114.07, 45.88, 31.46, 27.24, 26.78, 26.06, 22.59, 14.35.

Formation of 2,7-dibromo-10-hexyl-9-acridone (2b):

To a solution of 10-hexyl-9-acridone (336 mg, 1eq) in 15 ml of DMF, N-bromosuccinimide (854 mg, 4eq) was added in one portion. The temperature was heated until 70-80^{o}C, kept overnight, after which the reaction color became red. After cooling to room temperature, the reaction mixture was washed with water and extracted by dichloromethane for three times. The obtained top organic layer was dried on anhydrous $MgSO_4$. The mixture was concentrated in vacuum and the residue was purified by column chromatography on silica gel (petroleum ethers: DCM (4:1 v/v) as eluent to afford pure product as yellow solid (1.325g, 90%). ^{1}H NMR (250 MHz, $CDCl_3$): δ 8.65 (d, *J* = 2.5 Hz, 2H, Ar), 7.82 (d, *J* =2.5 Hz, 1H, Ar), 7.78 (d, *J* = 2.5 Hz, 1H, Ar), 7.38 (d, *J* = 10 Hz, 2H, Ar), 4.29 (t, *J* = 7.5 Hz, 2H, alkyl chain), 1.97-1.84 (m, 2H, alkyl chain), 1.66-1.26 (m, 6H, alkyl chain), 0.88-0.83 (m, 3H, alkyl chain). ^{13}C NMR (62.5 MHz, $CDCl_3$) δ 175.13, 140.02, 136.73, 129.94, 123.16, 116.75, 114.82, 46.55, 31.45, 27.01, 26.9, 26.49, 22.63, 14.01.

General method for the synthesis of compound A-DPA, A-2DPA and A-2PTz *(Buchwald-Hartwig cross coupling reaction):*

In the Schlenk flask, 2-bromo-10-hexyl-9-acridone or 2,7-dibromo-10-hexyl-9-acridone (1eq) and 4.4′-methoxydiphenyl amine (3eq) or phenothiazine (4eq) were dissolved in distillated toluene under argon atmosphere. The palladium catalyst $Pd(OAc)_2$ (0.2 eq), tri-tert-butylphosphine solution (^{t}Bu)$_3$P (0.2 eq) and sodium-tertbutoxide (10 eq) were added to the mixture reaction. The reaction mixture was stirred at 110^{o}C under argon atmosphere. Reaction mixture was carried out in 24h, then cooled to room temperature and extracted with DCM and water 3 times. The organic layer were collected and dried over anhydrous $MgSO_4$. The crude product was concentrated in rotary evaporator and further purification by silica gel column chromatography.

Formation of 2-(bis(4-methoxyphenyl)amino)-10-hexylacridin-9(10H)-one (A-DPA):

A mixture of 2-bromo-10-hexyl-9-acridone (450mg, 1eq) and 4.4′-dimethoxydiphenylamine (600mg, 2eq) were combined in 15ml of toluene as mentioned in general method. The crude solid was purified by column chromatography using petroleum ethers: EtOAc (9:1 v/v) to afford pure product A-DPA as red orange solid (535mg, 75%). IR (neat, cm^{-1}): 3111, 3066 (aromatic stretch), 1626 (C=O), 1031.5-1350.5 (C-N), 2953.9-2852.9 ($-C_6H_{13}$), 1258.2 (asymmetric C-O-CH_3 stretch). ^{1}H NMR (250 MHz, DMSO-d_6): δ 8.25 (d, *J* = 7.5 Hz, 1H, Ar), 7.77-7.68 (m, 4H, Ar), 7.39-7.22 (m, 2H, Ar), 7.02 (d, *J* =10 Hz, 4H, Ar), 6.91 (d, *J* = 10Hz, 4H, Ar), 4.41 (t, *J*= 5Hz, 2H, alkyl chain), 3.74 (s, 6H, $-OCH_3$), 1.75 (m, 2H, alkyl chain), 1.4-1.6 (m, 6H, alkyl chain), 0.86 (t, *J* = 7.5 Hz, 3H, alkyl chain). ^{13}C NMR (62.5 MHz, DMSO-d_6) δ 143.14, 141.39, 140.73, 126.59, 122.82, 115.5, 55.69, 31.45, 22.6, 14.36. HRMS (ESI+): calculated for $C_{33}H_{34}N_2O_3$ $[M+H]^+$: 507.2569; found: 507.2642.

Formation of 2,7-bis(bis(4-methoxyphenyl)amino)-10-hexylacridin-9(10H)-one (A-2DPA):

A mixture of 2,7-dibromo-10-hexyl-9-acridone (500mg, 1eq) and 4.4′-dimethoxydiphenylamine (1g, 4eq) were reacted in 15ml of toluene as mentioned in general method. The crude solid thus obtained was purified by column chromatography using petroleum ethers: ethyl acetate (4:1 v/v) to obtain A-2DPA as a red solid (540 mg, 50%). IR (neat, cm^{-1}): 3037.6 (aromatic stretch), 1684.2 (C=O), 1049.2-1372.4 (C-N), 2927.8-2832.8 ($-C_6H_{13}$), 1269.4 (asymmetric C-O-CH_3 stretch). ^{1}H NMR (250 MHz, DMSO-d_6) δ 7.67 (dd, J_1 = 2.5-7.5 Hz, 4H, Ar), 7.35 (dd, J_1 = 2.5-7.5 Hz, 2H, Ar), 6.98 (d, *J* =7.5 Hz, 8H, Ar), 6.88 (d, *J* = 7.5 Hz, 8H, Ar), 4.35 (t, *J*=7.5 Hz, 2H, alkyl chain), 3.72 (s, 12H), 1.82-1.67 (m, 2H, alkyl chain), 1.44-1.28 (m, 6H), 0.87-0.82 (t, *J* = 7.5 Hz, 3H, alkyl chain). ^{13}C NMR (62.5 MHz, $CDCl_3$) δ 176.46, 155.6, 142.61, 141.11, 136.44, 129.03, 125.78, 122.71, 118.16, 115.4, 114.77, 55.52, 46.23, 31.49, 27.42, 26.59, 22.64, 14.01. HRMS (ESI+): calculated for $C_{47}H_{47}N_3O_5$ $[M+H]^+$, 734.3516; found: 734.3588.

Formation of 10-hexyl-2,7-di(10H-phenothiazin-10-yl)acridin-9(10H)-one (A-2PTz):

A mixture of 2,7-dibromo-10-hexyl-9-acridone (100mg, 1eq) and phenothiazine (200mg, 4eq) were reacted in 10ml of toluene as mentioned in general method. The crude solid thus obtained was purified by column chromatography using petroleum ethers: ethyl acetate (4:1 v/v) to obtain A-2PTz as a light green solid (192 mg, 90%). IR (neat, cm^{-1}): 3059.9 (aromatic stretch), 1639.2 (C=O), 1049.2-1372.4 (C-N), 2923.9-2852.3 ($-C_6H_{13}$),

737.2 (C-S). ^{1}H NMR (250 MHz, $CDCl_3$): δ 8.88 (s, 1H, Ar), 7.95 (s, 2H, Ar), 7.44 (m, 4H, Ar), 7.25 (m, 2H, Ar), 7.03 (m, 4H, Ar), 6.47 (s, 2H, Ar), 4.66 (m, 2H, alkyl chain), 2.35-2.24 (m, 2H, alkyl chain), 1.75-1.44 (m, 6H, alkyl chain), 1.15-1.06 (m, 3H, alkyl chain). ^{13}C NMR (62.5 MHz, DMSO-d_6) δ 175.88, 144.17, 144.06, 142.54, 141.28, 134.55, 128, 127.85, 127.34, 123.51, 123.44, 120.4, 119.1, 116.89, 116.75, 114.86, 31.16, 22.7, 14.4. HRMS (ESI+): calculated for $C_{43}H_{35}N_3S_2$ $[M+H]^+$, 674.2222; found: 674.2294.

Formation of 2,7-bis(4-(bis(4-methoxyphenyl)amino)phenyl)-10-hexylacridin-9(10H)-one (A-2TPA) by Suzuki coupling reaction:

A mixture of 2,7-dibromo-10-hexyl-9-acridone (300mg, 1eq) and 4-(4,4,5,5-tetramethyl-1,3,2-dioxaborolan-2-yl)-N,N-bis(4-methoxyphenyl)aniline (850mg, 3eq), $Pd(PPh_3)_4$ (158mg, 0.2eq), K_2CO_3 (2.8g, 20eq) and few drops of Aliquat 336 were added in 15ml of toluene. The reaction was carried out in 24h at 110°C. The obtained crude solid was purified by column chromatography using mixture of petroleum ethers: EtOAc (4:1 v/v) to obtain A-2TPA as a yellow solid (303mg, 50%). IR (neat, cm-1): 3037.6 (aromatic stretch), 1647.2 (C=O), 1031.9-1371.1 (C-N), 2958.3-2833.9 (-C6H13), 1259.9 (asymmetric C-O-CH3 stretch). ^{1}H NMR (250 MHz, $CDCl_3$) δ 8.79 (s, 1H, Ar), 7.95 (d, J =7.5 Hz, 1H, Ar), 7.54 (t, J =10 Hz, 5H, Ar), 7.12 (d, J = 7.5 Hz, 8H, Ar), 7.03 (d, J = 10 Hz, 4H, Ar), 6.86 (d, J = 7.5 Hz, 8H, Ar), 4.36 (m, 2H, alkyl chain), 3.82 (s, 12H, alkyl chain), 1.97-0.87 (m, 11H, alkyl chain). ^{13}C NMR (62.5 MHz, DMSO-d6): δ 206.96, 156.29, 140.39, 133.16, 130.67, 127.52, 127.28, 122.22, 120.02, 115.44, 55.69, 31.31, 22.7, 14.1. HRMS (ESI+): calculated for $C_{59}H_{55}N_3O_5$ $[M+H]^+$, 886.4142.

PART 2: DONOR-ACCEPTOR HTMs WITH THIOXANTHONE SPECIES

III.2.1 Introduction

As a part of our continuous interest in developing new HTMs for hybrid perovskite solar cells, herein we report the synthesis and the characterization of thioxanthone derivatives. Thioxanthone has been studied in this work because of its rich chemistry possibilities, facile chemical modification-preparation and low cost. Moreover, the presence of sulfur atoms in its structure could enhance the affinity of HTM towards lead based perovskite layer to increase grain size and passivate coordinately unsaturated Pb(II) ions on the surface[51]. Therefore, they could be prominent candidates for HTMs in PSCs. They are also promising compounds because of their versatile photochemical applications and they have been employed as photo-initiators in polymerization[52–56] and exhibited thermal activated delayed fluorescence property in OLEDs[57–59], voltage stabilizer[60], etc.

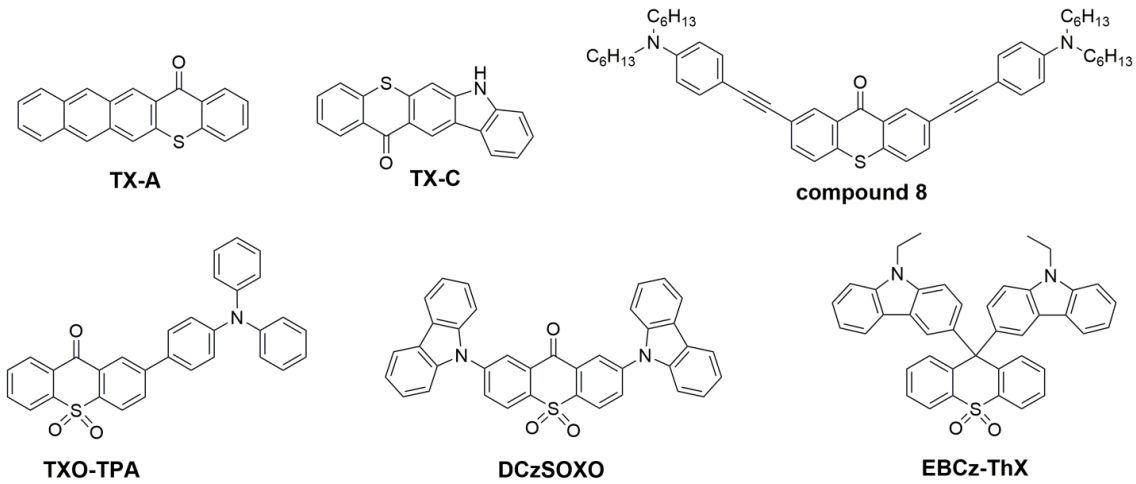

Figure 22 : Representative molecules of Thioxanthone in different applications. The chemical structure of TX-A[52,53], TX-C[55], compound 8[61], TXO-TPA[58], DCzSOXO[57] and EBCz-ThX[59] are reproduced.

In ***Figure 22***, some illustrative examples of thioxanthone-based organic molecules are presented. For example, TX-A, TX-C and compound **8** have been studied as photoinitiators for polymerization. They were constructed by incorporating an electron donor unit such as anthracene, carbazole or tertiary amine directly or indirectly with a π-linker. These visible light absorbing thioxanthone derivatives would combine with suitable hydrogen donor and oxidizing salts which are used to promote cationic polymerization of appropriate monomers. Thioxanthone is classified as type II photoinitiators for free radical polymerization[62]. Furthermore, they are also designed and

employed as thermal activated delayed fluorescence (TADF) materials for OLEDs[57–59]. For example, TXO-TPA, DCzSOZO and EBCz-ThX are such kind of materials. They possess high rate of intersystem crossing and high quantum yield of triplet formation[63,64]. The energy gap between the first singlet and triplet excited state of thioxanthone had been determined to be lower than 0.3 eV[65,66], thus they are possible for high efficient TADF materials.

The geometry of thioxanthone ring is planar[67] and thioxanthone itself can be considered as electron-deficient core, which could be combined with electron donor moiety to form push-pull charge transport materials. These new materials are expected to have appropriate HOMO and LUMO energy level and could match to perovskite layer for a good hole injection. Moreover, the sulfur atom in thioxanthone core acts as moderate electron donor unit or could be oxidized to sulfone unit to enhance electron accepting property. Due to its abundant chemistry ability, thioxanthone and their derivatives have been studied by experimental and theoretical[68,69] methods and allowing them to be used as promising materials in electronic or optoelectronic applications.

In this study, thioxanthone was used as electron acceptor unit. It is combined with various electron donor units and the HOMO-LUMO energy levels of these novel materials would be adjusted. Up to now, there is no study about Thioxanthone and its derivatives as hole transporting materials in PSCs. In addition, by changing from tertiary amine in Acridone (in ***part I***) to sulfur atoms in Thioxanthone, some molecules of two series compounds will be compared and discussed in this section.

III.2.2 Strategy and objectives

The aim of this study is to develop donor-acceptor structure with thioxanthone derivatives, to synthesize and to put investigation in their thermal, photophysical and electrochemical properties. Based on these properties, they could be employed as new hole transporting materials in perovskite solar cells. They were studied based on some following considerations:

- Intramolecular charge transfer due to push-pull effect in D-A molecules.
- Containing sulfur atoms –improving of perovskite/ HTM interfaces.
- Low cost, modifiable structure, facile preparation and purification.

Therefore, thioxanthone could be promising candidate for HTMs in photovoltaic application. The molecular structure of studied compounds is shown in ***Figure 23***.

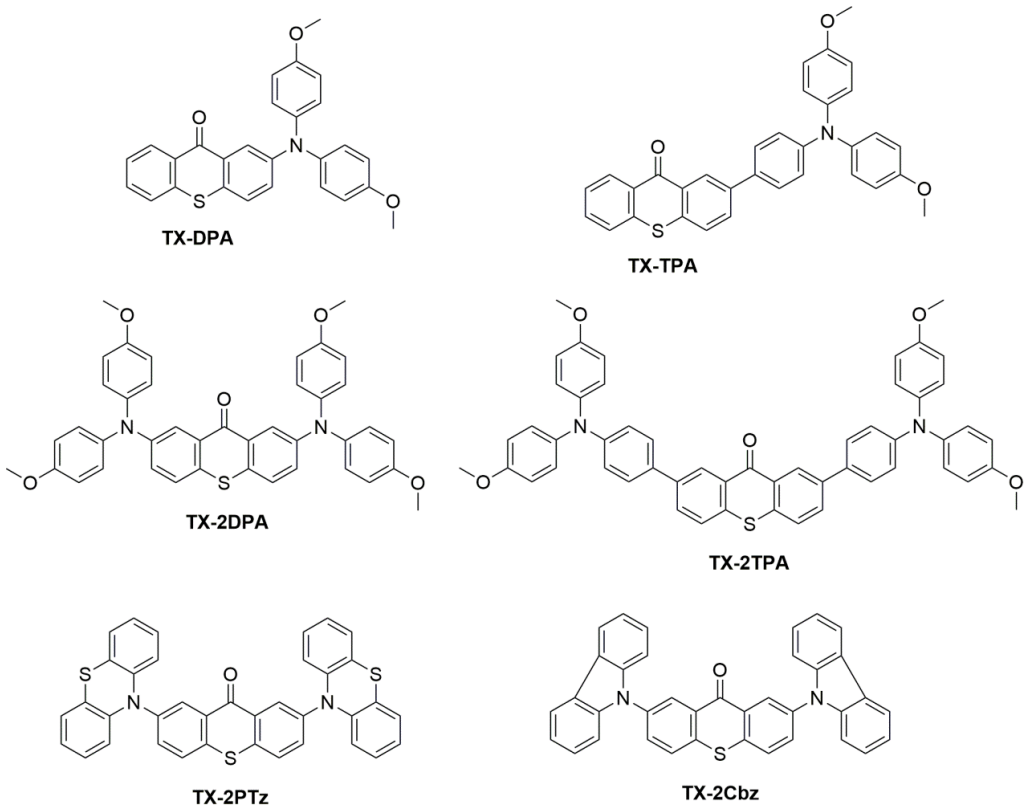

Figure 23: Chemical structure of Thioxanthone derivatives.

By incorporating of various electron donor groups such as 4,4'-dimethoxydiphenylamine (DPA), 4,4'-dimethoxytriphenylamine (TPA), phenothiazine (PTz) and carbazole (Cbz), D-A system (representative are TX-DPA and TX-TPA) and D-A-D system (representative are TX-2DPA, TX-2TPA, TX-2PTz and TX-2Cbz) were constructed and studied. Different features of these compounds such as ICT property, strength of various electron donor group, film morphology and HOMO-LUMO energy determination were fully investigated.

Similar to acridone derivatives, these compounds were synthesized by classical reaction such as Buchwald-Hartwig, Suzuki and Ullman coupling reaction (***Scheme 3***). These final compounds were purified by column purification and some of them could be recrystallized in appropriately solvent. The purity of final materials was confirmed by NMR, HRMS characterization before using as HTMs materials.

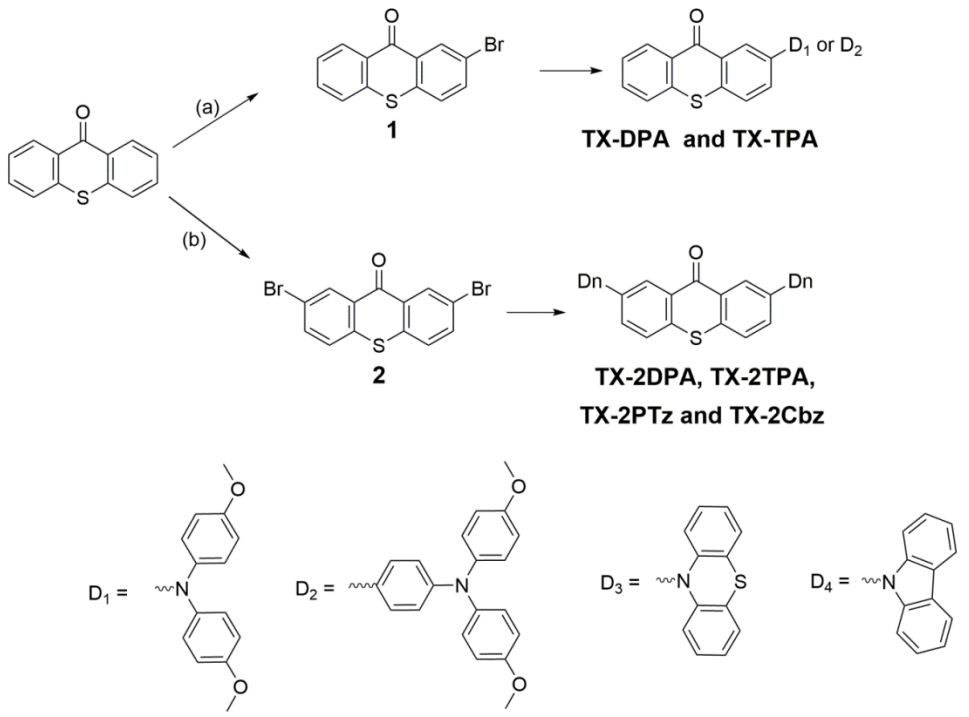

Scheme 3: Synthetic route of Thioxanthone derivatives. Reagents and conditions: (a) NBS, DMF, 70°C, overnight. (b) Br_2, I_2, AcOH 99-100%, 130°C, overnight. Buchwald-Hartwig reaction condition was used to synthesis of TX-DPA and TX-2DPA and TX-2PTz: NaOtBu, $PdCl_2(PPh_3)_4$, Toluene, 110°C, 24h. Suzuki coupling reaction was used to synthesis of TX-TPA and TX-2TPA: $Pd(PPh_3)_4$, Na_2CO_3, Toluene, 110°C, 24h. Ullman coupling reaction was used to synthesis of TX-2Cbz: Na_2CO_3, CuI, 18-crown-6, nitrobenzene, 160°C, 24h.

Thioxanthone is almost insoluble in many organic solvents[70]. It can be dissolved in concentrated sulfuric acid at ambient temperature to give a yellow colored liquid with intense green fluorescent or it can be totally dissolved in acetic acid at high temperature (130°C) for bromination. Because of very low solubility, monobromo-thioxanthone (**1**) was obtained in low efficiency ~ 29% by DMF at 70°C. Starting materials is still remained. Otherwise, dibromo-thioxanthone (**2**) has been tried in various conditions such as NBS/H_2SO_4/CF_3COOH or Br_2/$FeCl_3$/$CHCl_3$ but none of them are efficient. Finally, this bromination was successful (52%) with adding a small amount of iodine as catalyst and the reaction mixture was refluxed at 130°C in glacial acetic acid for 24h. Then, final compounds were synthesized by classical coupling reactions in optimized conditions determined in previous chapter. These target compounds were much soluble due to presence of methoxy groups (-OCH_3) in TX-(2)DPA and TX-(2)TPA. In case of TX-2PTz and TX-2Cbz, after purification by column chromatography, they were recrystallized in toluene to obtained pure yellow crystals.

III.2.3 Results and discussion

III.2.3.1 Thermal properties

Thermal stability was characterized by TGA and DSC in order to determine to determine decomposition temperature (T_d 5% weight loss) and glass transition T_g, respectively. All of them show high thermal stability (>290°C) which could avoid decomposition during electronic device fabrication. The higher molecular weight and higher rigid structure is, the higher decomposition temperature is. Similarly, the T_g values are increased from TX-DPA to TX-2Cbz which can promote the formation of amorphous films. All data are summarized in ***Table 1***.

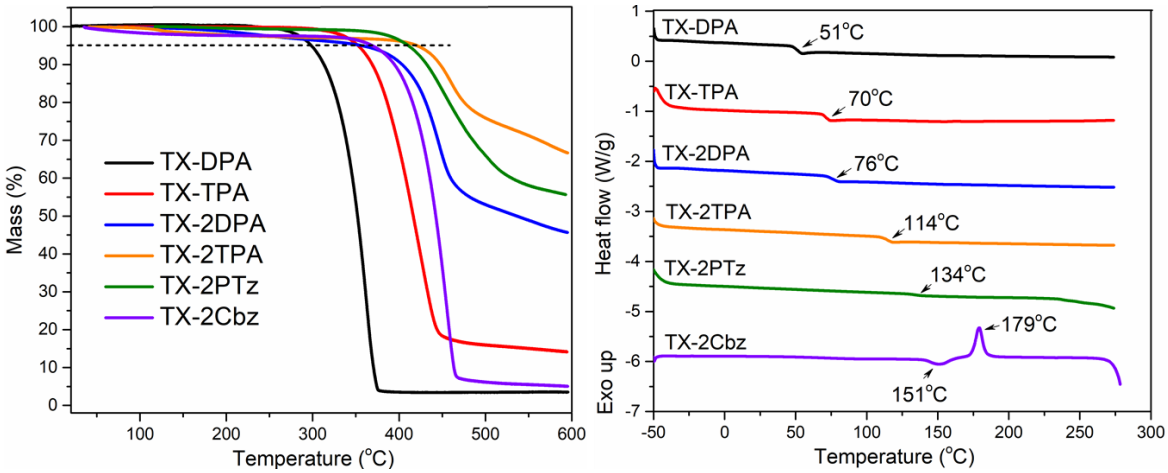

Figure 24: TGA (left) and DSC (right) curves of studied Thioxanthone molecules. Glass transition temperature Tg is obtained from the onset values of DSC and decomposition temperature Td is recorded by 5% weight loss in TGA.

To understand the thermal properties of all thioxanthone-amine derivatives at the molecular level, the ground state geometries of their structurewere calculated and optimized by modellisation DFT (***Figure 25***). In previous studied, the geometry of thioxanthone core is rather planar[67]. Diheral angles and bond distances between the thioxanthone core and the substituted groups were found to be dependent on the nature of the functional groups, in particular, substituted electron donor groups.

Double substituted groups TX-2DPA and TX-2TPA had nearly the same dihedral angles as TX-DPA and TX-TPA, approximately 30-35°. However, rigid carbazole and phenothiazine groups significantly increase the dihedral angles (from about 32° in TX-2DPA to 54° in TX-2Cbz and 97° in TX-2PTz). This is agreement with the higher T_g of TX-2PTz (134°C) and TX-2Cbz (151°C) in comparison with T_g of TX-2DPA (76°C) and TX-2TPA (114°C).

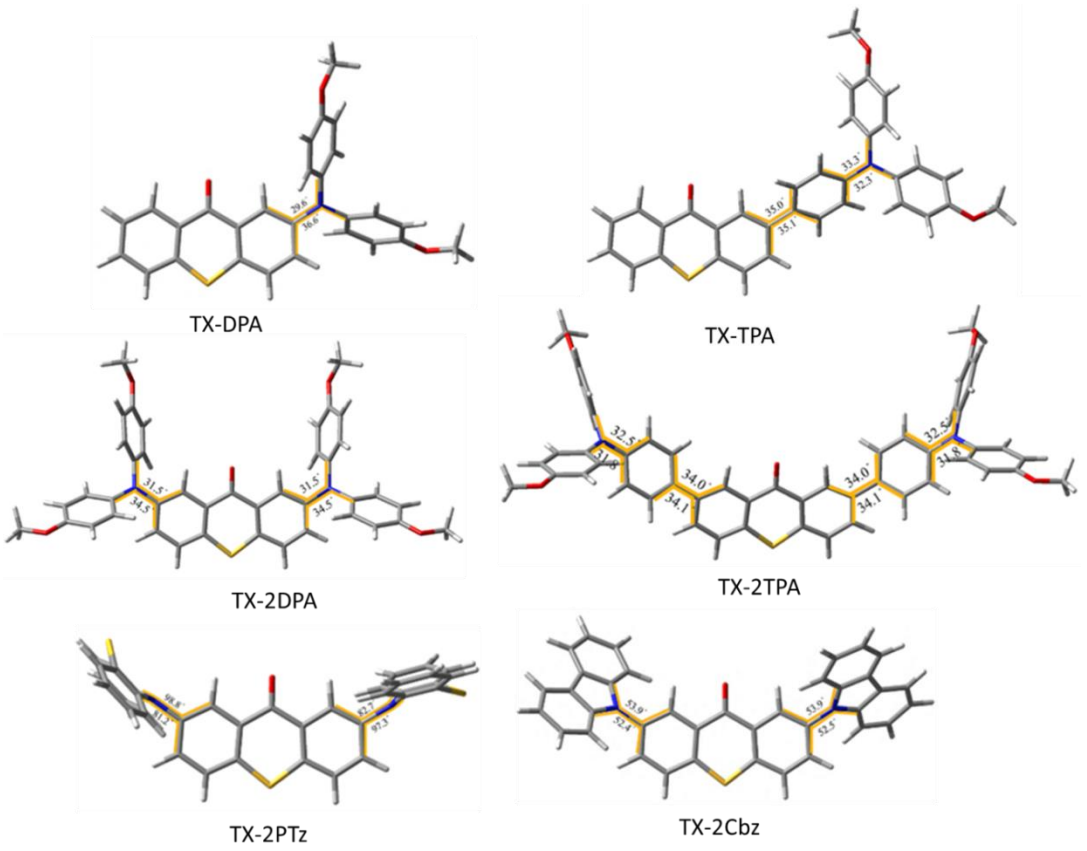

Figure 25: Optimized structures along with the dihedral angles (o) of all Thioxanthone derivatives simulated by B3LYP/6-31G(d,p) in gas phase.

All compounds possess 3D structure, which could avoid in more extent its crystallization in the solid thin film.

III.2.3.2 Optical properties

Optical properties of the synthesized compounds were studied by absorption-emission spectroscopy in solution and on neat film (***Figure 26***). All compounds have strong absorption bands located in the UV domain and other weaker absorption bands can be observed at the longer wavelength in the visible region.

The absorption band at 453 nm of TX-DPA and 480 nm of TX-2DPA in solution and in neat film could be attributed to ICT from the diphenylamine donor to the thioxanthone core. However, ICT band are blue-shifted to 353 nm and 362 nm in case of less conjugated molecules as TX-TPA and TX-2TPA, respectively. These differences could be explained by reducing donating strength of TPA compared to DPA, which was briefly discussed in Acridone-based section. Similarly, the donating ability of carbazole and phenothiazine are general weaker than that of diphenylamine, thus absorption peaks are shifted in shorter wavelength.

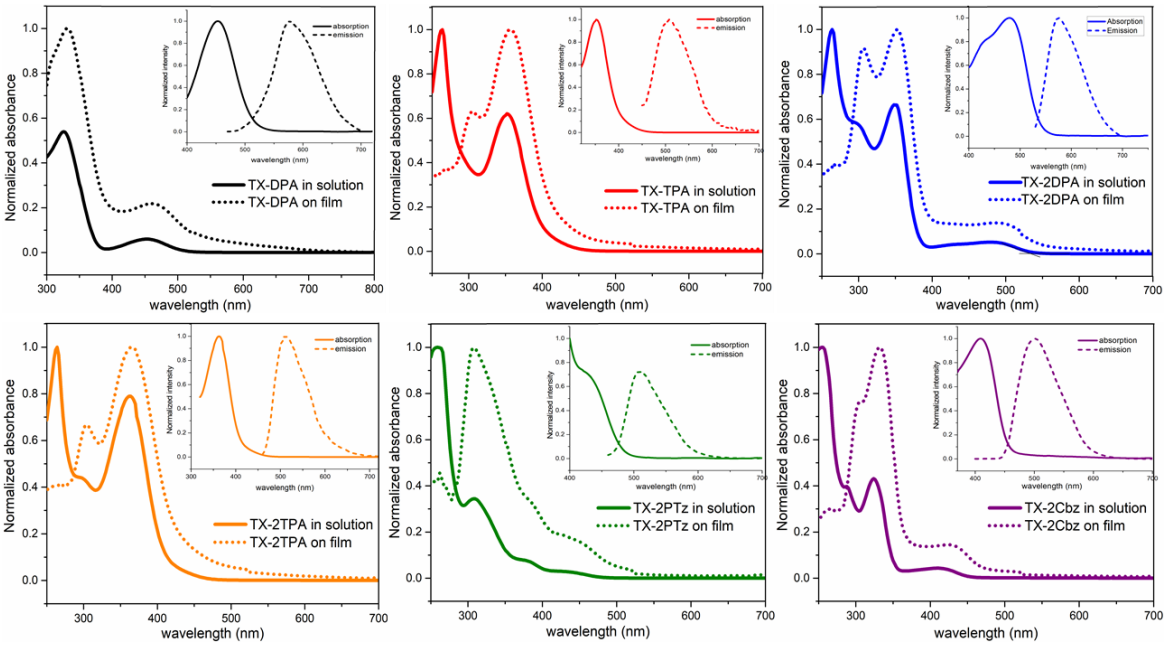

Figure 26: Absorption spectra of studied thioxanthone molecules in solution (dashed line) and on film (dot line) and emission spectra (inset)

No π-π stacking effect was demonstrated by comparison between absorption signal in solution and on film. From the onset values of the absorption maxima peak, the optical band gap of these molecules was calculated and the values were summarized in ***Table 6***. Fluorescence spectra were examined in dilute dichloromethane solution and all compounds emitted in green region with emission maxima in range of 501-576 nm. Their λ_{max} emissions are almost identical. For TX-DPA, TX-TPA, TX-2DPA, TX-2TPA and TX-2Cbz their Stokes shift were considered about 100-150 nm, which can be explained by their high flexibility in the molecular structure. In contrary, due to high steric hindrance of phenothiazine, small Stokes shift value is about 80 nm and 90 nm for TX-2PTz and TX-2Cbz, respectively.

Additionally, theoretical absorption spectra of thioxanthone derivatives were also studied by DFT calculation (***Figure 27***). In simulated absorption spectra, these compounds show main absorption peaks around 250-450 nm which assigned to the π-π^* transition and ICT transition. In case of TX-DPA, TX-2DPA and TX-2Cbz, their spectra appear minor peaks in the range of 420-550 nm, which is also attributed to ICT transition. These calculated results are in good accordance to experimental spectra.

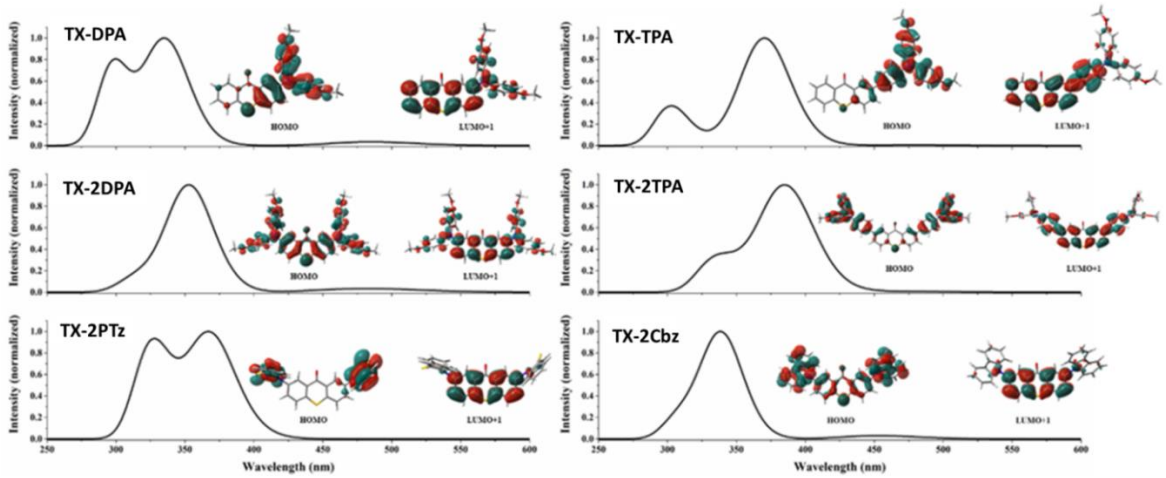

Figure 27: Simulated absorption spectra of studied Thioxanthone derivatives calculated by TD-B3LYP/6-31G(d,p) in gas phase.

Consideration of these orbitals in ***Figure 27***, electron distribution of TX-DPA, TX-2DPA, TX-2TPA and TX-2Cbz are localized in whole molecules in HOMO states which could be efficient for hole transfer process. Due to its less conjugation, the electron density of TX-2TPA is less distributed through thioxanthone core. This can impact to internal charge transfer of this compound. Especially, in case of TX-2PTz, two phenothiazine are almost perpendicular to thioxanthone which can interrupt to electronic coupling in TX-2PTz.

Their excitation energies and the corresponding oscillator strength are given in ***Table 5***.

Structure	λ_{cal} (nm)	*f*	Composition (%)	Character
TX-DPA	485	0.0170	HOMO→LUMO (99%)	ICT
	347	0.0002	HOMO-3→LUMO (93%)	n→π*
	344	0.2141	HOMO-1→LUMO (25%),	ICT, π→π*
			HOMO→LUMO+1 (70%)	ICT, π→π*
	333	0.1217	HOMO-1→LUMO (66%)	ICT, π→π*
			HOMO→LUMO+1 (19%)	ICT, π→π*
			HOMO→LUMO +2 (10%)	π→π*
TX-TPA	480	0.0039	HOMO→LUMO (99%)	ICT
	371	0.7401	HOMO→ LUMO+1 (97%)	ICT, π→π*
	350	0.0672	HOMO-1→LUMO (94%)	ICT, π→π*

	344	0.0004	HOMO-5→LUMO (31%)	n→π*
			HOMO-4→LUMO (65%)	n→π*
TX-2DPA	498	0.0196	HOMO→LUMO (99%)	ICT, π→π*
	459	0.0146	HOMO-1→LUMO (99%)	ICT, π→π*
	355	0.7400	HOMO→ LUMO+1 (96%)	π→π*
	348	0.0008	HOMO-6→LUMO (45%)	ICT, π→π*
			HOMO-5→LUMO (52%)	ICT, π→π*
TX-2TPA	479	0.0055	HOMO→LUMO (99%)	ICT
	468	0.0039	HOMO-1→LUMO (99%)	ICT
	387	1.2012	HOMO→ LUMO+1 (92%)	ICT, π→π*
	369	0.1584	HOMO-1→ LUMO+1 (93%)	ICT, π→π*
TX-2PTz	543	0.0000	HOMO→LUMO (97%)	ICT
	539	0.0000	HOMO-1→LUMO (97%)	ICT
	389	0.0000	HOMO→ LUMO+1 (90%)	ICT
	388	0.0001	HOMO-1→ LUMO+1 (88%)	ICT
TX-2Cbz	459	0.0102	HOMO→LUMO (99%)	ICT
	442	0.0063	HOMO-1→LUMO (99%)	ICT
	390	0.0000	HOMO-2→LUMO (98%)	ICT
	390	0.0001	HOMO-3→LUMO (98%)	ICT
	348	0.0006	HOMO-7→LUMO (95%)	n→π*
	340	0.4664	HOMO→ LUMO+1 (95%)	ICT, π→π*

Table 5: The excitation energies, oscillator strengths (f) and transition compositions for some lowest states by TD-B3LYP/6-31G(d,p) in gas phase using C-PCM.

III.2.3.3 Electrochemical properties

Cyclic voltammetry has been employed to investigate the redox behavior of studied thioxanthone derivatives and to determine corresponding HOMO and LUMO energy levels. The CV of these molecules are shown in ***Figure 28*** and related data are summarized in ***Table 6***.

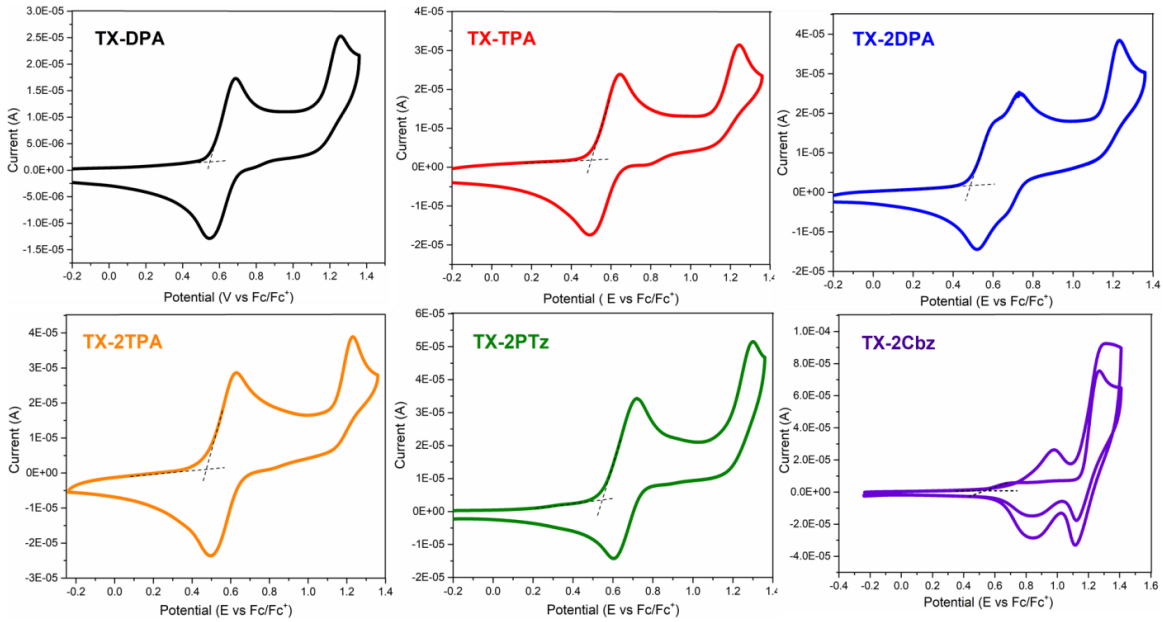

Figure 28: Cyclic voltammogram of studied thioxanthone molecules.

All compounds show multiple oxidation processes. The first oxidation potential could be belong to the formation of radical cation of the diphenylamine (0.55V and 0.48 V for TX-DPA and TX-2DPA), triphenylamine (0.49 V and 0.47 V for TX-TPA and TX-2TPA), phenothiazine (0.54 V) or carbazole (0.53 V) moieties. Thioxanthone core was oxidized at higher potential. CV of TX-2DPA shows two close oxidation peaks due to high conjugated molecule and strong D-A interaction between DPA and thioxanthone core. However, CV of TX-2TPA and TX-2PTz record only one oxidation peak. This could explain by less conjugated molecule, weak D-A interaction of these molecules. Especially, it shows more accurate in case of TX-2PTz where phenothiazine units are nearly perpendicular to thioxanthone. Therefore, TPA units or PTz units could be electrochemically oxidized at the same time. Their current peaks showed double than that of thioxanthone and that hypothesis have to be be confirmed.

Except TX-2Cbz, all molecules showed electrochemical stability in solution after a number of scan cycles. In case of TX-2Cbz, carbazole moieties were polymerized when increasing number of scans. These molecules have very close oxidation potentials with onset values in the range of 0.47-0.55 V versus Fc/Fc^+. The corresponding HOMO values of these compounds were determined from the oxidation onset potential values respect to Fc/Fc^+ and listed in ***Table 6***. Their LUMO values were determined by the optical band gap and the corresponding HOMO values.

In order to better understanding the optical properties and to evaluate the frontier molecular orbitals, energy levels of these studied compounds, the calculation method was carried out on the Gaussian09 program package by using DFT and time-dependent DFT methods.

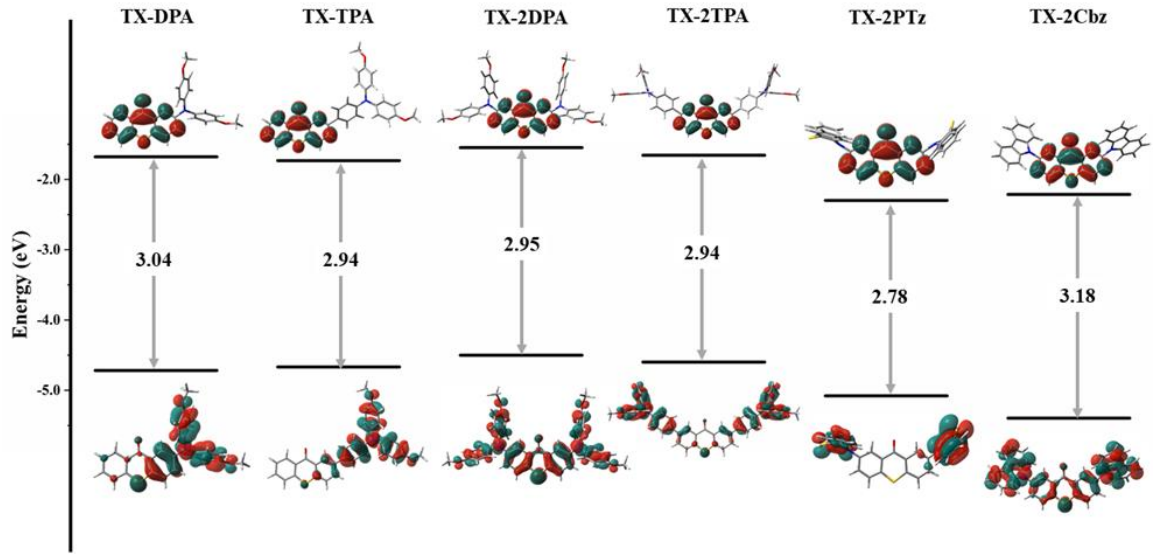

Figure 29: Frontier molecular energy diagram of all molecular structures calculated by B3LYP/6-31G(d,p) level in gas phase.

As displayed in ***Figure 29***, all molecules adopt twisted structure in their optimized structure, except the case of TX-2PT which adopts a nearly orthogonal D-A conformation. The LUMOs of all compounds are localized on the thioxanthone backbone due to the moderate electron-acceptor character of the carbonyl group while the HOMOs are mainly distributed on the electron-donor moieties. The calculated frontier HOMO-LUMO values are given in ***Table 6***. Interestingly, HOMO states of TX-DPA, TX-2DPA and TX-2Cbz are located over the whole molecule, which is prominent for charge transporting capability. In contrary, the HOMO of TX-2PTz is only dispersed on the phenothiazine moieties, due to its nearly perpendicular conformation between thioxanthone core and phenothiazine, with torsion angle 82.8-97.3^{o}. This could affect to hole mobility of this molecule.

III.2.3.4 Morphology and hydrophobicity

Film morphology of these molecules has been studied by AFM measurements. All of these molecules showed smooth films with average roughness in the range of 0.29 nm to 0.44 nm, except TX-2Cbz is higher roughness value of 1.76 nm due to low solubility in organic solvents. The related average roughness values are listed in ***Table 6***. As observed,

smooth films of TX-DPA, TX-2DPA, TX-TPA and TX-2TPA could be provided good interface interaction to perovskite layer. For TX-2PTz and TX-2Cbz, they are low solubility in Chlorobenzene due to rigid structure and lack of methoxy group. However, due to high glass transition, they can stay in amorphous structure so their morphology can be optimized by others solvents to improve film quality.

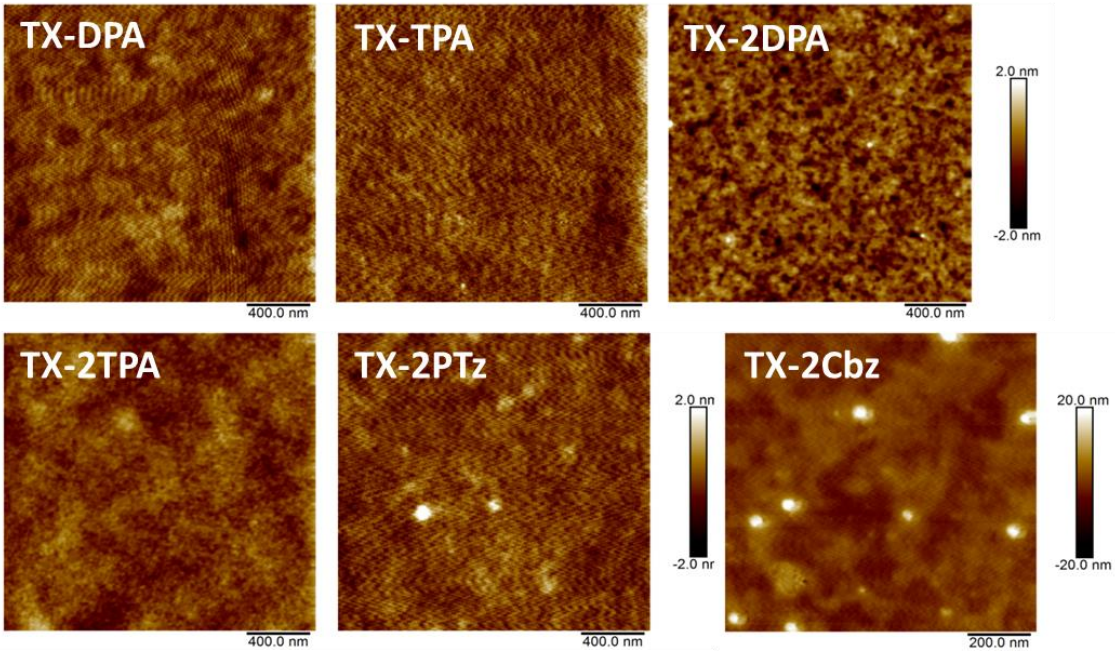

Figure 30: AFM images of studied thioxanthone molecules coated on glass substrate.

For HTMs, they should possess hydrophobicity to protect the perovskite layer out of moisture. Therefore, contact angle measurement was employed and these corresponding angle values of these films are shown in ***Figure 31***.

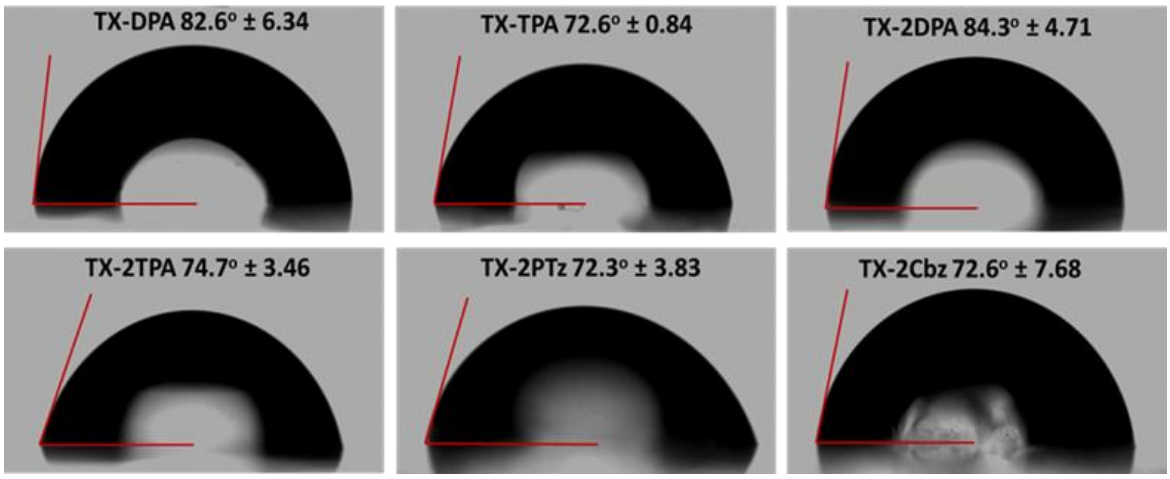

Figure 31: Contact angle measurement of water drop on studied thioxanthone molecules films.

All these molecules are hydrophobic and the average angle contact is in the range of 72.3° to 84.3°. These values could be increased by improving the film quality of these materials. Thereafter, these new materials could isolate perovskite layer out of moisture and avoid perovskite's degradation.

Compounds	T_g (^oC)	T_d (^oC)	λ_{abs} onset (nm)	λ_{abs} max (nm)	λ_{emiss} max (nm)	E_g (eV)	E^{onset} (eV)	E_{HOMO} (eV)	E_{LUMO} (eV)	R_q (nm)
TX-DPA	51	297	509	325, 453	576	2.43 (3.04)	0.55	-5.35 (-4.72)	-2.92 (-1.68)	0.358
TX-TPA	70	349	400	263, 353	508	3.10 (2.94)	0.49	-5.29 (-4.67)	-2.19 (-1.73)	0.294
TX-2DPA	76	355	533	262, 298 349, 480	575	2.32 (2.95)	0.48	-5.28 (-4.50)	-2.97 (-1.55)	0.439
TX-2TPA	114	418	409	263, 295, 362	510	3.03 (2.94)	0.47	-5.27 (-4.60)	-2.24 (-1.66)	0.304
TX-2PTz	134	408	482	259, 307 378, 427	508	2.57 (2.78)	0.54	-5.34 (-5.08)	-2.77 (-2.30)	0.357
TX-2Cbz	151	365	453	254, 288 323, 409	501	2.74 (3.18)	0.53	-5.33 (-5.4)	-2.59 (-2.21)	1.76

Table 6: Summary of thermal, photophysical, electrochemical data of thioxanthone derivatives. Value of optical bandgap E_g was determined by absorption onset or intersection between absorption and emission spectra. The calculated values of E_g. E_{HOMO} and E_{LUMO} are given in parenthesis. The average roughness R_q were determined from AFM measurement.

III.2.4 Comparison between Acridone and Thioxanthone molecules

The physical properties of acridone and thioxanthone molecules have been discussed in previous section. Here, the comparison between some molecules of Acridone (A-DPA, A-2DPA and A-2TPA) and Thioxanthone (TX-DPA, TX-2DPA and TX-2TPA) will be studied (***Figure 32***). By changing of the tertiary amine function in Acridone to sulfur atoms in thioxanthone, their properties would be changed.

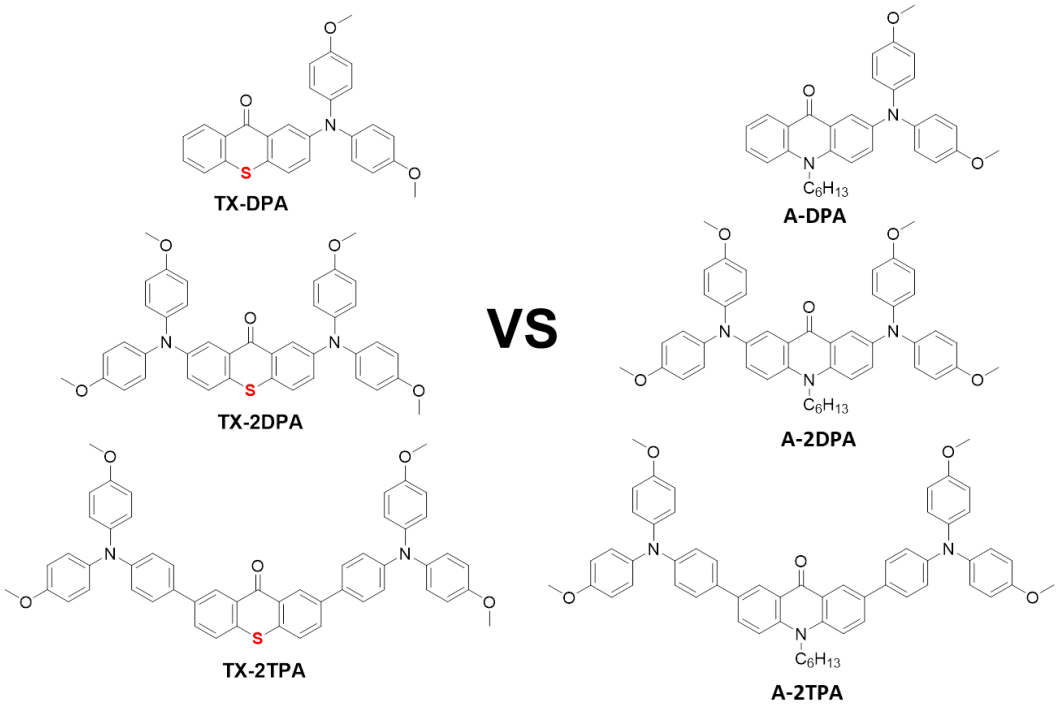

Figure 32: The comparison between Thioxanthone molecules (TX-DPA, TX-2DPA and TX-2TPA) and Acridone molecules (A-DPA, A-2DPA and A-2TPA).

The optical properties of these molecules have been compared (***Figure 33***). All of them exhibit nearly the same absorption spectra. For A-DPA, A-2DPA, TX-DPA and TX-2DPA, strong ICT has been observed in visible region while weak ICT has been recorded for A-2TPA and TX-2TPA.

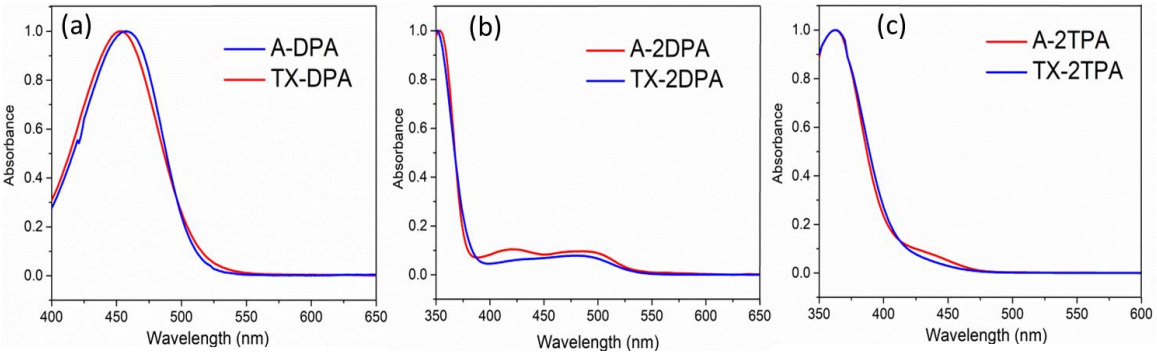

Figure 33: Comparison of absorption spectra of selected Acridone-Thioxanthone molecules.

By comparison of electron distribution in frontier HOMO orbitals of these molecules (***Figure 34***), the DFT calculation confirmed the trend observed in the optical properties. Thus, electron density are localized in whole molecule of A-DPA, A-2DPA, TX-DPA and TX-2DPA. As mentioned above, they are more conjugated molecules and strong D-A interaction. This related to ICT character and enhanced for hole mobility of these molecules. In contrast, electron distribution of HOMO orbitals are less concentrated in acridone core and thioxanthone core of A-2TPA and TX-2TPA. This affected to ICT and reduced charge transport property of these molecules.

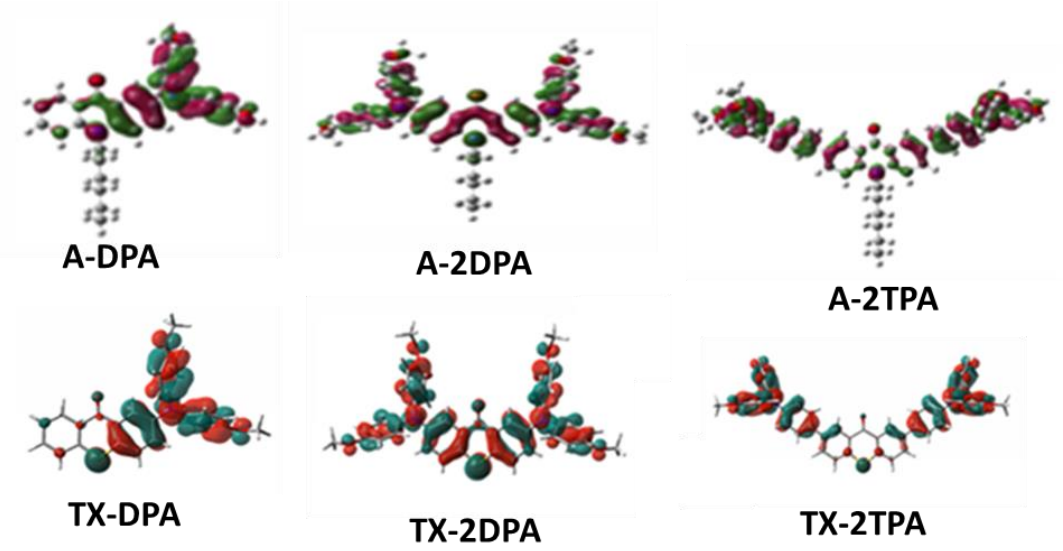

Figure 34: Comparison of simulated electron distribution in HOMO states of these Acridone-Thioxanthone molecules.

The electrochemical behavior of these molecules are nearly the same (***Figure 35***). However, for thioxanthone derivatives, they were oxidized in higher potential compared to acridone derivatives. This could be explained by the presence of N-H group or S atom in acridone core or thioxanthone one respectively. In fact, thioxanthone core is oxidized at 1.34 V[71] compared to 0.85V of acridone core.

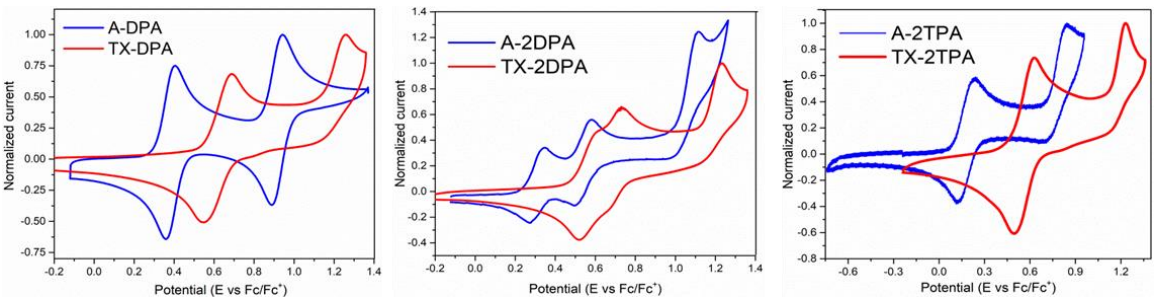

Figure 35: Comparison of absorption spectra of these Acridone-Thioxanthone molecules.

Therefore, they lead to different electrochemical properties of final compound. They also indicate that the electron donating ability of Acridone molecules are stronger than that of Thioxanthone molecules.

From energy aligment of these Acridone-Thioxanthone molecules to perovskite, their HOMO energy levels are all located above valence band of perovskite. However, HOMO energy levels of Thioxanthone molecules are closer to perovskite than Acridone molecules. This could be more efficient for charge transfer processes.

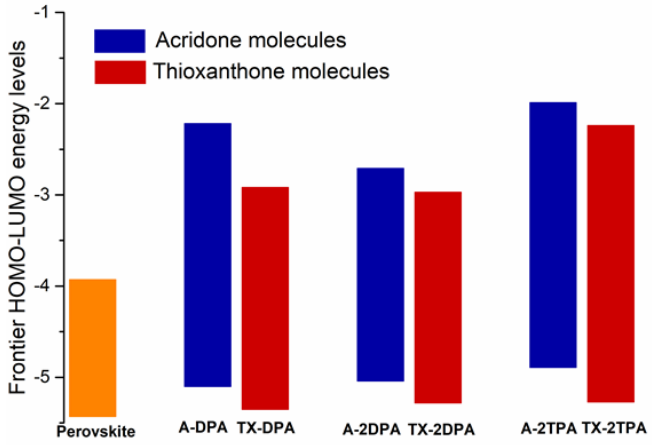

Figure 36 : Energy aligment of these Acridone-Thioxanthone molecules to perovskite.

Film morphology has been studied by AFM measurements and smooth films with small roughness were observed. However, due to the presence of long alkyl chain in Acridone molecules, a more hydrophobic surface was noticed than for surface with Thioxanthone molecules. On the other hand, thioxanthone compounds contain sulfur atoms which could have strong interaction with perovskite and improve perovskite/HTM interface.

To summarize, comparison between Acridone molecules and Thioxanthone molecules, reveals some advantages and disadvantages for HTM and PSCs as well. Acridone molecules exhibit strong electron donating ability, ICT and more hydrophobic. Whereas Thioxanthone molecules express good morphology, better compatibility in energy levels and interface contact to perovskite. Therefore, for photovoltaic application, they could be optimized as HTMs in PSCs by studying of thickness HTMs, amount of additives and thin film processing.

III.2.5 Conclusion and perspective

Thioxanthone derivatives have been designed and synthesized as new HTMs for PSCs from cheap precursor and short-step preparation. Thermal, optical, morphological and electrochemical properties have been investigated and some desirable properties were highlighted as new HTMs. The HOMO-LUMO energy levels of thioxanthone molecules are compatible to perovskite layer which support for holes collection and injection from perovskite to metal electrode. By these results, they indicated that these thioxanthone derivatives adopt all requirements of efficient HTMs for PSCs. Furthermore, these novel materials are under preparation and optimization as new HTMs in PSCs.

III.2.6 Experimental section

Formation of 2-bromo-9H-thioxanthen-9-one (1)

In the 100ml of round-bottom flask, thioxathen-9-one (2g, 1eq), NBS (6.7g, 4 eq) and 20 ml of DMF were added in one portion. The reaction was kept at 70^{o}C overnight and the color changed from yellow to red. When the reaction was quenched, the crude solution was extracted 3 times by distillated water and diethyl ethers to remove DMF. Then, the mixture was removed solvents and concentrated. Finally, the crude product was purified by column chromatography by eluent petroleum ethers: dichloromethane (3:2 v/v). The desired product was then recrystallized in toluene to obtain yellow-needle crystals (0.8g, 30% yield). ^{1}H NMR (250 MHz, $CDCl_3$) δ (ppm): 8.72, 8.71 (d, *J* =2.5 Hz, 1H), 8.61, 8.57 (dd, *J* =10 Hz, 1H), 7.71- 7.42 (m, 5H). ^{13}C NMR (62.5 MHz, $CDCl_3$) δ (ppm) 178.77, 136.85, 136.02, 135.23, 132.60, 132.45, 130.46, 130, 128.84, 127.56, 126.62, 126.07, 120.26.

Formation of 2,7-dibromo-9H-thioxanthen-9-one (2)

In the 3-neck round bottom flask, thioxanthen-9-one (2g, 1eq), Br_2 (3ml, 4eq), I_2 (29mg, 0.2% eq) and 30ml of glacial acetic acid were added in one portion. The reaction was condensed in 2 days at 120^{o}C (or until Br_2 solution was consumed). The reaction was quenched by water and continued stirring in 30 min. The mixture was extracted several times by water and dichloromethane until neutral. The organic phase was collected, dried over $MgSO_4$ and concentrated. Then the crude product was recrystallized in toluene to obtain yellow-needle crystals (1.8g, 52% yield). ^{1}H NMR (250 MHz, $CDCl_3$) δ (ppm): 8.75, 8.74 (d, *J* =2.5 Hz, 1H), 7.77-7.72 (d, *J* =12.5 Hz, 1H), 7.49, 7.46 (d, *J* = 7.5 Hz, 1H). ^{13}C NMR (62.5 MHz, $CDCl_3$) δ 180, 136.2, 135.9, 134.4, 133.1, 131.6, 121.3.

General method 1 for the synthesis of compound TX-DPA, TX-2DPA and TX-2PTz *(Buchwald-Hartwig coupling reaction)*

In the Schlenk flask, 2-bromo-9H-thioxanthen-9-one or 2,7-dibromo-9H-thioxanthen-9-one (1eq) and 4.4′-methoxydiphenyl amine were dissolved in distillated toluene under argon atmosphere. The palladium catalyst $PdCl_2(PPh_3)_4$ (0.2 eq) and sodium-tert-butoxide (10 eq) were added to the mixture reaction. The reaction mixture was stirred under argon atmosphere while the temperature was slowly raised to 110^oC. Reaction mixture was kept for 1 day, then cooled to room temperature and extracted with DCM followed by water wash 3 times. All organic layers were combined and dried on $MgSO_4$ and evaporated to get the crude product which was further purified by silica gel column chromatography.

Formation of 2-(bis(4-methoxyphenyl)amino)-9H-thioxanthen-9-one (TX-DPA)

A mixture of 2-bromo-9H-thioxanthen-9-one (300mg, 1eq) and 4.4′-dimethoxydiphenylamine (480mg, 2eq), $PdCl_2(PPh_3)_4$ (46mg, 0.2eq) and NaOtBu (1g, 10eq) were reacted in 15ml of toluene as mentioned in general method. The crude solid thus obtained was purified by column chromatography using petroleum ethers: ethyl acetate (4:1 v/v) to obtain a yellow solid (389mg, 86% yield). ^1H NMR (250 MHz, DMSO-d_6) δ 8.39, 8.35 (d, *J* =10 Hz, 1H,), 7.83-7.62 (m, 4H), 7.23, 7.18 (d, *J* = 12.5 Hz, 1H), 7.13, 7.1 (d, *J* = 7.5 Hz, 4H), 6.98, 6.94 (d, *J* =10 Hz, 4H), 6.81, 6.77 (dd, 1H), 3.76 (s, 6H). ^{13}C NMR (62.5 MHz, DMSO-d_6) δ 178.85, 156.82, 148.08, 139.71, 138.46, 137.28, 133.09, 129.56, 127.68, 124.92, 115.68, 55.72.

Formation of 2,7-bis(bis(4-methoxyphenyl)amino)-9H-thioxanthen-9-one (TX-2DPA)

A mixture of 2,7-dibromo-9H-thioxanthen-9-one (200mg, 1eq) and 4.4′-dimethoxydiphenylamine (386mg, 3eq), $PdCl_2(PPh_3)_4$ (28mg, 0.1eq) and NaOtBu (520mg, 10eq) were reacted in 15ml of toluene as mentioned in general method. The crude solid thus obtained was purified by column chromatography using petroleum ethers: ethyl acetate (9:1 v/v) to obtain a red solid (189mg, 50% yield). ^1H NMR (250 MHz, DMSO-d6) δ 7.66, 7.65(d, *J* =2.5 Hz, 1H), 7.61-7.57 (m, 1H), 7.19-7.15 (d, *J* = 10 Hz, 1H), 7.1, 7.07 (d, *J* = 7.5 Hz, 4H), 6.95, 6.92 (d, *J* =7.5 Hz, 4H,), 3.75 (s, 6H). ^{13}C NMR (62.5 MHz, DMSO-d_6) δ 184.41, 156.76, 147.76, 139.72, 129, 127.62, 115.63, 55.71.

Formation of 2,7-di(10H-phenothiazin-10-yl)-9H-thioxanthen-9-one (TX-2PTz)

A mixture of 2,7-dibromo-9H-thioxanthen-9-one (200mg, 1eq) and phenothiazine (325mg, 3eq), $PdCl_2(PPh_3)_4$ (38mg, 0.1eq) and NaOtBu (520mg, 10eq) were reacted in 15ml of toluene as mentioned in general method. The crude solid thus obtained was purified by column chromatography using petroleum ethers: ethyl acetate (9:1 v/v) to obtain a yellow solid (300mg, 90% yield). ^{1}H NMR (250 MHz, $CDCl_3$) δ 8.66 (d, J = 2.5 Hz, 1H), 7.81 (d, J = 10 Hz, 1H), 7.67, 7.65 (dd, J_1 = 2.5Hz, J_2 = 2.5Hz, 1H), 7.14 (dd, J_1 = 2.5Hz, J_2 = 2.5Hz, 2H), 6.93 (m, 4H), 6.46 (dd, J_1 = 2.5Hz, J_2 = 2.5Hz, 2H). ^{13}C NMR (62.5 MHz, $CDCl_3$) δ 178.76, 143.46, 140.59, 135.39, 133.22, 130.52, 129.76, 128.64, 127.3, 127.02, 123.47, 123.09, 118.02. HRMS (ESI-MS): calculated for $C_{37}H_{22}N_2OS_3$ $[M+H]^+$, 607.0894; found: 607.0967.

General method 2 for the synthesis of compound TX-TPA and TX-2TPA *(Suzuki coupling reaction)*

In the Schlenk flask, 2-bromo-9H-thioxanthen-9-one or 2,7-dibromo-9H-thioxanthen-9-one (1eq) and 4-methoxy-N-(4-methoxyphenyl)-N-(4-(4,4,5,5-tetramethyl-1,3,2-dioxaborolan-2-yl)phenyl)aniline were dissolved in distillated toluene under argon atmosphere. The palladium catalyst $Pd(PPh_3)_4$ (0.2 eq) and K_2CO_3 (10 eq) were added to the mixture reaction. The reaction mixture was stirred under argon atmosphere while the temperature was slowly raised to 110^{o}C. Reaction mixture was kept for 1 day, then cooled to room temperature and extracted with DCM followed by water wash 3 times. All organic layers were combined and dried on $MgSO_4$ and evaporated to get the crude product which was further purified by silica gel column chromatography.

Formation of 2-(4-(bis(4-methoxyphenyl)amino)phenyl)-9H-thioxanthen-9-one (TX-TPA)

A mixture of 2-bromo-9H-thioxanthen-9-one (300mg, 1eq), 4-methoxy-N-(4-methoxyphenyl)-N-(4-(4,4,5,5-tetramethyl-1,3,2-dioxaborolan-2-yl)phenyl)aniline (880mg, 2eq), $Pd(PPh_3)_4$ (237mg, 0.2eq) and K_2CO_3 (1.42g, 10eq) were reacted in 20ml of toluene as mentioned in general method. The crude solid thus obtained was purified by column chromatography using petroleum ethers: ethyl acetate (4:1 v/v) to obtain a yellow solid (290mg 54% yield). ^{1}H NMR (250 MHz, DMSO-d_6) δ 8.6 (d, J = 2.5 Hz, 1H), 8.46 (d, J = 7.5 Hz, 1H), 8.0 (dd, J = 10Hz, 1H), 7.86-7.72 (m, 3H), 7.61-7.54 (m, 3H), 7.07 (d, J=7.5 Hz, 4H), 6.92 (d, J = 7.5 Hz, 4H), 6.85 (d, J= 10 Hz, 2H), 3.74 (s, 6H). ^{13}C

NMR (62.5 MHz, DMSO-d_6) δ 179.22, 156.43, 148.93, 140.19, 138.68, 136.96, 134.89, 133.4, 131.03, 129.97, 129.09, 128.72, 127.48, 125.65, 119.61, 115.47, 55.69.

Formation of 2,7-bis(4-(bis(4-methoxyphenyl)amino)phenyl)-9H-thioxanthen-9-one (TX-2TPA)

A mixture of 2,7-dibromo-9H-thioxanthen-9-one (200mg, 1eq), 4-methoxy-N-(4-methoxyphenyl)-N-(4-(4,4,5,5-tetramethyl-1,3,2-dioxaborolan-2-yl)phenyl)aniline (540mg, 3eq), $Pd(PPh_3)_4$ (48mg, 0.1eq) and Na_2CO_3 (0.88g, 20eq) were reacted in 20ml of toluene as mentioned in general method. The crude solid thus obtained was purified by column chromatography using petroleum ethers: ethyl acetate (4:1 v/v) to obtain a yellow solid (359mg, 90% yield). ^{1}H NMR (250 MHz, DMSO-d_6) δ 8.6 (d, J = 2.5 Hz, 1H), 8.02, 7.98 (dd, J_1 = 2.5 Hz, J_2 = 2.5 Hz, 1H), 7.87 (d, J = 10 Hz, 1H), 7.6 (d, J= 10 Hz, 2H), 7.07 (d, J = 10Hz, 4H), 6.93 (d, J = 10Hz, 4H), 6.85 (d, J = 7.5 Hz, 2H), 3.74 (s, 6H). ^{13}C NMR (62.5 MHz, DMSO-d_6) δ 206.99, 156.45, 148.93, 140.18, 138.69, 134.85, 130, 127.49, 119.61, 115.48, 55.7.

Synthesis of 2,7-di(9H-carbazol-9-yl)-9H-thioxanthen-9-one (TX-2Cbz) (Ullman coupling reaction).

In the Schlenk flask, the mixture of 2,7-dibromo-9H-thioxanthen-9-one (200mg, 1eq) and carbazole 96% (300mg, 3eq), CuI (20mg, 0.2 eq), sodium carbonate (0.3g, 5 eq) and 18-crown-6 (30mg, 0.2eq) were added in one portion. Then, 15 ml of nitrobenzene was supplied. The reaction mixture was stirred under argon atmosphere while the temperature was slowly raised up to 160^{o}C. Reaction mixture was kept for 24h and then cooled to room temperature, filtered through silice layer by diethyl ethers. Organic layers were collected and evaporated to get the crude product which was then purified by silica gel column chromatography. The eluent is petroleum ethers: ethyl acetate (4:1 v/v) to obtain a yellow solid (150mg, 51% yield). ^{1}H NMR (250 MHz, DMSO-d_6) δ 8.64 (d, J = 2.5 Hz, 1H), 8.29-8.24 (m, 3H), 8.17, 8.13 (dd, J_1 = 2.5 Hz, J_2 = 2.5 Hz, 1H), 7.52-7.43 (m, 4H), 7.36-7.29 (m, 2H). ^{13}C NMR (62.5 MHz, DMSO-d_6) δ 178.42, 140.32, 136.2, 135.81, 132.02, 129.8, 126.97, 126.68, 123.46, 121.18, 109.93. HRMS (ESI-MS): calculated for $C_{37}H_{22}N_2OS$ [M+H]+, 543.1453; found: 543.1525.

PART 3: NEW HTMs WITH 9,9'-BIACRIDONE CORE

III.3.1 Introduction

As aforementioned, 9(10H)-Acridone precursor owns rich chemistry possibilities and in previous section, it has been incorporated to various electron donor moieties at 2,7-positions. Furthermore, it could be also functionalized at 9-position and 10-position. At N-H position, it could be combined with alkyl chain or alkoxy chain to improve solubility, raise the LUMO up and reduce the crystallinity[72]. Alkyl chain can be replaced by functional groups such as ethers, esters or acid amine and so on. At 9-position, C=O group can be considered as moderate acceptor moiety and could be replaced for instance by other stronger acceptor groups. Moreover, C=O group can be changed to C=C bridge by coupling reaction. By this way, with such changes, D-A molecule can be reveal as all donor *p*-type molecules. Then, the optoelectronic properties will be significantly changed. For example, fluorenone[73,74] and benzophenone[75] have been developed as new types of charge transporting materials in organic photovoltaic solar cells and perovskite solar cells (***Figure 37***).

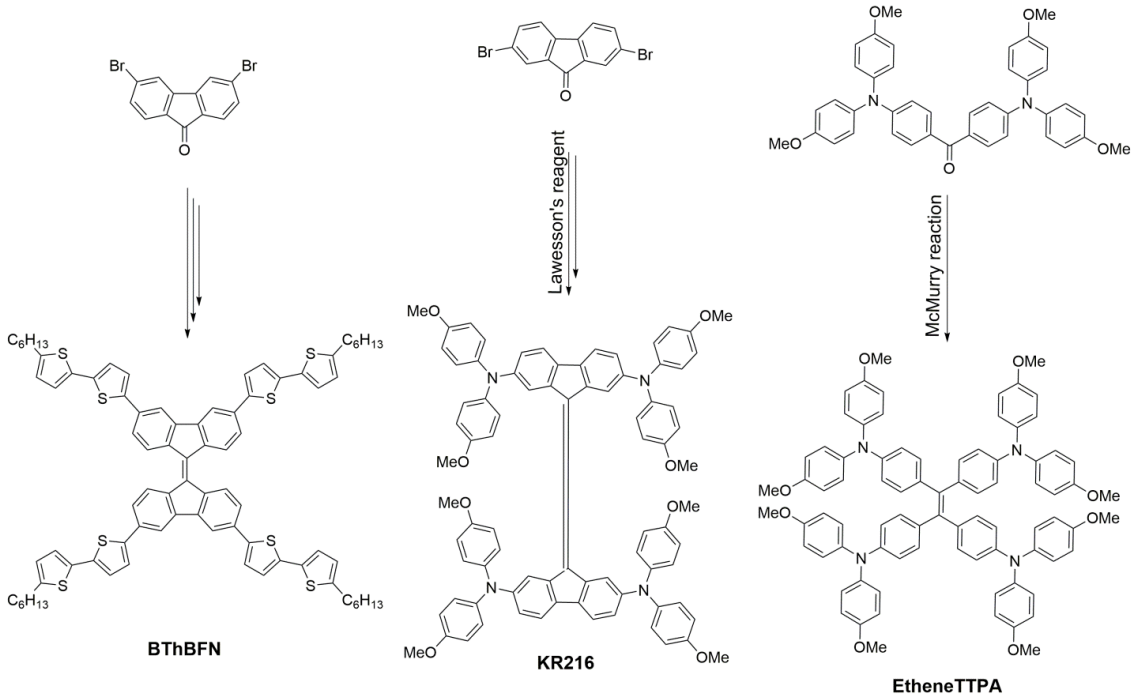

Figure 37: Some representative molecules have been employed in photovoltaic application.

By modifying C=O group to C=C ethylene bridge, twisted structure with large steric hindrance are obtained. Due to extended conjugation pathway, optical gap is

reduced and HOMO level is moving down. They are also employed and synthesized as symmetric structure with amorphous feature.

For example, BThBFN was prepared from 3,6-dibromo-9H-fluoren-9-one via several steps[76]. In which, two fluorene moieties are connected through a C=C double bond at the 9-position and two fluorene planes are twisted by 31^{o} due to the steric repulsion between the H atoms at the 1,8- and 1',8'- positions. DFT calculation suggested that this non-polycyclic aromatic compound is potential for singlet fission character in OPV application[77]. BThBFN was then used as *p*-type material in conventional solution-processed OPV which was composed of ITO/PEDOT:PSS/BThBFN:$PC_{71}BM$/Ca/Al structure. Due to low-lying HOMO level of BThBFN, the high V_{OC} (0.86 V) was obtained and even the incomplete morphology optimization, PCE of 1.3% was achieved, comparable to singlet fission OPV composed of pentacene and fullerene at that time.

Another successful material is KR216 which was prepared by straightforward two-step strategy and inexpensive synthetic procedure[73]. In particular, KR216 was synthesized via 2,7-dibromo-9H-fluoren-9-one precursor by coupling reactions using Lawesson's reagent and followed by Buchwald-Hartwig animation. In which, Lawesson's reagent is well known reagent in transformation of a carbonyl group into thio-carbonnyl group[78–80] and recently in olefination[73,74] as well as for the synthesis of wide range of heterocyclic compounds containing sulfur atoms. This reagent possesses some advantages such as requirements for small amount and short time reaction in thionation while in olefination, its reactions remain some unexpected products as polymeric materials[81], acting with this reagent[82] or incomplete reactions. Therefore, it needs to complete by Barton-Kellogg olefination[83,84] and transfer completely thio-carbonyl products to olefins. In the synthetic point of view, it makes difficult in purification and low selectivity of desired products.

The crystal structure of KR216 was different from that of Spiro-OMeTAD where the sp^3 central carbon atom is replaced by a double bond between two sp^2 hybridized carbon atoms. Therefore, the measured dihedral angles between the two-double connected fluorene (42.4^{0}) is much smaller than that of Spiro-OMeTAD (89.9^{o})[85]. Interestingly, different degree of distortion among the four bulky propeller shaped diphenyl amine is confirmed by XRD diffraction with the corresponding angles 15.2^{0}, 29.5^{0}, 44.2^{0} and 83^{0}. Due to the expansion of π-conjugation, KR216 shows a broader absorption maxima (466 nm) and lower optical band gap (2.41 eV) than that of Spiro-OMeTAD (390 nm and 3.0 eV, respectively). Thereafter, both of KR216 and Spiro-OMeTAD were employed as

HTM in PSCs, where the device with KR216 possesses high V_{OC} ~1023 mV, J_{SC} ~22.3 mA/cm^2 and FF ~ 0.77, yielded PCE of 17.8%. In comparison, lab-grade Spiro-OMeTAD as HTM owned V_{OC} ~1090 mV, J_{SC} ~20.6 mA/cm^2 and FF ~0.75, resulting PCE of 17.4%. Device performance with commercial Spiro-OMeTAD is a little bit higher with which PCE value equal to 18.4%. In this study, they emphasized that both organic impurities and metal residues may present in final materials which act as charge carrier traps or photo quenchers directly affecting to initial properties and photovoltaic performance[86,87].

Another example is EtheneTTPA, one of the efficient HTM in PSCs, competitive to Spiro-OMeTAD. Thus, EtheneTTPA was employed as HTM in PSCs with remarkable performance such as J_{SC} ~ 21.29 mA/cm^2, V_{OC} ~ 0.91 V, FF ~0.65 and correspond to overall PCE of 13.09% while that of Spiro-OMeTAD are J_{SC} ~ 21.27 mA/cm^2, V_{OC} ~ 0.94V, FF ~ 0.66 and overall PCE of 13.87%[75]. Hole mobility value of EtheneTTPA was determined by SCLC method which obtained $4.45.10^{-5}$ $cm^2V^{-1}s^{-1}$ comparable to that of Spiro-OMeTAD is $2.24.10^{-5}$ $cm^2V^{-1}s^{-1}$. Interestingly, it was synthesized from carbonyl precursor via McMurry coupling reaction. This kind of coupling reaction possesses advantages over the Lawesson's reagent and Barton-Kellogg reaction such as mild conditions and high yield, good selectivity in homocoupling reaction[88]. McMurry coupling reaction is great potential in synthetic approach of variety materials, from strained olefins to unusual molecules to natural products. Moreover, the reaction can be used in both of inter- and an intramolecular aspect[89].

In McMurry coupling reaction, ketones and aldehydes are reduced through reductive dimerization to form olefins by treatment of low-valent titanium reagents. Various reagents used for coupling reaction were synthesized and employed but low-valent titanium system seems to be effective reagent to obtain high yield olefins. The mechanism of carbonyl-coupling reaction has been suggested by prof. McMurry and summarized in ***Figure 38***.

This reaction takes place in two steps: (1) reductive dimerization of the initial ketone/aldehyde to form the carbon-carbon bond and (2) deoxygenation of the pinacolate intermediate to yield the alkene. By many previous studied, they demonstrated that the reaction takes place on the surface of a small, zero-valent titanium particles[91–93].

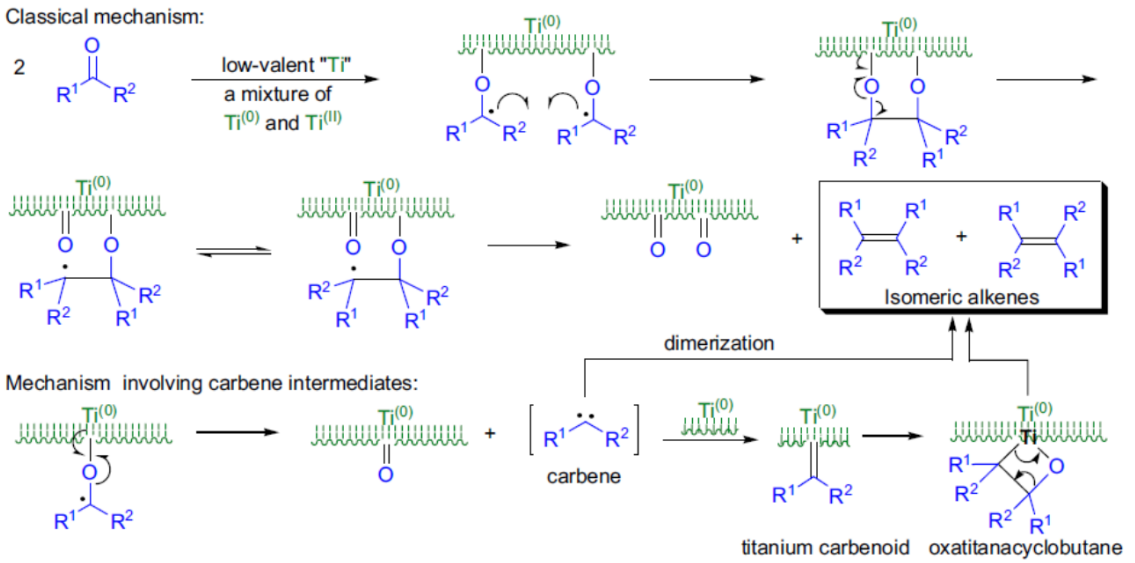

Figure 38: Mechanism of the carbonyl-coupling reaction. The figure was adapted from ref[90]

Nonetheless, in carbonyl coupling reaction, particular McMurry reaction which using low-valent titanium owned some requirements for an efficient reaction. First, the reactivity of the low-valent titanium reagent is significantly dependent on its method of preparation (solvents, temperature, reducing agent, etc). The solvent play an important role to stabilize Ti^0 particles during their formation and whether weak/strong coordinating solvent will support/prevent the reductive reagents from working, respectively. Second, the nature of carbonyl compounds would also affect to intermediates species formation. Third, to avoid acid-catalyzed hydrolysis during workup, a small amount of a weak base such as pyridine or trimethylamine is sometimes required and saturated carbonate/ammonia is added to assure basic medium in order to quench the reaction. That's why the reaction is difficult and high yields are difficult to obtain in the laboratory.

Nevertheless, McMurry coupling reaction has still been widely applied for intramolecular/intermolecular couplings[94] and mixed coupling reactions (homo/hetero-coupling) as well as synthesis of strained olefins or sterically hindered olefins[95], unusual molecules and natural products[96].

Thanks to McMurry coupling reaction, 9(10H)Acridone was modified from push-pull molecule to typical *p*-type molecule and their chemical structure are given in ***Figure 39***.

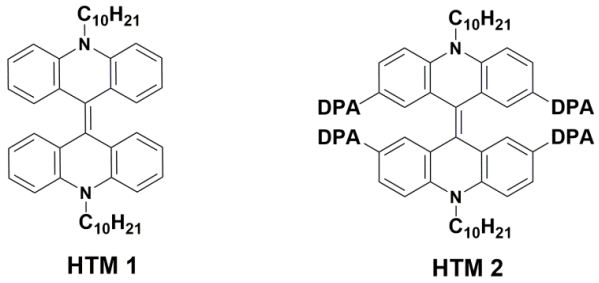

Figure 39: Representative molecules of coupling Acridone-core.

Furthermore, these bulky and 3D molecules are expected to form amorphous structure. From point of views, amorphous molecular structure are also promising candidate for charge transport materials due to their following advantages: They exhibit isotropic and homogenous properties which allow the formation of smooth, uniform amorphous thin film by either thermal or solution depositions[6,97,98]. These properties are among important factors to enhance device performance. Two rigid Acridone molecules are simply combined through diene (C=C) bridge to construct 9,9'-biacridone core (named as HTM 1 compound). The incorporation of number of bulky and heavy substituents arms in HTM 2 compound leads to glass formation easier, enlargement of molecular size and also enhance stability of glassy state. Moreover, electron-donor unit 4,4'-dimethoxydiphenylamine (coded as DPA) should help to improve hole mobility.

III.3.2 Strategies and objectives

From the study of Acridone derivatives in ***part 1***, These molecules were modified and become *p*-type molecules with McMurry homocoupling reaction. The purposes of this study are based on some following considerations:

- Improving electron delocalization property in whole 9,9'-biacridone core.
- Forming 3D - amorphous structure of these target molecules.
- Investigate the differences of physical properties between D-A molecules and *p*-type molecules.

First, these new materials were isolated from 9(10)-Acridone precursor via N-Alkylation to obtained intermediate product (compound 1). Then carbonyl group was reduced and formed C=C double bond by McMurry coupling reaction. The compound HTM 1 was formed directly from compound 1 through McMurry homocoupling reaction and named as 9,9'-biacridone backbone. Theoretically, this core is a versatile scaffold due to it owns twelve different sites for functionalization by substitution. Based on this modification, these final compounds, overcrowded polycyclic, HTM 1 and HTM 2 were synthesized by synthetic route as described in ***Scheme 5***.

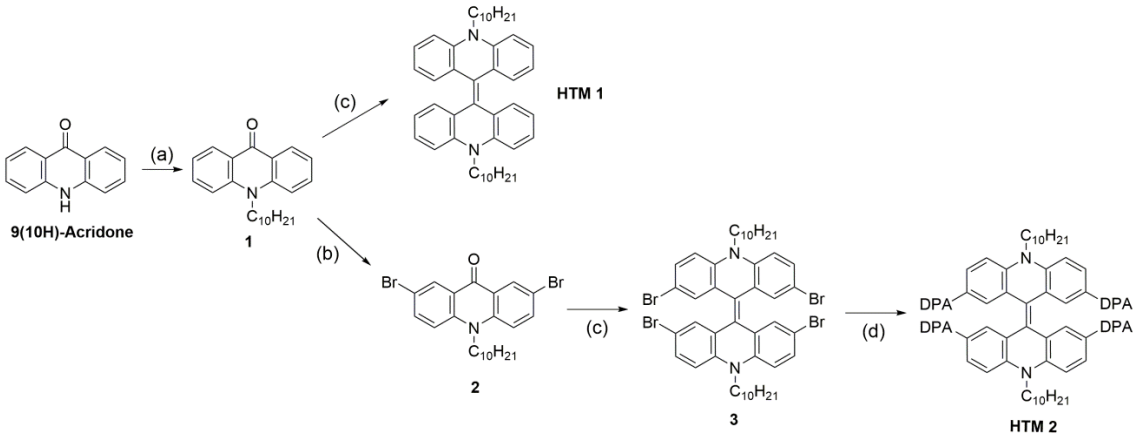

Scheme 45: Synthetic route of these new materials. Reagents and conditions: (a) NaOH, 1-bromodecane, DMSO, Aliquat 336, 110°C, 24h. (b) NBS, DMF, 70°C (c) Zn, THF, 0°C, $TiCl_4$, pyridine and (d) $Pd(OAc)_2$, tBu_3P, NaOtBu, Toluene, 110°C.

There are some important points we need to take into account. First, chemical activation of Zn dust is necessary, this step is carried out by stirring Zn dust with 5-10% HCl solution for 5 mins and then filtered, washed several times with water, acetone, ethanol and ethers. The freshly zinc powder is used immediately after drying by vacuum or air dried. Second, the coupling reaction is only occurred on surface of activated $Ti^{(0)}$, the appropriate ketone compound must be added after complete reduction of $TiCl_4$ by Zn. Low efficiency or no desired product is obtained if ketone/aldehyde compounds are added before complete reduction. Third, this kind of reaction is worked up in non-aqueous solution; therefore it should be quenched by basic solution to avoid acidic hydroxylation. In particularly, saturated K_2CO_3 solution or ammonium salts are often used for quenching reaction. Petroleum ethers are more suitable employed to extracted organic phase than halogen solvents (i.e., dichloromethane or chloroform).

As described in ***part 1***, Acridone precursor was alkylated by long alkyl chain to improve solubility. In this section, C_6H_{13} was replaced by $-C_{10}H_{21}$ to enhance solubility of these final compounds. Then, compound 1 was halogenated by NBS in DMF/70°C and followed by McMurry homocoupling reaction to form compound 3. Then, compound 3 was reacted with 4,4'-dimethoxydiphenylamine via Buchwald-Hartwig coupling reaction. The HTM 2 was obtained in low yield due to high steric effect and formation of various substituted products. Therefore, it is necessary to optimize reaction conditions to improve efficiency.

III.3.3 Results and discussion

Thermal behaviors of these molecules were investigated by thermogravimetric analysis (TGA) and differential scanning calorimetry (DSC) under argon atmosphere. TGA-DSC curves are given in ***Figure 40*** and their values of thermal decomposition (Td) and glass transition (T_g) temperatures are summarized in ***Table 8***. The T_d was determined at the 5% weight loss in TGA analysis. In ***Figure 40a***, moderate Td ~ 235^0C was determined and no T_g value was recorded. In both 1^{st} and 2^{nd} heating scan, it only shows up the crystallization peak and melting peak. It could be explained that HTM 1 exits in crystalline form.

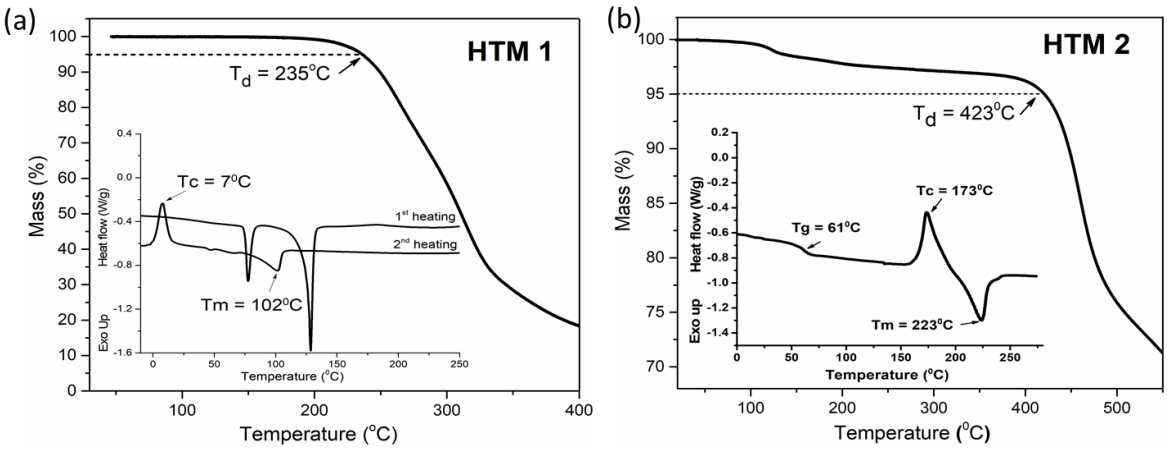

Figure 40: TGA-DSC measurements of HTM 1 (a) and HTM 2 (b).

In ***Figure 40b***, glass transition temperature T_g, crystallization temperature T_c and melting temperature T_m values of HTM 2 were observed. This compound can stay in both crystalline and amorphous states. Because of high molecular weight and bulky structure of HTM 2, high decomposition temperature of 423^0C was observed.

Optical properties of these compounds were studied by combination of both absorption-emission spectra (***Figure 41***). For comparison, push-pull molecule based compound 1was compared to typical *p*-type conjugated molecule HTM 1.

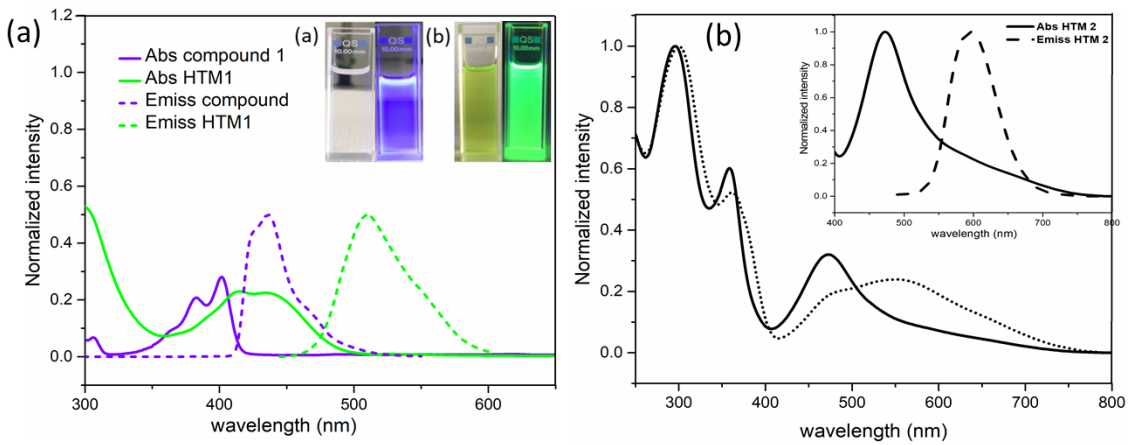

Figure 41: Absorption (solid line) and emission (dash line) of HTM 1-compound 1 (a) and HTM 2 (b) in diluted dichloromethane. The appearance of compound 1 and HTM 1 are under daylight and UV light (inset of 5a). Absorption spectrum of HTM 2 in solid state is short dot line.

In ***Figure 41a***, compound 1 (A-$C_{10}H_{21}$) showed maxima absorption at 401 nm which indicated that weak intramolecular charge transfer (ICT) due to it owns electron acceptor unit (C=O group) and electron donor unit (N-alkyl chain) and emitted at 435 nm. After coupling, HTM 1 shows a broad optical absorption in the visible region centered at 437 nm, affirming enhanced conjugation through 9-ylidene double bond with better π-electron delocalization. Interestingly, HTM 1 exhibits bright green emission in dilute dichloromethane solution in comparison to violet emission of compound 1 (inset figure). The Optical band gap (E_g) determined from the onset of the absorption spectra were 2.99 eV for compound 1 and reduced band gap of 2.54 eV for HTM 1. In ***Figure 41b***, the absorption-emission spectra of HTM 2 show maxima absorption at 472 nm which is red-shifted 25 nm compared to HTM 1 due to incorporation of electron donor moieties. Remarkably, the absorption spectrum of HTM 2 in solid state is broader and more red-shifted compared to that in solution which indicate that existence of strong intermolecular π-π stacking effect.

Thereafter, cyclic voltammetry has been used to investigate the redox behavior of synthesized molecular and to determine their HOMO-LUMO energy levels. The CV of HTM 1 shows only their irreversible oxidation peaks (***Figure 42a***). The oxidation onset potential of HTM 1 was recorded of -0.04 V vs Fc/Fc^+. The presence of "irreversible wave" in oxidation process could be explained by either an irreversible (slow) electron transfer or transform the product of electron transfer into another species by chemical steps[99]. This phenomenon could be indicated that they are result of a single redox couple while a reversible oxidation peak is about 60 mV away from an oxidation peak. A hypothesis is during reduction or oxidation, the addition or remove of one electron across the C=C double bond could be affected to twist structure and change aromatic system to a multi-electron system[100]. Thereafter, the cyclic voltammetry were characterized independently from low potential to high potential (red line) and high potential to low potential (blue line). These signals from both CV are a bit distinct which revealed that they are relatively stable in electrolyte solution. The HOMO energy value of HTM 1 was estimated to be -4.76 eV vs $E^{1/2}$ of Fc/Fc^+. According to the HOMO energy value and optical band gap, the LUMO energy value of HTM 1 was calculated to be -2.22 eV.

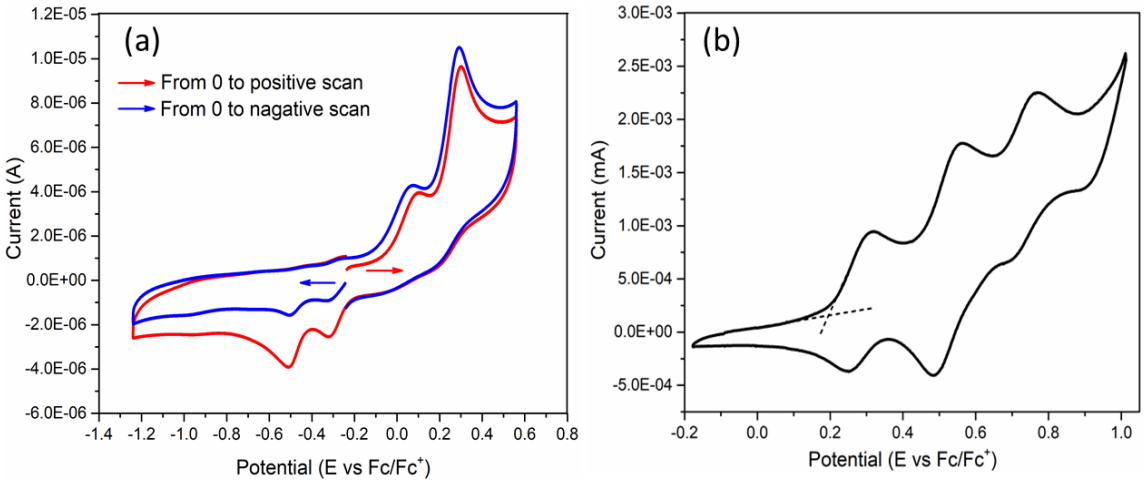

Figure 42: Cyclic voltammogram of HTM 1(a) and HTM 2 (b).

Similarly, the redox behavior of HTM 2 was determined by cyclic voltammetry measurements (***Figure 42b***). Multi-electron transfer oxidation was observed. Three identical oxidation peaks were obtained due to the oxidations of DPA moieties and 9,9'-biacridone core. In fact, ΔEp_1, ΔEp_2 and ΔEp_3 values are approximate 69 mV. It could be explained that single-electron transfer processes are occurring. However, the oxidation mechanism is more complicated in this case. Therefore, it should be deeply studied in the future. The potential oxidation onset was determined of 0.2 V and the HOMO energy value of HTM 2 was estimated to be -5.0 eV vs vacuum. Because of increasing number of electron donor units, the HOMO energy value of HTM 2 is lower than that of HTM 1 and due to reduced optical band gap, the LUMO energy value of HTM 2 is subsequent lower than that of HTM 1.

As shown in ***Figure 43***, DFT calculations was carried out and showed their optimized structure as well as frontier molecular orbitals and energy levels of these compounds. HTM 1 exhibits twisted structure in the core center. In ground state, 9,9'-biacridone is considered to be coplanar because of the presence of the double bond, but the repulsive interaction between the H_1-H_1' and H_8-H_8' protons forms the torsional structure of the dimer[101]. In HOMO and LUMO orbital distribution, electrons are distributed mainly in the 9,9'-biacridone core. Due to bulky structure, the DFT calculation of HTM 2 is under preparation.

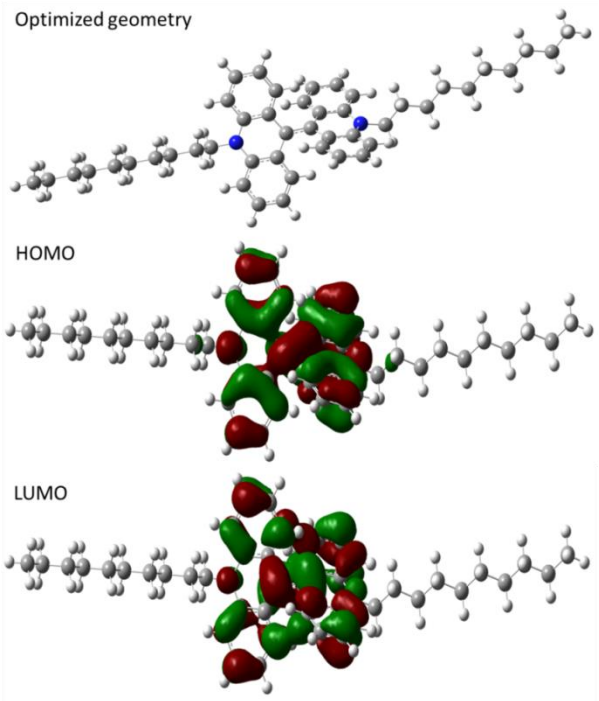

Figure 43: Optimized geometry of HTM 1 by DFT and electron density of HTM 1 in HOMO-LUMO states.

However, it could be predicted that in LUMO state, electrons are contributed in mainly the 99'-biacridone core and in HOMO state, the electron are located in four-side electron donor moieties. The related data of these molecules are summarized in ***Table 8***.

	T_g (^oC)	T_d (^oC)	λ_{abs} (nm)	$\lambda_{abs\ onset}$ (nm)	λ_{emiss} (nm)	E_g (eV)	E^{ox}_{onset} (V)	HOMO (eV)	LUMO (eV)
HTM 1	-	235	437	488	513	2.54	-0.04	-4.76	-2.22
HTM 2	61	423	472	556	597	2.23	0.2	-5.0	-2.77

Table 78: Summary of photo-physical, thermal and electrochemical data of these studied compounds. Tg is obtained from the onset values of DSC and Td is recorded by 5% weight loss in TGA.

III.3.4 Conclusion and perspective

To sum up this study, we studied the potential of the 9,9'-biacridone core as the novel π-conjugated system. These typical *p*-type molecules were modified from commercially available 9(10H)-Acridone by short-steps synthetic route via McMurry homocoupling reaction and Buchwald-Hartwig cross coupling reaction. Their properties were characterized and they exhibited several interesting characteristics such as extension π-conjugation system, high fluorescent and low optical band gap.

Moreover, due to 3D molecular structure, they are expected to be amorphous nature which would form smooth, uniform and defect-free film in device fabrication.

Moreover, HTM 2 is promising material for novel HTM in PSCs due to its compatible energy level to perovskite. Therefore, we believed that the development of efficient HTM based on 9,9'-biacridone core is possible through properly molecular engineering and optimization of device fabrication.

III.3.5 Experimental section

Formation of 10-decyl-9-acridone (compound 1)

In 100 ml 3-necks bottom, 9(10H)-acridone (1g, 1eq) was dissolved in 20 ml of DMSO and then NaOH solution (2g of NaOH in 3 ml of water, 10eq) and few drops of Aliquat 336 were added. The temperature was increased to 110^{o}C and refluxed under argon atmosphere. After 3 hours stirring, 1-bromodecane (2g, 1.5eq) was added dropwise to the mixture and then the reaction was kept overnight. The reaction was monitored by thin layer chromatography (TLC). After completion of the reaction, the mixture was reconstituted in dichloromethane (DCM), washed with water and the organic layer was dried over $MgSO_4$. The crude product was concentrated and then purified by silica gel column chromatography using DCM: ethyl acetate (EtOAc) (9:1 v/v) as eluent and then recrystallized in methanol. The final product is compound 1 as pale yellow crystals (1.5g, 88% yield). ^{1}H NMR (250 MHz, DMSO-d_6) δ 8.33 (d, *J* = 7.5 Hz, 1H, Ar), 7.78 (t, *J* = 15 Hz, 2H, Ar), 7.26 (t, *J* = 7.5 Hz, 1H, Ar), 4.34 (m, 1H, -CH_2) 1.71(m, 1H, alkyl chain), 1.47-1.15 (m, 16H, alkyl chain), 0.78 (m, 3H, alkyl chain). ^{13}C NMR (62.5 MHz, DMSO-d_6): δ 176.81, 141.82, 134.46, 127.19, 122.06, 121.47, 116.07, 61.17, 45.6, 33.03, 31.77, 29.48, 29.17, 27.24, 26.44, 25.99, 25.24, 22.54, 14.3.

Formation of 2,7-dibromo-10-decyl-9-acridone (compound 2)

To a solution of 10-decyl-9-acridone (0.5g, 1eq) in 15 ml of DMF, N-bromosuccinimide (1.275g, 4eq) was added in one portion. The temperature was heated until 70-80^{o}C, kept overnight, after which the reaction color became red. After cooling to room temperature, the reaction mixture was washed with water and extracted by ethyl acetate for three times to remove of DMF. The obtained top organic layer was dried over anhydrous $MgSO_4$. The mixture was concentrated in vacuum and the residue was recrystallized in methanol to afford pure product as yellow needle-crystals (0.9g, 90%). ^{1}H NMR (250 MHz, $CDCl_3$): δ 8.62 (t, *J* = 2.5 Hz, 2H, Ar), 7.88 (t, *J* =2.5 Hz, 1H, Ar), 7.85 (t, *J* = 2.5 Hz, 1H, Ar), 7.46 (t, *J* = 2.5 Hz, 1H, Ar), 7.42 (t, *J* = 2.5 Hz, 1H, Ar), 4.36

(t, *J* = 7.5 Hz, 2H, alkyl chain), 2.05-1.97 (m, 3H, alkyl chain), 1.72-1.44 (m, 13H, alkyl chain), 1.16-1.13 (m, 3H, alkyl chain). ^{13}C NMR (62.5 MHz, $CDCl_3$) δ 175.12, 140.01, 136.72, 129.93, 123.15, 116.74, 114.82, 46.54, 31.45, 27.0, 26.89, 26.49, 22.63, 14.01.

General procedure to synthesis of 2,2',7,7'-tetrabromo-10,10'-didecyl-10H,10'H-9,9'-biacridinylidene (compound 3) and HTM 1 via McMurry homocoupling reaction.

In the round bottom two-necks, the condenser was connected and argon, vacuum are supplied to remove total air. The temperature was kept at 0^{o}C and Zn, THF were added in the close system. $TiCl_4$ solution is added slowly to the mixture and kept during an hour at 0^{o}C. The color changed yellow to purple and then black suspension. Then, small volume of pyridine was added slowly to suspension and the reaction was refluxed for 2h at 70^{o}C. The corresponding ketone in distillated THF was added dropwise and continuing refluxed 12h. The reaction was quenched by 50ml of saturated K_2CO_3 and vigorously stirring 1 day until we obtain dark green solution. The crude solution was filtered through silice layer by diethyl ethers and covered first fraction. This fraction was removed solvent under reduced pressure and then precipitated in small volume of methanol. Yellow solid was filtered and dried under vacuum without further purification. ^{1}H and ^{13}C NMR was characterized to confirm structure of final compound.

HTM 1 was obtained as yellow solid (0.218g, 22% yield): ^{1}H NMR (250 MHz, $CDCl_3$) δ 8.01 (d, *J* = 5 Hz, 4H), 7.86 (m, 2H), 7.42 (m, 2H), 7.17 (m, 1H), 6.04 (d, *J* = 7.5 Hz, 1H), 4.22 (m, 1H), 4.09 (m, 1H), 2.34 (m, 6H), 2.03 (m, 13H), 1.64 (m, 3H). ^{13}C NMR (62.5 MHz, $CDCl_3$) δ 143.23, 127.71, 126.21, 124.44, 123.36, 119.14, 112.6, 65.5, 52.71, 45.22, 31.47, 29.16, 26.71, 22.08, 14.73, 13.51. HRMS (ESI+): calculated for $C_{46}H_{58}N_2$ $[M+H]^+$: 638.4600; found: 638.4601.

Compound 3 was obtained as light yellow solid (0.2g, 26% yield): ^{1}H NMR (250 MHz, $CDCl_3$) δ 7.31 (d, *J* = 2.5 Hz, 1H), 7.28 (d, *J* = 2.5 Hz, 1H), 6.65 (d, *J* = 2.5 Hz, 2H), 6.61 (s, 2H), 3.8 (s, 1H), 3.26 (t, *J* = 7.5 Hz, 2H), 1.53 (m, 3H), 1.42-1.28 (m, 11H), 0.97-0.91 (m, 3H). ^{13}C NMR (62.5 MHz, $CDCl_3$) δ 140.2, 131.5, 130.5, 126.3, 112.9, 111.8, 53.2, 46.3, 31.4, 26.6, 25.2, 22.7, 14.4.

Formation of 10,10'-didecyl-N2,N2,N2',N2',N7,N7,N7',N7'-octakis(4-methoxyphenyl)-10H,10'H-[9,9'-biacridinylidene]-2,2',7,7'-tetraamine (HTM 2) via Buchwald-Hartwig coupling reaction.

A mixture of 2,2',7,7'-tetrabromo-10,10'-didecyl-10H,10'H-9,9'-biacridinylidene (compound 3) (200mg, 1eq) and 4.4´-dimethoxydiphenylamine (400mg, 6eq) were dissolved in distillated toluene under argon atmosphere. The palladium catalyst $Pd(OAc)_2$ (0.2 eq), tri-tert-butylphosphine solution $(^tBu)_3P$ (0.2 eq) and sodium-tertbutoxide (10 eq) were added to the mixture reaction. The reaction mixture was stirred at 110^oC under argon atmosphere. Reaction mixture was carried out in 24h, then cooled to room temperature and extracted with DCM and water three times. The organic layer were collected and dried over anhydrous $MgSO_4$. The crude product was concentrated in rotary evaporator and purified by silica gel column chromatography using petroleum ethers: EtOAc (9:1 v/v) to afford pure product HTM 2 as red solid (15mg, 8% yield): ^1H NMR (250 MHz, $CDCl_3$) δ 8.01 (d, J = 7.5 Hz, 1H), 7.35; 7.31 (dd, J_1 = 2.5 Hz, J_2 = 2.5 Hz, 1H), 7.12 (d, J = 2.5 Hz, 1H), 6.9 (d, J = 10 Hz, 4H), 6.72 (d, J = 10 Hz, 4H), 6.56 (s, 4H), 3.8 (s, 6H), 3.79 (s, 3H), 2.05 (s, 1H), 1.51-1.11 (m, 11H), 0.88 (m, 3H). ^{13}C NMR (62.5 MHz, $CDCl_3$) δ 156.18, 154.22, 146.16, 141.25, 139.95, 126.81, 126.54, 121.91, 114.78, 114.57, 55.41, 53.43, 29.7, 29.06, 26.9, 14.06.

References

(1) Jiang, H. Organic Ambipolar Conjugated Molecules for Electronics: Synthesis and Structure - Property Relationships. *Macromol. Rapid Commun.* **2010**, *31*, 2007–2034.

(2) Sagawa, T.; Yoshikawa, S.; Imahori, H. One-Dimensional Nanostructured Semiconducting Materials for Organic Photovoltaics. *J. Phys. Chem. Lett.* **2010**, *1*, 1020–1025.

(3) Beaujuge, P. M.; Fréchet, J. M. J. Molecular Design and Ordering Effects in π-Functional Materials for Transistor and Solar Cell Applications. *J. Am. Chem. Soc.* **2011**, *133*, 20009–20029.

(4) Imahori, H.; Umeyama, T. Donor-Acceptor Nanoarchitecture on Semiconducting Electrodes for Solar Energy Conversion. *J. Phys. Chem. C* **2009**, *113*, 9029–9039.

(5) Bureš, F. Fundamental Aspects of Property Tuning in Push–pull Molecules. *RSC Adv.* **2014**, *4*, 58826–58851.

(6) Shirota, Y.; Kageyama, H. Charge Carrier Transporting Molecular Materials and Their Applications in Devices Charge Carrier Transporting Molecular Materials and Their Applications in Devices. *Chem. Rev.* **2007**, *107*, 953–1010.

(7) Dhingra, P.; Singh, P.; Rana, P. J. S.; Garg, A.; Kar, P. Hole-Transporting Materials for Perovskite-Sensitized Solar Cells. *Energy Technol.* **2016**, *4*, 891–938.

(8) Slama-Schwok, A.; Blanchard-Desce, M.; Lehn, J. M. Intramolecular Charge Transfer in Donor-Acceptor Molecules. *J. Phys. Chem.* **1990**, *94*, 3894–3902.

(9) Tao Jia, Chen Sun, Rongguo Xu, Zhiming Chen, Qingwu Yin, Yaocheng Jin, Hin-Lap Yip, Fei Huang, and Y. C. Naphthalene Diimide Based N-Type Conjugated Polymers as Efficient Cathode Interfacial Materials for Polymer and Perovskite Solar Cells. *ACS Appl. Mater. Interfaces* **2017**, *9*, 36070–36081.

(10) Annie Butler Ricks, Gemma C. Solomon, Michael T. Colvin, Amy M. Scott, Kun Chen, Mark A. Ratner, and M. R. W. Controlling Electron Transfer in Donor-Bridge-Acceptor Molecules Using Cross-Conjugated Bridges. *J. Am. Chem. Soc.* **2010**, *132*, 15427–15434.

(11) Kwon, Y. S.; Lim, J.; Yun, H.-J.; Kim, Y.-H.; Park, T. A Diketopyrrolopyrrole-Containing Hole Transporting Conjugated Polymer for Use in Efficient Stable Organic–inorganic Hybrid Solar Cells Based on a Perovskite. *Energy Environ. Sci.* **2014**, *7*, 1454.

(12) Qu, S.; Tian, H. Diketopyrrolopyrrole (DPP)-Based Materials for Organic Photovoltaics. *Chem. Commun.* **2012**, *48*, 3039.

(13) Haoliang Cheng , Xiaojuan Zhao , Yan Shen , Mingkui Wang , Lingyun Wang , Herbert Meier, D. C. Diketopyrrolopyrrole Based D-π-A-π-D Type Small Organic Molecules as Hole Transporting Materials for Perovskite Solar Cells. *J. Energy Chem.* **2017**, *27*, 1175–1182.

(14) Claudia Piliego, Thomas W. Holcombe, Jessica D. Douglas, Claire H. Woo, Pierre M. Beaujuge, and J. M. J. F. Synthetic Control of Structural Order in N -Alkylthieno[3,4- c]Pyrrole-4,6-Dione-Based Polymers for Efficient Solar Cells. *J. Am. Chem. Soc.* **2010**, *132*, 7595–7597.

(15) Xugang Guo, Rocio Ponce Ortiz, Yan Zheng, Myung-Gil Kim, Shiming Zhang, Yan Hu, Gang Lu, Antonio Facchetti, and T. J. M.; Hu, Y.; Lu, G.; Facchetti, A.; Marks, T. J. Thieno[3,4- c]Pyrrole-4,6-Dione-Based Polymer Semiconductors: Toward High-Performance, Air-Stable Organic Thin-Film Transistors. *J. Am. Chem. Soc.* **2011**, *133*, 13685–13697.

(16) John Jun-An Chen, Teresa L. Chen, BongSoo Kim, Daniel A. Poulsen, Justin L. Mynar, Jean M. J. Frechet, and B. M. Quinacridone-Based Molecular Donors for Solution Processed Bulk-Heterojunction Organic Solar Cells. *ACS Appl. Mater. Interfaces* **2010**, *2*, 2679–2686.

(17) Jeroen Brebels , Karine C.C.W.S. Klider , Mathias Kelchtermans , Pieter Verstappen , Melissa Van Landeghem , Sabine Van Doorslaer , Etienne Goovaerts, J. R. G.; Jean Manca , Laurence Lutsen , Dirk Vanderzande, W. M. Low Bandgap Polymers Based on Bay-Annulated Indigo for Organic Photovoltaics: Enhanced Sustainability in Material Design and Solar Cell Fabrication. *Org. Electron. physics, Mater. Appl.* **2017**, *50*, 264–272.

(18) Nikolov, P.; Petkova, I.; Köhler, G.; Stojanov, S. Deactivation Processes and Hydrogen Bonding of Excited N-Substituted Acridones. *J. Mol. Struct.* **1998**, *448*, 247–254.

(19) Nguyen, H. T.; Lallemand, M. C.; Boutefnouchet, S.; Michel, S.; Tillequin, F. Antitumor Psoropermum Xanthones and Sarcomelicope Acridones: Privileged Structures Implied in DNA Alkylation. *J. Nat. Prod.* **2009**, *72*, 527–539.

(20) Singh, P.; kaur, J.; Kaur, P.; Kaur, S. Search for MDR Modulators: Design, Syntheses and Evaluations of N-Substituted Acridones for Interactions with p-Glycoprotein and Mg2+. *Bioorganic Med. Chem.* **2009**, *17*, 2423–2427.

(21) Smith, J. A.; West, R. M.; Allen, M. Acridones and Quinacridones: Novel Fluorophores for Fluorescence Lifetime Studies. *J. Fluoresc.* **2004**, *14*, 151–171.

(22) Miyaji, H.; Sessler, J. L. Off-the-Shelf Colorimetric Anion Sensors. *Angew. Chemie - Int. Ed.* **2001**, *40*, 154–157.

(23) Chi-Yuan Yang, Ke Shi, Ting Lei, Jue Wang, Xiao-Ye Wang, Fang-Dong Zhuang, Jie-Yu Wang, and J. P. Epindolidione-Based Conjugated Polymers: Synthesis, Electronic Structures, and Charge Transport Properties. *ACS Appl. Mater. Interfaces* **2016**, *8*, 3714–3718.

(24) Eric Daniel Głowacki , Giuseppe Romanazzi , Cigdem Yumusak , Halime Coskun , Uwe Monkowius , Gundula Voss , Max Burian , Rainer T. Lechner , Nicola Demitri , Günther J. Redhammer , Nevsal Sünger, G. P. S. and S. S. Epindolidiones-Versatile and Stable Hydrogen-Bonded Pigments for Organic Field-Effect Transistors and Light-Emitting Diodes. *Adv. Funct. Mater.* **2015**, *25*, 776–787.

(25) Chenguang Wang, Shanyong Chen, Kai Wang, Shanshan Zhao, Jingying Zhang, and Y. W. Luminescent Dendrimers Composed of Quinacridone Core and Carbazole Dendrons: Structure, Electrochemical, and Photophysical Properties. *J. Phys. Chem. C* **2012**, *116*, 17796–17806.

(26) Chenguang Wang, Shipan Wang, Weiping Chen, Zuolun Zhang, H. Z. and Y. W. A Diphenylamino-Substituted Quinacridone Derivative: Red Fluorescence Based on Intramolecular Charge-Transfer Transition. *RSC Adv.* **2016**, *6*, 19308–19313.

(27) Weiping Chen, Shipan Wang, Guochun Yang, Siyan Chen, Kaiqi Ye, Zhonghan Hu, Zuolun Zhang, and Y. W. Dicyanomethylenated Acridone Based Crystals: Torsional Vibration Confinement Induced Emission with Supramolecular Structure Dependent and Stimuli Responsive Characteristics. *J. Phys. Chem. C* **2016**, *120*, 587–597.

(28) Dheyongera, J. P.; Geldenhuys, W. J.; Dekker, T. G.; Van Der Schyf, C. J. Synthesis, Biological Evaluation, and Molecular Modeling of Novel Thioacridone Derivatives Related to the Anticancer Alkaloid Acronycine. *Bioorganic Med. Chem.* **2005**, *13*, 689–698.

(29) Bahr, N.; Tierney, E.; Reymond, J. L. Highly Photoresistant Chemosensors Using Acridone as Fluorescent Label. *Tetrahedron Lett.* **1997**, *38*, 1489–1492.

(30) Nadaraj, V.; Thamarai Selvi, S.; Mohan, S. Microwave-Induced Synthesis and Anti-Microbial Activities of 7,10,11,12-Tetrahydrobenzo[c]Acridin-8(9H)-One Derivatives. *Eur. J. Med. Chem.* **2009**, *44*, 976–980.

(31) Chow, W.-C.; Zhou, G.-J.; Wong, W.-Y. Electron-Deficient Acridone Derivatives as a New Functional Core Towards Low-Bandgap Metallopolyynes. *Macromol. Chem. Phys.* **2007**, *208*, 1129–1136.

(32) Vezzu, D. a K.; Deaton, J. C.; Shayeghi, M.; Li, Y.; Huo, S. Acridinone / Amine (Carbazole) - Based Bipolar Molecules : Efficient Hosts for Emitters. *New York* **2009**, 8–11.

(33) Daniel Lumpi, Brigitte Holzer, Johannes Bintinger, Ernst Horkel, Simon Waid, Heinz D. Wanzenbock, Martina Marchetti-Deschmann, D.; Christian Hametner, Emmerich Bertagnolli, I. K. and J. F. Substituted Triphenylamines as Building Blocks for Star Shaped Organic Electronic Materials. *New J. Chem.* **2015**, *39*, 1840–1851.

(34) Wan, Z.; Jia, C.; Zhou, L.; Huo, W.; Yao, X.; Shi, Y. Influence of Different Arylamine Electron Donors in Organic Sensitizers for Dye-Sensitized Solar Cells. *Dye. Pigment.* **2012**, *95*, 41–46.

(35) Guo, Z.; Zhu, W.; Tian, H. Dicyanomethylene-4H-Pyran Chromophores for OLED Emitters, Logic Gates and Optical Chemosensors. *Chem. Commun.* **2012**, *48*, 6073–6084.

(36) Sharma, B. K.; Shaikh, A. M.; Agarwal, N.; Kamble, R. M. Synthesis, Photophysical and Electrochemical Studies of Acridone-Amine Based Donor–acceptors for Hole Transport Materials. *RSC Adv.* **2016**, *6*, 17129–17137.

(37) Frisch, M. J. E. A., Trucks, G. W., Schlegel, H. B., Scuseria, G. E., Robb, M. A., Cheeseman, J. R.,& Nakatsuji, H. (2009. Gaussian 09, Revision D. 01. 2009., 2009.

(38) Carol Hua, Aditya Rawal, Thomas B. Faust, Peter D. Southon, Ravichandar Babarao, J. M. H. and D. M. D. Exploiting Stable Radical States for Multifunctional Properties in Triarylamine-Based Porous Organic Polymers. *J. Mater. Chem. A* **2010**, *4*, 1166–1169.

(39) Richard J. Bushby , Daniel Gooding, M. T. & M. E. V. High-Spin p-Doped Arylamine Polymers. *Mol. Cryst. Liq. Cryst. Sci. Technol. Sect. A. Mol. Cryst. Liq. Cryst.* **1999**, *334*, 167–176.

(40) Bushby, R. J.; Gooding, D.; Vale, M. E. High-Spin Polymeric Arylamines. *Philos. Trans. R. Soc. A Math. Phys. Eng. Sci.* **1999**, *357*, 2939–2957.

(41) Kim, H.; Im, S. H.; Park, N. Organolead Halide Perovskite : New Horizons in Solar Cell Research. *J. Phys. Chem. C* **2014**, *118*, 5615–5625.

(42) Jung, K.; Lee, J.; Kim, J.; Chae, W. S.; Lee, M. J. Solution-Processed Flexible Planar Perovskite Solar Cells: A Strategy to Enhance Efficiency by Controlling the ZnO Electron Transfer Layer, PbI2phase, and CH3NH3PbI3morphologies. *J. Power Sources* **2016**, *324*, 142–149.

(43) Taame Abraha Berhe, Wei-Nien Su, Ching-Hsiang Chen, Chun-Jern Pan, Ju-Hsiang Cheng, Hung-Ming Chen, Meng-Che Tsai, Liang-Yih Chen, A. A. D. and B.-J. H. Organometal Halide Perovskite Solar Cells: Degradation and Stability. *Energy Environ. Sci.* **2016**, *9*, 323–356.

(44) Chen, B.; Yang, M.; Priya, S.; Zhu, K. Origin of J-V Hysteresis in Perovskite Solar Cells. *J. Phys. Chem. Lett.* **2016**, *7*, 905–917.

(45) Ameen, S.; Nazeeruddin, M. K. Perovskite Solar Cells: Influence of Hole Transporting Materials on

Power Conversion Efficiency. *ChemSusChem* **2016**, *9*, 10–27.

(46) Hui-Seon Kim, Chang-Ryul Lee, In-Hyuk Jang, Weekyung Kang, and N.-G. P. Effect of Overlayer Thickness of Hole Transport Material on Photovoltaic Performance in Solid-Sate Dye-Sensitized Solar Cell. *Bull. Korean Chem. Soc.* **2012**, *33*, 670–674.

(47) Kim, G. W.; Shinde, D. V.; Park, T. Thickness of the Hole Transport Layer in Perovskite Solar Cells: Performance versus Reproducibility. *RSC Adv.* **2015**, *5*, 99356–99360.

(48) Bi, D.; Yang, L.; Boschloo, G.; Hagfeldt, A.; Johansson, E. M. J. Effect of Different Hole Transport Materials on Recombination in CH 3NH3PbI3 Perovskite-Sensitized Mesoscopic Solar Cells. *J. Phys. Chem. Lett.* **2013**, *4*, 1532–1536.

(49) Facchetti, A. π-Conjugated Polymers for Organic Electronics and Photovoltaic Cell Applications. *Chem. Mater.* **2011**, *23*, 733–758.

(50) Abdallah, M.; Le, H.; Hijazi, A.; Schmitt, M.; Graff, B.; Dumur, F.; Bui, T. T.; Goubard, F.; Fouassier, J. P.; Lalevée, J. Acridone Derivatives as High Performance Visible Light Photoinitiators for Cationic and Radical Photosensitive Resins for 3D Printing Technology and for Low Migration Photopolymer Property. *Polymer (Guildf).* **2018**, *159*, 47–58.

(51) Bi, D.; Li, X.; Milić, J. V.; Kubicki, D. J.; Pellet, N.; Luo, J.; LaGrange, T.; Mettraux, P.; Emsley, L.; Zakeeruddin, S. M.; *et al.* Multifunctional Molecular Modulators for Perovskite Solar Cells with over 20% Efficiency and High Operational Stability. *Nat. Commun.* **2018**, *9*, 1–10.

(52) Balta, D. K.; Arsu, N.; Yagci, Y.; Jockusch, S.; Turro, N. J. Thioxanthone−Anthracene: A New Photoinitiator for Free Radical Polymerization in the Presence of Oxygen. *Macromolecules* **2007**, *40*, 4138–4141.

(53) Balta, D. K.; Arsu, N. Photodimerization of Thioxanthone-Anthracene: Formation of Monochromophoric Type II Initiator. *Des. Monomers Polym.* **2016**, *19*, 222–226.

(54) Temel, G.; Arsu, N.; Yagci, Y. Polymeric Side Chain Thioxanthone Photoinitiator for Free Radical Polymerization. *Polym. Bull.* **2006**, *57*, 51–56.

(55) Yilmaz, G.; Tuzun, A.; Yagci, Y. Thioxanthone-Carbazole as a Visible Light Photoinitiator for Free Radical Polymerization. *J. Polym. Sci. Part A Polym. Chem.* **2010**, *48*, 5120–5125.

(56) Yilmaz, G.; Aydogan, B.; Temel, G.; Arsu, N.; Moszner, N.; Yagci, Y. Thioxanthone-Fluorenes as Visible Light Photoinitiators for Free Radical Polymerization. *Macromolecules* **2010**, *43*, 4520–4526.

(57) Wang, Z.; Li, Y.; Cai, X.; Chen, D.; Xie, G.; Liu, K. K.; Wu, Y. C.; Lo, C. C.; Lien, A.; Cao, Y.; *et al.* Structure-Performance Investigation of Thioxanthone Derivatives for Developing Color Tunable Highly Efficient Thermally Activated Delayed Fluorescence Emitters. *ACS Appl. Mater. Interfaces* **2016**, *8*, 8627–8636.

(58) Wang, H.; Xie, L.; Peng, Q.; Meng, L.; Wang, Y.; Yi, Y.; Wang, P. Novel Thermally Activated Delayed Fluorescence Materials-Thioxanthone Derivatives and Their Applications for Highly Efficient OLEDs. *Adv. Mater.* **2014**, *26*, 5198–5204.

(59) Jeon, Y. P.; Kim, K. S.; Lee, K. K.; Moon, I. K.; Choo, D. C.; Lee, J. Y.; Kim, T. W. Blue Phosphorescent Organic Light-Emitting Devices Based on Carbazole/Thioxanthene-S,S-Dioxide with a High Glass Transition Temperature. *J. Mater. Chem. C* **2015**, *3*, 6192–6199.

(60) Wutzel, H.; Jarvid, M.; Bjuggren, J. M.; Johansson, A.; Englund, V.; Gubanski, S.; Andersson, M.

R. Thioxanthone Derivatives as Stabilizers against Electrical Breakdown in Cross-Linked Polyethylene for High Voltage Cable Applications. *Polym. Degrad. Stab.* **2015**, *112*, 63–69.

(61) Nazir, R.; Balčiunas, E.; Buczyńska, D.; Bourquard, F.; Kowalska, D.; Gray, D.; Maćkowski, S.; Farsari, M.; Gryko, D. T. Donor-Acceptor Type Thioxanthones: Synthesis, Optical Properties, and Two-Photon Induced Polymerization. *Macromolecules* **2015**, *48*, 2466–2472.

(62) Cokbaglan, L.; Arsu, N.; Yagci, Y.; Jockusch, S.; Turro, N. J. 2-Mercaptothioxanthone As a Novel Photoinitiator for Free Radical Polymerization. *Macromolecules* **2003**, *36*, 2649–2653.

(63) G. Neumann, M.; H. Gehlen, M.; V. Encinas, M.; S. Allen, N.; Corrales, T.; Peinado, C.; Catalina, F. Photophysics and Photoreactivity of Substituted Thioxanthones. *J. Chem. Soc. Faraday Trans.* **1997**, *93*, 1517–1521.

(64) Fouassier, J.; Ruhlmann, D. Relations Structure-Properties Dans Les Photoamorceurs de Polymerisation-7.Interactions Photosensibilisateur/Photoamorceurs Dans Des Milieux Photopolymerisables. *Eur. Polym. J.* **1993**, *29*, 505–512.

(65) Ishijima, S.; Higashi, M.; Yamaguchi, H. Magnetic Circular Dichroism and Circular Dichroism Spectra of Xanthones. *J. Phys. Chem.* **1994**, *98*, 10432–10435.

(66) Ley, C.; Morlet-Savary, F.; Jacques, P.; Fouassier, J. P. Solvent Dependence of the Intersystem Crossing Kinetics of Thioxanthone. *Chem. Phys.* **2000**, *255*, 335–346.

(67) Rai-Constapel, V.; Kleinschmidt, M.; Salzmann, S.; Serrano-Andrés, L.; Marian, C. M. Thioxanthone: On the Shape of the First Absorption Band. *Phys. Chem. Chem. Phys.* **2010**, *12*, 9320–9327.

(68) Shizuo Ishijima, Miwako Higashi, Hiroyuki Yamaguchi, Mari Kubota, T. K. The Photoelectron Spectra of Xanthone, Thioxanthone, and Acridone. *J. Electron Spectros. Relat. Phenomena* **1996**, *82*, 71–74.

(69) Mundt, R.; Villnow, T.; Ziegenbein, C. T.; Gilch, P.; Marian, C.; Rai-Constapel, V. Thioxanthone in Apolar Solvents: Ultrafast Internal Conversion Precedes Fast Intersystem Crossing. *Phys. Chem. Chem. Phys.* **2016**, *18*, 6637–6647.

(70) Green, W. *Industrial Photoinitiators*; 2010.

(71) A, E. S. S.; Tsai, E. W.; Throckmorton, L.; Rajeshwar, K.; Mckellar, R.; Baar, M.; Kluba, M.; Marynick, D. S.; Ternay, A. L. ELECTROCHEMISTRY OF THIOXANTHENE, THIOXANTHONE AND RELATED COMPOUNDS IN ACETONITRILE. *J. Electroanal. Chem.* **1986**, *210*, 45–67.

(72) García, G.; Fern, M. P.; Fern, M. Theoretical Study of the Effect of Alkyl and Alkoxy Lateral Chains on the Structural and Electronic Properties of π -Conjugated Polymers. **2010**, 0–8.

(73) Kasparas Rakstys, Michael Saliba, Peng Gao, Paul Gratia, Egidijus Kamarauskas, Sanghyun Paek, Vygintas Jankauskas, and M. K. N. Highly Efficient Perovskite Solar Cells Employing an Easily Attainable Bifluorenylidene-Based Hole-Transporting Material. *Angew. Chemie - Int. Ed.* **2016**, *55*, 7464–7468.

(74) Brunetti, F. G.; Gong, X.; Tong, M.; Heeger, A. J.; Wudl, F. Strain and Hückel Aromaticity: Driving Forces for a Promising New Generation of Electron Acceptors in Organic Electronics. *Angew. Chemie - Int. Ed.* **2010**, *49*, 532–536.

(75) Choi, H.; Do, K.; Park, S.; Yu, J. S.; Ko, J. Efficient Hole Transporting Materials with Two or Four

N,N-Di(4-Methoxyphenyl)Aminophenyl Arms on an Ethene Unit for Perovskite Solar Cells. *Chem. - A Eur. J.* **2015**, *21*, 15919–15923.

(76) So Kawata, Junki Furudate, Takuya Kimura, Hiroko Minaki, Ayaka Saito, H. K. and Y.-J. P. Controlling the Excited-State Energy Levels of 9,9′-Bifluorenylidene Derivatives by Twisting Their Structure to Attaining Singlet Fission Character in Organic Photovoltaics. *J. Mater. Chem. C* **2017**, *5*, 4909–4914.

(77) Smith, M. B.; Michl, J. Singlet Fission. *Chem. Rev.* **2010**, *110*, 6891–6936.

(78) Ozturk, T.; Ertas, E.; Mert, O. Use of Lawesson's Reagent in Organic Syntheses. *Chem. Rev.* **2007**, *107*, 5210–5278.

(79) Cherkasov, R. a.; Kutyrev, G. a.; Pudovik, A. N. Organothiophosphorous Reagents in Organic Synthesis. *Tetrahedron* **1985**, *41*, 2567–2624.

(80) Cava, M. P.; Levinson, M. I. Thionation Reactions of Lawesson's Reagents. *Tetrahedron* **1985**, *41*, 5061–5087.

(81) Lakshmikantham, M. V; Levinson, M.; Menachery, M.; Cava, M. P. Thioquinones. Generation of Dithioanthraquinone. *J. Org. Chem.* **1986**, *51*, 411–412.

(82) Shabana, R.; Boulos, L. S.; Shaker, Y. M. The Reaction of Lawesson's Reagent with Trihydroxy Compounds. *Heteroat. Chem.* **1999**, *10*, 1–6.

(83) Olefination, B. Barton-Kellogg Olefination. **2010**, 249–253.

(84) ter Wiel, M. K. J.; Vicario, J.; Davey, S. G.; Meetsma, A.; Feringa, B. L. New Procedure for the Preparation of Highly Sterically Hindered Alkenes Using a Hypervalent Iodine Reagent. *Org. Biomol. Chem.* **2005**, *3*, 28.

(85) Michael Saliba, Simonetta Orlandi, Taisuke Matsui, Sadig Aghazada, Marco Cavazzini, Juan-Pablo Correa-Baena, Peng Gao, Rosario Scopelliti, Edoardo Mosconi, Klaus-Hermann Dahmen, Filippo De Angelis, Antonio Abate, Anders Hagfeldt, Gianluca Poz, M. G. and M. K. N. A Molecularly Engineered Hole-Transporting Material for Efficient Perovskite Solar Cells. *Nat. Energy* **2016**, *1*, 15017.

(86) M. Degbia, M.Ben Manaa, B. Schmaltz, n, N.Berton, J. Bouclé , R. Antony, F. T. Carbazole-Based Hole Transporting Material for Solid State Dye-Sensitized Solar Cells: Influence of the Purification Methods. *Mater. Sci. Semicond. Process.* **2016**, *43*, 90–95.

(87) Özlem Usluer, Mamatimin Abbas, Guillaume Wantz, Laurence Vignau, Lionel Hirsch, Eftychia Grana, Cyril Brochon, Eric Cloutet, and G. H. Metal Residues in Semiconducting Polymers: Impact on the Performance of Organic Electronic Devices. *ACS Macro Lett.* **2014**, *3*, 1134–1138.

(88) McMurry, J. E. Carbonyl-Coupling Reactions Using Low-Valent Titanium. *Chem. Rev.* **1989**, *89*, 1513–1524.

(89) Mc Murry, J. E. Organic Chemistry of Low-Valent Titanium. *Acc. Chem. Res.* **1974**, *7*, 281–286.

(90) Czako, B. K. L. *Stategic Applications of Named Reactions in Organic Synthesis*; Elsevier academic press, 2005.

(91) McMurry, J. E.; Fleming, M. P.; Kees, K. L.; Krepski, L. R. Titanium-Induced Reductive Coupling of Carbonyls to Olefins. *J. Org. Chem.* **1978**, *43*, 3255–3266.

(92) Duan, X. F.; Zeng, J.; Lü, J. W.; Zhang, Z. Bin. Insights into the General and Efficient Cross McMurry Reactions between Ketones. *J. Org. Chem.* **2006**, *71*, 9873–9876.

(93) Villiers, C.; Ephritikhine, M. New Insights into the Mechanism of the McMurry Reaction. *Angew. Chem. Int. Ed. Engl.* **1997**, *36*, 2380–2382.

(94) Furstner, A. *Active Metals: Preparation, Characterization and Applications*; Furstner, A., Ed.; VCH.

(95) Edmonds, M.; Abell, A. *Modern Carbonyl Olefination*; 2004.

(96) Furstner, A. The McMurry Reaction and Related Transformations. In *Transition metals for organic synthesis*; Beller, M.; Bolm, C., Eds.; VCH, 1998; pp. 381–401.

(97) Shirota, Y. Photo- and Electroactive Amorphous Molecular Materials—molecular Design, Syntheses, Reactions, Properties, and Applications. *J. Mater. Chem.* **2005**, *15*, 75–93.

(98) Hiroshi Kageyama, Hitoshi Ohishi, Masatake Tanaka, Y. O. and Y. S. High-Performance Organic Photovoltaic Devices Using a New Amorphous Molecular Material with High Hole Drift Mobility, Tris[4-(5-Phenylthiophen-2-Yl)Phenyl]Amine. *IEEE* **2010**, *16*, 1528–1536.

(99) Brownson, D. A. C.; Banks, C. E. *The Handbook of Graphene Electrochemistry*; 2014.

(100) Cohen, Y.; Klein, J.; Rabinovitz, M. Stable Polycyclic Anions: Dianions from Overcrowded Ethylenes. *J. Chem. Soc. Chem. Commun.* **1986**, 1071–1073.

(101) Pogodin, S.; Agranat, I. Overcrowding Motifs in Large PAHs. An Ab Initio Study. *J. Org. Chem.* **2002**, *67*, 265–270.

Chapter IV

Planar Donor-Acceptor

Hole transporting materials

CHAPTER 4: DONOR-ACCEPTOR HTMs WITH THIENO [3,4-c]PYRROLE-4,6-DIONE

IV.1. Introduction and objectives

As aforementioned, donor-acceptor conjugated small molecules provide number of advantages such as strong intramolecular charge-transfer (ICT), adjustable energy levels for an appropriate energy alignment with the perovskite absorber, therefore modifiable optical and electrochemical properties. Remarkable, D-A conjugated molecules with planar structure could enhance intermolecular interaction in solid thin film and thus improving charge carrier mobility.

The D-A approach not only allows effective tuning the bandgap but also adjusts frontier molecular energy of push-pull molecules. The design, synthesis and incorporation of adequate donor and acceptor units are important factors in developing D-A molecules as efficient HTMs in PSCs. Although both the donor and acceptor units affect to energy levels through orbital hybridization, the HOMO and LUMO are still significantly localized on the donor and acceptor units, respectively. Electron donor moieties have been chosen to adjust HOMO levels and compatible to the valence band of perovskite layer. The choice of acceptor units would impact to the exciton dissociation and electron blocking property to the conductance band of perovskite. Depending on strong/weak donor-acceptor interactions, they could lead to high/low electron delocalization properties and enhance/reduce charge mobilities-conductivities. Therefore, many researches of adequate donor and acceptor units have been carried out on structure-property relationship to optimize device performances

In literature, benzodithiophene[1] (BDT), dithienothiophene[2] (DTT), carbazole[3] (Cbz), dithienosilole[4] (DTS), dithieno[3,2-*b*:2',3'-*d*]pyrrole[5,6] (DTP) and triarylamine[7] are representative examples of strong electron-donating moieties[8] (***Figure 1***) . They have been employed as electron-donor building blocks for either donor materials or D-A materials of multi-disciplinary organic electronics such as organic photovoltaics[9,10], ambipolar field-effect transistors (FETs)[11], OLEDs[12] and so on. In organic photovoltaics domain, these donor blocks have just applied in bulk heterojunction polymer solar cells, but rarely studied in perovskite solar cells (PSCs). However, they could be prominent materials for PSCs. Up to date, triarylamine is still versatile platform for organic, dye-sensitized and perovskite solar cells[13].

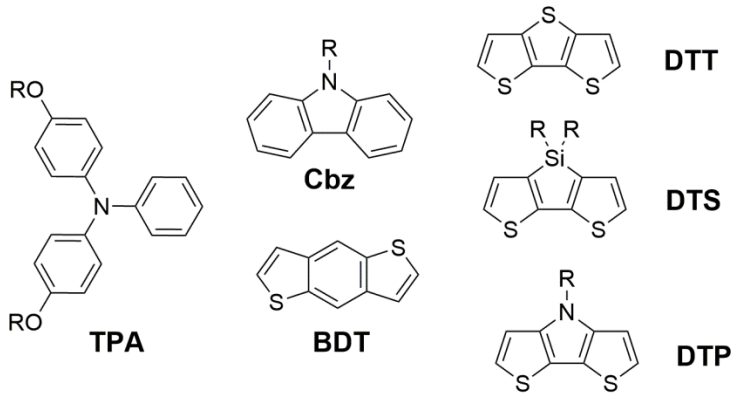

Figure 1: Representative of electron-donating blocks for D-A molecules.

Concerning acceptor blocks, they have been widely applied in bulk heterojunction polymer solar cells but they are severely limited in PSCs. For example, 1,4-diketopyrrolopyrrole (DPP)[14–16], 2,1,3-benzothiadiazole (BT)[17–20], isoindigo (ID)[21–23], thienoisoindoledione (TID)[24,25], bithiopheneimide (BTI)[26–28] and their derivatives are outstanding strong electron-withdrawing and have been constructed in conjugated polymers and conjugated small molecules. In particular, these imide-functionalized aromatic such as thienoisoindoledione (TID), thieno[3,4-c]pyrrole-4,6-dione (TPD), bithiopheneimide (BTI) are attractive acceptor units (***Figure 2***). They are strong electron acceptor units and could be used as a central π-bridge or terminal units in D-A molecules.

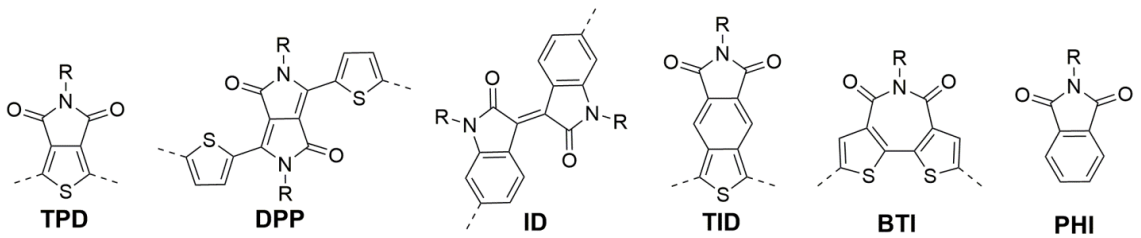

Figure 2: Representative imide-functionalized arenes as electron-acceptor blocks for D-A structure.

Furthermore, N-alkylation of imide backbone will improve solubility and solid-state packing without disrupting close π-π stacking which is required for efficient carrier transport. Especially, if these acceptors units are incorporated to thiophene and its derivatives, intramolecular S…O interactions involving correspond imide C=O groups and the neighbor S atoms can occur as configuration "locks" to enhance π-system coplanarity[29–31]. Among them, thieno[3,4-*c*]pyrrole-4,6-dione[32–36] (TPD) could be promising acceptor unit due to its geometry and small aromatic resonance energy, promote quinoidal character[37] to achieve favorable properties such as high backbone coplanarity, enhance electron delocalization and reduce bandgap of target molecules. According to these favorable characteristics, planar-rigid-fully conjugated molecules

would be constructed and they are expected to improve π-π stacking effect which is beneficial for π-electron delocalization (***Figure 3***).

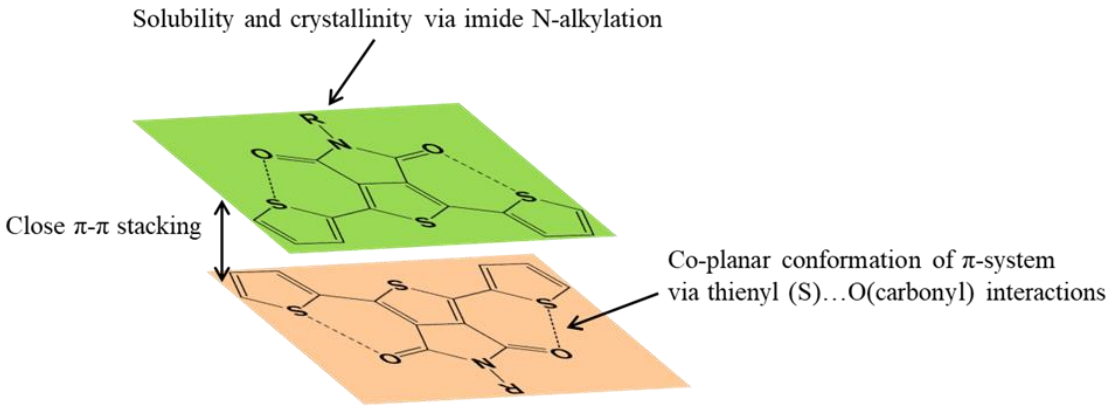

Figure 3: D-A strategy of imide-functionalized small molecules.

In this chapter, these studied molecules are composed by strong electron-donor unit TPA and strong electron-deficient unit TPD and linked by different length of π-spacer. In literature, numerous studies of molecular modification such as alternating electron-rich or electron-poor moieties-substitution, size of π-conjugation systems, steric geometry and charge carrier mobility have been investigated. However, the investigation of π-bridge has been rarely mentioned[38,39] . This is also one of the crucial factors which influence to charge transport property as well as photovoltaic performance. As studied in ***chapter II***, thiophene and thieno[3,2-*b*]thiophene have been widely used as π-linker as well as electron-donor moiety. Additionally, among of fused thiophene rings, dithienothiophenes and dithieno[3,2-*b*:2',3'-*d*]pyrrole are also prominent electron-rich building block as well as good π-conjugation linker for organic materials. Therefore, in this study, thiophene, thieno[3,2-*b*]thiophene and dithieno[3,2-*b*:2',3'-*d*]pyrrole have been subjected as π-linkers. The impact of the chemical nature and the different lengths on their properties will be discussed below.

In this chapter, four new compounds based on strong push-pull molecules were designed and synthesized. Their chemical structures are shown in ***Figure 4***. More specifically, The methoxy group (-OCH_3) is replaced by methylthio group (-SCH_3) to compare resonance effects. Furthermore, sulfur atoms in –SCH_3 are expected for good interfacial contact with perovskite absorber. TPA-O(or S)CH_3 were selected as electron-donating units. Thus, some previous studies demonstrated that holes were generated under illumination which would be rapidly localized on the sulfur atoms and formed sulfide radical species[40]. Then, this trapped holes will quickly transfer from perovskite

absorber to back contact and therefore improving hole transport property[41–43]. Moreover, lone pair of the sulfur atoms can interact through electronic attraction with the positive charge of the metal in perovskite layer and this passivation effect will improve the photovoltaic performance along with reducing hysteresis[44]. Thieno[3,4-*c*]pyrrole-4,6-dione (TPD) was served as electron-accepting unit. Thiophene, thieno[3,2-b]thiophene and dithieno[3,2-*b*:2',3'-*d*]pyrrole are chose and compared as variety π-linker length. These molecules have been studied and expected to have some following properties.

- Firstly, they are expected to have strong intramolecular charge transfer, low optical band gap and low-lying HOMO energy level to compatible with valence band of perovskite absorber.
- Secondly, they possess planar structures and good solubility. This could promote for strong π-π stacking effect; enhance intermolecular charge transfer and HTM/perovskite interfaces.
- Thirdly, these molecules are well-developed conjugation systems, thus they are foreseen high hole mobility and conductivity materials.
- Finally, they are expected to employ in PSCs without using dopants/additives. By their physical properties, we can discuss about possibilities for dopant-free HTMs.

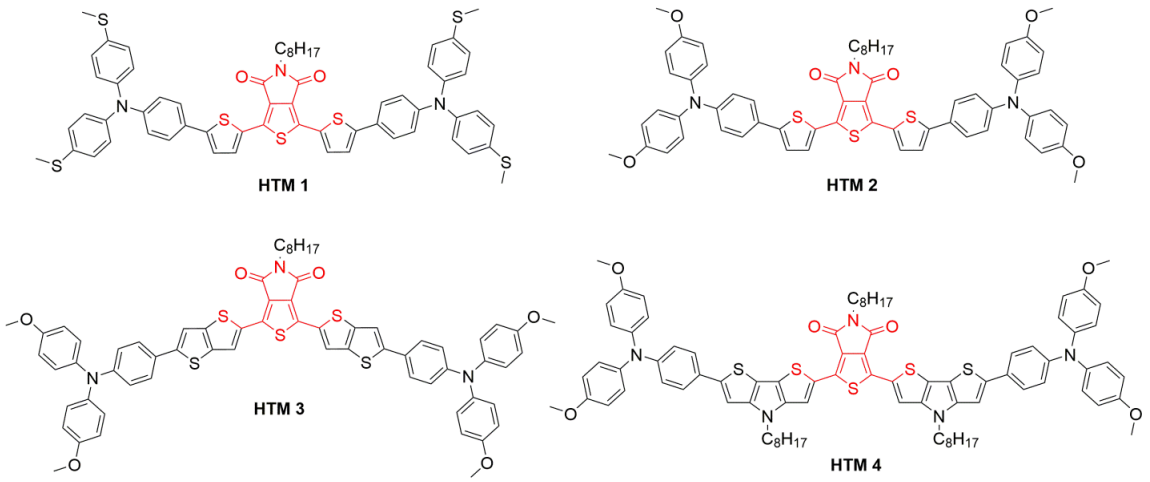

Figure 4: Studied molecules planar structure based TPD.

IV.2. Strategies

These molecules were synthesized based on some classical reactions such as Bromide-Lithium exchange reaction and Stille coupling reaction. These reactions requires to work up in inert atmosphere such as n-BuLi / -78°C / THF and continuously supply argon.

Firstly, 4-bromo-N,N-bis(4-(methylthio)phenyl)aniline (compound 1) was synthesized by similar protocol[45] to that for the synthesis of 4-bromo-N,N-bis(4-methoxyphenyl)aniline (compound 2) which was mentioned in previous chapters. Its procedure was briefly described in experimental section.

Secondly, some of intermediate compounds have been prepared prior to synthesis of target HTMs. In particular, 4-octyl-4H-dithieno[3,2-*b*:2',3'-*d*]pyrrole has been synthesized according protocol in literature[46]. Long alkyl chain (-C_8H_{17}) was used to improve solubility of final compounds. Then, compound 4 was synthesized by Bromide-Lithium exchange reaction (***Scheme 1***). Similarly, compound 3 was synthesized by similar protocol via commercial product thieno[3,2-b]thiophene. In detail, compound 3 and 4 were synthesized under controlled conditions (dried THF, -78°C, under supplied Argon) and equivalents (0.9 eq of n-BuLi and 0.9 eq of Cl-$SnBu_3$, dropwise in an hour) because of symmetric structure and highly active of H-proton in α-position of precursors DTP and thieno[3,2-b]thiophene. Compound 3, compound 4 and their isomers (two – $SnBu_3$ substituted) were obtained with medium yields. However, both of these compounds 3 and 4 were directly used for next steps without losing in column purification.

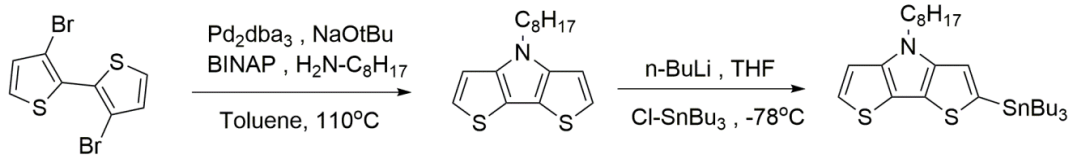

3,3'-dibromo-2,2'-bithiophene 4-octyl-4*H*-dithieno[3,2-*b*:2',3'-*d*]pyrrole compound **4**

Scheme 1: Synthesis of DTP and compound 4.

Thirdly, 1,3-dibromo-5-octyl-4H-thieno[3,4-c]pyrrole-4,6(5H)-dione (TPD-2Br) was synthesized via bromination of commercial available product 5-octyl-4H-thieno[3,4-c]pyrrole-4,6(5H)-dione (TPD) based on previous studied[47] and is described in ***Scheme 2***. It is difficult to do halogenation of TPD by various bromination conditions such as NBS/chloroform-acetic acid, NBS/DMF/70°C, Br_2/acetic acid/130°C, Br_2-I_2/H_2SO_4 because none of them were worked and no desired product was obtained.

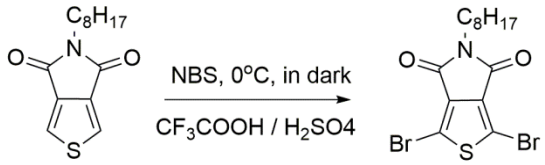

TPD TPD-2Br

Scheme 2: Synthesis of TPD-2Br

In literature[47], they mentioned that TPD could be halogenated by NBS and mixture of sulfuric acid/trifluoroacetic acid as solvent but did not report proportion of two strong acids. Therefore, the yield of title product was not high and quantitative losing in purification. In literature, a study of solvents for the bromination reaction of deactivated aromatic compounds has been done[48] and demonstrated that ratio of those acids would be significantly affected to final compound. For instance, TPD is classified as one of deactivated aromatic compounds. For this bromination, trifluoroacetic acid CF_3COOH was chose as most effective solvent, with NBS as reactant and catalytic H_2SO_4 as the active source of electrophilic bromine. By this study, they showed the efficiency of the reaction is depended on the concentration of sulfuric acid. Without H_2SO_4, the reaction does not occur, but if the ratio in volume of H_2SO_4/CF_3COOH is higher than 0.4, hydrolysis of the trifluoromethyl group begins to be observed[49] and a ratio between 0.3 and 0.4 allows a good conversion. In this synthetic route, the optimized ratio of H_2SO_4 : CF_3COOH is 0.33. High yielded TPD-Br compound is obtained and recrystallized in methanol without further column purification. This intensive study is also useful applied for various deactivated aromatic compounds.

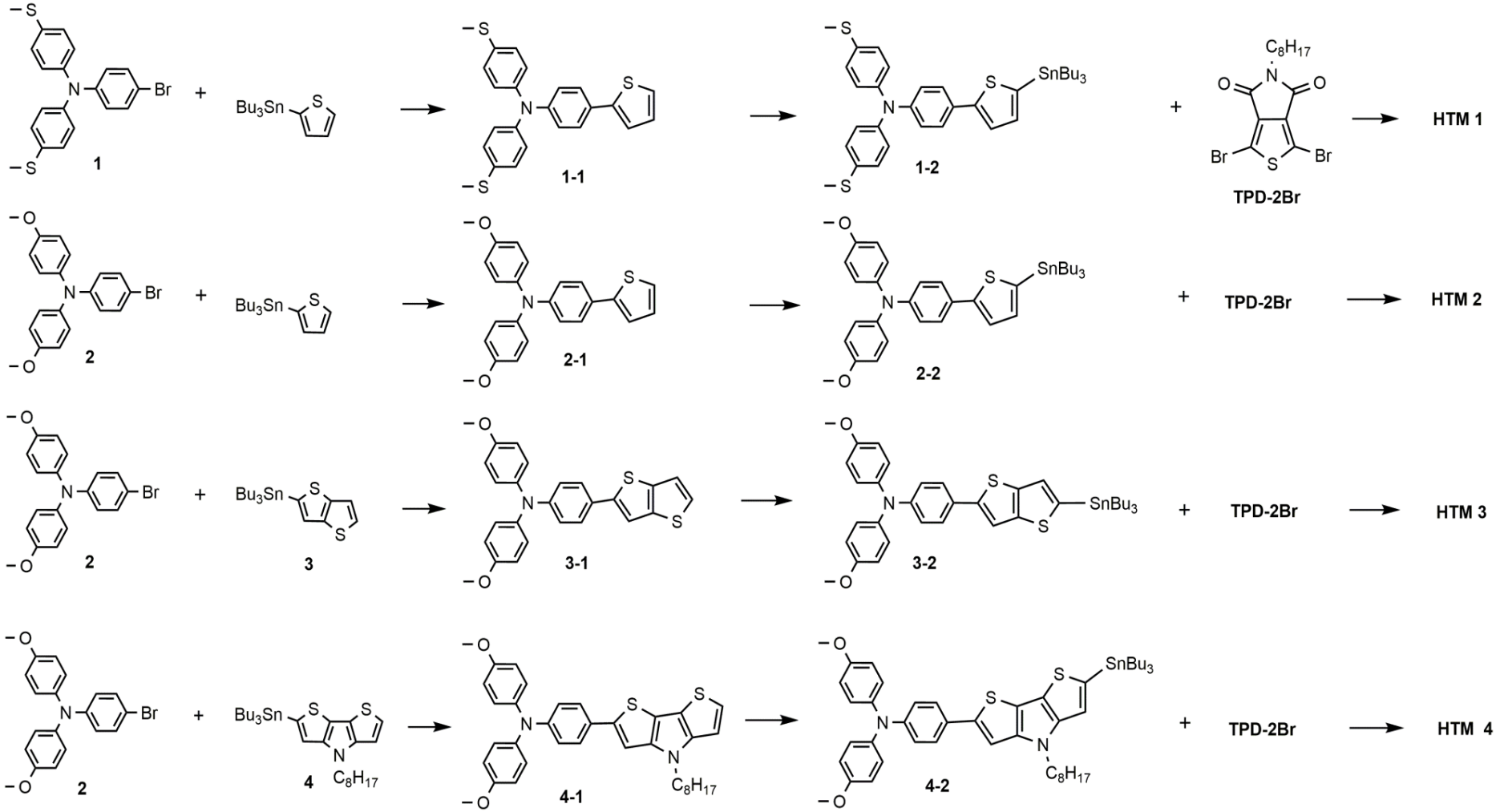

Scheme 3: Synthetic route of TPD-based planar structure molecules. Conditions and reagents: Stille coupling reaction: $Pd(PPh_3)_4$, Toluene, 110°C, 24h and Lithium-brom exchange reaction: n-BuLi, THF, -78°C, Cl-$SnBu_3$, 8h.

However, due to symetricical structure of Thieno[3,2-b]thiophene, it is difficult to conduct synthesis of compound 3-1. According to ***Scheme 3***, compound 3-1 had been synthesized as this procedure, the reaction is only obtained overall of 16% yield. Therefore, it has been optimized by synthetic route in ***Scheme 4***. Even one step longer than previous procedure, the advantage of this way is improved efficiency of overall reactions up to 90%. Because in thieno[3,2-b]thiophene, the activity of two hydrogen atoms at α-position are similar, therefore it is necessary to protect one side reaction by TIPSCl as a protective group[50] with high yield (88%). Then, another side of thieno[3,2-b]thiophene is reacted to tributyltin chloride and followed by Stille coupling reaction. Finally, the protective group is cleaved by desilylation of TBAF in THF and obtain quantitative amount of compound 3-1 (90% yield).

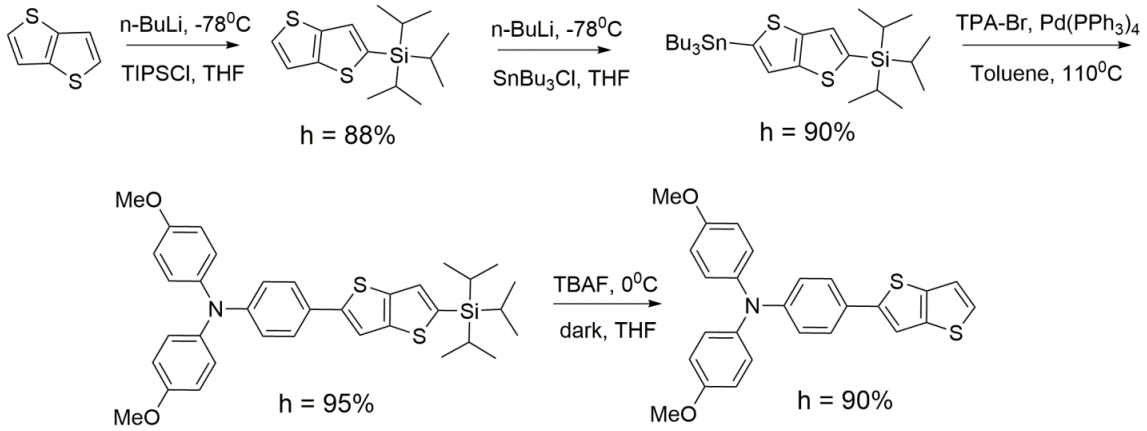

Scheme 4: Optimized procedure to synthesis of compound 3-1 in high yield.

Finally, these target compounds (HTM 1-4) were synthesized (***Scheme 3***) by Stille coupling reaction and purified by column chromatography with moderate yields. As expected, due to highly conjugated molecules, all new compounds exhibited strong fluorescence effect in daylight and under UV light. Their structures are characterized by NMR, HRMS and their properties was investigated by absorption-emission, cyclic voltammetry, AFM and then DFT calculations will be used to investigate and compare to experimental results.

IV.3. Results and discussion

IV.3.1 Optical properties

The optical properties of these compounds have been investigated by absorption and emission spectroscopy in solution and on thin film (***Figure 5*** and ***Figure 6***). Relevant data are summarized in ***Table 1***.

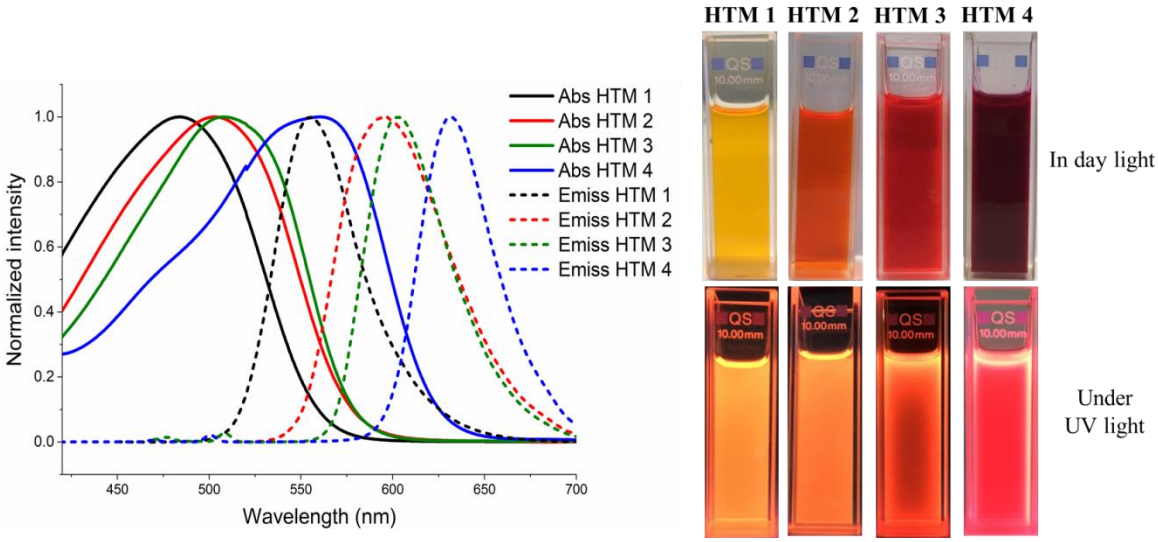

Figure 5: Normalized absorption- emission in solution of studied molecules in diluted dichloromethane (left) and in the right, appearance of these solutions in daily light (top) and under UV 365 nm (bottom).

All of these compounds exhibit strong absorption in visible domain with absorption maxima are 483, 502, 511 and 561 nm for HTM 1, HTM 2, HTM 3 and HTM 4, respectively. As expected, these molecules showed intense intramolecular charge transfer (ICT) characteristics. While replacing thiomethyl group (-SCH_3) in HTM 1 by methoxy group (-OCH_3) in HTM 2, it leads to 19 nm red-shifted. It could be explained due to electron donating ability of–SCH_3 is weaker[51] than the -OCH_3 unit. The absorption spectra of HTM 2 and HTM 3 are negligible changed when replace thiophene by thieno[3,2-b]thiophene as π-bridge. Interestingly, replacing thiophene by dithieno[3,2-*b*:2',3'-*d*]pyrrole, the $\lambda_{abs\ max}$ of HTM 4 is 60 nm redshifted compare to HTM 2 due to increasing π-conjugation length. Moreover, dithieno[3,2-b:2',3'-d]pyrrole is also electron donor groups. By increasing number of electron donating units, it is more redshifted in absorption spectra. Once increasing π-conjugation length, the energy band gaps of these molecules are reduced consequently (2.21 eV for HTM 1; 2.14 and 2.13 eV for HTM 2 and HTM 3 and 1.98 eV for HTM 4). The emission spectra are in agreement with the absorption spectra. All of these compounds exhibit strong fluorescence properties and they emitted in green-yellow region. From both absorption and emission spectra, the optical ban gap could be calculated by the absorption onset wavelength or intersection of absorption-emission spectra.

The appearances of these molecules are observed in daily light and under UV 365 nm. As a result, longer conjugation system, color change in absorption and emission are observed. The values of molar extinction coefficient (ε) were determined at wavelength of

absorption maxima and the values are listed in ***Table 1***. The relative high ε is attributed to the planarity of these molecules. From the absorption spectra of these compounds on film (***Figure 6***), it can be seen that there are no significant shifts on going from solution to the solid state of HTM 1 and HTM 2. It suggests that there's negligible aggregation phenomenon or π-π interaction between the conjugated main chains.

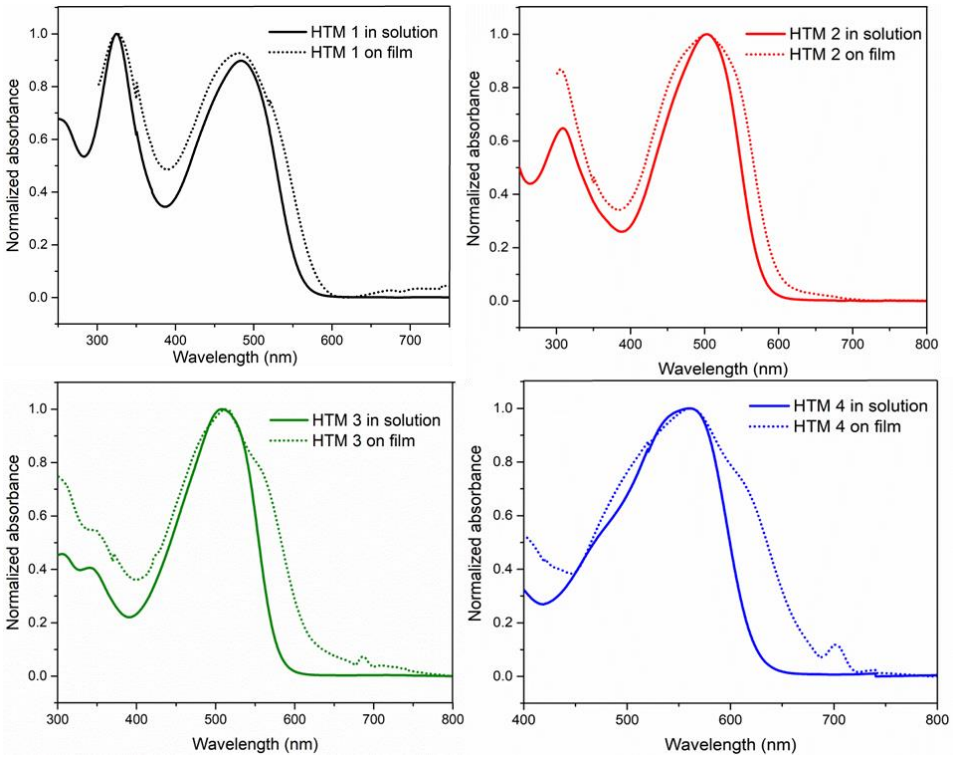

Figure 6: Normalized absorption spectra of HTM 1, HTM 2, HTM 3 and HTM 4 in dilute dichloromethane and on films.

However, absorption spectra of HTM 3 and HTM 4 film exhibited an additional shoulder in the long wavelength. It reveals the presence of a well-ordered assembly molecular in the solid state. This could induce π-π stacking effect which improve intermolecular charge transfer and hole mobility.

Because of these compounds absorb intensively in visible region, it could impact to screen effect to the perovskite absorber. Therefore, we prepared $MAPbI_3$ film on mp-TiO_2 and HTMs on $MAPbI_3$ and then compared their absorbance (***Figure 7***). Naturally, perovskite materials could absorb all incoming light in visible domain. These results indicated that all of their absorbance is overlapped under the absorption band of perovskites. Thus, it could avoid or no competition of absorption to perovskite absorber[52].

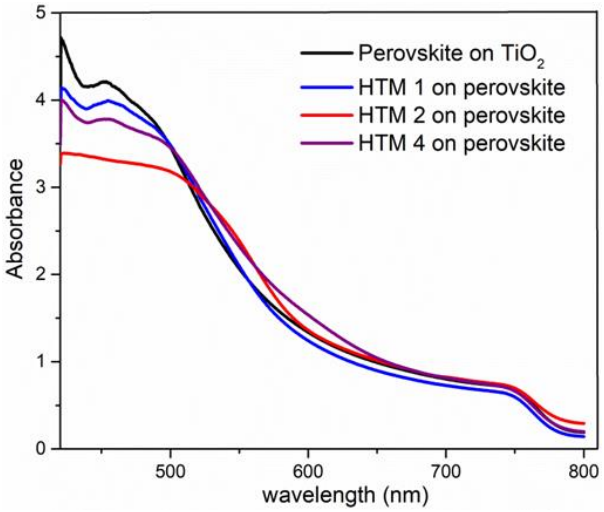

Figure 7: Comparison of absorbance of $MAPbI_3/TiO_2$ and HTMs/$MAPbI_3$ films.

IV.3.2 Electrochemical properties

The electrochemical properties of these compounds have been investigated in 0.1M tetrabutylammonium hexylfluorophosphate (n-Bu_4NPF_6) in dichloromethane solution by using cyclic voltammetry (CV) at a scan rate of 50 mV/s. Their oxidation CV are given in ***Figure 8*** and listed in ***Table 1***.

The cyclic voltammograms of these molecules shows multiple oxidation processes. The first oxidation signals are ascribed to the oxidation of the triphenylamine groups (TPA(OCH_3) or TPA(SCH_3)). In case of HTM 1, TPA(SCH_3) was oxidized at 0.36V while TPA(OCH_3) of HTM 2 was oxidized at 0.48V. It could be explained by the different of electron donating ability between –SCH_3 and –OCH_3. The interaction between the 3p orbital of S and the π-orbitals of carbon (in –SCH_3) is weaker than that between 2p orbital of O and the π-orbitals of carbon (in –OCH_3)[53]. Thus, when increasing strength of electron-rich units, the oxidation can be easier occurred. A comparison between HTM 2 and HTM 3 has been done when thiophene was replaced by thieno[3,2-b]thiophene. Due to rich electron moieties, HTM 3 was oxidized at lower potential (0.22V) than HTM 2. Similarly, by changing from thieno[3,2-b]thiophene (in HTM 3) to dithieno[3,2-*b*:2',3'-*d*]pyrrole (DTP) (in HTM 4), the first oxidation was reduced to 0.1V vs Fc/Fc^+.

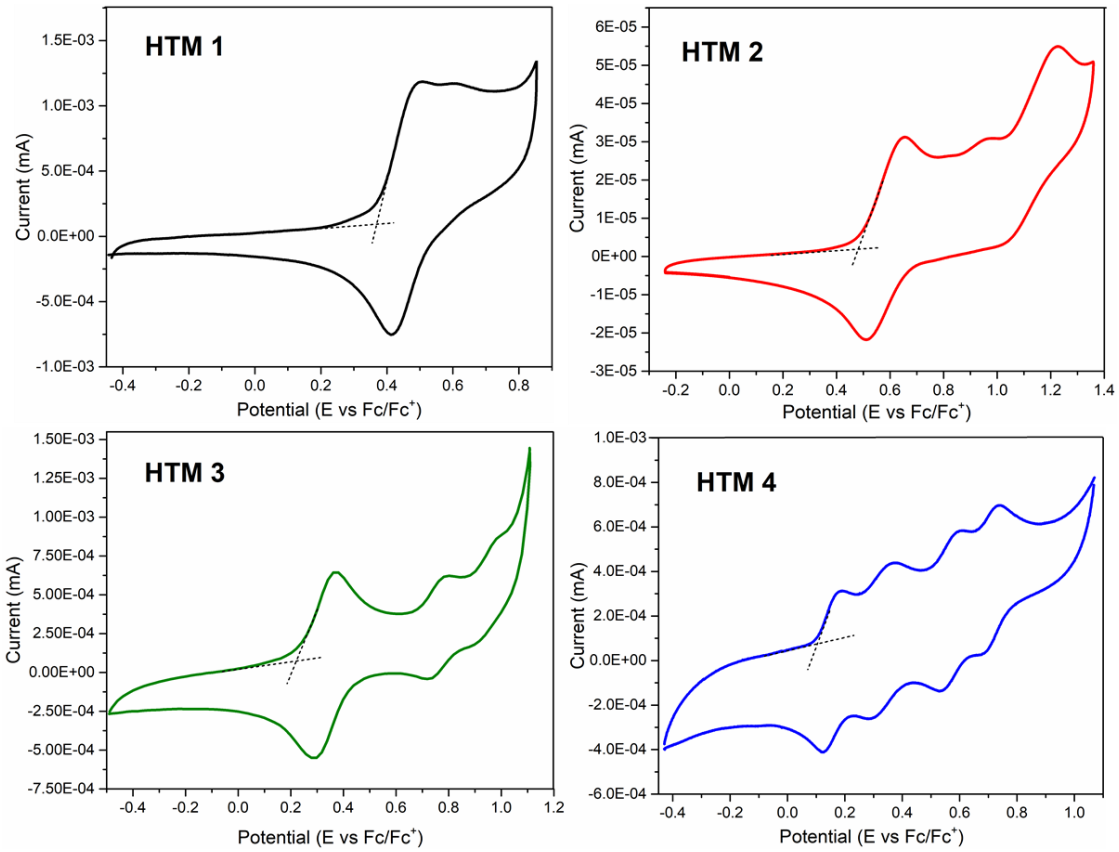

Figure 8: Cyclic voltammograms of studied molecules-based TPD measured in 0.1 M (n-Bu)$_4$N$^+$PF$_6^-$ electrolyte solution at scan rate 50 mV/s (the Fc/Fc$^+$ redox couple is used as internal standard).

Especially, CV of HTM 4 shows clearly multiple electron transfer processes. In which, two of first oxidation peaks could be attributed to oxidation of TPA species and two of last oxidation peaks were attributed to oxidized DTP moieties. Four single electron transfer processes were occurred consequently due to long and well π-conjugated electron localization in this molecule. The relatively low oxidation potential could be explained due to incorporation of electron-rich DTP units. This rigid, fused DTP ring results in extensive π-conjugation of the molecule, therefore it leads to low oxidation potential. In fact, increasing the conjugation length from thiophene (in HTM 2) to thieno[3,2-b]thiophene (HTM 3) and dithieno[3,2-*b*:2',3'-*d*]thiophene (in HTM 4) reduces significantly the oxidation potential. The HOMO energy levels of these molecules were calculated from the onset of the oxidation peak ($E^{ox\ onset}$) vs $E^{1/2}$ of Fc/Fc$^+$. The LUMO energy levels were estimated from the HOMO energy values and the optical band gaps. All related data are summarized in ***Table 1***.

	$\lambda_{abs\ max}$ (nm)	λ_{abs} onset	ε ($M^{-1}.cm^{-1}$)	λ_{emis} max	E_g (eV)	$E^{ox\ onset}$ (eV)	HOMO (eV)	LUMO (eV)
HTM 1	483	560	$1.05.10^5$	554	2.21	0.37	-5.17	-2.96
HTM 2	502	579	$0.96.10^5$	595	2.14	0.48	-5.28	-3.16
HTM 3	511	580	$0.92.10^5$	603	2.13	0.22	-5.02	-2.88
HTM 4	562	625	$0.92.10^5$	631	1.98	0.10	-4.90	-2.93

Table 1: Summary of the thermal, optical and electrochemical properties of compounds HTM 1-4. Absorption-emission spectra were recorded in dilute solution (~10^{-5} M in dichloromethane). Oxidation potentials were determined vs Fc/Fc^+; E_{HOMO} = -($E^{ox\ onset}$ + 4.8) eV. E_{LUMO} = E_g + E_{HOMO}. Optical band gaps were estimated from absorption edge of the product in solution.

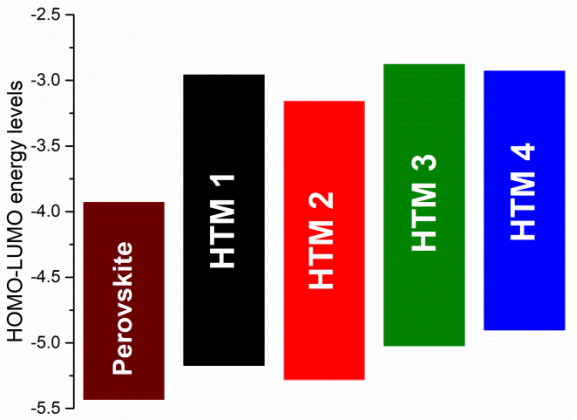

Figure 9: HOMO-LUMO energy levels of these molecules compare to perovskite.

From energy alignment diagram of these molecules (***Figure 9***), all HOMO energy levels are above valence band of perovskite layer. In fact, HOMO energy levels of HTM 1 and HTM 2 are closer than that of HTM 3 and HTM 4. This could be efficient for hole hopping process from perovskite to HTM. However, due to strong electron donating ability and well-conjugated molecules, HTM 3 and HTM 4 could possess high hole mobility and conductivity. Therefore, charge transport mobilities of these molecules should be measured to confirm above mentioned suggestion.

IV.3.3 AFM measurements

The film morphology of these compounds has been investigated in solid state by AFM measurements (***Figure 10***). All of them show smooth thin film average roughness in the range of 0.3 nm to 0.7 nm. They could provide good interface contact to perovskite layer. As mentioned above, they exhibit good π-π stacking effect in solid state. Indeed, these compounds can improve intermolecular charge transfer and hole mobility.

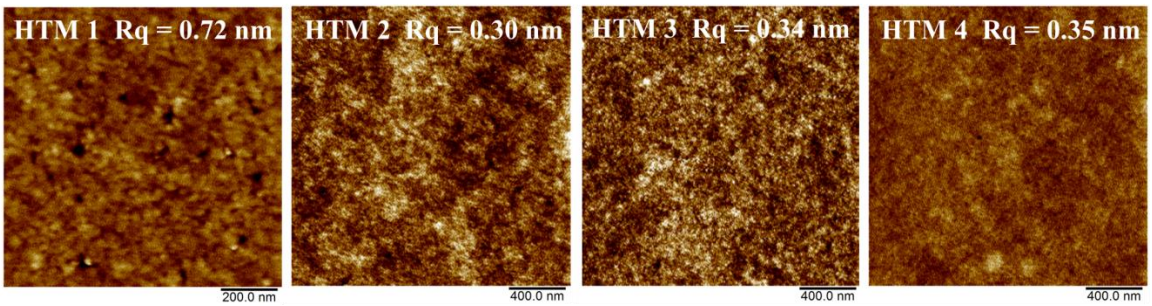

Figure 10: AFM images of these compounds coated on glass substrates.

Furthermore, the AFM images of the perovskite film on TiO_2, pristine PEDOT:PSS film, HTMs film on perovskite and HTMs on PEDOT:PSS were prepared and shown in ***Figure 11***. The results reveal that both the perovskite and PEDOT:PSS film are uniform but exhibit relatively high roughness. However, after coating thin layer of HTMs on the top of the perovskite and PEDOT:PSS layers, the surface becomes smoother with complete coverage by HTM.

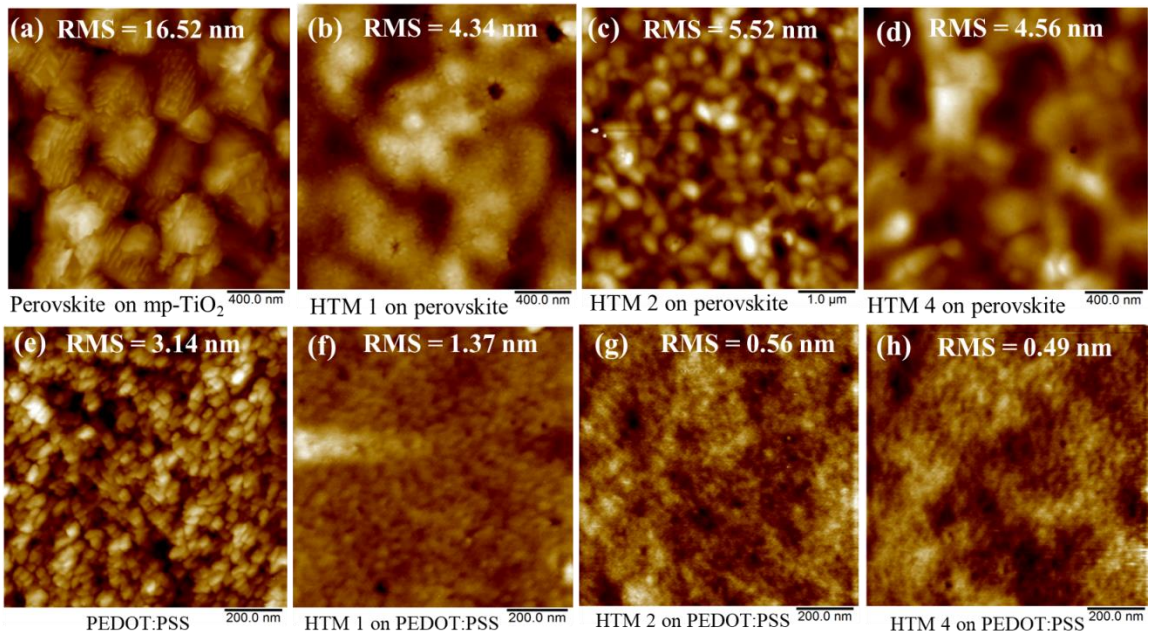

Figure 11: AFM images of $MAPbI_3$ on TiO_2 (a), HTM 1 on $MAPbI_3$ (b), HTM 2 on $MAPbI_3$ (c), HTM 4 on $MAPbI_3$ (d), PEDOT:PSS on ITO (e), HTM 1 on PEDOT:PSS (f), HTM 2 on PEDOT:PSS (g) and HTM 4 on PEDOT:PSS (h).

The average roughness (RMS) of perovskite is 16.5 nm, which was critically reduced to 4.3 nm, 5.5 nm and 4.6 nm after coating by layer of HTM 1, HTM 2 and HTM 4, respectively. Similarly, the RMS value of PEDOT:PSS film is 3.1 nm which is also reduced to 1.4 nm, 0.6 nm and 0.5 nm by coating of HTM 1, HTM 2 and HTM 4, respectively. From comparison of morphology and average roughness of these HTMs

film on perovskite and PEDOT:PSS surface, these results indicated that these HTMs could be suitable applied for either normal configuration or inverted configuration. These HTMs could potential full coverage perovskite layer and create uniform HTM layer on the top of perovskite.

IV.3.4 Theoretical studies

Theoretical calculations were performed to understand the molecular properties of these studied compounds by using density functional theory (DFT) method. As shown in ***Figure 12***, the optimized structure of HTM 1 and HTM 2 are almost planar and the dihedral angle between TPD core and neighbor thiophene units is almost 0^{o} [54].

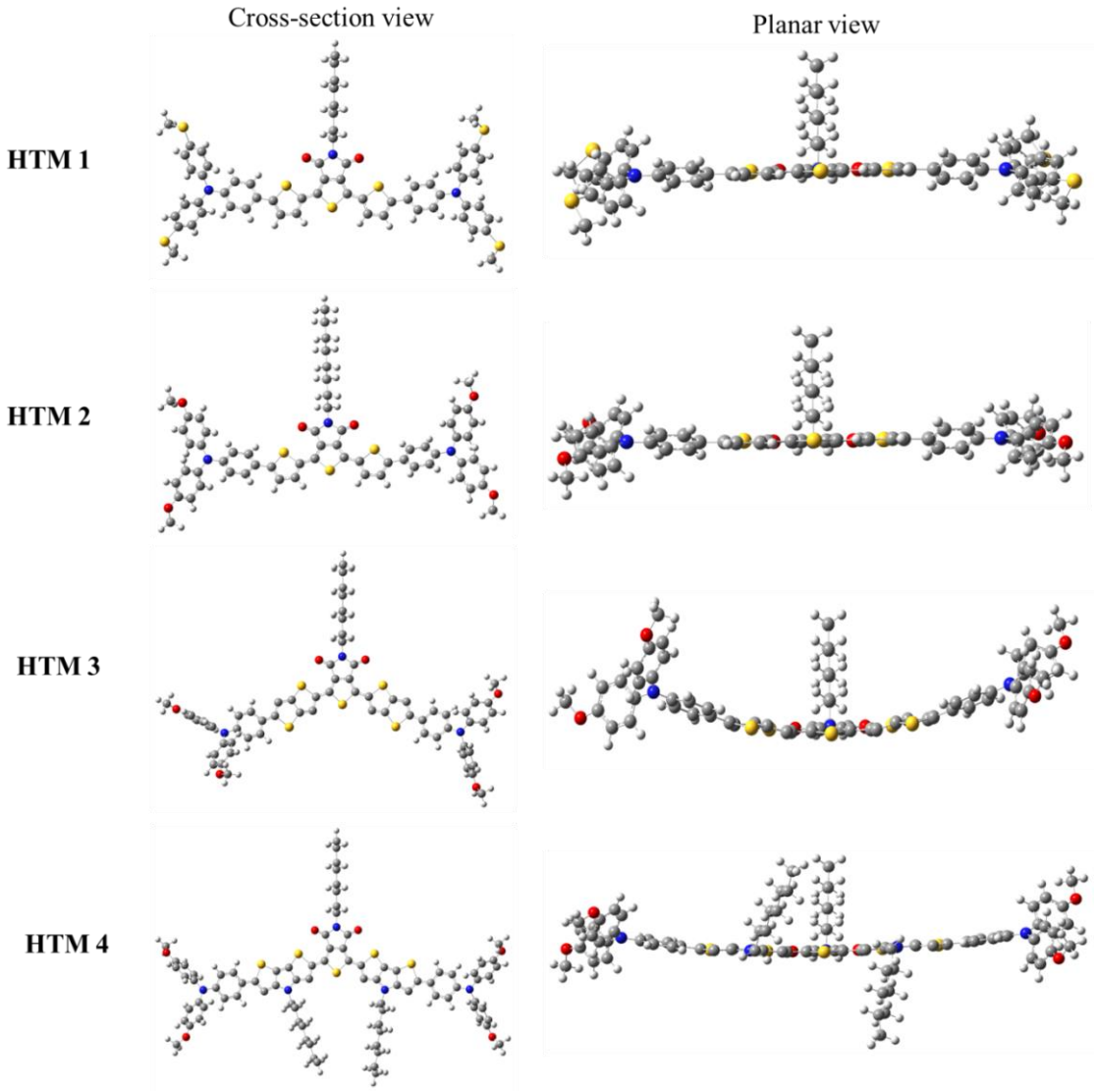

Figure 12: Optimized geometry of studied compounds in cross-section view (left) and planar view (right): S yellow, O red, N blue, C gray.

As suggested, these molecules can exist S...O interaction which leads to planar conformation. However, HTM 3 and HTM 4 showed non-planar molecular configurations. In fact, that could be explained because calculations were simulated in gas phase. Thienothiophene or dithienopyrrole could be allowed to rotate from planarity and lead to bending[55].

The simulated HOMO and LUMO energy levels of these compounds have been calculated by DFT (B3LYP/6-31G-d) method. Optimized structures and electron distribution of the frontier molecular orbitals are shown in ***Figure 13***.

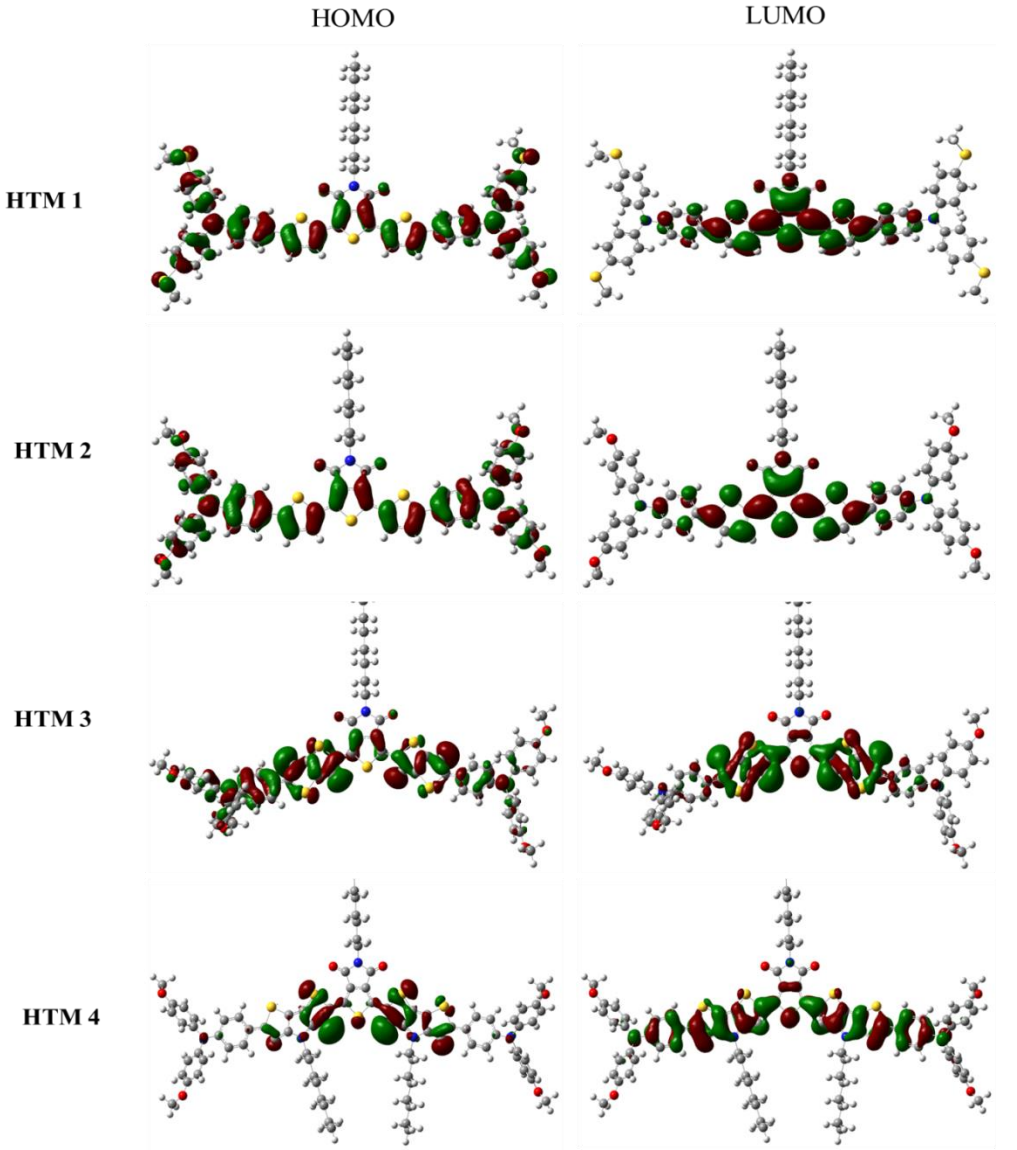

Figure 13: The distribution of electron cloud in frontier molecular HOMO-LUMO energy level of studied compounds by DFT (B3LYP/6-31G-d) method.

As observed, electron distribution in the HOMO state of HTM 1 and HTM 2 are well delocalized in whole of the molecules. This could improve intramolecular charge

transfer and increase charge transport property. However, electron density is concentrated in the core of HTM 3 and HTM 4. In fact, electrons should be distributed in donor units such as thienothiophene, dithienopyrrole or TPA. To be more accurate, these compounds should be subjected to other DFT methods to confirm these cases.

In LUMO state, electron density is localized on TPD central and peripheral thiophene. These DFT results are in agreement to objectives of this study that HTM 1 and HTM 2 possess planar structure in central backbone. This not only enhance intramolecular-intermolecular charge transfer but also efficient for charge transport properties in device performances.

IV.4. Conclusions and perspectives

To summarize, a series of new small donor-acceptor HTMs based on Thieno[3,4-c]pyrrole-4,6-dione (TPD) have been designed, synthetized and characterized to investigate their photophysical-electrochemical properties. They are illustrative for highly conjugated molecules with strong ICT character and relatively planar molecular structure. Thus, they are expected to be efficient HTMs in PSCs.

Some valuable investigations have been determined through their characters. First, by replacing methoxy group $–OCH_3$ to thiomethyl group $–SCH_3$ at *p*-position, we realized that the strength of electron donor unit is slightly reduced. However, the sulfur atoms are compatible to perovskite layer and create good interface of HTM/perovskite. Second, when increasing of π-bridge, the conjugation length is prolonged and reduced optical band gap. It could be potential for electron delocalization in whole molecules and improve charge mobility. The optical band gap is narrow enough for charge separation and avoids charge recombination. Finally, due to their planarity structure, they are favorable for uniform film formation due to improvement of stacking effect. This is not only support for intramolecular charge transfer but also enhance intermolecular charge transfer. Furthermore, they are under investigation of hole mobility and conductivity as well as optimization of PSCs.

In perspective, these compounds are promising candidate for dopant-free HTMs in PSCs because they possess strong donor-acceptor interaction, planar structure, highly conjugation system and good film formation. In future work, these novel HTMs would be employed in dopant-free PSCs along with inverted configuration PSCs.

IV.5. Experimental section

Formation of 4-bromo-N,N-bis(4-(methylthio)phenyl)aniline (compound 1)

In 100ml of Schlenk flask, 4-bromoaniline (0.5g, 1eq), 4-iodothioanisole (2.18g, 3eq), CuCl (15mg, 0.05eq), 1,10-phenanthroline (26mg, 0.05eq), KOH (2.4g, 15eq) and 15ml of toluene are added in one portion. Vacuum and argon were supplied three times to remove all of air, oxygen…Temperature was raised up to 110^{o}C and kept for 3 days. Then, the reaction was filtered through silice layer and extracted by DCM and water twice times, collected organic solution, dried over $MgSO_4$. The crude product was concentrated by reduce pressure and purified by column chromatography, eluent is mixture of petroleum ethers and ethyl acetate (9:1 v/v). The desired product is yellow solid (800mg, 66% yield). ^{1}H NMR (250 MHz, DMSO-d_6) δ 7.39 (d, *J* =10 Hz, 2H), 7.20 (d, *J* =7.5 Hz, 4H), 6.95 (d, *J* =7.5 Hz, 4H), 6.86 (d, *J* =10 Hz, 2H), 2.43 (s, 6H). ^{13}C NMR (62.5 MHz, DMSO-d_6) δ 146.91, 144.31, 133, 132.62, 128.24, 127.18, 126.84, 125.36, 124.59, 114.13, 15.74.

Formation of 4-octyl-4H-dithieno[3,2-b:2',3'-d]pyrrole (DTP) according to procedure in literature[56]

In 100ml Schlenk flask, a mixture of 3,3'-dibromo-2,2'-bithiophene (1g, 1eq), Pd_2dba_3 (0.07g, 0.025eq), BINAP (2,2'-bis(diphenylphosphino)-1,1'-binaphthyl) (192mg, 0.1eq), NaOtBu (5.93g, 20eq) and 15ml of distillated toluene were added in one portion, then argon and vacuo were supplied for several times. The temperature of reaction was increased up to 110^{o}C and vigorous stirring for 1 hour. Then, n-octylamine (0.43g, 1.1eq) was added by syringe and the reaction was kept in 24h at 110^{o}C. After cooling to ambient temperature, the reaction was filtered through silice layer, extracted by diethyl ethers and water twice times, collected organic phase and then dried over $MgSO_4$. The crude product was obtained after concentration under reduced pressure and purified by column chromatography with eluent cyclohexane: ethyl acetate (9:1 v/v). The desired product was obtained as yellow oil (0.79g, 88% yield). ^{1}H NMR (250 MHz, DMSO-d_6) δ 7.31 (d, *J* = 5 Hz, 2H), 7.21 (d, *J* = 5 Hz, 2H), 4.24 (t, *J* = 7.5 Hz, 2H), 1.17 (t, *J* = 7.5 Hz, 12H), 0.81 (t, *J* = 5 Hz, 3H). ^{13}C NMR (62.5 MHz, DMSO-d_6) δ 145.29, 129.33, 128.63, 123.68, 113.87, 112.40, 46.93, 31.64, 30.30, 29.07, 29.04, 26.81, 26.69, 22.50, 14.37.

Formation of 1,3-dibromo-5-octyl-4H-thieno[3,4-c]pyrrole-4,6(5H)-dione (compound TPD-2Br) according to procedure in literature[57].

The compound 5-octyl-4H-thieno[3,4-c]pyrrole-4,6(5H)-dione (noted TPD) is available commercially product. In round bottom, 5-octyl-4H-thieno[3,4-c]pyrrole-4,6(5H)-dione (0.4g, 1eq) was dissolved in a mixture of sulfuric acid (2ml) and trifluoroacetic acid (6.6 ml). At 0°C, NBS (0.83g, 3eq) was added in portion wise to the solution and the reaction was kept overnight in dark. The obtained brown-red solution was added slowly to 200 ml of distillated water. The white precipitates was filtered and dissolved again in DCM. The crude solution was dried over $MgSO_4$ and then concentrated. The desired product was obtained by recrystallization in methanol as off-white crystals (520mg, 80% yield). ^{1}H NMR (250MHz, $CDCl_3$) δ 3.59 (t, *J* = 7.5 Hz, 2H), 1.66-1.57 (m, 2H), 1.31-1.27 (m, 12H), 0.87 (t, *J* = 7.5 Hz, 3H). ^{13}C NMR (62.5 MHz, $CDCl_3$) δ 160.39, 134.78, 112.92, 38.83, 31.77, 29.1, 28.25, 26.78, 22.62, 14.08.

General procedure to synthesis of these compounds 1-1, 2-1, 3-1 and 4-1 (Stille coupling reaction).

In a dry Schlenk flask, 4-bromo-N,N-bis(4-methoxyphenyl)aniline (compound **1**) or 4-bromo-N,N-bis(4-(methylthio)phenyl)aniline (compound **2**) (1eq), 2-(tributylstannyl)thiophene (1.5 eq), $Pd(PPh_3)_4$ (0.1 eq) and 15 ml of toluene were added, respectively. Vacuum and argon were supplied several times to remove totally air. The temperature was kept at 110°C under argon atmosphere. The reaction was kept overnight and monitored by thin layer chromatography (TLC). The reaction was then quenched and quickly filtered through silice layer, using dichloromethane as eluent. The filtrate was then washed with water, dried over $MgSO_4$ and concentrated under reduced pressure. The crude product was then purified by column chromatography with appropriate eluent giving the pure tilted compound.

The compound 1-1 was obtained as yellow oil (1.09g, 90% yield). ^{1}H NMR (250 MHz, $CDCl_3$) δ 7.45 (m, 1H), 7.41 (m, 1H), 7.20 (m, 1H), 7.19 (s, 1H), 7.11-7.03 (m, 5H), 6.96 (s, 1H), 6.93 (s, 1H), 6.88 (t, *J* = 5Hz, 2H), 6.84 (t, *J* = 5Hz, 2H), 3.80 (s, 6H). ^{13}C NMR (62.5 MHz, $CDCl_3$) δ 156.02, 148.25, 144.69, 140.78, 128.04, 126.69, 126.66, 123.60, 121.80, 120.72, 114.82, 55.52, 22.79.

The compound 2-1 was obtained as yellow oil (0.51g, 63% yield). ^{1}H NMR (250 MHz, $CDCl_3$) δ 7.22 (s, 1H), 7.22 (s, 1H), 7.21 (s, 1H), 7.19-7.18 (m, 5H), 7.08-7.06 (m, 4H), 7.04-7.03 (m, 2H), 2.49 (s, 6H). ^{13}C NMR (62.5 MHz, $CDCl_3$) δ 146.79, 144.97, 144.15, 132.14, 128.70, 128.49, 128.04, 126.80, 124.88, 124.12, 123.55, 122.32, 41.37, 29.10, 26.86, 22.69, 17.44, 16.78, 13.68, 11.51.

The compound 3-1 was obtained as yellow solid (1.5g, 90% yield) ^{1}H NMR (250 MHz, $CDCl_3$) δ 7.42 (d, *J* = 10 Hz, 2H), 7.34 (s, 1H), 7.32 (d, *J* = 7.5 Hz, 1H), 7.24 (d, *J* = 7.5 Hz, 1H), 7.09 (d, *J* = 10Hz , 4H), 6.94 (d, *J* = 7.5 Hz, 2H), 6.85 (d, *J* = 10 Hz, 4H), 3.81 (s, 6H). ^{13}C NMR (62.5 MHz, $CDCl_3$) δ 156.03, 156, 155.67, 148.49, 146.69, 141.06, 140.54, 140.08, 137.51, 131.76, 126.75, 126.72, 126.56, 126.47, 126.39, 126.02, 121.96, 120.91, 120.34, 119.59, 114.75, 114.65, 113.75, 55.5.

The compound 4-1 was obtained as yellow oil (0.98g, 49% yield). ^{1}H NMR (250 MHz, DMSO-d_6) δ 7.53 (s, 1H), 7.49, 7.45 (d, *J* = 10 Hz, 2H), 7.30, 7.28 (d, *J* = 5 Hz, 1H), 7.23, 7.21 (d, *J* = 5 Hz, 1H), 7.03, 7.0 (d, *J* = 7.5 Hz, 4H), 6.91, 6.88 (d, *J* = 7.5 Hz, 4H), 6.80, 6.77 (d, *J* = 7.5 Hz, 2H), 4.24 (t, *J* = 12.5 Hz, 2H), 3.73 (s, 6H), 1.76 (t, *J* = 12.5 Hz, 2H), 1.28-1.16 (m, 14H), 0.79 (t, *J* = 12.5 Hz, 3H). ^{13}C NMR (62.5 MHz, DMSO-d_6) δ 156.19, 147.95, 145.58, 144.85, 141.03, 140.36, 127.46, 127, 126.12, 123.84, 120.24, 115.89, 114.27, 112.19, 107.41, 55.66, 31.64, 30.27, 29.09, 26.68, 22.49, 14.38.

General procedure to synthesis of compounds 1-2, 2-2, 3, 3-2, 4 and 4-2 (Bromide-Lithium exchange reaction)

In dry Schlenk flask, these compounds (1eq) and 30 ml of distilled THF are stirred vigorously under argon atmosphere. The temperature is cooled down to -78^{0}C by N_2 liquid and, n-BuLi (1.2 eq) is added dropwise to solution during 30 minutes. After 1 hour, the temperature is slowly to room temperature and tributyltin chloride (1.5 eq) is added slowly by syringe. The reaction is kept overnight. Color changed from light yellow to red yellow. Solvent is removed under reduced pressure, then extract crude product by diethyl ethers and water three times, collected organic phase and dried over $MgSO_4$. The crude product is concentrated and use for next steps without purification.

General procedure to synthesis of these final compounds HTM 1, HTM 2, HTM 3, HTM 4 (Stille coupling reaction)

In a dry Schlenk flask, compound 1-2 (for HTM 1) or compound 2-2 (for HTM 2) or compound 3-2 (for HTM 3) or compound 4-2 (for HTM 4) (2.5eq), TPD-2Br (1eq), $Pd(PPh_3)_4$ (0.1 eq) and 15 ml of toluene were added, respectively. Vacuum and argon were supplied several times to remove totally air. The temperature was kept at 110^{o}C under argon atmosphere. The reaction was kept overnight and monitored by thin layer chromatography (TLC). The reaction was then quenched and quickly filtered through

silice layer, using dichloromethane as eluent. The crude organic solution is collected and concentrated under reduced pressure. The crude product was then purified by column chromatography with appropriate eluent giving the pure tilted compound.

The compound HTM 1 was obtained as orange solid (0.5g, 50% yield) ^{1}H NMR (250 MHz,$CDCl_3$) δ 7.93 (d, *J* = 2.5 Hz, 1H), 7.42 (d, *J* = 5 Hz, 2H), 7.15 (s, 1H), 7.13 (d, *J* = 2.5 Hz, 2H), 7.12 (d, *J* = 2.5 Hz, 2H), 6.99 (d, *J* = 2.5 Hz, 2H), 6.97 (d, *J* = 2.5 Hz, 2H), 6.95 (s, 2H), 3.59 (t, *J* = 5 Hz, 1H), 2.42 (s, 6H), 1.61-1.55 (m, 5H), 1.49 (s, 3H), 0.87-0.83 (m, 9H). ^{13}C NMR (62.5 MHz, $CDCl_3$) δ 162.7, 147.36, 144.57, 136.19, 132.75, 128.37, 127.98, 127.08, 126.84, 125.24, 123.35, 122.75, 43.72, 31.79, 29.22, 27.84, 27.0, 26.85, 22.63, 17.53, 14.10.

The compound HTM 2 was obtained as red solid (0.3g, 50% yield). ^{1}H NMR (250 MHz, DMSO-d_6) δ 7.7 (d, *J* = 5 Hz, 1H), 7.28 (d, *J* = 5Hz, 2H), 7.11 (d, *J* = 2.5 Hz, 1H), 6.96 (d, *J* = 10 Hz, 4H), 6.86 (d, *J* = 10 Hz, 4H), 6.62 (d, *J* = 7.5 Hz, 2H), 4.0 (t, *J* = 7.5 Hz, 1H), 3.71 (s, 6H), 1.63-1.42 (m, 2H), 1.31-1.08 (m, 10H), 0.89-0.76 (m, 5H). ^{13}C NMR (62.5 MHz, $CDCl_3$) δ 162.72, 156.24, 149.01, 148.07, 140.26, 136.22, 131.15, 130.19, 127.72, 126.94, 126.66, 125.09, 122.74, 119.88, 114.79, 55.49, 31.79, 29.70, 29.22, 29.18, 29.56, 27.84, 27.01, 26.84, 22.62, 17.51, 14.09, 13.60. HRMS (ESI-MS): calculated for $C_{62}H_{57}N_3O_6S_3$ [M+H]+, 1036.3410; found: 1036.3479.

The compound HTM 3 was obtained as red solid (0.73g, 42%) ^{1}H NMR (250 MHz, $CDCl_3$) δ 8.25 (s, 1H), 7.35 (d, *J* = 7.5 Hz, 2H), 7.22 (s 1H), 7.06 (d, *J* = 7.5 Hz, 4H), 6.89 (s, 2H), 6.84 (d, *J* = 10 Hz, 4H), 3.81 (s, 6H), 3.66 (t, *J* = 7.5 Hz, 1H), 1.71-1.58 (m, 4H), 1.41-1.17 (m, 8H), 0.95-0.85 (m, 4H). ^{13}C NMR (62.5 MHz, $CDCl_3$) δ 162.60, 156.20, 149.76, 148.90, 142.23, 140.24, 138.43, 136.48, 132.46, 128.11, 126.96, 126.46, 125.79, 122.41, 119.81, 114.77, 113.27, 55.48, 31.82, 29.22, 27.86, 27.06, 26.85, 22.65, 17.51, 14.11, 13.62.

The compound HTM 4 was obtained as purple solid (0.35g, 68% yield). ^{1}H NMR (250 MHz, $CDCl_3$) δ 8.18 (s, 1H), 7.42 (s, 2H), 7.09 (d, *J* = 5 Hz, 4H), 7.03 (s, 1H), 6.93 (d, *J* = 5 Hz, 2H), 6.86 (d, *J* = 5 Hz, 4H), 4.2 (t, *J* = 5 Hz, 2H), 3.82 (s, 6H), 3.7 (t, *J* = 5 Hz, 1H), 1.91 (t, *J* = 2.5 Hz, 2H), 1.73 (t, *J* = 5 Hz, 1H), 1.69-1.62 (m, 1H), 1.4-1.26 (m, 18H), 0.95-0.85 (m, 6H). ^{13}C NMR (62.5 MHz, $CDCl_3$) 167.9, 157.7, 156.1, 145.9, 138.2, 136.9, 132.2, 128.4, 125.3, 122.8, 115.2, 59.7, 55.8, 39.8, 31.9, 29.3, 27.3, 22.7, 14.1.

References

(1) Tingting Zhu, Deyu Liu, Kaili Zhang, Yonghai Li, Zhe Liu, Xudong Gao, Xichang Bao, M. S. and R. Y. Rational Design of Asymmetric Benzodithiophene Based Photovoltaic Polymers for Efficient Solar Cells. *J. Mater. Chem. A* **2018**, *6*, 948–956.

(2) Wenjing Yi, Shuai Zhao, Huiliang Sun, Yuhe Kan, Jianwu Shi, Shisheng Wan, Chunli Li, and H. W. Isomers of Organic Semiconductors Based on Dithienothiophenes: The Effect of Sulphur Atoms Positions on the Intermolecular Interactions and Field-Effect Performances. *J. Mater. Chem. C* **2015**, *3*, 10856–10861.

(3) Roosa J. Sippola, Afshin Hadipour, Tuuva Kastinen, Paola Vivo, T. I. H.; Tom Aernouts, J. P. H. Carbazole-Based Small Molecule Electron Donors: Syntheses, Characterization, and Material Properties. *Dye. Pigment.* **2018**, *150*, 79–88.

(4) Yohei Adachi, Yousuke Ooyama, Yi Ren, Xiaodong Yin, Frieder Jäkle, and J. O. Hybrid Conjugated Polymers with Alternating Dithienosilole or Dithienogermole and Tricoordinate Boron Units. *Polym. Chem.* **2018**, *9*, 291–299.

(5) Hung-I Lu, Chih-Wei Lu, Ying-Chi Lee, Hao-Wu Lin, Li-Yen Lin, Francis Lin, Jung-Hung Chang, Chih-I Wu, and K.-T. W. New Molecular Donors with Dithienopyrrole as the Electron- Donating Group for Efficient Small-Molecule Organic Solar Cells. *Chem. Mater* **2014**, *26*, 4361–4367.

(6) Manohar Reddy Busireddy, Venkata Niladri Raju Mantena, Narendra Reddy Chereddy, Balaiah Shanigaram, Bhanuprakash Kotamarthi, Subhayan Biswas, Ganesh Datt Sharmac, J. R. V. A Dithieno[3,2-b:2′,3′-d]Pyrrole Based, NIR Absorbing, Solution Processable, Small Molecule Donor for Efficient Bulk Heterojunction Solar Cells. *Phys. Chem. Chem. Phys.* **2016**, *18*, 32096–32106.

(7) Ning, Z.; Tian, H. Triarylamine: A Promising Core Unit for Efficient Photovoltaic Materials. *Chem. Commun.* **2009**, 5483–5495.

(8) Huang, J.; Huang, H. *Organic and Hybrid Solar Cells*; Huang, J.; Huang, H., Eds.; Springer US, 2014.

(9) Liu, X.; Chen, H.; Tan, S. Overview of High-Efficiency Organic Photovoltaic Materials and Devices. *Renew. Sustain. Energy Rev.* **2015**, *52*, 1527–1538.

(10) Kaur, N.; Singh, M.; Pathak, D.; Wagner, T.; Nunzi, J. M. Organic Materials for Photovoltaic Applications: Review and Mechanism. *Synth. Met.* **2014**, *190*, 20–26.

(11) Wang, C.; Dong, H.; Hu, W.; Liu, Y.; Zhu, D. Semiconducting π-Conjugated Systems in Field-Effect Transistors: A Material Odyssey of Organic Electronics. *Chem. Rev.* **2012**, *112*, 2208–2267.

(12) Takimiya, K.; Osaka, I.; Nakano, M. π-Building Blocks for Organic Electronics: Revaluation of "Inductive" and "Resonance" Effects of π-Electron Deficient Units. *Chem. Mater.* **2014**, *26*, 587–593.

(13) Wang, J.; Liu, K.; Ma, L.; Zhan, X. Triarylamine: Versatile Platform for Organic, Dye-Sensitized, and Perovskite Solar Cells. *Chem. Rev.* **2016**, *116*, 14675–14725.

(14) Hongmei Qin, Lisheng Li, Fangqing Guo, Shijian Su, Junbiao Peng, Y. C. and X. P. Solution-Processed Bulk Heterojunction Solar Cells Based on a Porphyrin Small Molecule with 7% Power Conversion Efficiency. *Energy Environ. Sci.* **2014**, *7*, 1397–1401.

(15) Tamayo, A. B.; Walker, B.; Nguyen*, T.-Q. A Low Band Gap, Solution Processable

Oligothiophene with a Diketopyrrolopyrrole Core for Use in Organic Solar Cells. *J. Phys. Chem. C* **2008**, *112*, 11545–11551.

(16) Hongyu Wang , Feng Liu , Laju Bu , Jun Gao , Cheng Wang , Wei Wei, and T. P. R. The Role of Additive in Diketopyrrolopyrrole-Based Small Molecular Bulk Heterojunction Solar Cells. *Adv. Mater.* **2013**, *25*, 6519–6525.

(17) Coffin, R. C.; Peet, J.; Rogers, J.; Bazan, G. C. Streamlined Microwave-Assisted Preparation of Narrow-Bandgap Conjugated Polymers for High-Performance Bulk Heterojunction Solar Cells. *Nat. Chem.* **2009**, *1*, 657–661.

(18) Park, S. H.; , AnshumanRoy , Serge Beaupre, S. C.; Coates, N.; , Ji Sun Moon , Daniel Moses, Mario Leclerc, K. L. and A. J. H. Bulk Heterojunction Solar Cells with Internal Quantum Efficiency Approaching 100%. *Nat. Photonics* **2009**, *3*, 297–303.

(19) Nicolas Blouin, Alexandre Michaud, David Gendron, Salem Wakim, Emily Blair, Rodica Neagu-Plesu, Michel Belletete, G. D.; Ye Tao, M. L. Toward a Rational Design of Poly(2,7-Carbazole) Derivatives for Solar Cells. *J. Am. Chem. Soc.* **2008**, *130*, 732–742.

(20) Ming Wang, Xiaowen Hu, Peng Liu, Wei Li, Xiong Gong, Fei Huang, and Y. C. Donor-Acceptor Conjugated Polymer Based on Naphtho[1,2- c:5,6- c]Bis[1,2,5]Thiadiazole for High-Performance Polymer Solar Cells. *J. Am. Chem. Soc.* **2011**, *133*, 9638–9641.

(21) Ergang Wang, Zaifei Ma, Zhen Zhang, Koen Vandewal, Patrik Henriksson, O. I.; Fengling Zhang, and M. R. A. An Easily Accessible Isoindigo-Based Polymer for High-Performance Polymer Solar Cells. *J. Am. Chem. Soc.* **2011**, *133*, 14244–14247.

(22) Stalder, R.; Mei, J.; Graham, K. R.; Estrada, L. A.; Reynolds, J. R. Isoindigo, a Versatile Electron-Deficient Unit for High-Performance Organic Electronics. *Chem. Mater.* **2014**, *26*, 664–678.

(23) Stalder, R.; Mei, J.; Reynolds, J. R. Isoindigo-Based Donor-Acceptor Conjugated Polymers. *Macromolecules* **2010**, *43*, 8348–8352.

(24) Wade A. Braunecker, Zbyslaw R. Owczarczyk, Andres Garcia, Nikos Kopidakis, Ross E. Larsen, Scott R. Hammond, David S. Ginley, and D. C. O. Benzodithiophene and Imide- Based Copolymers for Photovoltaic Applications. *Chem. Mater.* **2012**, *24*, 1346–1356.

(25) Jessica D. Douglas, Gianmarco Griffini, Thomas W. Holcombe, Eric P. Young, Olivia P. Lee, Mark S. Chen, and J. M. J. F. Functionalized Isothianaphthene Monomers That Promote Quinoidal Character in Donor-Acceptor Copolymers for Organic Photovoltaics. *Macromolecules* **2012**, *45*, 4069–4074.

(26) Xugang Guo, Rocio Ponce Ortiz, Yan Zheng, Yan Hu, Yong-Young Noh, Kang-Jun Baeg, Antonio Facchetti, and T. J. M. Bithiophene-Imide-Based Polymeric Semiconductors for Field-Effect Transistors: Synthesis, Structure-Property Correlations, Charge Carrier Polarity, and Device Stability. *J. Am. Chem. Soc.* **2011**, *133*, 1405–1418.

(27) Jianhui Hou, Mi-Hyae Park, Shaoqing Zhang, Yan Yao, Li-Min Chen, Juo-Hao Li, and Y. Y. Bandgap and Molecular Energy Level Control of Conjugated Polymer Photovoltaic Materials Based on Benzo [1,2-b:4,5-B′] Dithiophene. *Macromolecules* **2008**, 6012–6018.

(28) Nanjia Zhou , Xugang Guo , Rocio Ponce Ortiz , Shiqiang Li , Shiming Zhang , Robert P. H. Chang , Antonio Facchetti, and T. J. M. Bithiophene Imide and Benzodithiophene Copolymers for

Efficient Inverted Polymer Solar Cells. *Adv. Mater.* **2012**, *24*, 2242–2248.

(29) Pomerantz, M. Planar 2,2′-Bithiophenes with 3,3′- and 3,3′,4,4′-Substituents. A Computational Study. *Tetrahedron Lett.* **2003**, *44*, 1563–1565.

(30) Philippe Berrouard, Francois Grenier, Jean-Remi Pouliot, Eric Gagnon, Christian Tessier, and M. L. Synthesis and Characterization of 5-Octylthieno[3,4-c]Pyrrole-4,6-Dione Derivatives as New Monomers for Conjugated Copolymers. *Org. Lett.* **2011**, *13*, 38–41.

(31) Hui Huang, Zhihua Chen, Rocio Ponce Ortiz, Christopher Newman, Hakan Usta, Sylvia Lou, Jangdae Youn, Yong-Young Noh, Kang-Jun Baeg, Lin X. Chen, Antonio Facchetti, and T. M. Combining Electron-Neutral Building Blocks with Intramolecular"conformational Locks" Affords Stable, High-Mobility P- and N-Channel Polymer Semiconductors. *J. Am. Chem. Soc.* **2012**, *134*, 10966–10973.

(32) Jiayun Zhou, Mario Leclerc, Zhao Li, Jianfu Ding, and Ye Tao, Jean-Remi Pouliot, Salem Wakim, Ta-Ya Chu, J. L. Bulk Heterojunction Solar Cells Using Thieno[3,4- c]Pyrrole-4,6-Dione and Dithieno[3,2- b:2′,3′- d]Silole Copolymer with a Power Conversion Efficiency of 7.3%. *J. Am. Chem. Soc.* **2011**, *133*, 4250–4253.

(33) Clément Cabanetos, Abdulrahman El Labban, Jonathan A. Bartelt, Jessica D. Douglas, William R. Mateker, Jean M. J. Fréchet, Michael D. McGehee, and P. M. B. Linear Side Chains in Benzo[1,2-b:4,5-B′]Dithiophene-Thieno[3,4-c] Pyrrole-4,6-Dione Polymers Direct Self-Assembly and Solar Cell Performance. *J. Am. Chem. Soc.* **2013**, *135*, 4656–4659.

(34) Yingping Zou, Ahmed Najari, Philippe Berrouard, Serge Beaupre, Badrou Reda Aıch, Ye Tao, and M. L. A Thieno[3, 4-c]Pyrrole-4, 6-Dione-Based Copolymer for Efficient Solar Cells. *J. Am. Chem. Soc.* **2010**, *132*, 5330–5331.

(35) Xugang Guo, Rocio Ponce Ortiz, Yan Zheng, Myung-Gil Kim, Shiming Zhang, Yan Hu, Gang Lu, Antonio Facchetti, and T. J. M.; Hu, Y.; Lu, G.; Facchetti, A.; Marks, T. J. Thieno[3,4- c]Pyrrole-4,6-Dione-Based Polymer Semiconductors: Toward High-Performance, Air-Stable Organic Thin-Film Transistors. *J. Am. Chem. Soc.* **2011**, *133*, 13685–13697.

(36) Ahmed Najari , Serge Beaupré , Philippe Berrouard , Yingping Zou , Jean-Rémi Pouliot , Charlotte Lepage-Pérusse, and M. L. Synthesis and Characterization of New Thieno[3,4-c]Pyrrole-4,6-Dione Derivatives for Photovoltaic Applications. *Adv. Funct. Mater.* **2011**, *21*, 718–728.

(37) Enwei Zhu , Bin Ni , Baofeng Zhao , Jiefeng Hai , Linyi Bian , Hongbin Wu, W. T. Synthesis and Photovoltaic Characterization of Dithieno[3,2-b:2′,3′-d]Thiophene-Derived Narrow-Bandgap Polymers. *Macromol. Chem. Phys.* **2014**, 227–234.

(38) Xuepeng Liu , Fantai Kong , Fuling Guo , Tai Cheng , Wangchao Chen, T. Y.; Jian Chen , Zhan'ao Tan, S. D. Influence of π-Linker on Triphenylamine-Based Hole Transporting Materials in Perovskite Solar Cells. *Dye. Pigment.* **2016**, *139*, 129–135.

(39) S. Paek, I. Zimmermann, P. Gao, P. Gratia, a K. Rakstys, G. Grancini, Mohammad Khaja Nazeeruddin, Malik Abdul Rub, b Samia A. Kosa, K. A. A. and A. M. A. Donor–π–donor Type Hole Transporting Materials: Marked π-Bridge Effects on Optoelectronic Properties, Solid-State Structure, and Perovskite Solar Cell Efficiency. *Chem. Sci.* **2016**, *7*, 6068–6075.

(40) Kamat, P. V; Christians, J. A. Role of Hole Conductors in Quantum Dot and Organometal

Perovskite Based Solid State Solar Cells. In *ECS Meeting Abstracts*; 2014; Vol. MA2014-01, p. 1282.

(41) Hou, Y.; Zhou, Z. R.; Wen, T.; Qiao, H.; Lin, Z. Q.; Ge, B.; Yang, H. Enhanced Moisture Stability of Metal Halide Perovskite Solar Cells Based on Sulfur-Oleylamine Surface Modification. *Nanoscale Horizons* **2018**.

(42) Kim, Y. J.; Park, C. E. Following the Nanostructural Molecular Orientation Guidelines for Sulfur: Versus Thiophene Units in Small Molecule Photovoltaic Cells. *Nanoscale* **2016**, *8*, 7654–7662.

(43) Nie, R.; Mehta, A.; Park, B. W.; Kwon, H. W.; Im, J.; Seok, S. Il. Mixed Sulfur and Iodide-Based Lead-Free Perovskite Solar Cells. *J. Am. Chem. Soc.* **2018**, *140*, 872–875.

(44) Nakita Kimberly Noel, Antonio Abate, Samuel David Stranks, Elizabeth Parrott, Victor Burlakov, Alain Goriely, and H. J. S. Enhanced Photoluminescence and Solar Cell Performance via Lewis Base Passivation of Organic-Inorganic Lead Halide Perovskites. *ACS Nano* **2014**, *8*, 9815–9821.

(45) Daniel Lumpi, Brigitte Holzer, Johannes Bintinger, Ernst Horkel, Simon Waid, Heinz D. Wanzenbock, Martina Marchetti-Deschmann, D.; Christian Hametner, Emmerich Bertagnolli, I. K. and J. F. Substituted Triphenylamines as Building Blocks for Star Shaped Organic Electronic Materials. *New J. Chem.* **2015**, *39*, 1840–1851.

(46) Guy Koeckelberghs, Wouter Vanormelingen, Wim Dehaen, Thierry Verbiest, A.; Samyna, P. and C. Improved Synthesis of N-Alkyl Substituted Dithieno[3,2- b:2', 3'-d]Pyrroles. *Tetrahedron* **2005**, *61*, 687–691.

(47) Kwan Wook Song, Min Hee Choi , Jang Yong Lee, D. K. M. Opto-Electrical and Density Functional Theory Analysis of Poly(2,7-Carbazole-Alt-Thieno[3,4-c]Pyrrole-4,6-Dione) and Photovoltaic Behaviors of Bulk Heterojunction Structure. *J. Ind. Eng. Chem.* **2014**, *20*, 290–296.

(48) Duan, J.; Zhang, L. H.; Dolbier, Jr., W. R. A Convenient New Method for the Bromination of Deactivated Aromatic Compounds. *Synlett* **1999**, *1999*, 1245–1246.

(49) R.E.Banks. *Organofluorlne Chemistry: Principles and Commercial Applications*; 1994.

(50) Rücker, C. The Triisopropylsilyl Group in Organic Chemistry: Just a Protective Group, or More? *Chem. Rev.* **1995**, *95*, 1009–1064.

(51) Miquel Planells, Antonio Abate, Derek J. Hollman, Samuel D. Stranks, Vishal Bharti, Jitender Gaur, Dibyajyoti Mohanty, Suresh Chand, H. J. S. and N. R. Diacetylene Bridged Triphenylamines as Hole Transport Materials for Solid State Dye Sensitized Solar Cells. *J. Mater. Chem. A* **2013**, *1*, 6949–6960.

(52) Paek, S.; Qin, P.; Lee, Y.; Cho, K. T.; Gao, P.; Grancini, G.; Oveisi, E.; Gratia, P.; Rakstys, K.; Al-Muhtaseb, S. A.; *et al.* Dopant-Free Hole-Transporting Materials for Stable and Efficient Perovskite Solar Cells. *Adv. Mater.* **2017**, *1606555*, 1–7.

(53) Govindan, V.; Yang, K. C.; Fu, Y. S.; Wu, C. G. Low-Cost Synthesis of Heterocyclic Spiro-Type Hole Transporting Materials for Perovskite Solar Cell Applications. *New J. Chem.* **2018**, *42*, 7332–7339.

(54) Guo, X.; Zhou, N.; Lou, S. J.; Hennek, J. W.; Butler, M. R.; Boudreault, P. T.; Strzalka, J.; Morin, P.; Leclerc, M.; Lo, J. T.; *et al.* Bithiopheneimide − Dithienosilole/Dithienogermole Copolymers for E Ffi Cient Solar Cells: Information from Structure − Property − Device Performance Correlations

and Comparison to Thieno[3,4 - c]Pyrrole- 4,6-Dione Analogues. *J Am Chem Soc* **2012**, *134*, 18427–18439.

(55) Salzner, U.; Aydin, A. Improved Prediction of Properties of π-Conjugated Oligomers with Range-Separated Hybrid Density Functionals. *J. Chem. Theory Comput.* **2011**, *7*, 2568–2583.

(56) Liu, J.; Zhang, R.; Sauvé, G.; Kowalewski, T.; McCullough, R. D. Highly Disordered Polymer Field Effect Transistors: N-Alkyl Dithieno[3,2-b:2′,3′-d]Pyrrole-Based Copolymers with Surprisingly High Charge Carrier Mobilities. *J. Am. Chem. Soc.* **2008**, *130*, 13167–13176.

(57) Akinori Saeki, Saya Yoshikawa, Masashi Tsuji, Yoshiko Koizumi, Marina Ide, Chakkooth Vijayakumar, and S. S. A Versatile Approach to Organic Photovoltaics Evaluation Using White Light Pulse and Microwave Conductivity. *J. Am. Chem. Soc.* **2012**, *134*, 19035–19042.

CONCLUSIONS AND PERSPECTIVES

My doctoral thesis was focused on the rational design and molecular engineering of a variety of small organic molecules as novel hole transporting materials. The main objectives were to study the relationship between the molecular structure and device performance, to bring fundamental understandings of the requirements properties of the HTMs and further to improve photovoltaic performances in perovskite solar cells. They were synthesized via cheap precursors and classical chemistry reaction with short-steps, facile preparation and purification. Their intrinsic properties have been characterized by different physical-chemical characterizations to confirm their structure, purity and possibilities for HTMs.

Firstly, the *p*-type small organic molecules based on Thieno[3,2-b]thiophene have been investigated. Different molecular configurations have been studied and compared in their properties and device performances. Their HOMO and LUMO energy levels are in good alignment with the energy levels of the perovskite absorber. Moreover, these materials exhibit good interfacial contact with perovskite which could enhance hole injection from perovskite into HTM. Remarkable PCE of 13.7% was obtained using TT-2,5 TPA as linear conjugated molecule. Whereas, non- linear conjugated molecule TT-3,6 TPA was only recorded PCE of 0.7%. Therefore, better photovoltaic performance has been obtained for longer conjugated molecule and higher hole mobility. Interestingly, promising 3D molecular structure TT-4 TPA shows amorphous nature, large steric hindrance which is desirable for homogeneous film morphology. The initial PCE of 13.66% was recorded with high J_{SC} value.

Secondly, donor-acceptor molecular HTMs based on 9(10H)Acridone and Thioxanthone have been studied. These species have been investigated due to their rich chemistry possibilities, facile preparation and low-cost. The unsymmetrical D-A and symmetrical D-A-D structure molecules have been elaborated by incorporation with various electron donor groups such as diphenylamine (DPA), triphenylamine (TPA), phenothiazine and carbazole. These molecules exhibited intramolecular charge transfer

which could improve hole mobility. Their HOMO-LUMO energy levels are compatible to the valence band of the perovskite that could facilitate hole transfer process. Moreover, they possess high thermal stability, smooth film with negligible roughness and hydrophobicity. By changing from tertiary amine group of Acridone to sulfur atom of Thioxanthone, their physical properties have been compared. They exhibit some advantages-disadvantages features which could affect to device performances. Some of these new compounds have been employed as HTMs in PSCs. In an extended part of Acridone derivatives, 9,9'-biacridone core as a new HTMs has been studied. It was modified from Acridone derivatives to *p*-type molecules by McMurry homocoupling reaction. They possess 3D structure which is expected for amorphous structure, large steric hindrance with homogeneous film morphology.

Finally, planar donor-acceptor molecular HTMs have been designed and elaborated based on Thieno[3,4-c]pyrrole-4,6-dione species. By strong donor-acceptor interaction, they exhibited strong intramolecular charge transfer, long absorption wavelength and low optical band gap. Due to planar molecular structure, good π-π stacking effect has been demonstrated which could enhance intermolecular charge transfer. High hole mobility and conductivity are expected with such materials. These latter could be used as additive-free HTMs for PSCs.

To summarize, several molecules in my thesis have been investigated. They demonstrated how a small modification on the molecular structure such as different atoms, various electron donors, or the length of the π-conjugated system can affect the properties of the materials and consequently improve photovoltaic performances. The strategies of rational design by simple synthetic schemes with a minimized number of steps were discussed, enabling to tune of favorable characteristics which are necessary for efficient HTMs in perovskite solar cells such as high hole mobility, matching energy levels, thermal stability, and hydrophobicity.

In perspectives, these materials have been designed for photovoltaic application. They will be employed as novel HTMs in PSCs. A promising 3D molecule TT-4TPA will be further exploited in device optimization to improve device performance. The class of planar donor-acceptor molecules based Thieno[3,4-c]pyrrole-4,6-dione will be employed in PSCs as efficient HTM and additive-free HTM as well. To further improve PSCs performance, we need to take into account not only development of new HTMs but also

optimize the device fabrication to increase power conversion efficiency of PSCs, reproducibility as well as their stability in long-term operation. Moreover, due to strong light emitting property, these new materials could be investigated as visible light absorbing photo-initiators for polymerization and thermally activated delayed fluorescence based materials.

GENERAL APPENDIX

All used chemicals and solvents were purchased from chemical companies and used as received without further purification, unless mentioned otherwise. Toluene was dried by distillation from sodium metal. Purification of products was performed by column chromatography on silica gel from Merck with a grain size of 0.04–0.063 mm (flash silica gel, Ge- duran Si 60) eluting with analytically pure solvents. For analytical thin layer chromatography, "60 F254" aluminum substrates coated with silica gel from Merck were used.

NMR (^{1}H and ^{13}C) spectra were recorded on a Bruker DPX-250 FT- NMR spectrometer. Chemical shifts are given in ppm using the residual solvent signal as internal reference.

Mass spectroscopy was performed by the Spectropole of Aix-Marseille University (France). ESI mass spectral analyses were recorded with a 3200 QTRAP (Applied Biosystems SCIEX) mass spectrometer. The HRMS mass spectral analysis was performed with a QStar Elite (Applied Biosystems SCIEX) mass spectrometer.

UV/Vis spectra were measured on a Jasco (V-570) UV/Vis/NIR spectrophotometer. The fluorescence spectra were recorded in dichloromethane using a Jasco FP 6200 spectrometer.

Thermogravimetric analysis (TGA) was carried out on a TA Instrument Q50 TGA under argon flow at a heating rate of 20°Cmin^{-1}. The temperature of thermal degradation (T_d) was measured at the point of 5% weight loss. Differential scanning calorimetry (DSC) was performed on a TA Instruments Q100 calorimeter, calibrated with indium and flushed with argon.

The oxidation potential (E_{ox}) of the investigated compounds were measured in dichloromethane by cyclic voltammetry, scan rate 100 mV s^{-1}, with tetrabutylammonium hexafluorophosphate (0.1M) as a supporting electrolyte in a standard one-compartment, three-electrode electrochemical cell under an argon stream using a VSP BioLogic potentiostat. The working, reference and counter electrodes were platinum disk (Ø = 1 mm), Pt wire pseudoreference, and gold electrodes, respectively. Ferrocene was used as an internal standard, and the potentials were referred to the reversible formal potential of this compound.

The atomic force microscopy (AFM) experiments were performed in tapping mode with a Nanoscope V controller coupled with an Icon microscope from Bruker. Measurements were carried out in air at room temperature.

Contact angles (CA) were determined using a D SA10-Mk2 (Krüss, Germany) in air at room temperature with a 5 µL ultrapure water drop. For each sample, five drops per sample were analysed. The reported contact angle values correspond to the average of all measurements with an error bar corresponding to the standard deviation.

Computational details: All quantum mechanical calculations were computed using Gaussian Package.[39] All geometry optimizations were performed using density functional theory (DFT) with the global hybrid exchange-correlation functional B3LYP[40,41] and all minima on the potential energy surface were verified via a calculation of vibrational frequencies, ensuring no imaginary frequencies were present. The Pople double-zeta basis set with a double set of polarization functions on non-hydrogen atoms (6-31G(d,p))[42] was used throughout. This computational approach was chosen in consistency with previous works, as it provides good agreement with experimental data. Excited states were probed using time dependent density functional theory (TD-DFT) using the same functional. All transitions (singlet-singlet) were calculated vertically with respect to the singlet ground state geometry. Solvent effects were taken into account by using the implicit polarizable continuum model (PCM).[43,44] DCM where chosen in analogy with the experiments. Computed spectra were simulated by convoluting each transition with Gaussians functions -centered on each absorption maximum- using a constant full width at half maximum (FWHM) value of 0.2 eV.

X-ray diffraction: X-ray diffraction data for compound **TT-3,6-TPA and A-2TPA** were collected by using a VENTURE PHOTON100 CMOS Bruker diffractometer with Micro-focus IµS source MoKα radiation. Crystals were mounted on a CryoLoop (Hampton Research) with Paratone-N (Hampton Research) as cryoprotectant and then flashfrozen in a nitrogen-gas stream at 100 K. For compounds, the temperature of the crystal was maintained at the selected value (100K) by means of a 700 series Cryostream cooling device to within an accuracy of ±1K. The data were corrected for Lorentz polarization, and absorption effects. The structures were solved by direct methods using SHELXS-97[1] and refined against F^2 by full-matrix least-squares techniques using

SHELXL-2017[2] with anisotropic displacement parameters for all non-hydrogen atoms. Hydrogen atoms were located on a difference Fourier map and introduced into the calculations as a riding model with isotropic thermal parameters. All calculations were performed by using the Crystal Structure crystallographic software package WINGX.[3] CCDC 1811031 contains the supplementary crystallographic data for this paper. These data can be obtained free of charge from the Cambridge Crystallographic Data Centre via http://www.ccdc.cam.ac.uk/Community/Requestastructure.

Solar cell device fabrication in Japan: PSCs were fabricated on FTO-coated glass with the sheet resistance of FTO approximately 7 Ω cm^{-2}. Initially, FTO electrodes were patterned by etching FTO with 2 M HCl and zinc powder. Substrates were then cleaned sequentially in detergent, water, ethanol and acetone. After UV-induced ozone treatment, a compact layer of TiO_2 (around 50 nm in thickness) was deposited by spraying a solution of 300 μL titanium diisopropoxide bis(acetylacetonate) (Aldrich) in 4 mL of ethanol and annealed at 500 ºC for 30 min. A 300-nm thick mesoporous TiO_2 (DSL 18NR-T, DYESOL) film was spin-coated onto the compact-TiO_2/FTO substrate at speed of 5000 r.p.m. for 30s and calcinated at 500 ºC for 30 min in air to remove organic components. After transferring the films to a N_2-filled glove box, the perovskite layers were then deposited by spin-coating a mixed precursor solution of methylammonium iodide and lead Iodide (1:1 molar ratio, final concentrations 1.1 M lead Iodide and 1.1 M methylammonium iodide) in dimethylsulphoxide (DMSO) at speed of 1000 r.p.m. and 5000 r.p.m. for 45 and 20 s, respectively. During spinning, toluene (0.5 mL) was dripped on the substrates to extremely uniform and dense perovskite layers via a CH_3NH_3I–PbI_2–DMSO intermediate phase [10]. The thickness of $CH_3NH_3PbI_3$ perovskite layer was approximately 400 nm. The films were annealed at 120ºC for 10 min in the glovebox. Sequence, a solution containing TT-2,5-TPA or TT-3,6-TPA HTM in chlorobenzene at solid concentration of 37.3 mg/mL was spin-cast onto $CH_3NH_3PbI_3$ perovskite layer speed of 3000 r.p.m. for 30s. To improve the charge carrier mobility of HTM layers as well the photovoltaic performance of PSCs, the HTM solutions were added 24 μL of 4-tert-butylpyridine (96%, Sigma-Aldrich), 14 μL lithium bis (trifluoromethanesulfonyl)imide (LiTFSI, Tokyo chemical industry) solution (516.7 mg LI-TSFI in 1 ml acetonitrile, 99.8%, Sigma-Aldrich), and 6 μl of tris(2-(1H-pyrazol-1-yl)-

4-tertbutylpyridine) cobalt(III) bis(trifluoromethylsulphonyl)imide (FK209, Luminescence Technology Corp.) solution (375.8 mg FK209 in 1 ml acetonitrile). The devices in this study have the active areas of 0.2 cm^2.

Solar cell device fabrication in Korea: The processing in fabrication of mesoscopic perovskite solar cells via one-step coating was followed as previous literature (***Scheme 1***). Initially, FTO electrodes were patterned by etching FTO with 37% HCl and zinc powder. Substrates were then cleaned sequentially in detergent, water, ethanol and acetone. After UV-induced ozone treatment, a compact layer of TiO_2 (around 50 nm in thickness) was deposited by spin coating a solution of 100 μL titanium diisopropoxide bis(acetylacetonate) (Sigma-Aldrich) in 1.27 mL of 1-butanol at speed of 2800 r.p.m. for 25s and annealed at 125 ºC for 5 min. A 300-nm-thick mesoporous TiO_2 (DSL 18NR-T, DYESOL) film was spin-coated onto the compact-TiO_2/FTO substrate at speed of 2800 r.p.m. for 20s and annealed at 125 ºC for 5 min, then calcinated at 500 ºC for 60 min in air to remove organic components. In ambient temperature, the perovskite layers were then deposited by spin-coating a mixed precursor solution of MAI and PbI_2 (1:1 molar ratio) in DMSO and DMF at speed of 4000 r.p.m. for 25s. After 10s spinning, diethyl ether (0.5 mL) was dripped on the substrates to extremely uniform and dense perovskite layers via a CH_3NH_3I–PbI_2–DMSO intermediate phase. The thickness of $CH_3NH_3PbI_3$ perovskite layer was approximately 400 nm. The films were annealed at 65ºC for 1 min and 100 ^{0}C for 9 min. Sequence, a solution containing TT-4-TPA in chlorobenzene at solid concentration of 60 mg/mL was spin-cast onto $CH_3NH_3PbI_3$ perovskite layer speed of 3000 r.p.m. for 30s. To improve the charge carrier mobility of HTM layers as well the photovoltaic performance of PSCs, the HTM solutions were added 4.3 μL of 4-tert-butylpyridine (96%, Sigma-Aldrich), 2.4 μL lithium bis (trifluoromethanesulfonyl)imide (LiTFSI, Tokyo chemical industry) solution (520 mg LI-TSFI in 1 ml acetonitrile, 99.8%, Sigma-Aldrich). The devices in this study have the active areas of 0.13 cm^2.

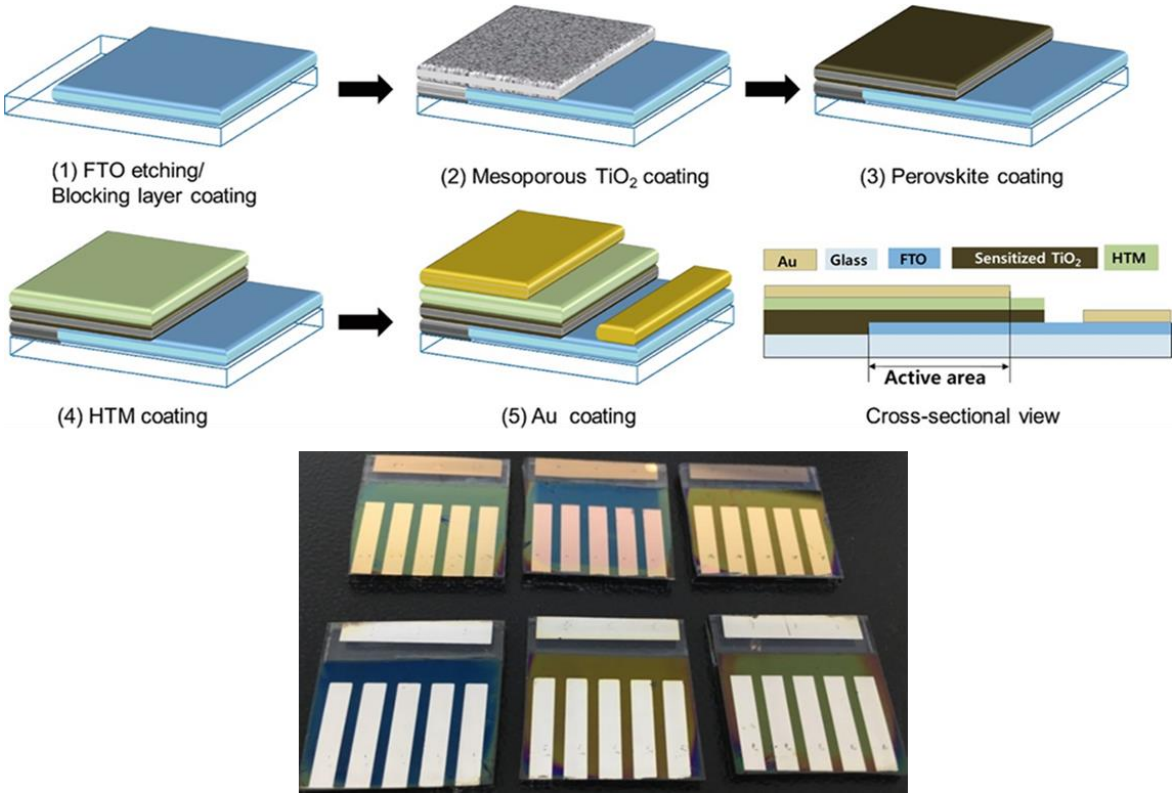

Scheme 1: Procedure to fabrication of typical mesoscopic perovskite solar cells (top). Figure adapted from reference. PSCs used various HTMs with Ag or Au as metal electrode.

Solar cells measurement and characterization: The *J-V* characteristics of the PSCs using TT-2,5 TPA and TT-3.6 TPA HTM layers were measured by using a 6243 DC voltage current source/monitor under illumination of 100 mW cm^{-2} (WXS-50S-1.5, solar simulator equipped with an AM 1.5 filter). The light intensity was calibrated with a monocrystalline silicon solar cell. During the *J-V* measurement, the aperture with area of 0.2 cm^2 is used and the temperature of device is kept at 25 ºC. While the reverse *J-V* curves were scanned from 1.2 to -0.1 V with 0.0065 V steps, integrating the signal for 16.7 mS, the forward *J-V* curves were scanned from -0.1 to 1.2 V with 0.026 V steps, integrating the signal for 1.67 S.